

Zahra
Gholamvand

Development of novel integrated photocatalytic adsorbents (IPCAs) for organics removal from water & wastewater

PhD

Zahra Gholamvand

2015

Development of novel integrated photocatalytic adsorbents (IPCAs) for organics removal from water & wastewater

Zahra Gholamvand M.Sc.

Thesis Submitted for the Award of PhD

School of Chemical Sciences
Dublin City University

Supervisors
Dr. Kieran Nolan
Dr. Anne Morrissey

2015

To my dear Mom and Dad

Declaration

I hereby certify that this material, which I now submit for assessment on the programme of study leading to the award of PhD is entirely my own work, and that I have exercised reasonable care to ensure that the work is original, and does not to the best of my knowledge breach any law of copyright, and has not been taken from the work of others save and to the extent that such work has been cited and acknowledged within the text of my work.

Signed: _____ ID No.: _____ Date: _____

Abstract

The presence of pharmaceutical compounds in the aquatic environment and their possible effects on living organisms has emerged as a serious environmental concern particularly as conventional wastewater treatments such as adsorption, ozonation, UV and bio-degradation can only partially remove them. Among various treatment technologies, considerable attention has been paid to semiconductor photocatalysis due to complete degradation of organic compounds, minimization of waste disposal and energy consumption and cost reduction. Titanium dioxide (TiO_2) is the most widely studied semiconductor photocatalyst for water treatment. However, there are few problems associated with TiO_2 photocatalysts such as UV light requirement due to wide band gap, poor photocatalytic efficiency due to high recombination rate of photo-generated electron-hole pairs, particle aggregation, small porosity and specific surface area, expensive recovery and reuse which impede its application as an industrial wastewater treatment process. Graphene, the most recent member of carbonaceous nanomaterials has been extensively studied for wide variety of applications due to its unique electronic, mechanical and thermal properties. High surface area exfoliated graphene sheets with tuneable surface chemistry is an attractive two-dimensional platform for anchoring various type of metallic and semiconducting materials in order to enhance their performance for catalysis, sensing, electronic, optoelectronic, thermoelectric, energy conversion and storage application. This research has focused on the synthesis and modification of TiO_2 nanomaterials with graphene to overcome TiO_2 disadvantages and modify TiO_2 photocatalysts with a primary objective of enhancing its photocatalytic performance under UV light irradiation and developing visible-light responsive TiO_2 -based photocatalysts. For this purpose different TiO_2 nanostructures with different dimensionality (nanoparticle, nanotube, nanofiber and beads) were modified with graphene oxide via solution mixing, sol-gel and hydrothermal methods. The result were compared with commercially available Degussa P25 TiO_2 particles as a bench mark. Few pharmaceutical model compounds (diclofenac, carbamazepine, famotidine etc.) were used in order to study photocatalytic efficiency of these composites and degradation kinetics of drugs under UV and visible light using HPLC. Promising results were obtained proving the enhancement of UV and visible light photocatalytic activity of graphene incorporated composite comparing to pure TiO_2 nanostructures. In synthesis procedure graphene acts like a structure directing agent. For example more uniform TiO_2 nanoparticles with smaller crystallite size, higher visible absorption, higher surface area and higher porosity can be synthesised in presence

of graphene oxide compared to similar materials without graphene. It was found that TiO₂ nanotubes with diameters less than 15 nm immobilised on the surface of the graphene showed the highest photocatalytic activity under both UV and visible light as a result of mesoporous structure of nanotubes and facilitated charge transfer between one-dimensional TiO₂ and two dimensional graphene sheets. We found that hydrothermal process is an efficient method to produce graphene/TiO₂ composites from graphene oxide since crystallisation of TiO₂ and reduction of graphene oxide can be done in one pot without need for post annealing or reduction treatments. Analytical techniques such as FTIR, RAMAN and UV-Vis spectroscopy, AFM, SEM and TEM microscopy, XRD, contact angle, four point probe conductivity measurements and BET had revealed that high adsorption and photocatalytic activity is related to graphene oxide planar structure, oxygen containing functional groups, and large surface area. Adsorption properties of graphene oxide were studied using freeze dried graphene oxide sponge under different experimental conditions. The result indicate that graphene oxide is extraordinarily capable of extracting wide range of pharmaceutical compounds rather rapidly (equilibrium reached in less than an hour comparing days for activated carbon) with a higher efficiency than that of activated carbon. According to microscopic images, XRD, EDX, NMR and thermal analysis we suggested that GO initiates crystallisation of the pharmaceutical on its surface and entire solution rather than physical adsorption. It can be due to low surface energy of graphene oxide as a suitable nucleation and growth site for compounds dissolved in water.

An important highlight of current work is using Graphene oxide which is produced economically and in large scale with improved dispensability and adsorption properties instead of expensive pristine graphene. Finally nanomaterials especially catalysts prepared by these simple and scalable method are potentially attractive for commercial employment.

Keywords: Graphene oxide, TiO₂, Nanoparticles, Nanotubes, Nanofibers, Photocatalysis, Pharmaceutical, Adsorption.

Table of Content

ACKNOWLEDGEMENTS.....	1
CHAPTER 1: INTRODUCTION	2
1.1. Motivation: water scarcity.....	2
1.2. Water pollution: organic compounds.....	3
1.3. Pharmaceutical pollution	4
1.3.1. Occurrence of pharmaceuticals in raw water	4
1.3.2. Occurrence of pharmaceuticals in drinking water	6
1.3.3. Risks and hazards	7
1.4. Pharmaceuticals removal from conventional wwtps	8
1.5. Tertiary treatments for pharmaceuticals removal	11
1.5.1. Advanced oxidation processes (aops)	12
1.5.2. Adsorption	14
1.6. Semiconductor photocatalysis for water treatment	15
1.7. Thesis aims and objectives	17
1.8. Thesis structure	19
CHAPTER 2: BACKGROUND & LITRATURE REVIEW	20
2.1. Introduction	20
2.2. Photocatalysis: theory and principles	20
2.3. Why TiO ₂	22
2.4. Structure and properties of TiO ₂	22
2.5. Modification of pristine TiO ₂	23
2.5.1. Morphological modification	23
2.5.2. Sensitisation (surface modification)	27
2.5.3. Doping (band-gap modification)	28
2.6. TiO ₂ modified by carbonaceous nanomaterials.....	28
2.6.1. Activated carbon/ TiO ₂	29
2.7. Carbon allotropes.....	30
2.8. Graphene: definition and structure	31
2.9. Graphene: properties and applications	32
2.10. Graphene: synthesis methods.....	32
2.10.1. Micromechanical cleavage.....	33
2.10.2. Epitaxial growth and chemical vapour deposition (CVD)	33
2.10.3. Intercalation-exfoliation method	34
2.10.4. Ion exchange-exfoliation method	35

2.10.5. Liquid phase exfoliation (shear-mixing method)	35
2.11. Oxidation/ reduction method	36
2.11.1. Oxidation to graphite oxide	37
2.11.2. Graphene oxide (GO)	38
2.11.3. Reduction methods	38
2.12. Comparison of graphene production methods	41
2.13. Photocatalysis enhancement in carbon nanotube/ TiO ₂	42
2.14. Graphene/ TiO ₂ composite.....	44
2.15. Photocatalytic degradation of pollutants by rGO/ TiO ₂	46
2.16. Mechanism of photocatalytic enhancement in graphene/ TiO ₂	46
CHAPTER 3: MATERIALS & METHODS	49
3.1. Introduction	49
3.2. Materials and chemical reagents.....	49
3.3. Apparatus	50
3.3.1. UV irradiation experimental set-up	51
3.3.2. General method for UV-photocatalysis studies.....	52
3.3.3. Visible irradiation set-up	53
3.3.4. General method for visible-photocatalysis studies	54
3.3.5. Control experiments.....	54
3.3.6. HPLC-UV chromatographic methods	54
3.4. Material synthesis and experimental section of chapter 4.....	55
3.4.1. Chemicals	55
3.4.2. Synthesis of GO film and GO sponge.....	57
3.4.3. Immobilisation of GO on the surface of porous substrates	59
3.4.4. Synthesis of Dolomite/GO composite	60
3.4.5. Adsorption experiments: Graphene oxide.....	61
3.4.6. Adsorption experiments: GO/Dolomite and other substrates.....	62
3.5. Material synthesis and experimental section of chapter 5.....	64
3.5.1. Chemicals	64
3.5.2. Sol-gel synthesis of TiO ₂ nanoparticles	64
3.5.3. In-situ synthesis of TiO ₂ nanoparticles on GO	65
3.5.4. Immobilisation of pre-synthesised TiO ₂ on GO	67
3.6. Material synthesis and experimental section of chapter 6.....	68
3.6.1. Chemicals	68
3.6.2. Synthesis of TiO ₂ nanotubes (TNTs)	68
3.6.3. Synthesis of TNTs/rGO	69
3.6.4. Synthesis of rGO/ TiO ₂ nanofiber composite (TNFs/rGO)	70

3.7. Material synthesis and experimental section of chapter 7.....	70
3.7.1. Chemicals	70
3.7.2. Synthesis of TiO ₂ beads (TBs)	70
3.7.3. Synthesis of rGO/TBs	71
3.8. Analytical methods	71
3.8.1. High performance liquid chromatography (HPLC).....	71
3.8.2. UV/Vis Spectroscopy and Beer-Lambert.....	72
3.9. Characterisation techniques	73
3.9.1. Field Emission Scanning Electron Microscopy (FESEM)	73
3.9.2. Transmission Electron Microscopy (TEM) and SAED.....	74
3.9.3. Powder X-Ray Diffraction (XRD)	75
3.9.4. Attenuated Total Reflectance Fourier Transform Infrared Spectroscopy (ATR -FTIR)....	77
3.9.5. Raman Spectroscopy.....	77
3.9.6. UV-Visible Spectroscopy	79
3.9.7. BET Gas adsorption Isotherm	80
CHAPTER 4: GRAPHENE AND GRAPHENE OXIDE AS AN ADSORBENT	84
4.1. Introduction	84
4.2. Result and Discussion.....	87
4.2.1. Morphological study.....	87
4.2.2. FTIR characterisation of GO and rGO	99
4.2.3. XRD characterisation of GO and rGO.....	100
4.2.4. Surface area measurements of GO and rGO.....	102
4.2.5. UV/Vis spectroscopy of GO and rGO	106
4.2.6. Raman spectroscopy characterisation of GO and rGO	107
4.2.7. Liquid phase exfoliation of graphene (LPE).....	112
4.3. Graphene oxide integrated adsorbents	114
4.3.1. Characterisation of dolomite/GO integrated adsorbent	114
4.3.2. Adsorption Studies	119
4.3.3. Batch adsorption experiments of pharmaceuticals	127
4.4. Adsorption Kinetic study.....	128
4.4.1. Pharmaceutical adsorption by GO	128
4.4.2. Mechanism of adsorption	133
4.4.3. Pharmaceutical cocktail adsorption.....	141
4.5. Summary	146
4.6. Conclusion.....	146
CHAPTER 5: TiO₂ NANOPARTICLE/GRAPHENE NANO-COMPOSITE SYNTHESIS AND PHOTOCATALYSIS PROPERTIES.....	148

5.1. Introduction	148
5.2. Result and Discussion.....	149
5.2.1. Sol-gel synthesis of TiO ₂ nanoparticles on GO.....	149
5.2.2. Immobilization of pre-synthesised TiO ₂ P25 nanoparticles on GO.....	156
5.2.3. Adsorption Properties of GO/TiO ₂ Nano-composites	164
5.2.4. Photocatalytic properties of nano-particulate GO/TiO ₂ composites	168
5.2.5. Photocatalytic reduction of GO to rGO in GO/TiO ₂ composite.....	173
5.2.6. Thermal and Hydrothermal reduction of GO in GO/TiO ₂ composite.....	176
CHAPTER 6: TiO₂ NANOTUBES/GRAPHENE COMPOSITE SYNTHESIS AND	
PHOTOCATALYTIC PROPERTIES.....	186
6.1. Introduction	186
6.2. Results and Discussion	187
6.2.1. TiO ₂ nanotubes	187
6.2.2. UV and Visible light Photocatalytic Properties.....	197
6.2.3. TiO ₂ nanofiber	201
6.3. Conclusion.....	206
CHAPTER 7: TiO₂ BEADS/GRAPHENE COMPOSITE SYNTHESIS AND	
PHOTOCATALYTIC PROPERTIES.....	208
7.1. Introduction	208
7.2. Results and Discussion	208
7.3. UV and Visible light Photocatalytic activity.....	211
7.4. Conclusion.....	213
CHAPTER 8: CONCLUSION	214
CHAPTER 9: FUTURE WORK	217
REFERENCES... ..	219

List of figure

Figure 1-1: Breakdown of fresh water resources	3
Figure 1-2: water contaminant's pathway.....	4
Figure 1-3: Pathways for the contamination of the surface and ground water by pharmaceuticals.....	5
Figure 1-4: A diagram of a modern sewage treatment plant with different possible processes	9
Figure 1-5: Removal of drug residues in a STP. Concentrations in influent (raw sewage), effluent of biological filter (trickling filter) and effluent of activated sludge in $\mu\text{g/l}$	10
Figure 2-1. Mechanism of the photocatalytic effect of TiO_2	21
Figure 2-2: Crystal structures of anatase (a), rutile (b) and brookite (c).....	23
Figure 2-3: Schematic illustration of structural dimensionality of TiO_2 attached to the surface of graphene	24
Figure 2-4: Various morphology of zero-dimensional TiO_2 , (a): TEM image of flower-like TiO_2 particle (b): SEM image of hierarchical TiO_2 microspheres, (c): SEM of TiO_2 meso-porous spheres, and (d) TEM image of TiO_2 hollow spheres	25
Figure 2-5: Various morphologies of 1-D TiO_2 ; (a): nanotubes via electrospinning, (b): nanotube array via Ti Anodisation, (c): nanofibres via hydrothermal deposition on Ti foil, (d): nanotube via alkaline hydrothermal, (e): hierarchical TiO_2 nanorods grown on electrospun TiO_2 nanofibres via hydrothermal, (f): nanowires via hydrothermal method	27
Figure 2-6: Schematic illustration of carbon allotropes.....	31
Figure 2-7: Schematic illustration of scotch-tape method followed by transfer on silicon wafer.....	33
Figure 2-8: Synthesis and transfer of graphene by CVD; (a), (b) Growing 2D graphene on a surface of a metal. (c) Polymer casting on top of graphene, (d) etching away the metal substrate, (e) stamping graphene on the substrate of choice, (f) dissolving the sacrificial polymer layer	34
Figure 2-9: Schematic description of different exfoliation methods; (a) Ion intercalation (ions: yellow spheres), swelling, and then agitation results in an exfoliated dispersion. (b) Ion exchange of charges between the layers (red spheres) with other larger ions (yellow spheres) which results in exfoliated dispersion after agitation. (c) Sonication assisted exfoliation of layered crystal in a “good” solvents result in exfoliated nanosheets stabilized against re-aggregation. In the contrary in a “bad” solvents re-aggregation and sedimentation will occur	36
Figure 2-10: Schematic illustration of rGO synthesis via oxidation-reduction of graphite	37
Figure 2-11: Lerf-Klinowsky model for chemical structure of graphite oxide	38
Figure 2-12: Reduction process of graphite oxide paper (b) rGO dispersed after reduction by hydrazine. Below each vial is a three-dimensional molecular model of GO (carbon in grey, oxygen in red and hydrogen in white) and rGO; (c) A proposed reaction pathway for epoxide reduction by hydrazine ...	40
Figure 2-13: TiO_2/CNT morphologies and inter-phase contact. (a) Random mixture of TiO_2 nanoparticles and CNTs, (b) TiO_2 coated CNTs, and (c) CNTs wrapped around large TiO_2 nanoparticles	44

Figure 2-14: Proposed mechanism for photocatalysis enhancement in graphene/TiO ₂ composites, (I) graphene act as an electron trapper and shuttle, (II) graphene act as a photosensitizer and produces charge carriers due to interacting with photons (a) and act as impurity and doping agent reducing the band gap of the TiO ₂ due to the Ti-O-C bonds formation, (III) Surface Plasmon resonance under NIR irradiation leads to photothermal effect of rGO. Thermal energy promotes carrier mobility on rGO sheets and thus results in the improved photodegradation activity.....	47
Figure 3-1: photograph and schematic of photochemical reactor with labelled components	52
Figure 3-2: Indoor visible light photocatalytic reaction set-up irradiated by a Halogen lamp.	53
Figure 3-3: Graphene synthesis procedure via oxidation-reduction method	57
Figure 3-4: Experimental procedure for making graphene oxide: (1)Microwave assisted expansion of graphite (a) to EG (b); (2)Oxidizing with sulphuric acid and KMnO ₄ to form a green paste (d); (3)Adding water and H ₂ O ₂ gradually under controlled temperature using ice bath (e) to obtain golden yellow suspended graphite oxide flakes (f); (4, 5) Washing with 1 L of HCl solution and water using repeating centrifuge and discarding the supernatant, this will cause gradual exfoliation of graphite oxide into paste like GO solution (h).....	58
Figure 3-5: Photograph of freeze-dried GO foam, rGO foam and GO paper	59
Figure 3-6: GO coated substrate: porous glass/GO (1), dolomite/GO (2), silica/GO (3), bare substrates (a), coated with GO (b).....	60
Figure 3-7: Process of making dolomite/GO adsorbent using three different meshes of dolomite before coating (a-c), after mixing GO solution (d) with bare dolomite they create a gel which holds dolomite particle stable (e) and makes uniformly GO coated dolomite after drying the gel (a ₁ -c ₁)	61
Figure 3-8: Adsorption column set up for adsorption test of bare and GO coated substrates	63
Figure 3-9: Chemical structure of TTIP and IPA.....	64
Figure 3-10: BERGHOF hydrothermal reactor with controlled time, pressure and temperature equipped with magnetic stirring.....	65
Figure 3-11: Flow chart of TiO ₂ and TiO ₂ nanoparticle sol-gel in-situ synthesis on GO	66
Figure 3-12: photographs of (a): TiO ₂ sol and sol-gel synthesised GO/TiO ₂ composite with 2, 5, 10, 15 and 20%wt (1 to 6), (b): Pure TiO ₂ nanoparticles, (c): 5% wt GO/TiO ₂ composite after drying, (d): Sample GO-PS-5 (5% wt GO/TiO ₂ after hydrothermal treatment at 170 °C for 24 hrs).....	67
Figure 3-13: photographs of (a): GO/P25 TiO ₂ dispersion with 0, 0.5, 1, 2, 5, 10, and 20%wt, (b) and (c): Pure TiO ₂ and GO/P25 composites after drying.....	68
Figure 3-14: Chemical structure of Hexadecylamine	70
Figure 3-15: schematic process of synthesising TiO ₂ beads (1-4), and two different routes for synthesising graphene wrapped TiO ₂ beads (a and b).....	71
Figure 3-16: schematic diagram of HPLC system with different modules.....	72
Figure 3-17: Representation of Beer-Lambert law, showing the various components as outlined in Equation 3-3 ²⁶³	73
Figure 3-18: Interaction of x-ray with crystallographic plane in specimen according to Bragg's Low ..	76

Figure 3-19: Raman spectra of (a): multilayer, (b): single layer graphene	78
Figure 3-20: Comparison between Raman spectra of increasing layers of graphene	79
Figure 3-21: Gas adsorption mechanism to measure the specific surface area	83
Figure 4-1: SEM images of expandable graphite flakes before expansion. In higher magnification image (b) steps which shows layered structure of graphite are visible.....	88
Figure 4-2: Graphite flake size distribution diagram	88
Figure 4-3: Schematic illustration of expansion of expandable graphite.....	89
Figure 4-4: SEM images of worm like expanded graphite (EG).....	90
Figure 4-5: Schematic structure of graphite and graphene building blocks ³⁰¹	90
Figure 4-6: SEM micrograph of (a-e) GO sponge in different magnifications, (f) GO sheet surface, (g) GO single sheet edge, (h) photograph of GO sponge.....	92
Figure 4-7: Low magnification side view SEM micrograph of an rGO paper cross section prepared by vacuum drying of GO solution followed by hydrazine reduction	93
Figure 4-8: TEM image of atomically transparent and thin GO sheets (a), HETEM of single layer GO sheet (b), SAED pattern of GO (c)	94
Figure 4-9: AFM image of GO sheets (a), height profile along the blue line (b)	95
Figure 4-10: Structure of GO proposed by Ruess (a), Scholz-Bohem (b) and Dékány (c)	96
Figure 4-11: TEM micrograph of HrGO and schematic inset showing the restoration of sp^2 domains after reduction	97
Figure 4-12: TEM image of HrGO (a,b), SAED image of HrGO (c)	97
Figure 4-13: SEM images of chemically reduced GO (HrGO).....	98
Figure 4-14: (a) FTIR spectrum of GO sheets and corresponding vibrations, (b) FTIR spectrum of GO in comparison with thermally reduced GO in air (AT-rGO), chemically reduced GO with hydrazine (HrGO) and vacuum reduced GO (VT-rGO).....	99
Figure 4-15: FTIR spectra of GO sponge, film and rGO (a) and images of each material (b-d).....	100
Figure 4-16: XRD pattern of GO and thermally reduced rGO.....	101
Figure 4-17: N_2 adsorption-desorption isotherm and BJH accumulative pore size distribution (inset) of GO and rGO sponges.....	103
Figure 4-18: Titration plots to determine complete cation replacement point.....	105
Figure 4-19: schematic illustration of MB wet adsorption and N_2 dry adsorption mechanism.....	106
Figure 4-20: UV/vis spectra of GO and rGO suspension.....	107
Figure 4-21: Raman spectra for graphite, thermally reduced GO (our method) and commercial graphene nano-platelets. Spectra are normalised to [0, 1] and numerically averaged over 10 measurements for each sample. Their magnified 2D bands are shown in right panels.	109
Figure 4-22: 2D band of commercial graphene nano-platelets fitted with Lorentzian equation which confirms Bernal stacking of graphene layers.....	110
Figure 4-23: Raman spectra of GO, thermally reduced graphene oxide in vacuum (VT-rGO) and hydrazine reduced graphene oxide (HrGO)	112

Figure 4-24: Raman spectra of liquid-phase exfoliated graphene (b) comparing with HrGO (a), the 2D band of exfoliated graphene nano-sheets (c)	113
Figure 4-25: SEM micrographs of charred dolomite.....	115
Figure 4-26: Dolomite trigonal crystal structure (a), atom's position in each unit cell	116
Figure 4-27: SEM images of Graphene oxide/dolomite composite. Graphene oxide covers dolomite partially (a), high magnification of dolomite surface showing granular morphology of dolomite (b), dolomite recrystallized flower-like morphology (c) and in higher magnification (d)	117
Figure 4-28: XRD spectra of bare dolomite and Dolomite/ graphene oxide composite	118
Figure 4-29: N ₂ adsorption isotherm of Dolomite/GO composite	118
Figure 4-30: Concentration of MB solution after 3rd filtration (a), removal efficiency of filters (b) ..	121
Figure 4-31: Adsorption efficiency of different GO integrated adsorbents within six adsorption experiments.....	121
Figure 4-32: MB solution after first and sixth filtration through dolomite and dolomite/GO adsorbents	122
Figure 4-33: The amount of adsorption (bars) and pH (black dots) for GO integrated adsorbents....	123
Figure 4-34: Final concentration of MB in solutions containing GO integrated adsorbents	124
Figure 4-35: The variation of the concentration versus time for dolomite/GO composite	124
Figure 4-36: Maximum adsorption capacity of MB for GO, rGO and dolomite/GO	124
Figure 4-37: GO mixed with 100 mg/L of MB at different pHs (top photo) and MB solution after removing GO comparing with the blank MB (left side of bottom photo).....	125
Figure 4-38: effect of pH on adsorption of MB on dolomite/GO adsorbent.....	126
Figure 4-39: The effect of initial concentration of MB on the final concentration	126
Figure 4-40: Adsorption of MB by commercial graphene (a mixture and b infiltrate) comparing with the chemically reduced graphene oxide (a mixture and d infiltrate)	127
Figure 4-41: Molecular structure of Diclofenac (right) and carbamazepine (left)	127
Figure 4-42: UV-Vis absorption spectra of carbamazepine adsorption by GO	128
Figure 4-43: Concentration versus time (a), adsorption capacity versus time (b), pseudo-second-order kinetic fit (c) and the adsorption isotherm for diclofenac and famotidine	129
Figure 4-44: effect of pH (a) and adsorbent concentration (b) on amount of adsorption (q _e) and the removal efficiency.....	131
Figure 4-45: The structure of dissolved diclofenac and the adsorption mechanism on GO.....	131
Figure 4-46: equilibrium concentration (C _e) and adsorption capacity (q _e) versus GO concentration for diclofenac, famotidine and solifenacin	133
Figure 4-47: Image of three different GO concentration mixed with diclofenac, solifenacin and famotidine (a) and the mixture after settling for 15 min (b). Chemical structure of diclofenac (c), famotidine (d) and Solifenacin (e).....	134
Figure 4-48: SEM images of GO sponge after adsorption of diclofenac with different magnification (a-d), growth mechanism (e,f).....	136

Figure 4-49: TEM images of diclofenac crystals grown on the surface of GO sheets first shot (a) and second shot after few second electron beam exposure	137
Figure 4-50: EDX spectra of GO sponge after adsorption of diclofenac.....	137
Figure 4-51: Optical microscopy image of collected diclofenac precipitate (a), and original source of diclofenac (b), DSC data of original diclofenac comparing the as grown precipitate (c), digital image of 500 mg.L ⁻¹ diclofenac solution before and after introducing the GO paper	138
Figure 4-52: SEM image of as-grown diclofenac crystals on the surface of GO paper at different magnifications.....	139
Figure 4-53: Contact angle of GO film (a) and GO film after diclofenac adsorption (b)	140
Figure 4-54: SEM images of GO sponge after adsorption of famotidine (a) solifenacin (b)	141
Figure 4-55: UV-vis adsorption spectra of six drugs before and after adsorption	141
Figure 4-56: Pharmaceutical cocktail removal with initial concentration of 5, 25 and 50 mg/l by GO dosage of 0.01, 0.05 and 0.1 g/l by time of adsorption (A) pseudo-second order kinetic plot of adsorption (B) bar charts summarizing amount of adsorption and removal efficiency versus initial concentration and graphene oxide dosage (C and D).....	143
Figure 4-57: Adsorption isotherm of pharmaceutical mixture and Freundlich adsorption isotherm (inset graph)	145
Figure 5-1: SEM images of TiO ₂ /GO composite with (A) 0 wt% GO; (B) 2 wt% GO; (C) 10 wt% GO; (D) 15 wt% GO; (E) 20 wt% GO; (F) 100 wt% GO.....	150
Figure 5-2: Proposed mechanism for TiO ₂ /GO composite formation via sol-gel process. TTIP in IPA as TiO ₂ precursor (A) is added to water/IPA under controlled pH which initiates hydrolysis of the precursor (D) yielding a clear homogeneous TiO ₂ sol. TiO ₂ agglomerate particles formation after condensation and drying the sol (E). In the presence of GO in water/IPA during the hydrolysis, GO regarding to abundant functional groups acts as a substrate which encourage uniform nucleation on its surface (B) and hinders growth during condensation (C).....	151
Figure 5-3: Raman spectra of liquid-phase exfoliated pristine graphene (A) with the representative TEM image of a single graphene nano-sheet (B). SEM image of TiO ₂ synthesised via sol-gel process in pristine graphene dispersion.	152
Figure 5-4: High-resolution TEM images of in-situ synthesised TiO ₂ on graphene oxide sheets (TiO ₂ with 5 wt% GO) (A-E) showing the morphology of the composite and also the shape and crystallinity of TiO ₂ particles. The corresponding SAED pattern assigned to (101), (004) and (200) lattice planes. Two sets of 6 dot can be distinguished in this pattern which is related to crystalline pristine areas of underlying graphene oxide	154
Figure 5-5: SEM images of P25 TiO ₂ /GO (GO-P25-X wt% X=2, 5, 15, 20) composite prepared by simple mixing of previously dispersed P25 powder with GO dispersion. A and B: tilted image and top surface image of GO-P25-2 wt% respectively. C and D: GO-P25-5 wt%. E and F: GO-P25-10 wt% G and H tilted image and high magnification image of GO-P25-20 wt%	156
Figure 5-6: EDX elemental mapping of 4 different spots on GO-P25-20 wt% composite	157

Figure 5-7: A and B: Bright-field TEM images of TiO ₂ P25 with 5 wt% GO composite (GO-P25-5). C: high resolution TEM image of TiO ₂ particles on GO surface. D: corresponding SAED pattern of GO-P25-5 composite showing the poly-crystallinity of TiO ₂	158
Figure 5-8: X-ray diffraction pattern of sol-gel as-synthesised TiO ₂ /GO composite versus commercial P25 TiO ₂ immobilised on GO surface and their corresponding lattice indices and polymorph structure (A=Anatase, R=Rutile)	160
Figure 5-9: Anatase (101) diffraction peak with the corresponding Lorentz peak fitting for (A) P25/GO (sample GO-P25-5 wt%) and (B) TiO ₂ /GO synthesised by sol-gel (sample GO-PS-5 wt%). The (101) peak for as-synthesised TiO ₂ by sol-gel is a shouldered peak which was de-convoluted into two peaks which small peak on the shoulder represents very small amount of (110) rutile shifted and broadened due to very small size.	161
Figure 5-10: X-ray diffraction of sol-gel synthesised TiO ₂ powder comparing with (a) GO-PS-5 wt%, (b) as-synthesised TiO ₂ without any treatment, (c) TiO ₂ powder calcined at 450 °C for 2 hours	162
Figure 5-11: (A): Raman spectra of sol-gel synthesised TiO ₂ and TiO ₂ /GO composite (inset: enlarged area of graphene's D and G band modes). (B) Raman spectra of commercial P25 TiO ₂ powder with assigned vibration modes. (C): Raman spectra of as-synthesised TiO ₂ powder in comparison with P25	163
Figure 5-12: (A and C) The effect of graphene oxide content on adsorption of diclofenac by GO/P25 mixture (GO-P25-X wt%) and sol-gel synthesised GO/TiO ₂ nanoparticles (GO-PS-X wt%) where X=0, 1, 2, 5, 10, 20, 100. The amount of diclofenac adsorption per gram of catalyst by time (B and D). GO-P25-0 and GO-PS-0 are TiO ₂ samples without any graphene oxide and graphene oxide-only samples are included for comparison.....	166
Figure 5-13: Second-order kinetic plots for the diclofenac adsorption by GO/P25 mixture and sol-gel synthesised GO/TiO ₂	167
Figure 5-14: UV Photocatalytic activity of GO-P25-X and GO-PS-X (X=0 to 20 wt%). (A and C): Concentration of diclofenac versus dark adsorption time and UV irradiation time. (B and D): -Ln(C/C ₀) versus irradiation time and Pseudo-first order kinetic fitting. (E and F): Degradation efficiency of diclofenac versus time. In all experiments the initial concentration of diclofenac is 100 mg/L and catalyst mass loading of 0.3 g/L.....	169
Figure 5-15: Adsorption isotherm of GO-P25-5 wt%, inset graph: BJH pore size distribution and cumulative pore volume with surface area and pore information extracted from BET and BJH plots	172
Figure 5-16: Plot of concentration vs adsorption and irradiation time (A) and Pseudo-first order kinetic plot (B) of sol-gel synthesised GO-PS-5 wt% (NA: as-synthesised with no processing, UV3: Recovered composite powder after 3 hours of UV irradiation, UV6: Recovered composite powder after 6 hours of UV irradiation.....	174
Figure 5-17: Raman spectra of as-synthesised GO-PS-5 wt% before and after 3 hours of UV irradiation	175

Figure 5-18: Excited-State Interaction between TiO_2 and Graphene Oxide leading to partial reduction of GO to rGO and photocatalytic degradation of organic pollutant at the same time	175
Figure 5-19: Dark and UV removal of 100 mg/l of Diclofenac (A, C) with degradation kinetic plots (B, D) for GO-P25-5 wt% and GO-PS-5 wt% as-synthesised composite compared with annealed and hydrothermally treated samples. Photolysis of diclofenac without any catalyst and pure P25 and TiO_2 synthesised powder as reference is also included.	177
Figure 5-20: Degradation efficiency of as-synthesised GO-P25-5 wt% (A) and GO-PS-5wt% (B) comparing reduced composite by thermal and hydrothermal treatments. The straight line defines the $t_{1/2}$ which is the time that 50% of diclofenac is being degraded	178
Figure 5-21: N_2 adsorption isotherms and their corresponding BJH pore size distribution (inset graphs) of sol-gel synthesised GO-PS-5 wt% (A, B and C) and GO-P25-5 wt% (D, E and F) as-synthesised, calcined at 450 °C and hydrothermally treated respectively from top to bottom.....	180
Figure 5-22: TEM images of GO-PS-5 wt% (A, B) and GO-P25-5 wt% (C, D) hydrothermally treated at 170 C for 20 hrs	182
Figure 5-23: SEM images of GO-PS-5 wt%, hydrothermally reduced (A) and calcined (B) and GO-P25-5 wt%, hydrothermally reduced (C) and calcined (D).....	183
Figure 5-24: X-ray diffraction patterns of GO-PS-5 wt% (A) and GO-P25-5 wt% (B) composites before and after hydrothermal (HT) and calcination (CA).....	185
Figure 6-1: TEM images of TNTs formed by 24 hrs of hydrothermal treatment at 110, 130, 180 °C for A, B and C respectively.....	188
Figure 6-2: Four different morphologies observed during alkaline hydrothermal reaction of TiO_2 . Nanotubes (I), nanosheets (II), nanorods or nanowires (III), and nanofibers or nanobelts (IV). a, b and c are crystallographic axes	189
Figure 6-3: TEM images of TNTs hydrothermally synthesised TNTs at 150 °C for 24 hrs. HRTEM image of B shows that TNTs are 15-20 nm in outer diameter and 3 nm thick walls composed of multi layers of titanate sheets rolled into micron length TNT nanotubes	189
Figure 6-4: SEM images of hydrothermally synthesised TNTs at 150 °C for 24 hrs.....	190
Figure 6-5: (A): XRD of as-synthesised TNTs compared with starting P25 powder, calcined TNTs at 450 °C for 2 hrs (TNT-CA) and hydrothermally treated TNTs at 150 °C for 20 hrs (TNT-HT). (B): Raman spectra of as-synthesised TNTs comparing P25 TiO_2 powder and hydrothermally treated TNTs (TNT-HT)	191
Figure 6-6: SEM images of TNTs synthesised at 150 °C for 24 hrs; (A,B) after second hydrothermal treatment at 150 °C for 24 hrs (TNT-HT). (C, D) after calcination at 450 °C for 2 hrs (TNT-CA). 192	
Figure 6-7: (A, C): TEM images of 10 wt% rGO-TNT-HT composite and HRTEM image of nanotubes. (B,D): TEM and HRTEM image of one-pot synthesized 10 wt% rGO-TNP	193
Figure 6-8: XRD of GO and rGO/TNT composite synthesise via different routes	194
Figure 6-9: SEM images of 10 wt% rGO/TNT composites; rGO-TNT-CA (a1, 2, 3), rGO-TNT-HT (b1, 2, 3), rGO-TNP-HT (c1, 2, 3)	195

Figure 6-10: Raman spectra of 10 wt% rGO-TNP-HT composite.....	196
Figure 6-11: N ₂ adsorption isotherms of TNTs and 10 wt% rGO-TNT composites prepared via different routes.....	197
Figure 6-12: UV and visible light photocatalytic activity of Photolysis of TNT-HT, rGO-TNP-10, rGO-TNT-10-HT, rGO-TNT-10-CA in comparison with rGO/TiO ₂ nanoparticle composites rGO-PS-10-HT and rGO-P25-10-HT towards degradation of 35 mg ml ⁻¹ of famotidine. All HT composites were treated hydrothermally at 150 °C for 24 hrs, CA samples were annealed at N ₂ atmosphere at 450 °C for 2 hrs. In each label 10 represent the wt% of graphene in composite.	200
Figure 6-13: SEM images of TiO ₂ nanofibers synthesised by hydrothermal treatment of P25 in 10 M NaOH at 200 °C for 24 hours.....	201
Figure 6-14: Dependence of morphological phase diagrams on hydrothermal conditions.....	202
Figure 6-15: TEM images of as-synthesised TiO ₂ nanofibers	202
Figure 6-16: Raman spectra of annealed TiO ₂ nanofibers comparing with P25 TiO ₂ source.....	203
Figure 6-17: SEM images of TiO ₂ nanofibers calcined at 450 °C for 2 hrs (A, B) and images of rGO-TiO ₂ nanofiber containing 10 wt% of graphene after thermal reduction	204
Figure 6-18: UV and photocatalytic activity of TiO ₂ nanofibers and rGO/TiO ₂ nanofibers	205
Figure 6-19: photo of rGO and GO/TiO ₂ nanotubes one minute after shaking.....	207
Figure 7-1: SEM images of hydrothermally treated and calcined TiO ₂ beads TBs (a1,2 ,3) and TiO ₂ beads with 10 wt% reduced graphene oxide rGO-TBs after hydrothermal treatment (b1, 2, 3)	209
Figure 7-2: TEM images of rGO-TBs showing the poly-crystallinity and mesoporous structure of TiO ₂ beads	210
Figure 7-3: XRD patterns of TiO ₂ beads and TiO ₂ beads with 10 wt% graphene composite	210
Figure 7-4: N ₂ adsorption isotherms of 10 wt% rGO-TBs composite with BJH pore distribution (inset)	211
Figure 7-5: UV and Visible-light photocatalytic activities of pure TiO ₂ beads (TBs) calcined at 450 °C and TiO ₂ beads with 10 wt% rGO composite (rGO-TBs) hydrothermally reduced at 170 °C for 10 hrs comparing photolysis degradation towards degradation of 35 mg/L famotidine with catalyst dosage of 0.3 g/L.....	212
Figure 9-1: Proposed pilot scale reactor in order to study performance of graphene/TiO ₂ composite in a continuous flow of real wastewater under solar light irradiation	218

List of Tables

Table 1-1: Commonly occurring trace contaminants of pharmaceuticals fated in aquatic environment	6
Table 1-2: Comparison of oxidizing potential of various oxidizing agents	13
Table 1-3: Most common AOPs evaluated for water and wastewater treatment	14
Table 2-1: Review of graphene production techniques	42
Table 3-1: Source and description of materials used	50
Table 3-2: Apparatus and their application in this project	51
Table 3-3: Chromatographic conditions for pharmaceutical pollutant models	55
Table 3-4: Physical properties of the substrates for GO immobilisation	56
Table 3-5: Molecular structure and physical properties of methylene blue and pharmaceuticals used as pollutant models	56
Table 4-1: GO and rGO XRD peak information	101
Table 4-2: Surface characteristic of GO and rGO obtained from N ₂ adsorption isotherms based on BET and BJH models	104
Table 4-3: Surface areas determined by N ₂ adsorption (BET) and MB adsorption	106
Table 4-4: Raman band position and ratio of GO and rGO	112
Table 4-5: Surface area and porosity of Dolomite/GO and dolomite composite	119
Table 4-6: Kinetic Parameters for the Adsorption of diclofenac and famotidine by GO	130
Table 4-7: Kinetic parameters of 5, 25 and 50 mg/L of diclofenac using three dosage of GO	144
Table 4-8: Freundlich adsorption isotherm parameters calculated from the inset graph of Figure 4-57	145
Table 5-1: Adsorption kinetic parameters of GO/P25 composites	167
Table 5-2: Adsorption kinetic parameters of sol-gel synthesised GO/TiO ₂ composites	167
Table 5-3: Photocatalysis and kinetic parameter for GO/P25 composites	170
Table 5-4: Photocatalysis and kinetic parameter for sol-gel GO/PS composites	170
Table 5-5: N ₂ adsorption data for GO/TiO ₂ composites containing 5 wt% graphene oxide	172
Table 5-6: Photocatalytic, kinetic parameters and sheet resistance of GO-PS-5 wt% as-synthesised composite, recovered composite powder after 3 hours of UV irradiation and recovered composite powder after 6 hours of UV irradiation	174
Table 5-7: Surface area and Photocatalysis parameter of as-synthesised GO-P25-5 wt% and GO-PS-5wt% composite and reduced composite by thermal and hydrothermal treatment	178
Table 5-8: BET Surface area and BJH pore size distribution data of as-synthesised GO-PS-5 wt% and GO-P25-5 wt% and after thermal and hydrothermal treatment	181
Table 5-9: BET Surface area and BJH pore size distribution data of GO-PS-20 wt% before and after calcination	184
Table 6-1: BET surface area and pore characterisation of TNT and rGO-TNT composites	197

Table 6-2: UV and Visible-light photocatalytic activities of various rGO/TNT composites in comparison with rGO/TiO ₂ nanoparticle composites for degradation of famotidine	199
Table 6-3: UV and Visible-light photocatalytic activities of pure TiO ₂ nanofiber and with 10 wt% rGO composite comparing photolysis for degradation of 35 mg/L famotidine with catalyst dosage of 0.3 g/L	206
Table 7-1: UV and visible light photocatalysis data for TBs and rGO/TBs	212

If you thought that science was certain - well that is just an error on your part.
(Richard P. Feynman)

ACKNOWLEDGEMENTS

I would like to acknowledge Marie Curie Initial Training Network funded by the EC-FP7 People Programme, ATWARM (Advanced Technologies for Water Resource Management) and QUESTOR in Queens University Belfast for the financial support and managing this project. I also would like to acknowledge the financial and technical support of the Tyndall National Institute through the SFI-funded National Access Programme (Project NAP340 and NAP750) which allowed me to have access to the state-of-the-art Electron Microscopes.

I must also thank my supervisors, Kieran and Anne for their guidance, support and patience whilst allowing me the room to work independently. Thanks to my lab colleagues David, Ross, Cecilia and my friend Roya for their support and kindness.

I would like to thank all the technical staff in the School of Biotechnology, Chemical Sciences, Mechanical Engineering and the NCSR specially Dave Allen for helping me with Raman measurements and David Cunningham for his technical advice on HPLC.

Special thanks to Nikolay Petkov and Patrick Carolan from Tyndall for helping me in electron microscopy imaging and Paul Roseingrave for managing NAP projects and facilitating my regular visits from Tyndall in Cork.

Finally, I would like to express my love and gratitude to my family specially mom and dad who always encouraged me to learn more and stood by me and made it possible to be far away from home. The last but not least I would like to thank my husband Ali for his love, support and incredible patience during these years and my late night works.

CHAPTER 1: INTRODUCTION

Based on the World Health Organization (WHO) drinking water quality committee's report, in the last decade traces of pharmaceuticals, typically at levels in the nanograms to low micrograms per litre range, have been reported in the water cycles around the world, including surface waters, wastewater, groundwater and, to a lesser extent, drinking-water¹. Their presence in water, even at these very low concentrations, has raised concerns regarding the potential risks to human health from exposure to traces of pharmaceuticals via drinking-water. Although present at levels of $\mu\text{g/l}$, pharmaceutical drugs are designed to be biologically active and may pose a threat to human health and the environment over long period of time. In this chapter the occurrence and fate of pharmaceuticals compounds in water and wastewater and an introduction to the advanced wastewater treatment will be reviewed briefly with the main focus on advanced oxidation processes and specifically photocatalysis as an advanced complementary treatment to remove pharmaceutical from water.

1.1. Motivation: Water Scarcity

Water is one of the world's most important resources for all human life, as with all animal and plant life on the planet. According to United Nations Environment Programme report the total volume of fresh water resources on Earth is about 35 million km^3 , which of these, only about 200 000 km^3 - less than 0.5 % of all freshwater resources- is usable for human. (See Figure 1-1)². Water withdrawals are predicted to increase by 50 % by 2025 in developing countries, and 18 % in developed countries. But there is no 'creation' of 'new' fresh water on the planet for the increasing population. As a result to save fresh water resources, processing and reusing domestic and industrial wastewater seems inevitable. To achieve this, all different types of pollutants in wastewater or surface water should be categorized and new technologies to remove them from the stream should be developed.

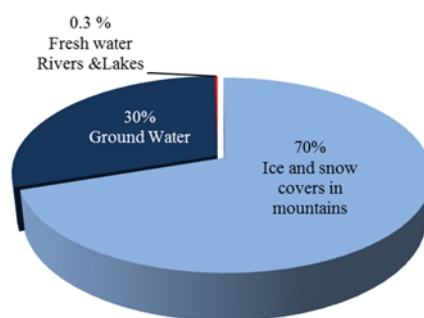


Figure 1-1: Breakdown of fresh water resources (Source: United Nations Environment Programme ³⁾)

1.2. Water pollution: Organic compounds

More than 100,000 synthetic chemicals are used in a variety of domestic, industrial, and agricultural applications ⁴ which some traces will end up in aquatic environment through different pathways. Numerous studies have documented that many of these compounds, including herbicides, pesticides, flame retardants and plasticizers, detergent metabolites, personal care products, pharmaceuticals, and petroleum products are introduced into waste water ^{5,6} and this contaminated water (wastewater) treated, and returned back to a natural water-body. Many studies confirmed that a large amount of contaminants are incompletely degraded or removed by regular wastewater treatment and a larger amount are introduced to water bodies directly from agricultural land field runoff and industry discharge without any further treatment which will end up in rivers, lakes, groundwater and other resources of drinking water. In such a cycle as shown in Figure 1-2, persistent organic pollutants could pass all barriers such as wastewater treatment or underground passage and would appear in raw waters used for drinking water production and destroy aquatic environment in long period of time. Many reviews documented the occurrence, fate and environmental and health risk assessments of organic compounds (OCs) in wastewaters, surface water, groundwater and drinking water ⁶⁻⁸.

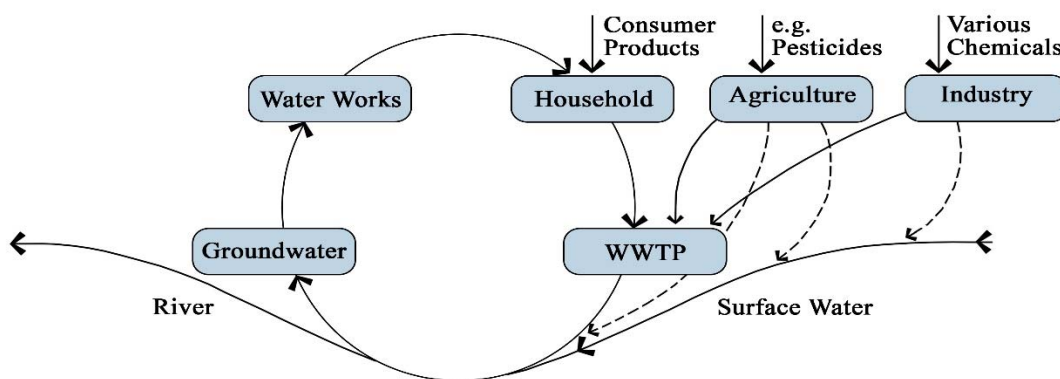


Figure 1-2: water contaminant's pathway

1.3. Pharmaceutical Pollution

Generally speaking, environmental pollutants as described earlier may be described as unwanted chemical substances which break down slowly and have a negative impact on various organisms. On the basis of a wide definition such as this, pharmaceutical residues can be considered as an important class of environmental pollutants. The use of pharmaceutical and prescribed drugs, including antibiotics, synthetic hormones, continues to increase each year. Drugs (apart from some used for diagnosis) are designed to have some kind of effect on the patient's organs or tissues or on microorganisms present inside or on the patient. This means that they can also affect other organisms, such as plants, mammals, fish and lower order species. Most drugs are designed to be swallowed. In order to survive its passage through the stomach without being broken down by the acid environment and gastric enzymes, the pharmaceutical substance must be resistant. Drugs have been deliberately given properties that can distinguish them from other chemicals: they are chemically stable and they have a biological effect on many cells and organisms. As a result exerted or unused pharmaceuticals can be persistently present in the environment and act as a contaminant with hazardous effect on living organisms^{9,10}.

1.3.1. Occurrence of pharmaceuticals in raw water

Up to now traces of pharmaceuticals, typically at levels in the nano-grams to low micro-grams per litre range, have been reported in the water cycle, including surface waters, wastewater, ground-water, and to a less extent, drinking-water. A search has been successfully conducted for drugs used for a large number of indications, although the majority of investigations have concentrated on analgesic/anti-inflammatory agents, antibiotics, hormone preparations, and antihypertensive agents. As illustrated in Figure 1-3, pharmaceuticals enter the environment through many routes, including human or animal excreta, wastewater effluent, treated sewage

sludge, industrial waste, and medical waste from health-care and veterinary facilities, landfill leachate and bio-solids. Figure 1-3 compiles possible sources and pathways for the occurrence of drug residues in the environment.

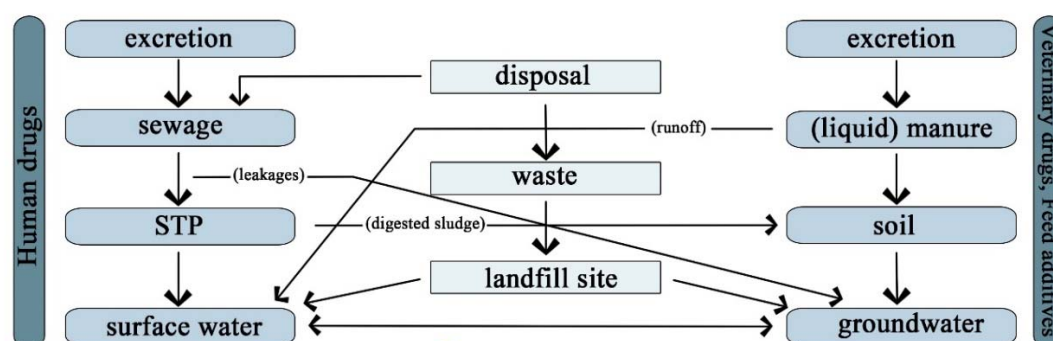


Figure 1-3: Pathways for the contamination of the surface and ground water by pharmaceuticals

As an important source of pollution drugs that are administered to humans and animals leave the body either as the active ingredient or an intermediate metabolite via urine and faeces with their fate dependent upon a number of factors. Human drugs, once used, nearly always end up in the sewage system, which in turn usually leads to a sewage treatment plant and eventually the receiving waters. Drugs directly enter the soil layers or are added to farmland via the spread of manure. These residues can have a direct effect on farmland or eventually, through leaching processes, reach the ground water sources ^{4,11}. However the majority of pharmaceuticals end up in sewage that is normally centrally treated at conventional wastewater treatment plant where they were only removed partially through adsorption onto suspended solids as the main mechanism. This results in approximately 60% of these compounds being incorporated into the sludge, with significant quantities of the active ingredient and any metabolic breakdown products lost in the final effluent, which ends up in either surface or ground waters. The most cited reference in the peer-reviewed literature on the occurrence of pharmaceuticals in surface waters is the survey by the United States Geological Survey, in which more than 50 pharmaceuticals in 139 streams across 30 states in the USA were investigated during 1999 and 2000 by Kolpin et al. ¹². According to literatures the most representative pharmaceutical compounds detected in urban wastewaters are antibiotics, lipid regulators, anti-inflammatories, antiepileptics, tranquillizers, anti-depressants and X-ray contrast media and some types of hormones as it has been classified in Table 1-1. Some of these compounds are not removed by conventional wastewater treatment plant so they were reported in surface water, ground water and drinking water in several areas around the world.

Table 1-1: Commonly occurring trace contaminants of pharmaceuticals fated in aquatic environment around the world

Pharmaceutical	Action	References
Diclofenac, Acetylsalicylic acid, Naproxen Carboxyibuprofen, Ibuprofen, Indomethacin, ketoprofen, phenazone, Dextropropoxyphene, codeine, fenoprofen, hydrocodone, meclofenamic acid, phenylbutazone, famotidine	Analgesic/antiphlogistic, Anti-inflammatory	13-17
Caffeine	Psychomotor stimulants	18,19
Erythromycin, , tetracycline Ciprofloxacin, lincomycin Chloramphenicol, Amoxycilin, Sulfamethoxazole	Antibiotic	13-15,20
Clofibric acid, Bezafibrate	Lipid regulator agent	13
Diazepam, fluoxetine	Tranquillizers, Anti- depressant	17,21,22
Carbamazepine, Primidone	Antiepileptic	6
Salicylic acid, mefenamic acid	Multi-purpose	14,15,17
Iopromide, Iopamidol	Contrast media	23,24
Metoprolol, propranolol, Atenolol	antihypertensive agents (beta-blockers)	13-15,17
Nonylphenol,estradiol-17, mestranol, 17 α - ethinylestradiol, progesterone, testosterone Estrone, 17 β -estradiol	Hormones and endocrine disruptors	12,24-26

1.3.2. Occurrence of pharmaceuticals in drinking water

There is increasing concern that active pharmaceutical compounds are finding their way into drinking water due to increasing surface and ground water pollution, and the reuse of sewage effluents in areas of water scarcity. Among the more commonly recorded compounds are antibiotics, painkillers, beta-blockers, lipid-reducing drugs and sex steroids from birth control and hormone ²⁷. Owing to the practical difficulties such as high cost and lack of availability of an straightforward analytical method to detect and measure the concentration of pharmaceuticals in drinking water as well as the lack of standard and regulations there is not any specific program to monitor the occurrence of drugs in drinking water in most of countries ²⁸. So the majority of the data in this issue comes from targeted research projects and investigations. To date, more than 16 pharmaceuticals have been detected in treated drinking

water worldwide, as reported in the peer-reviewed literature^{29,30}. The concentration of detected drugs in tap water is ranging from nano-grams to low micrograms per litre in several countries in Europe, including Germany, France, the Netherlands and Italy^{16,31-33}. Reddersen et al. found phenazone in Berlin drinking-water, with the highest concentration of 400 ng/l³⁴. Various types of antibiotic have also been detected in surface and drinking water in Korea, USA, Australia and France³⁵⁻³⁹.

As mentioned before to date more than 100 pharmaceuticals have been identified in sewage or surface water but only 16 drugs or drug metabolites have been reported to occur in various drinking water samples. This means that many of these compound naturally degrade in aquatic environment and many others are removed by advanced treatments technologies. From compounds listed in Table 1-1 and reviewing many literatures, *bezafibrate*, *clofibric acid*, *carbamazepine*, *ibuprofen* and *diclofenac* and *anti-inflammatory drugs* have been found as the most frequent pharmaceutical compounds in drinking water^{15,40-43}. These compounds are very persistent and hardly degrade with conventional wastewater treatment technologies and most of advanced technique such as photo-fenton, and ozone. So in current research diclofenac, carbamazepine and famotidine (as an inflammatory drug) were chosen as a model to test the newly developed photocatalyst material's ability to remove pharmaceuticals residues from sewage or raw waters used for drinking water supply.

1.3.3. Risks and Hazards

Many reports published by World Health Organisation (WHO), national Environmental Protection Agencies (EPAs) and United Nations' World Water Assessment Programme (WWAP) and numerous other research literatures increase the public concern about the health risk of organic chemicals and pharmaceuticals present in water on human and other living organism⁴⁴. They may impose toxicity virtually on any level of the biological hierarchy, i.e. cells, organs, organisms, population, ecosystems, or the ecosphere. In addition, certain classes of pharmaceuticals like antibiotics may cause long-term and irreversible change to the micro-organism's genome, making them resistant in their presence, even at low concentrations^{45,46}. More importantly though, the presence of the endocrine disrupting compounds (EDCs) are known to disrupt the human and animals endocrine system⁴⁷⁻⁴⁹. Although the concentrations of individual pharmaceuticals found in European environments are often too low to provoke these ecotoxicological effects but a typical exposure situation in the environment is normally a multi-component mixture of low-effect concentrations of individual pharmaceuticals which may synergistically induce risk for human health and environment. There are currently a little documented examples of pharmaceuticals adversely affecting wildlife including the feminisation

of male fish, and diclofenac killing vultures. For example diclofenac, used as a veterinary pharmaceutical, has killed tens of millions of vultures in Asia. Experimental evidence has confirmed that diclofenac is the cause of this mass poisoning of wildlife. Anti-inflammatory drugs also appear to be highly toxic to birds ⁵⁰. The same challenges also exist for the concern about the effect of trace concentrations of pharmaceuticals in drinking-water on human health. However because of knowledge gaps and lack of data in terms of assessing risks associated with long-term exposure to low concentrations of pharmaceuticals and the combined effects of mixtures of pharmaceuticals, serious action should be taken to remove pharmaceutical completely from drinking water and decrease the level of risk by decreasing the level of pharmaceutical contaminant in wastewater effluent and surface water using advanced technologies.

1.4. Pharmaceuticals removal from conventional WWTPs

According to the literatures the main source of pharmaceuticals in surface water originates from municipal wastewater effluent. In general, municipal STPs have not been designed to remove residues of trace organics such as pharmaceuticals but to reduce the concentrations of pathogens and bulk organics. A schematic of a typical wastewater treatment process is shown in Figure 1-4. The steps of a sewage treatment process are often divided into primary, secondary and tertiary. Primary treatment is largely a mechanical process to separate solids, however depending on local plant conditions and requirements this step may also include fat oils and grease removal, pH adjustment, temperature adjustment and an initial sedimentation. Secondary treatment is a largely biological process. The most common type of secondary wastewater treatment is activated sludge. This process uses an aeration tank containing the primary treated or screened sewage or industrial wastewater combined with microorganism that degrade the organic in wastewater.

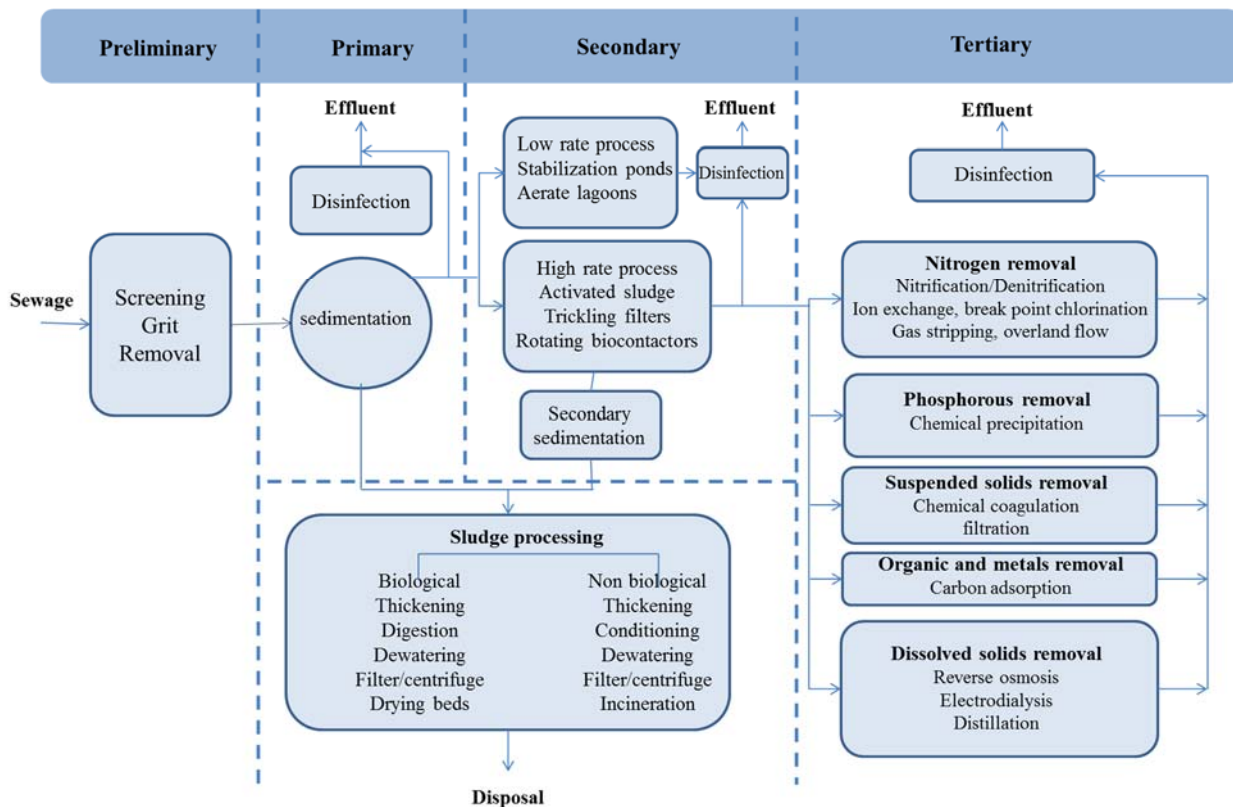


Figure 1-4: A diagram of a modern sewage treatment plant with different possible processes

This solution is then pumped to a settling tank where the microorganisms sink to the bottom and are either removed as sludge or re-circulated back into the aeration tank. The supernatant from the settling tank flows either to a tertiary treatment step where nutrients and/or micro-pollutants are removed or discharged to the surface water (river or lakes) without further treatment. Another word, tertiary treatment is considered as a polishing step for further purification possibly for specific contaminants. In the tertiary treatment of sewage, the fluid from the secondary treatment process is cleansed of phosphate and nitrate ions that might cause pollution. The ions are precipitated as solids, often by combining them with calcium or iron, and the ammonia is released by oxidizing it to nitrate in the nitrification process. Adsorption to activated charcoal or advanced oxidation processes (AOPs) would be applied in this step to remove pharmaceuticals as well as other organic pollutants in order to reduce the BOD (Droste 1997).

However high concentration of pharmaceutical is detected in secondary treatment effluent. Generally the fate of pharmaceuticals and their remains is governed by its chemical and biological persistence, sorption behaviour, evaporation ability and the technology used for sewage purification ⁵¹. The pharmaceuticals can be removed by different ways as follow:

- **Photodegradation** naturally by sun after discharge or in tertiary treatment by UV

- **Biodegradation** naturally by micro-organism in environment or by activated sludge
- **Adsorption** naturally by soil in ponds and river basin or by activated carbon in tertiary treatment
- **Volatilisation** naturally or in aeration and air stripping steps
- **Oxidation** by advanced processes in tertiary treatment

For most pharmaceuticals the extent of removal by air stripping and aeration is negligible because of their low volatility ⁵². Due to the high polarity, acidity and solubility of most pharmaceuticals and the corresponding metabolites, their sorption to suspended solids and subsequent removal by sedimentation as primary and secondary sludge is not significant ⁵³⁻⁵⁵. The biological removal of pharmaceutical varies strongly from compound to compound. For example as shown in Figure 1-5 the removal rate varies from 6% for fenofibric acid to 71% for indomethacine. The removal rate of different compounds also varies for different secondary treatment process. As illustrated in Figure 1-5 the removal rate of indomethacine via biological filter and activated sludge are very close whereas for diclofenac there is a huge difference of 66% between the removal rates of the two process. However regardless of the type of secondary treatment high concentration of pharmaceuticals ranging from 850 ng/l for clofibric acid to 100 ng/l for ibuprofen are still present in effluent of STPs.

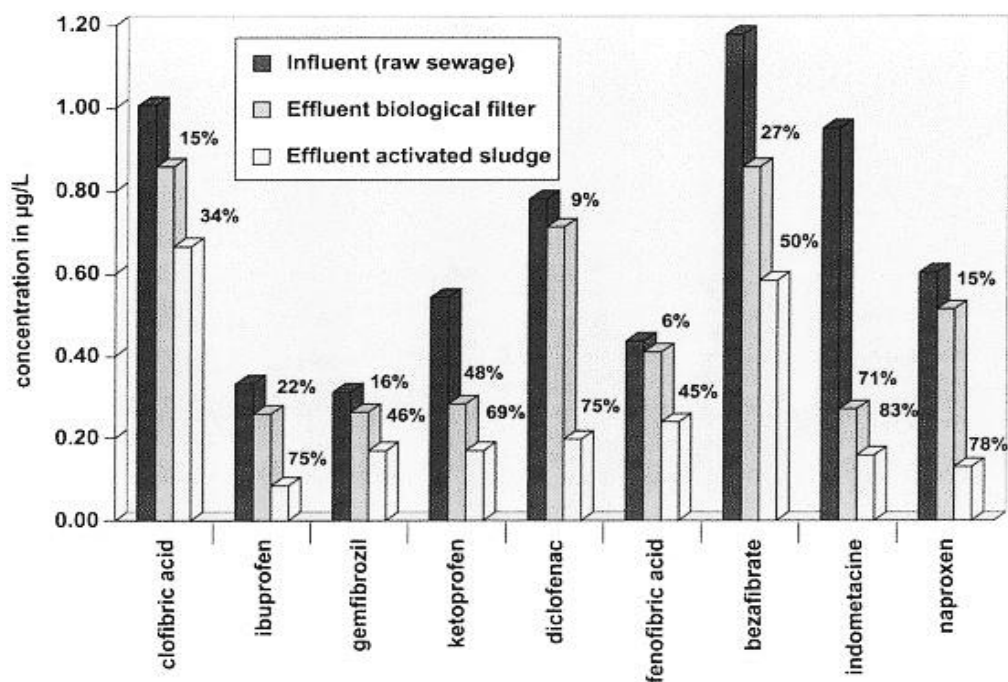


Figure 1-5: Removal of drug residues in a STP. Concentrations in influent (raw sewage), effluent of biological filter (trickling filter) and effluent of activated sludge in µg/l. ⁵⁶

Another research conducted by Scheytt et al.⁵⁷ showed that Ibuprofen is often removed beyond the quantification limit ($\geq 90\%$); Naproxen shows significant removal (50–80%) and partial removal is also seen for diclofenac (20–40%). Finally, no removal is found for the antiepileptic drug carbamazepine. Comparable results were found in other literatures. A research by Joss et al.⁵⁸ has revealed high concentrations of intact diclofenac, carbamazepine and roxithromycin in biological treatment effluent, however more than 90% of Ibuprofen is transformed during the biological treatment. In summary these investigations and large and growing number of other surveys, has proved that pharmaceutical compounds are extremely resistant to biological degradation processes and usually exit intact from conventional wastewater treatment plants. Therefore, most of researches has been directed towards the application of non-biological processes for the destruction of pharmaceuticals in waters with emphasis on advanced oxidation processes (AOPs)^{59,60}.

1.5. Tertiary treatments for Pharmaceuticals removal

Biodegradation, adsorption in activated carbon, air stripping, incineration, ion-exchange, coagulation-precipitation, membrane separation, thermal and catalytic oxidation, oxidation by permanganate, chlorine, ozone and hydrogen peroxide are widely used conventional water treatment process for organic pollutants removal from water. Each process has some shortcomings and to overcome this, researchers are looking for some new technologies. For example air stripping process, commonly used for the removal of volatile organic compounds for aqueous media, merely transfers the pollutants from liquid phase to gaseous phase rather than destroy them completely. In the process of adsorption in activated carbon, the spent carbon must be either regenerated or incinerated, which converts adsorbed pollutant to innocuous by-product. Membranes such as those used for reverse osmosis, nanofiltration and ultrafiltration can be used for direct removal of some pharmaceuticals but the process is expensive and is not environmental friendly. Chlorination and ozonation are two water disinfection and destructive oxidation technologies in water treatment process. However, chlorination-based water disinfection process may form potentially toxic and carcinogenic disinfection by-products (DBPs) such as trihalomethanes.

The main focus of this project is the efficiency of photocatalysis process by employing new composite materials. To achieve this one should have clear understanding of advanced oxidation processes and oxidant species involve in photocatalysis process. Therefore in this section advanced oxidation process will be reviewed briefly following by fundamental aspects heterogeneous photocatalysis in combination with adsorption in more detail.

1.5.1. Advanced oxidation processes (AOPs)

The strong potential of tertiary treatments called Advanced Oxidation Processes (AOPs) organic pollutant break down is universally recognized today, and many researchers around the world are devoting their efforts to the development of these processes ⁶¹⁻⁶⁴. Advanced Oxidation Processes rely mainly on the formation of short-lived oxygen containing intermediates, such as hydroxyl radical (OH^\bullet) or superoxide ($O_2^{\bullet-}$). The hydroxyl radical is highly reactive, short-lived, non-selective reagent that is easy to produce. These TiO_2 processes use traditional oxidants (H_2O_2 and/or O_3) with additional stimuli such as ultra-violet (UV) light to create highly reactive species (hydroxyl radicals) to oxidize substances. AOPs are able to oxidize substances like saturated organic molecules and pesticides, which are very difficult to treat using other methods. These AOPs include H_2O_2/UV , O_3/UV , $H_2O_2/O_3/UV$, TiO_2/UV and vacuum ultraviolet (VUV) processes ⁶⁵. AOPs can be broadly defined as aqueous phase oxidation methods based on highly reactive species such as (primarily but not exclusively) *hydroxyl radicals* (OH^\bullet) leading to the destruction of the target pollutant through different reaction systems. Hydroxyl radicals is produced via different methods which include heterogeneous and homogeneous photocatalysis based on near ultraviolet (UV) or solar visible irradiation, electrolysis, ozonation, the Fenton's reagent, ultrasound and wet air oxidation, while less conventional but evolving processes include ionizing radiation, microwaves, pulsed plasma and the ferrate reagent. Regarding to its high standard reduction potential of 2.8 V in acidic media ^{66,67}, hydroxyl radicals are able to oxidize almost all organic compounds that cannot be oxidized by conventional oxidants (e.g., oxygen and chlorine). The oxidation potential of various oxidizing agents has been compared in Table 1-2. Hydroxyl radicals react with dissolved compounds and the first reaction initiates a series of various oxidation reactions. The goal of the oxidation of compounds is complete mineralization, where the organic compounds are converted to carbon dioxide and water. A useful attribute of the hydroxyl radicals is their very low selectivity and high power that can even destroy pollutants that are not amenable to biological treatments ⁶⁸.

Table 1-2: Comparison of oxidizing potential of various oxidizing agents ⁶⁹

Oxidizing species	EOP (V)	EOP relative to chlorine
Positively charged hole on TiO ₂	3.20	2.35
Fluorine	3.06	2.25
Hydroxyl radical	2.80	2.06
Atomic oxygen	2.42	1.78
Ozone	2.08	1.52
Hydrogen peroxide	1.78	1.30
Chlorine	1.36	1.00
Oxygen (molecular)	1.23	0.90

The most common AOPs developed for water and wastewater remediation are presented in Table 1-3. Some of these processes such as photolysis with more than 3000 applications in Europe (as a disinfection process) and a large number in the US (for treating groundwater pollutants) are commercially available ^{70,71}. Other processes such as combinations of H₂O₂, O₃ and UV, Fenton's reagent, super-critical water oxidation and ionizing radiation have all been used at full scale. Photocatalysis and ultrasound have been assessed only at laboratory bench and pilot scales. AOPs developed for aqueous wastes treatment include ozonation, UV radiation, Fenton processes, hydrogen peroxide (H₂O₂) and catalysts such as titanium dioxide (TiO₂). These methods can be applied separately, in combinations or even sequentially. They have proven to effectively oxidise a broad variety of organic pollutants at both low and high concentrations and they are promising in the ultimate removal of pharmaceuticals. The chemical reactions involved are essentially the same as if the pollutants were slowly oxidised in the environment, but the oxidation rate is billions of times faster. AOPs lead not only to the decomposition of target pollutants, but also to complete mineralization if the treatment time is sufficient, although it is often not necessary to operate the processes to this level of treatment and therefore the target pollutants are usually degraded to biodegradable intermediates. The remarkable advantage of AOPs over all chemical and biological processes is that they are totally “environmental-friendly” as they neither transfer pollutants from one phase to the other (as in chemical precipitation, adsorption and volatilization) nor produce massive amounts of hazardous sludge (as in activated sludge processes).

Table 1-3: Most common AOPs evaluated for water and wastewater treatment ⁷²

Photochemical processes	Non-photochemical processes
UV oxidation processes	Ozonation
UV/H ₂ O ₂	Fenton
UV/O ₃	Ultrasound (US)
UV/H ₂ O ₂ /O ₃	US/H ₂ O ₂ , US/O ₃ , US/Fenton
UV/Ultrasound	Electrochemical oxidation
Photo-Fenton	Supercritical water oxidation
Photocatalysis	Ionizing radiation
Sonophotocatalysis	Electron-beam irradiation
Vacuum UV (VUV)	Wet-air oxidation
Microwave	Pulsed plasma

1.5.2. Adsorption

Several types of adsorbent (activated carbon, minerals and molecular imprinted polymers) have characteristics that justify their ability to remove pharmaceuticals. However yet filtration over granular activated carbon (GAC) and adsorption by powder activated carbon (PAC) is the only industrial and well-known process for removing pharmaceuticals and other micro-pollutants for tertiary wastewater treatment and drinking water ⁷³. Activated carbon is most commonly applied as a powdered feed or in a granular form in packed bed filters. Granular activated carbon (GAC) is used at many water treatment plants in the United States and Canada. The GAC can be used as a replacement for conventional filters, thus providing both adsorption and filtration. Alternatively, GAC can be applied post-conventional filtration as an adsorbent bed. One of the more common uses of PAC is for controlling tastes and odours ⁷⁴. In controlled pH even relatively high concentrations of pharmaceuticals such as carbamazepine, diclofenac, and bezafibrate can be almost completely removed with the exception of clofibric acid because clofibric acid is less prone to adsorption. Carbamazepine showed the highest adsorption capacity of the selected pharmaceuticals. After GAC filtration in a full scale waterworks, diclofenac and bezafibrate were not detected above LOQ and the concentrations of carbamazepine were reduced by more than 75% and that of clofibric acid by 20% ⁷⁵. The removal efficiency of each compound depends on different parameters such as solubility, Pk_a and chemical properties of the compound and acidity, porosity, chemistry and surface properties of the adsorbent. The advantages of adsorption especially by activated carbon is the simplicity and applicability for wide range of compounds. However for efficient performance regular regeneration of the carbon is

required which is expensive. In the case of PAC, the long contact times and possible need for a batch system/coagulation also adds to system complexity which must be considered.

In conclusion adsorption process merely concentrate the pollutants by transferring them from solution to solid phase. The next problem, then, becomes how to properly disposal of the new pollutant-rich streams. Therefore, management of active species with strict environmental legislation drives the development of clean and green processes, to mineralize and completely degrade all organic and inorganic contaminants before they are disposed into the environment. In addition the spent activated carbon must be regenerated or incinerated to convert the adsorbed pollutants to totally innocuous products. However during chemical regeneration, adsorbed compounds are released to the regenerating medium that should be disposed to the environment after all or release to the air in the form of CO₂ during incineration which has more negative impact on environment considering the global warming. So incorporating a photocatalyst with AC can overcome both regeneration and disposal of the pollutant at the same time.

1.6. Semiconductor photocatalysis for water treatment

Among the other AOPs, photocatalytic degradation processes assisted by a semiconductor metal oxide and oxygen (as primary oxidizing agent), earn increasing importance in the area of wastewater treatment. This field gained prominent attentions in 1972 after the pioneering work of Fujishima and Honda on photocatalytic water splitting on a single crystalline TiO₂ photocatalyst^{76,77}. This finding opened the frontiers of photocatalysis for other type of applications such as environmental decontamination. Photocatalysis, by definition, ‘is a change in the rate of chemical reactions or their generation under the action of light in the presence of substances called “photocatalysts” that absorb light and accelerate the rate of chemical transformations of other compounds on their surface without being used.

Four years later after Fujishima’s break through, Carey et al. first reported the photocatalytic degradation of organic molecules, biphenyl and chlorobiphenyl derivatives, in the presence of TiO₂⁷⁸. Since then various classes of organic compounds have been partially degraded or completely mineralized in UV irradiated aqueous TiO₂ suspensions and enormous number of works have been published demonstrating the efficiency of the use of TiO₂ in photocatalytic processes as a mean of wastewater detoxification⁷⁹⁻⁸². As suggested by Pelizzetti^{83,84}, TiO₂ has the potential to detoxify industrial wastewater to a lower limit of 100ppm TOC and completely mineralize pollutants (0.01 ppm < TOC <100 ppm) in water for drinking and industrial purposes. Considering that this processes require mild operation conditions of temperature and pressure, offer the possibility of use of natural resources such as sunlight, which

should result in considerable economic savings; use low cost and chemical stable TiO_2 and in many cases result in total mineralization of the pollutants without any waste disposal problem. Besides it does not require an addition of any other strong oxidants or consumables reagents which are favourable in large scale plants.

Heterogeneous photocatalytic reaction is based on the irradiation of semiconductor particles, such as titanium dioxide (TiO_2), by UV light having energy more than the band gap energy of the semiconductor particles. Due to irradiation of the semiconductor particles by suitable UV light, holes and electrons generate within the semiconductor particles, and they create active species that oxidize or reduce the adsorbed organic and inorganic compounds gradually. The TiO_2 /UV process as a heterogeneous Photocatalysis is known to have many important advantages over other conventional methods which can be summarized as follows:

- The high oxidation power of TiO_2 leads to the mineralization of almost all organic pollutants dissolved or dispersed in water by enough contact time. Even carbon tetrachloride, which is considered as hydroxyl radical resistant, can be mineralized ⁸⁵.
- Many toxic and precious metal ions in water can be transformed from one oxidation state to less toxic or less soluble states and recovered from the environment ⁸⁶.
- The process end products are carbon dioxide, water and mineral acids which are environmentally benign.
- Atmospheric oxygen is used as oxidant and no other oxidant is required.
- The catalysts are cheap, non-toxic, stable, biologically and chemically inert, insoluble in water and reusable.
- Low energy UVA light is required for catalyst activation, and even solar light can be used with catalyst modification.

It is a great challenge to the scientific community in designing a suitable reactor for photocatalytic process. Normally in laboratory, slurry reactor is used to perform the small-scale experiments where solid catalyst particles are dispersed in water. But in larger scale it encounters some limitations such as internal mass transfer due to particle agglomeration and transport of light, shielding effect by other catalyst particles, uniform light distribution, etc. Furthermore the application of the TiO_2 mediated photoreactions is still experiencing a series of technical challenges: (1) separation of TiO_2 catalyst after water treatment is considered the major obstacle; (2) catalyst development with a strong absorption in the visible spectrum region; (3) prolonging the life time of produced electron-hole pairs; and (4) increasing the photocatalytic efficiency of the catalyst at low concentration of pollutants. Therefore, there is a need for modifying TiO_2

with other materials or methods to create new photocatalyst composite which can solve the as mentioned problems and work more efficiently using natural sunlight as a sustainable energy source.

With advances in new material synthesis, titanium photocatalysis is becoming one of the most promising technologies for water purification among other AOPs. Therefore, photocatalysis using advanced composite materials is considered as a potential alternative for efficient pharmaceutical elimination from aqueous wastes and this alternative is the subject of the present research. However as discussed earlier the concentration of pharmaceuticals are typically low ($\mu\text{g/L}$ or less) causing low frequent collision with TiO_2 photocatalyst, which makes the reaction rate very slow. So developing a new class of TiO_2 catalyst combined with an efficient adsorbent can overcome the existing problems of TiO_2 and introduce photocatalysis as an efficient, environmental friendly and cheap technique to commercial wastewater and drinking water treatment plants.

1.7. Thesis aims and objectives

The aim of this project is to design and optimise an efficient nano-photocatalyst composite with employing titanium oxide as the catalyst and graphene- the new material of the century- as the adsorbent and electron conductor in order to enhance the catalyst function. The focus is on assembly and interfacial coupling of different morphologies of TiO_2 nanostructures such as nano-particle, nano-tube nano-fibre, and meso-porous beads on reduced graphene oxide (rGO) sheets via different chemical methods such as sol-gel and hydrothermal. This research is particularly aimed at establishing firm structure via tuning the morphology of TiO_2 combining with the exceptional properties of graphene to overcome TiO_2 limitation such as charge recombination, narrow light absorbance window, post recovery of the catalyst, poor adsorption of the pollutants and small surface area. The main objective of this thesis can be summarise as follow:

- i. Synthesis of the graphene oxide and reducing it to the graphene using thermal and chemical reduction method and studying their adsorption properties and kinetic of adsorption towards removing dyes and pharmaceutical and proposing an adsorption mechanism. An extensive characterisation had been done in terms of morphology, degree of graphitisation, number of layers and the amount of functional groups and defects on the basal plane of graphene using Raman spectroscopy, UV/Vis spectroscopy and conductivity measurement of the GO and rGO films

- ii. Using graphene oxide as a platform to synthesis of the following different types of TiO₂ nanomaterials using wet chemistry techniques, sol-gel, and hydrothermal:
 - 1. TiO₂ nanoparticles on the surface of graphene sheets using a sol-gel method and simple mixing of commercially available TiO₂ with GO
 - 2. TiO₂ nanotubes and nanofibres on the surface of graphene sheets using hydrothermal method
 - 3. Covering pre-synthesised and functionalised meso-porous TiO₂ beads with rGO
- iii. Characterization of the synthesized nano-composites using different physical and chemical techniques in order to:
 - 1. Study the effect of surface characteristics, morphology, composition and electronic properties on performance of the nano-composite as an active catalyst for purification of water under UV and visible light irradiation
 - 2. Study the effect of dimensionality on the photocatalytic activity through specific surface area, and morphology
 - 3. Investigate the effect of different operating variables and graphene content on photocatalytic properties of the composite
 - 4. Examine the effect of GO reduction method on morphology, structure and resulting photocatalytic activity
- iv. Evaluation of the performance of selective nanomaterials as photocatalyst for adsorption and degradation of different pharmaceuticals and investigate the effect of graphene content and dimensionality of the TiO₂ on photocatalytic properties of the composite

1.8. Thesis Structure

This thesis is organized into seven chapters. In **first chapter** a brief introduction on pharmaceutical occurrence in surface and drinking water and inefficiency of conventional wastewater treatment plants as the main source of pollution was reviewed and applicability of several alternative advanced techniques with their advantages and disadvantages followed by a summary of the objectives of current project were outlined. **Chapter 2** presents a literature broad survey into the pertinent areas of this investigation. This includes an introduction into the basics of photocatalysis, the relevant influencing parameters and different methods to enhance photocatalytic efficiency form doping to morphology modification. A detailed review on fundamental, synthesis and properties of graphene oxide as the main adsorbent of current research was also presented in this chapter. The detail of chemicals, synthesis methods, experimental procedures and protocols and characterisation methods used in this thesis are given in **Chapter 3**, followed by the main work of the thesis in subsequent chapters. In **Chapter 4**, GO and rGO are extensively studies with many analytical techniques such as UV/Vis and Raman spectroscopy, XRD, FTIR, SEM, TEM and AFM and the adsorption properties of GO sponges and GO modified adsorbent is examined. **Chapter 5** is about synthesis, characterisation and photocatalysis degradation of pharmaceuticals using TiO₂ nanoparticles modified with GO and the effect of synthesis method on structure, surface area, adsorption capacity and photocatalytic activity is discussed. In **Chapter 6** one-dimensional morphologies of TiO₂ (Nanotube and nanofibres) in combination with GO were studied in same strategy as chapter 5. In **Chapter 7** meso-porous TiO₂ micro size spheres were synthesised and covered with GO and after reduction were studied towards pharmaceutical degradation. Finally, comparison of all different strategies, conclusion, considerations and implications of the present work summarised in **Chapter 8**. Finally comments and suggestions for future work were outlined in **Chapter 9**.

CHAPTER 2: BACKGROUND & LITRATURE REVIEW

2.1. Introduction

The term of **photocatalysis** consists of photochemistry and catalysis which implies the light irradiation on a catalyst (semiconductors) and promoting a chemical reaction. A photodegradation process is usually a photo-oxidation reaction due to the presence of oxygen. The **photocatalyst** is the agent capable to combine both reactants (light and oxygen) to promote the degradation of a third agent which is the pollutant. Semiconductors with a primary focus on TiO_2 has been applied to a variety of application of environmental interest such as hydrogen generation, solar cells and water and air purification. Variety of semiconductors such as TiO_2 , SnO_2 , Fe_2O_3 , ZnO , CdS , CeO_2 , WO_3 , MoS_2 and ZnS etc. under irradiation of UV or visible light can initiate redox reactions of organic compounds to give CO_2 , water and other associated smaller intermediates in water treatment process. So far TiO_2 is the most common semiconductor for this purpose which will be discussed in more detail later. However there are two major challenges on using TiO_2 which hamper its application in wastewater treatment. (I) Immobilisation of TiO_2 such that the material can be easily removed and recycled without affecting the efficiency and reaction rates. (II) Development of visible light active TiO_2 such that sustainable solar light can be harnessed. Overcoming these drawbacks is the present focus of current research in TiO_2 photocatalysis with the aid of 2D graphene sheets as a platform. Therefore in this chapter some fundamental of photocatalysis will be discussed followed by reviewing few methods of TiO_2 modifications focusing on Graphene and the mechanism of photocatalysis enhancement in graphene/ TiO_2 composites.

2.2. Photocatalysis: Theory and Principles

Semiconductors are usually employed as photocatalysts because of their electronic structure characterized by a filled valence band and an empty conduction band. The energy difference between the conduction band and the valence band is called band-gap energy. When a photon with an energy of $h\nu$ matches or exceeds the band gap energy of the semiconductor, an electron is promoted from the valence band into the conduction band leaving a hole behind (Figure 2-1). These electron-hole pairs can recombine and dissipate the input energy as heat, get trapped in

metastable surface states, or react with electron donors and electron acceptors adsorbed on the semiconductor surface or within the surrounding electrical double layer of the charged particles.

The basic elementary processes of a semiconductor photocatalyst are:

- (i) Light absorption and electron-hole pair generation
- (ii) Charge separation and transport
- (iii) Chemical reactions at the surface

The holes and electrons are very important for photocatalytic degradation due to producing strong oxidising species such as hydroxyl, peroxide and superoxide radicals. After a series of reaction listed below, H_2O_2 and highly reactive radicals, such as OH^\bullet , O_2^\bullet will be generated. These OH^\bullet then react with the organic materials and produce CO_2 and H_2O .

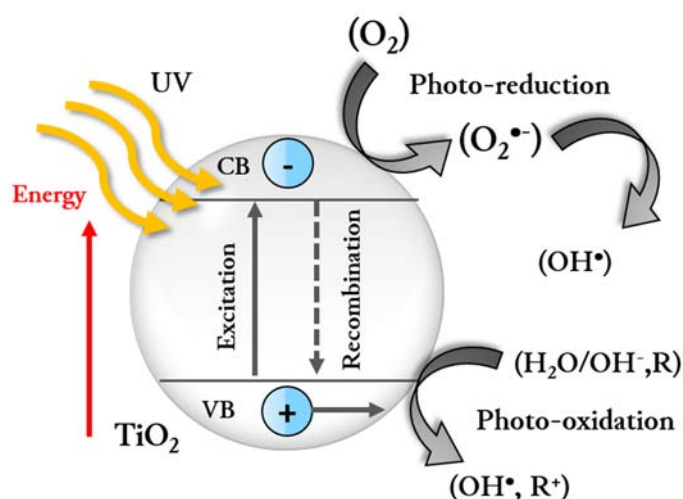
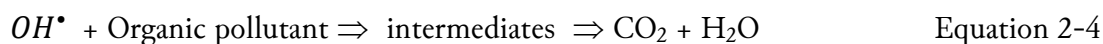
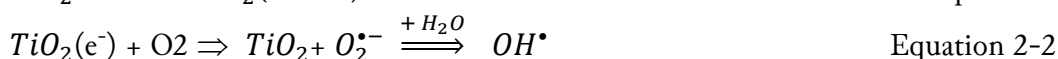


Figure 2-1. Mechanism of the photocatalytic effect of TiO_2

Most organic photodegradation reactions are due to the oxidizing power of the holes either directly or indirectly; however, to prevent a charge build-up providing a reducible species continuously to react with electrons is necessary. In photocatalysis purification of water, dissolved oxygen acts electron acceptor to produce superoxide and prevent charge build-up.

2.3. Why TiO₂

Knowing the band gap energy of the semiconductor (E_g), the required threshold wavelength of light source can be easily calculated by a simple equation ⁸⁷:

$$\lambda = \frac{1240}{E_g} \quad \text{Equation 2-5}$$

The wavelength of an efficient light source should be equal or less than the threshold wavelength of that corresponding semiconductor to activate it. It is proved that lower band gap energy of semiconductor is preferable as it can be activated by higher wavelength visible light, which exhibits low energy ^{88,89}. The p-type semiconductors such as dichalcogenides for example CdS, ZnS and MoS₂ usually possess small band-gap while most of them suffer serious stability problems and are rarely used as a photocatalyst. It is generally found that only n-type semiconductor oxides are stable towards photoanodic corrosion although such semiconductors usually have large band-gap energy, thus they can only absorb UV light. TiO₂ is an n-type semiconductor due to the oxygen vacancies.

2.4. Structure and Properties of TiO₂

TiO₂ is the most extensively studied material for photocatalysts because of its strong oxidizing power, low toxicity, and long-term photostability. TiO₂ exists mainly in three polymorphs in nature, anatase (tetragonal), rutile (tetragonal), and brookite (orthorhombic). Among these crystal structures, rutile and anatase are commonly used in photocatalysis. Generally, anatase is considered to have higher photoactivity than other phases. The lattice structure of rutile and anatase can be described in terms of TiO₆ octahedra chains as illustrated in Figure 2-2. Rutile and anatase have similar crystal structures that are both tetragonal but different in assembly pattern of octahedral chains by distortion of each octahedron. The difference in lattice structure of anatase and rutile causes different density and electronic band structure leading to different band gap of 3.2–3.3 eV for anatase and 3.0–3.1 eV for rutile corresponding to the absorption thresholds of 388 and 413 nm wavelength respectively. The rutile form is extensively utilized for pigments due to its high refractive index while anatase is more commonly used as a photocatalyst in near UV/Vis region (< 380 nm). The rutile has the higher recombination rate for the excess charged carriers compared to anatase form. The recombination inhibits the charge transfer from catalyst to reactants at catalyst surface. The rutile phase is the thermodynamically stable form and the anatase phase transfer to rutile phase when the temperature above 600 °C ⁹⁰⁻⁹².

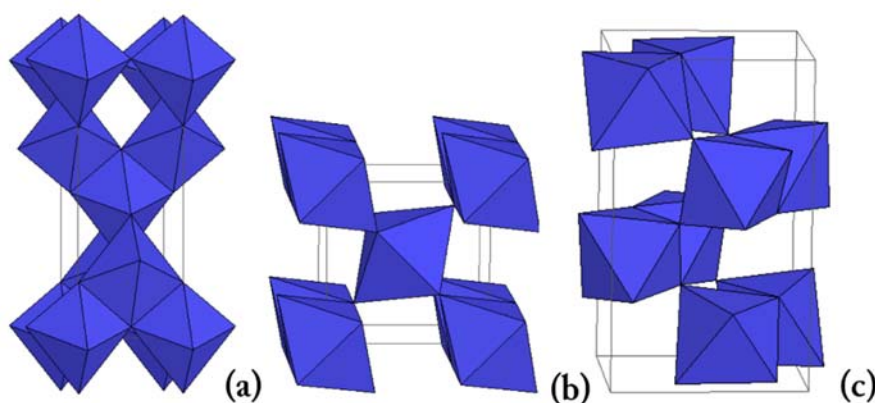


Figure 2-2: Crystal structures of anatase (a), rutile (b) and brookite (c)

2.5. Modification of pristine TiO₂

As mentioned earlier there are few challenges that hinders TiO₂ photocatalysis and limits its application in wastewater treatment. The first challenge is complicated post recovery of TiO₂ nanoparticles which demands ultra-high speed centrifugation or ultra –filtration leading to increase the cost and energy consumption of the process. This can be resolved with immobilisation of TiO₂ on a substrate such that the material can be easily removed and recycled. This can be configured in either a suspended form (TiO₂ coating on the surface of bigger particles of different materials) or an immobilised form (Thin film TiO₂ coating on stationary surfaces such as glass, foams, ceramics, wool, stainless steel, silica and carbon fibres mats). Although the latter has notable advantages such as the prevention of light scattering, ease of removal, and easy reuse however decreases the active surface area of TiO₂ tremendously leading to the considerable decrease in photocatalysis rate⁹³. Therefore achieving the same removal rates and efficiency using TiO₂ coating on suspended particle especially porous solids with high surface area is the overall goal. The second challenge is the development of visible light sensitised TiO₂ composite such that cheaper visible light sources or solar light can be harnessed. In this section few modification to achieve these goals will be reviewed briefly.

2.5.1. Morphological modification

The morphology, roughness and size of TiO₂ particles can affect the light-scattering properties of the catalyst, as well as the degree of photon penetration. The transport properties of the reactants and products within the aggregate can also alter the effectiveness of TiO₂. A photocatalytic nanomaterial with a high aspect ratio is desirable because the needle-like structure may retain a high photocatalytic surface area and a high degree of photon absorption even after the agglomeration. So far numerous research has been done in order to enhance TiO₂

function by modifying morphology and dimensionality of TiO_2 nanostructures from zero dimension spherical particles to 1-D nanowires, nanotubes, and 3-D porous TiO_2 as shown in Figure 2-3. So our aim is to study the synergic effect of TiO_2 dimensionality when they combine with graphene sheets as adsorbent and charge transfer media.

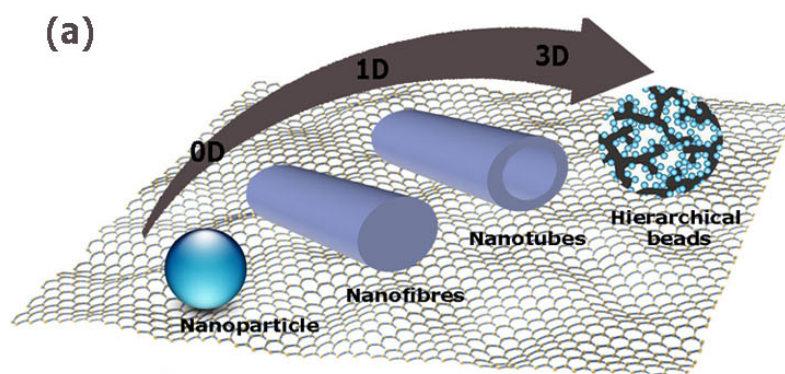


Figure 2-3: Schematic illustration of structural dimensionality of TiO_2 attached to the surface of graphene sheet

2.5.1.1. Zero-D TiO_2 particles

Zero-dimensional TiO_2 spherical particles are the most common form of TiO_2 for many application especially when depositing thin films are required. They can have diameter ranging from 4 nm to few hundred microns. Basically they have equal feature in every dimension and charge generation and transfer will be the same in every direction of the particle. Useful and interesting properties derived from their high specific surface area and a high pore volume and pore size which provides more accessible surface area and increases the rate of mass transfer for organic pollutant adsorption. This type of morphology are typically prepared via controlled sol-gel hydrolysis of organometallic TiO_2 precursor such as titanium alkoxide in the presence of a polymer to provide a porous structure. In this method polymer acts as a template therefore the structure of the polymer plays an important role in the final morphology of the synthesised TiO_2 . For example using polystyrene beads as the template one can produce hollow TiO_2 spheres after burning PS. All the structures synthesised via this method need to be further treated by hydrothermal treatment to produce porous or hierarchical structures followed by annealing at temperatures higher than 400 °C for decomposition of organic molecules of polymeric template and TiO_2 alkoxide as well as increasing the crystallinity of TiO_2 .

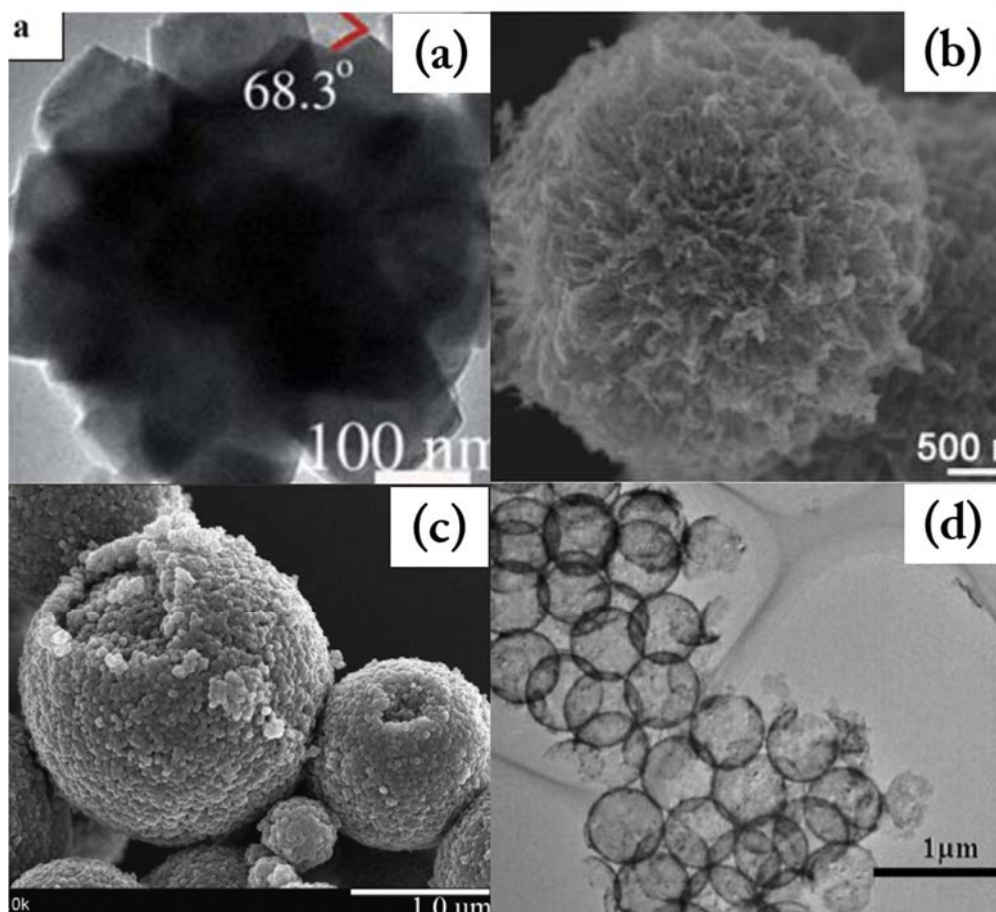


Figure 2-4: Various morphology of zero-dimensional TiO_2 , (a): TEM image of flower-like TiO_2 particle ⁹⁴, (b): SEM image of hierarchical TiO_2 microspheres ⁹⁵, (c): SEM of TiO_2 meso-porous spheres ⁹⁶, and (d) TEM image of TiO_2 hollow spheres ⁹⁷

2.5.1.2. 1-D TiO_2 nanowires, nanotubes and nanofibres

One-dimensional TiO_2 nanostructures, such as fibres and tubes have been comprehensively studied during the past two decades because of the possible practical applications in various fields, including photocatalysis, dye-sensitized solar cells, sensors, lithium ion batteries, biomedicine, catalysis, and supercapacitors. Because of their unique properties such as well-defined size, morphology, composition, high aspect-ratio structure, chemical stability, large specific surface area, excellent electronic and ionic charge transfer, they are very attractive materials for as mentioned application especially in photocatalysis field. First of all their higher surface-to-volume ratio enables a reduction in the hole–electron recombination rate and a high interfacial charge carrier transfer rate which both are favourable for photocatalytic reactions. Secondly hollow structure of TiO_2 nanotubes allows more efficient adsorption of the organic molecules on the surface and inside of the tubes. Hydrothermal method, sol–gel method, vapour deposition method, electrospinning method and anodisation are the most common methods to

prepare one dimensional TiO₂ nanostructures. Figure 2-5 shows the various kinds of 1-D TiO₂ nanostructures that can be synthesised using these methods including TiO₂ nanotubes, nanofibres and nanowires ⁹⁸.

- a) **Hydrothermal method:** is usually conducted in a closed sealed Teflon-lined autoclave heated above boiling point of the solvent. The creation of the supercritical fluid (above liquid-gas critical point) is responsible to create hierarchical structures in hydrothermal process. In terms of the reactants the synthesis method can be divided into the acid-hydrolysis hydrothermal and alkali-hydrothermal approaches. In the former method, the reactants are usually titanium salts like chlorides and titanium alkoxide with inorganic acids, and in the latter method are usually TiO₂ nanoparticles and strong hydroxide solution. The product in most cases is anatase, and dissolution–recrystallization of TiO₂ powder into titanate nanosheets and rolling these sheets to nanotubes after ion-exchange with HCl is the proposed mechanism of this method ⁹⁹⁻¹⁰¹.
- b) **Sol-gel method:** The sol-gel method has been used normally for the preparation of TiO₂ nanoparticles however in presence of special confinement such as polymer chains, surfactant or template, growth of the 1-D nanostructure can be achieved. The essential precursor for sol-gel method is organometallic source of metal oxide mainly alkoxides such as TBT and TTIP. Through the sol-gel, TiO₂ nanoparticles are aligned according to their crystal orientations and so form a TiO₂ nanowire. This process is also known as the “oriented attachment” mechanism ¹⁰²⁻¹⁰⁴.
- c) **Vapour deposition method:** includes chemical vapour deposition (CVD) and physical vapour deposition (PVD), which is significant methods for producing a high degree of crystallinity (usually single crystal TiO₂) for fundamental studies. Although this method are able to produce uniform forest of vertically aligned nanowires with precise control over length and diameter however, this method requires expensive equipment and the cost is too high for mass production ¹⁰⁵⁻¹⁰⁷.
- d) **Electrospinning:** uses high voltage electric fields to spin out the liquid precursors through a fine orifice, forming fibrous structures. Generally, the synthesis of electrospun TiO₂ nanofibres involves the following four steps: (1) preparation of a sol with titania precursor; (2) mixing of the sol with a polymer template to obtain the desirable consistent solution for electrospinning; (3) electrospinning of the solution to obtain composite nanofibres mat, and (4) calcination of the as-prepared nanofibres to burn the polymer and crystallise amorphous TiO₂ particles into crystalline TiO₂ nanofibres ¹⁰⁸⁻¹¹³
- e) **Anodization of Titanium foil:** a powerful tool for the fabrication of vertically aligned mono-size TiO₂ tubes. Anodization is typically conducted in an electrolyte containing

hydrogen fluoride (HF)-based aqueous solution. A titanium foil electrode and counter electrode are soaked in the electrolyte passing a constant voltage through for specific time which results in formation of vertically aligned TiO_2 nanotube arrays on the foil surface with straight channels against the foil. This structural characteristic provides superior photocatalytic decomposition of organic pollutants because of facile diffusion of organic pollutants into the TiO_2 nanotubes. Thin walls are another advantageous feature which reduce the recombination rate of electron-hole because the half-thickness of the nanotube wall is significantly less than the carrier diffusion length in TiO_2 . The morphology of 1-D TiO_2 especially their length and diameter affects the photocatalytic performance. However this process is very slow and the starting TiO_2 foil is expensive so not very practical for mass production for large scale photocatalysis application¹¹⁴⁻¹¹⁶.

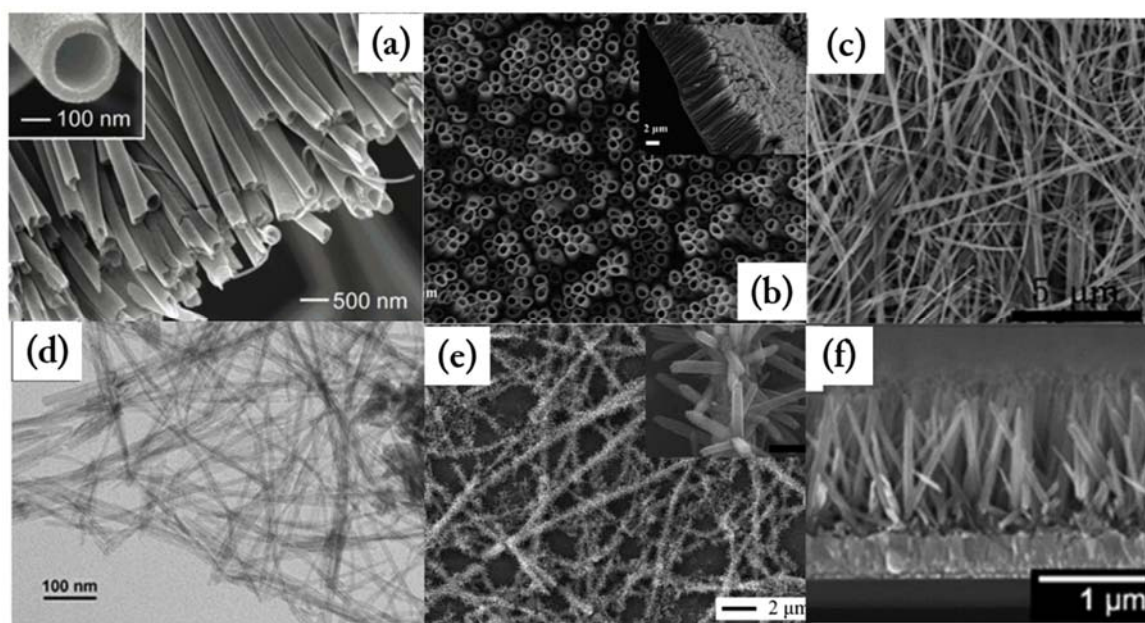


Figure 2-5: Various morphologies of 1-D TiO_2 ; (a): nanotubes via electrospinning, (b): nanotube array via Ti Anodisation, (c): nanofibres via hydrothermal deposition on Ti foil, (d): nanotube via alkaline hydrothermal, (e): hierarchical TiO_2 nanorods grown on electrospun TiO_2 nanofibres via hydrothermal, (f): nanowires via hydrothermal method

2.5.2. Sensitisation (Surface modification)

Dye sensitization is a useful tool to induce visible light photocatalysis on the surface of wide band gap semiconductors like TiO_2 . These surface adsorbed dye molecules are excited upon illumination by visible light and inject electrons into the conduction band (CB) of TiO_2 due to the more negative potential of the lowest unoccupied molecular orbital (LUMO) of the dye

molecules as compared to the conduction band potential of TiO_2 ^{117,118}. These electrons hop over quickly to the surface of TiO_2 where they are scavenged by molecular oxygen to form superoxide radical $\text{O}_2^{\bullet-}$ and hydrogen peroxide radical OOH^{\bullet} which then attack the aromatic rings of organic pollutants forming intermediates and mineralizing them to carbon dioxide and water¹¹⁹. It is also possible to sensitize TiO_2 with conjugated polymers such as poly(fluorine-co-thiophene) (PFT) instead of a dye in order to extend the light absorption to 500 nm. Coupling TiO_2 with another narrow band gap semiconductors like Bi_2S_3 , CdS , CdSe and V_2O_5 which are capable of absorbing visible light. The basic principle of this technique is similar to dye sensitization¹²⁰.

2.5.3. Doping (Band-gap modification)

Many non-metal and metallic atom have been used for doing TiO_2 in order to enhance photocatalytic activity under visible light irradiation. Non-metals species such as Nitrogen, sulphur, Boron and carbon can substitute O or Ti atoms in TiO_2 lattice which generates states just above the valence band maxima that can mix with O 2p valence states to narrow down the band gap of TiO_2 ^{119,121}. Halogen like fluorine, chlorine and Iodine can occupy substitutional as well as interstitial sites in TiO_2 lattice and shift adsorption threshold of TiO_2 to the visible region of spectrum¹²²⁻¹²⁴. Various transition metals like Fe, V, Cr, Mn, Co, Ni and Cu have been doped into the bulk of TiO_2 substituting Ti^{4+} ions. Many other metals such as Au, Ag and Pt has been deposited on the surface of TiO_2 to scavenge photogenerated electrons due to their suitable Fermi level position^{125,126}. In summary, doping (metals/non-metals) generates impurity levels in the band gap of TiO_2 . If these states lie close to the band edges they can overlap with band states and can narrow the band gap. High photocatalytic activity is achieved if the carriers can be transferred efficiently from these states to the surface. Therefore photocatalytic activity is determined by the competition between this charge carrier promotion rate to surface and the recombination rate. Through a different mechanism, doping TiO_2 surface with metal deposition does not change energy level or band gap. It can only reduce recombination processes by effectively trapping electrons and additionally extending absorption into the visible region doping¹²⁷. However the major drawback with adding a dopant is complexity and high cost of mass production process particularly when metals such as Ag or Pt are applied.

2.6. TiO_2 modified by carbonaceous nanomaterials

One of the TiO_2 modification methods for enhancing light adsorption is to immobilize it on a suitable, high surface area substrate such as porous silica, zeolite, activated carbon or nano-clay. In addition to light adsorption enhancement these porous materials can also act as

adsorbent which adsorb pollutants at their surface and expose more pollutant molecule to TiO_2 and adsorbed oxidant species for degradation. Among the porous materials, carbon-based materials are preferable due to their abundance and non-toxicity, unique electronic properties, acidity, adsorption capacity, large specific surface area and their unique pore structure. A lot of researchers compared the functionality of the carbon based materials such as activated carbon and carbon fibres with other inert supports such as zeolites, silica, alumina and porous glass in photocatalysis reactions and observed a synergy between TiO_2 and different kinds of AC on the photocatalytic activity of model pollutant molecules. TiO_2 can be synthesised or immobilised on carbonaceous materials via different techniques including mechanical mixing, aqueous suspensions, sol-gel, hydrothermal, CVD, low temperature hydrolysis, resin calcination, microwave assisted digestion and sonochemical methods ¹²⁸. It has been found that the photocatalytic activity of TiO_2 increases on carbon-based materials due to enhanced TiO_2 distribution on their surface and the ability of adsorbing organic pollutants specially the ones with aromatic benzene ring in their structures. Different forms of carbon materials, with varying properties, play an important role in heterogeneous catalysis. Conventional carbonaceous materials such as graphite, carbon black, activated carbon and carbon fibre paper have been used extensively as a substrate for immobilising various type of catalysts due to their inert nature, stability in harsh environment and fast charge transfer due to their high conductivity. More recently, new carbon materials such as carbon nanotubes (CNTs), carbon nano-fibres, fullerenes and most recently graphene have emerged as attractive materials in the field of photocatalysis.

2.6.1. Activated Carbon/ TiO_2

Activated carbon (AC) was one of the first carbonaceous materials used for modifying the properties of TiO_2 . AC possesses a porous amorphous structure with porosity spanning the macro (>25 nm), meso (1–25 nm) and micro (<1 nm) pore ranges with large specific surface area (typically 900–1200 m^2/g). When combine into AC/ TiO_2 composite, AC can increase photocatalytic activity of the composite comparing pure TiO_2 for three reason:

1. AC can concentrate pollutants on the surface of TiO_2 via physical and chemical adsorption.
2. Electron affinity of activated carbon can increase the acidity of the hydroxyl functional groups on TiO_2 surface which enhances the interaction between some pollutants and alkaline intermediate with TiO_2 ^{129,130}
3. AC also adsorb intermediates produced during degradation which facilitate their further oxidation by as produced species.

Liu et al. reported superior activity of TiO₂/AC over P25 pure TiO₂ towards phenol degradation in wide range of pHs¹³¹⁻¹³³. Kean et al. also reported synergy effect between AC and TiO₂ and considerable enhancement of pharmaceutical photodegradation from water¹³⁴⁻¹³⁶. Several authors argued that the development of TiO₂ photocatalysts anchored on AC, not only to avoid the disadvantages of filtration for post recovery of fine TiO₂ particles, but also to lead to high photodecomposition efficiency for large numbers of pollutant¹³⁷⁻¹⁴⁴.

However AC/TiO₂ composites have some drawbacks as well such as light penetration into the fluid reactor as a result of AC black colour. On the other side obviously, only TiO₂ on the external surface of AC can be excited by light and induce the photocatalytic reaction, so the main percentage of the TiO₂ which is loaded into the interior pores of the AC are not accessible which decreases the photocatalysis yield. Therefore developing a porous adsorbent support with less interior pores and more exposed surface and open pores (such as graphene) looks promising in the field of supported TiO₂ photocatalyst.

2.7. Carbon allotropes

Carbon is one of the most versatile and important elements in the periodic table. Having a valency of four it has the ability to attain a stable electronic configuration by covalently binding to other carbon atoms or to a wide range of other elements, forming a myriad of compounds. Two naturally occurring polymorphs of carbon is diamond and graphite. Graphite is composed of strata of sp² hybridised carbon atoms bound in a trigonal planar atomic arrangement giving a hexagonal lattice; the individual planes are graphene layers. The graphene planes stack on top of each other, held together by weak van der Waals forces acting on the delocalised p orbital system which give all the unique properties to graphite.

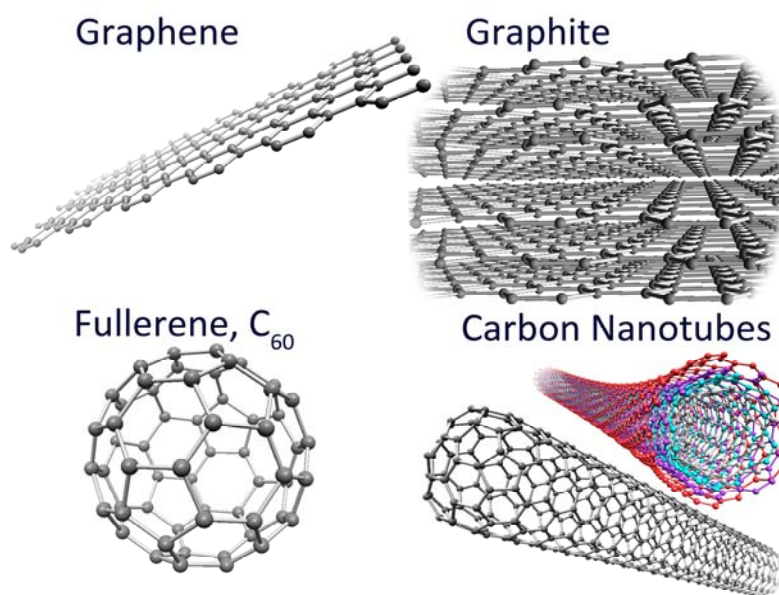


Figure 2-6: Schematic illustration of carbon allotropes ¹⁴⁵

Helical microtubules of graphitic carbon named “Carbon nanotube” was discovered by Sumio Iijima and co-workers in 1991 ¹⁴⁶. CNTs can be visualised as rolled-up sheets of graphene; the various related allotropes of carbon are shown in Figure 2-6. In 2004, Geim and Novoselov reported the first identification of graphene layers isolated from bulk graphite ¹⁴⁷. In this section we first review graphene, its properties, synthesis methods, characterisation and applications. Then modification of TiO₂ with carbon nanotubes and graphene will be reviewed. In final section of this chapter the mechanism of photocatalysis enhancement with graphene will be discussed in more detail.

2.8. Graphene: Definition and Structure

Definition - Graphene is the name given to a monolayer (or few layers) of sp² hybridised carbon atoms packed tightly into a two-dimensional honeycomb lattice and can be considered as the basic building block for graphitic materials of all other dimensionalities ¹⁴⁸. Until its discovery by Geim and Novoselov in 2004 ¹⁴⁷, graphene was widely thought to be thermodynamically unstable and considered a purely academic material with uses in theoretical physics. After being recognised by the award of the Nobel Prize in physics in 2010 to both Geim and Novoselov for isolation and characterisation of graphene, numerous experimental research have focused on graphene due to its intriguing electrical and mechanical properties ^{149,150}.

At 1840s, Schafhaeutl started working on splitting graphite using chemical exfoliation methods with strong acids ¹⁵¹. Since then, many forms of graphite oxide have been produced, characterised and modelled ; all either using covalent attachment of carbon-oxygen functional groups (oxidation with strong acids) or the insertion of small ions such as alkali metals

(intercalation method) to increase inter-layer spacing of graphite ¹⁵²⁻¹⁵⁵. All of these graphitic products are chemically distinct from the starting material. The ideal sp^2 hybridised hexagonal network of carbon atoms is disrupted by these chemical functionalities as functional groups are attached to local sp^3 hybridised sites and distorted the basal plane of graphene which result in totally different physical and chemical properties of the original graphite ^{152,154}. For the first time, repeatedly peeling slices of graphite using adhesive tape led to isolation and observation of a single layer graphene by Geim and co-workers ¹⁵⁶. This work sparked a great deal of scientific interest that has made graphene one of the most exciting and fast-moving research topics in science.

2.9. Graphene: properties and applications

Graphene has remarkable properties including high Young's modulus (~ 1100 GPa), fracture strength (125 GPa), thermal conductivity (~ 5000 W $m^{-1}K^{-1}$), fast mobility of charge carriers (200,000 cm^2 $V^{-1}s^{-1}$) and theoretical specific surface area (2630 m^2 g^{-1}), unique optical transparency, tuneable band-gap plus fascinating transport phenomena such as room temperature quantum Hall effect ^{157,158}. In a defect-free sample of graphene the charge carriers can maintain high mobility at high carrier concentrations ($>10^{12}$ cm^{-2}), giving ballistic transport over length scales of a few hundred nanometres ¹⁵⁹ which could lead to ultra-fast integrated circuits. Known as the strongest materials in the world, graphene can be added into polymers and metals in miniscule fraction as reinforcement filler and enhance and make light and tough composite materials ¹⁶⁰⁻¹⁶². Applications requiring high surface area coupled with high electrical conductivity include electrochemical supercapacitors, lithium ion batteries, solar cells, fuel cells, sensors and catalyst supports has attracted a lot of interest ^{163,164}. Other application of graphene are liquid crystalline displays, biomedicine, biosensors, drug delivery, optoelectronics, laser, terahertz antenna, ultra-sensitive photodetectors, field effect transistors, transparent conductive films for touchscreen and flexible displays and LEDs ^{165,166}.

2.10. Graphene: synthesis methods

The key problem with graphene is the mass-production of high quality graphene. In this section different methods of synthesising graphene (and other 2D materials) will be review briefly and will be compared in terms of scalability and simplicity of the methods. Graphene oxide synthesis will be discussed in more detail since is the main synthesis method for the graphene production used in current thesis. Besides, there are few other methods employed to produce graphene including organic synthetic protocols, in situ electron beam-irradiation of ultrathin poly(methylmethacrylate) (PMMA) nanofibers, arc discharge of graphite under

suitable conditions, thermal fusion of polycyclic aromatic hydrocarbons, conversion of nanodiamonds, sodium reduction of ethanol, and unzipping of carbon nanotubes which are not the subject of this thesis.

2.10.1. Micromechanical cleavage

Micromechanical cleavage (scotch tape method) ¹⁶⁷ involved sticking scotch tape on the surface of highly oriented pyrolytic graphite (HOPG) and repeatedly peeling it off. The tape was then pressed on silicon with a 300nm oxide layer and flakes of graphene were imaged optically with a visible contrast on the colourful oxide layer. The exfoliation and transfer method is illustrated schematically in Figure 2-7. The most pristine monolayer graphene with the largest flake sizes ranging up to millimetre length scales can be obtained by this method. However it is a labour-intensive, slow and very inefficient process with an extremely low yield and only suitable for fundamental science studies. As a result micromechanical cleavage cannot be scaled up for any realistic applications.

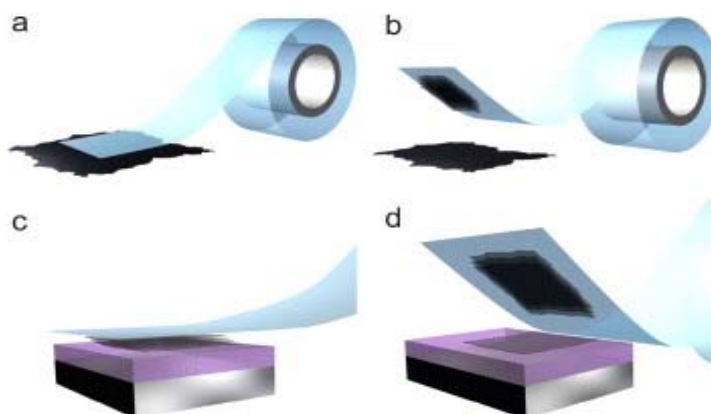


Figure 2-7: Schematic illustration of scotch-tape method followed by transfer on silicon wafer ¹⁶⁷

2.10.2. Epitaxial Growth and Chemical vapour deposition (CVD)

De Heer et.al at the Georgia Institute of Technology developed an epitaxial method in which graphene grows out of silicon carbide at high temperature due to evaporation of silicon in ultra-high vacuum. This leaves behind small islands of graphitized carbon. Epitaxial growth of graphene requires rigid processing conditions including atomically clean highly polished SiC surfaces, ultra-high vacuum very high temperatures typically of the order of 1300 °C, along with subsequent high temperature annealing to improve graphitisation ¹⁶⁸.

The second substrate-based method is chemical vapour deposition (CVD) of graphene on transition metal films such as Cu, Ni, Ru and etc. based on the carbon diffusion-saturation of a transition metal upon exposure to a hydrocarbon gas such as methane carried by Ar and hydrogen at high temperature (800-1000 °C). During cooling the substrate, the solubility of carbon in the transition metal decreases and a thin film of carbon grows on the surface ^{169,170}. The CVD grown graphene can be transferred to any substrate such as silicon, glass and polymer sheets by etching away the underlying metal ¹⁷¹. Considering the large area of depositions high quality, and transfer possibility to the polymer sheets, this method is promising for transparent conducting applications such as sensors, LEDs, FE-transistors, touchscreens and flexible electronics ^{172,173}. However thermally grown films of graphene are simply not suited to a wide variety of applications such as coatings, free-standing graphene films devices, composite materials, membranes and catalyst supports so developing a solution-processable, scalable and cheaper methods is mandatory.

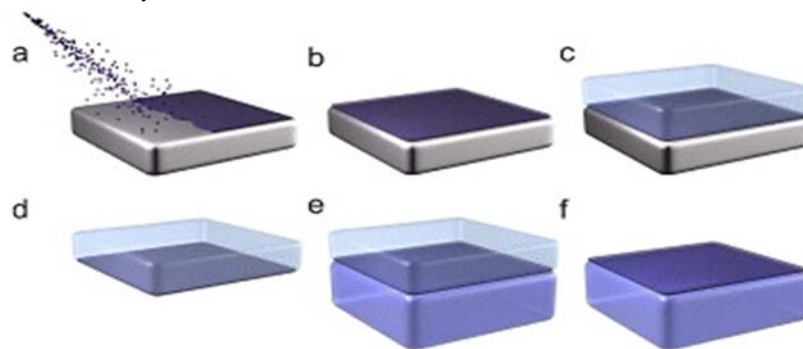


Figure 2-8: Synthesis and transfer of graphene by CVD; (a), (b) Growing 2D graphene on a surface of a metal. (c) Polymer casting on top of graphene, (d) etching away the metal substrate, (e) stamping graphene on the substrate of choice, (f) dissolving the sacrificial polymer layer ¹⁶⁷

2.10.3. Intercalation-exfoliation method

Due to the layered nature, graphite can strongly adsorb guest molecules into the spacing between layers, creating intercalated compounds which can cause the exfoliation of layers by applying a driving force. Intercalation, often ionic species, increases the layer spacing, weakening the interlayer van-der Waals bonds and reducing exfoliation energy barrier. Intercalants molecules such as n-butyllithium or IBr can transfer charges to the layers, resulting in a further reduction of interlayer binding ¹⁷⁴⁻¹⁷⁶. Subsequent treatment such as thermal shock or ultrasonication in a liquid completes the exfoliation process. The exfoliated nanosheets can be stabilized electrostatically by a surface charge, surfactant addition or re-dispersion into a suitable

solvent¹⁷⁷. Although this method tends to give large fraction of mono-layer, however, they are mostly damaged and contain lots of holes on graphene basal plane. Another disadvantages of this method is very high sensitivity to the ambient condition which mandate intercalation in oxygen free glove boxes.

2.10.4. Ion exchange-exfoliation method

Ion exchange methods is based on based on intercalation layered material such as clays with small ion such as Cs or Li then exchange them with protons by soaking them in acidic solutions. These protons can then be exchanged for bulky organic ions (for example, tetrabutylammonium cations) leading to substantial swelling. Consequently swelling facilitates exfoliation through ultrasonication or shear mixing to give negatively charged nanosheets. This method is more versatile for synthesis of inorganic layered materials such as TiO₂, clays and transition metal dichalcogenides (TMDs)^{178,179}.

2.10.5. Liquid phase exfoliation (Shear-mixing method)

The most recent strategy for exfoliation, discovered and developed by Coleman's group from Ireland, is to expose the layered material to ultrasonic waves in a solvent or water-surfactant solution¹⁸⁰⁻¹⁸². Such waves generate cavitation bubbles that collapse into high-energy jets, breaking up the layered crystallites and producing exfoliated nanosheets. Modelling has shown that if the surface energy of the solvent is similar to that of the layered material, the energy difference between the exfoliated and reaggregated states will be very small, removing the driving force for reaggregation¹⁸³⁻¹⁸⁵. Defect-free Graphene, h-BN and TMDs have been exfoliated in this way by using solvents such as N-methyl-pyrrolidone^{186,187}. Similarly, ultrasonication in surfactant or polymer solutions gives nanosheets that are electrostatically or sterically stabilized¹⁸⁸. For a liquid-phase dispersion to be successful, the graphene must be exfoliated from a parent graphite stack and then stabilised against its natural tendency to re-aggregate by surfactants. Disadvantages of this method is removing the solvent from the flake because most of suitable solvent have high boiling point which makes it difficult to evaporate even after heating in vacuum oven. The other limitation is the small size of the flake because of break down during sonication and wide range of number of layers. The concentration and extent of mono-layer is also considerably small.

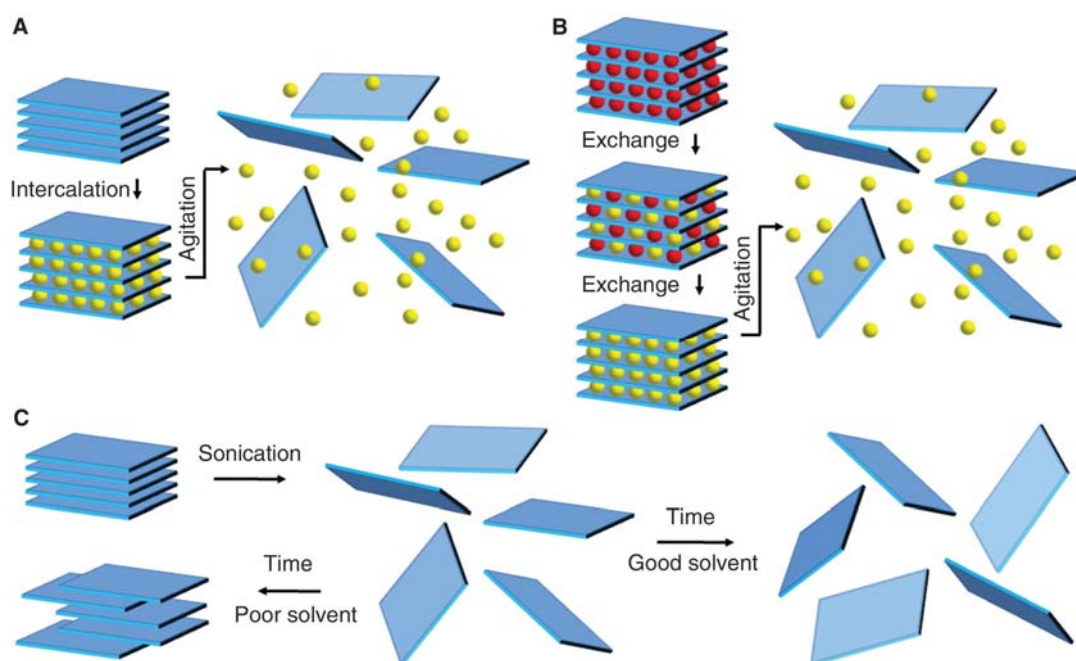


Figure 2-9: Schematic description of different exfoliation methods; (a) Ion intercalation (ions: yellow spheres), swelling, and then agitation results in an exfoliated dispersion. (b) Ion exchange of charges between the layers (red spheres) with other larger ions (yellow spheres) which results in exfoliated dispersion after agitation. (c) Sonication assisted exfoliation of layered crystal in a “good” solvents result in exfoliated nanosheets stabilized against re-aggregation. In the contrary in a “bad” solvents re-aggregation and sedimentation will occur ¹⁸⁹.

2.11. Oxidation/ Reduction method

The oldest method of exfoliating layered crystals is oxidation and subsequent dispersion into suitable solvents and final partial reduction. Graphite can be treated with strong oxidizers such as sulphuric acid and potassium permanganate resulting in addition of hydroxyl and epoxide groups to the graphite basal plane which is named “graphite oxide”. Graphite oxide is heavily oxygenated, bearing hydroxyl and epoxide functional groups on their basal planes, making it strongly hydrophilic. The resulting hydrophilicity allows water intercalation and large-scale exfoliation to yield graphene oxide upon ultrasonication or agitation ¹⁹⁰. The dispersed flakes are predominantly monolayers, typically hundreds of nanometers across, and stabilized against re-aggregation by a negative surface charge at concentrations of 1 to 8 mg/ml. Dispersed graphene oxide can be chemically reduced in the liquid phase but will then aggregate unless surfactant or polymer stabilizers are present. As shown schematically in Figure 2-10, generally this process can be divided into the following steps:

- I. Oxidation of graphite to graphite oxide
- II. Dispersing graphite oxide into an stable dispersion of graphene oxide (GO)
- III. Reduction of Graphene oxide (GO) to Reduced Graphene Oxide (rGO)

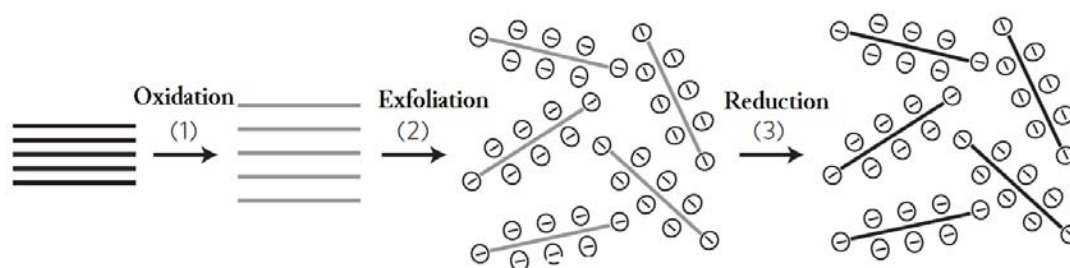
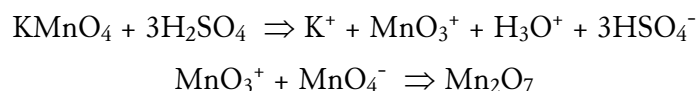


Figure 2-10: Schematic illustration of rGO synthesis via oxidation-reduction of graphite ¹⁹¹

2.11.1. Oxidation to graphite oxide

For the first time in 1859 Brodie made graphite oxide by adding KClO_3 to a slurry of graphite in fuming nitric acid and determined a net molecular formula of $\text{C}_{2.19} \text{H}_{0.80} \text{O}_1$ for it ¹⁹². Almost 100 years later, Hummers and Offeman developed an alternate oxidation method by reacting graphite with a mixture of potassium permanganate (KMnO_4) and concentrated sulfuric acid (H_2SO_4), achieving similar levels of oxidation ¹⁵⁵. This method is still the primary routes for forming GO and base of the current research too. Although in Hummer's method potassium permanganate is known as oxidant, however in the presence of sulphuric acid the active oxidant is diamanganese heptoxide based on the following reaction:



The bimetallic heptoxide is far more reactive than monometallic tetraoxide and this is the compound that oxidises graphite in Hummer's method. This strong oxidant converts hydrophobic graphite to hydrophilic graphite oxide that easily forms a colloidal dispersion in water. This is due to the attachment of hydroxyl ($-\text{OH}$), carboxyl ($-\text{COOH}$) and epoxy ($\text{C}-\text{O}-\text{C}$) groups to the graphite. The level of the oxidation can be varied on the basis of the method, the reaction conditions and the precursor graphite used. Therefore still an exact formula for the graphite oxide composition has not been identified and several models are still being debated in the literature ¹⁹⁰. The most established model proposed by Lerf and Klinowsky is shown in Figure 2-11. In this model the sp^2 -bonded carbon network of graphite is strongly disrupted and a significant fraction of this carbon network is bonded to hydroxyl groups or participates in epoxide groups. Minor components of carboxylic or carbonyl groups are thought to populate the edges of the layers in graphite oxide ¹⁵². So "Graphite oxide" consists of a layered structure of 'graphene oxide' sheets that are strongly hydrophilic such that intercalation of water

molecules between the layers readily occurs increasing the interlayer spacing between the graphene oxide sheets from 6 to 12 Å with increasing relative humidity.

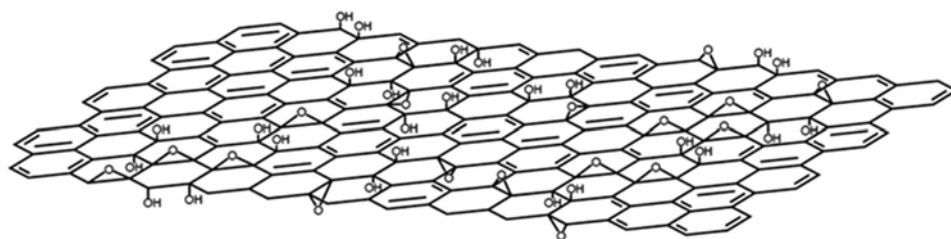


Figure 2-11: Lerf-Klinowsky model for chemical structure of graphite oxide ¹⁵²

2.11.2. Graphene oxide (GO)

“Graphene oxide” must be distinguished from graphite oxide. Chemically, graphene oxide is similar, if not identical to graphite oxide, but structurally is a single layer of graphite oxide stacked structure, exfoliated using sonication, agitation or stirring in water for long enough time. The exfoliation can be confirmed by thickness measurements of the single graphene oxide sheet (~1 nm height) using atomic force microscopy (AFM). The measurement of the surface charge (zeta potential) of graphene oxide sheets shows that they are negatively charged in water which suggests that electrostatic repulsion between charged GO sheets is the reason for the stability of GO dispersion in water. Chemically GO consists of sp^2 -bonded carbon domains disrupted by a large number of covalently bonded hydroxyl or carboxyl groups which interrupted electronic properties of graphene. However these functional groups provides highly dispersed processable GO dispersion in high concentrations (up to 8 mg.ml⁻¹) which with the aid of suitable strategy can be reduced to rGO with reasonable electronic properties for many applications ¹⁹³. Graphene oxide has attracted a lot attention as a new class of adsorbent for water purification purposes. Many studies were used GO in different forms such as dispersion, sponges, powder or they incorporated it into a polymer to form membranes and granules. It has been proposed that the interaction between metal ions and organic pollutants without benzene ring with GO functional groups, and interaction of organic molecules with benzene ring via π - π attraction with sp^2 domain of GO, are the main mechanism that describes large adsorption capacity of GO ¹⁹⁴⁻¹⁹⁷.

2.11.3. Reduction methods

While graphene oxide is electrically insulating owing to disruption of the ‘graphitic’ networks, subsequent reduction via chemical, thermal and hydrothermal method and

combination of them can restore some of these disrupted areas to some extent. Numerous work by a number of groups tried to convert GO back to graphene by aggressive reduction, to give higher degree of reduction of graphene oxide (rGO). Many papers have reported limited in removing the chemical functional groups from the graphene basal plane, thus giving a partial restoration of expected graphene properties. All these reported results share one common problem. The process of chemically oxidising the graphene, to date, has not been completely reversible. The functional groups attached to the graphene basal plane severely disrupt the electronic structure of graphene. Each functionalised carbon site represents a sp^3 hybridised carbon atom as opposed to the sp^2 hybridised form that would normally contribute an electron to the delocalised p system of pristine graphene. The presence of these functionalised sites in graphene turn it into an insulator or semiconductor. Methods such as chemical reduction, thermal methods and ultraviolet-assisted methods has produced electrically conducting rGO suitable for most of non-electronic applications.

2.11.3.1. Chemical Reduction

At early time, Stankovich et al. proposed to reduce a GO film in hydrazine at 100 °C for 24h¹⁹⁸. Among many strong reductants, hydrazine monohydrate is the most attractive option because of slight reactivity with water comparing to other which make it possible to reduce aqueous dispersion of GO with it. The reduction process typically occurs through addition of H_2 across the alkene, coupled with the extrusion of nitrogen gas (Figure 2-12c). Such a process is gentle enough to leave other functionalities, such as cyano and nitro groups, untouched.

While effective at removing oxygen functionality, the disadvantages of using chemical methods of reduction, hydrazine in particular, is the introduction of heteroatomic impurities such as nitrogen which tends to remain covalently bound to the surface of graphene oxide, likely in the form of hydrazones, amines, aziridines or other similar structures^{199,200}. Residual C-N groups have a profound effect on the electronic structure of the resulting graphene, functioning as n-type dopants. No simple route exists for removing these impurities has been reported yet. In the following years, some other reducing agents were also developed such as hydroquinone, sodium borohydride ($NaBH_4$), dimethylhydrazine²⁰¹. For example Lee et al. reported the C:O ratio of 6:2 with 14.5 %wt of C-1s bond (which is related to the sp^3 carbon) and 2.4 %wt nitrogen with the sheet resistance of $780\text{ K}\Omega\text{ sq}^{-1}$ for their best rGO reduced by hydrazine while these numbers are 5:3, 13.4 %wt, 0 %wt and $59\text{ K}\Omega\text{ sq}^{-1}$ respectively for rGO reduced by $NaBH_4$ ²⁰². Nevertheless, none of these reduction methods can recover the graphene structure completely and some oxygen-containing groups are still irremovable according to the

C/O atomic ratio of the rGO by combustion, indicating that reduced graphene oxide is not the same as pristine graphene.

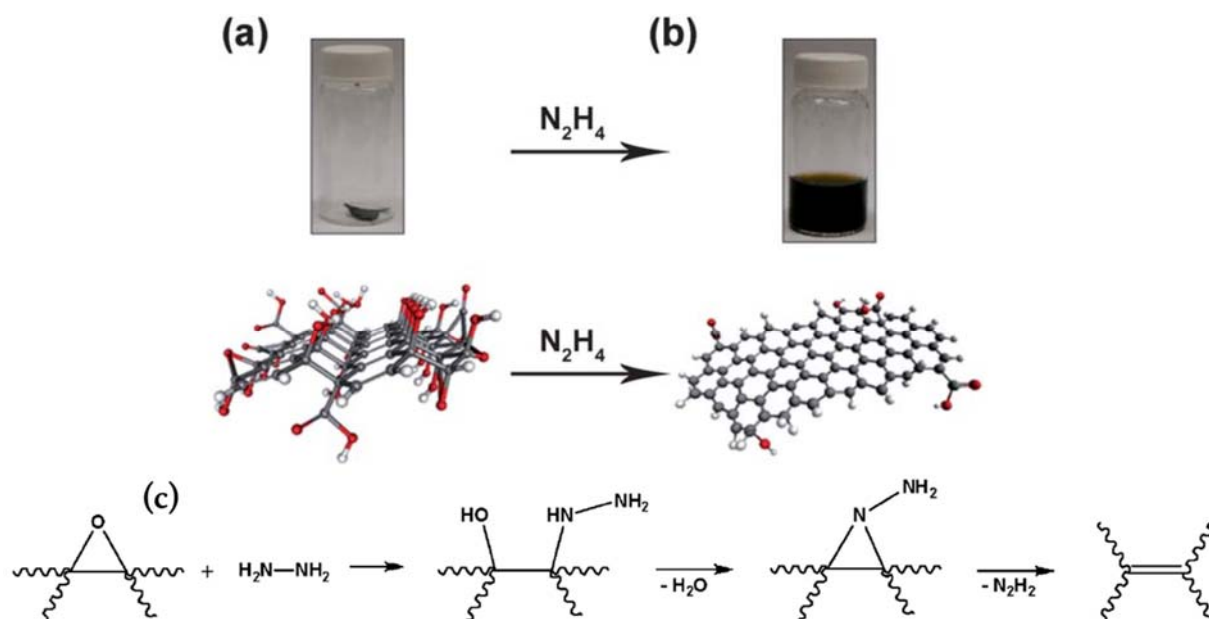


Figure 2-12: Reduction process of graphite oxide paper (b) rGO dispersed after reduction by hydrazine. Below each vial is a three-dimensional molecular model of GO (carbon in grey, oxygen in red and hydrogen in white) and rGO²⁰³; (c) A proposed reaction pathway for epoxide reduction by hydrazine²⁰⁴

2.11.3.2. Thermal Reduction

Thermal treatment of graphite oxide is another route to obtain reduced graphene platelets. Thermal gravimetric analysis of GO assesses that thermal reduction which is contributed to restoration of graphitic C, is generally happens at temperatures above 180 °C with the release of H₂O, CO, and CO₂ in the gas phase. The latter process originates vacancies and defects in the graphene basal plane and consumes the edges. The GO weight loss is attributed to the decomposition of functional groups anchored directly to GO or non-covalently attached debris on GO. An extensive research by Hun et al.²⁰⁵ proposed that from room temperature to 130 °C, mild vaporization of intercalated H₂O molecules is happening. Within the range of 140–180°C, GO crystals are partially exfoliated because of the drastic vaporization of intercalated H₂O and from 180 to 600°C, removal of the main carboxyl groups occurs which results in decreasing the interlayer spacing of the rGO. Within 600–800°C, more residual carboxyl and partial hydroxyl groups are being removed promoting further reduction, however at temperatures higher than 800 °C, defects starts to be generated due to C=C opening during the removal of the residual hydroxyl and partial epoxide groups^{200,206}.

2.11.3.3. UV-assisted reduction

TiO₂ nanoparticles can generate photoelectrons under UV irradiation, which in the presence of holes scavenger such as ethanol, these free electrons can be transferred to GO to partially reduce it, producing a black suspension of TiO₂ anchored rGO sheets in ethanol ²⁰⁷. The TiO₂ was suggested to act as a photocatalyst, transferring photoelectrons from the TiO₂ to the graphene oxide sheets. Kamat et al. confirmed the reduction of GO in the presence of TiO₂ by measuring the absorbance of the suspension and conductivity of the composite ²⁰⁸. Although this methods cannot be used to produce pure reduced graphene oxide for many application, however it is important for the current research to know that the conductivity and charge transport properties of the TiO₂/GO composite will actually enhance after photocatalysis experiment and reuse.

2.12. Comparison of graphene production methods

According to the reviewed literature as summarised in Table 2-1, sonication-assisted liquid-phase exfoliation seems the most promising method for mass production of high quality graphene. However the extent of the monolayer graphene are quite low. Besides anchoring TiO₂ to the surface of pristine graphene produced by this method is quite challenging and requires complicated functionalization chemistry. Therefore in current thesis we focused on oxidation-reduction method which yield large amount of mono-layer reduced graphene oxide containing useful functional groups. The yield of this method in high as well and few gram of graphene oxide can be made in each synthesis batch. Literature survey to find the most efficient method to reduce graphene oxide suggested that various aggressive chemical reduction, thermal annealing processes and other methods remove some of the functional groups but not all of them. XPS, FT-IR, NMR and some other analytical technique has confirmed that even after these harsh treatments there is still a substantial population of oxygen functionalities often carboxyl and epoxide species that are extremely difficult to remove once formed. Whilst the presence of residual functional groups and defects in rGO may be deteriorate their electronic properties and degrade their application in electronic devices, however they are advantageous for some polymer reinforcement applications and anchoring inorganic nanoparticles on their surface without the need for functionalization due to the interaction of the inorganic particles with the residual functional groups. This makes synthesis method of the composite quite straightforward and justifies the application of rGO as a suitable catalyst support for TiO₂.

Table 2-1: Review of graphene production techniques ²⁰⁹

Method	Advantages	Disadvantages
Mechanical exfoliation	Low cost No special equipment required High quality, no functional groups, defect-free basal plane Large area flakes	Slow process Extremely low yield No mass production possibility Limited to single flake fundamental experiments
Epitaxial growth	Compatible with CMOS processing	Intensive surface preparation required Largely multilayer graphitic domain High temperature processing Limited substrate choice
CVD growth	Large area graphene coatings Compatible with CMOS High quality graphene High monolayer yield Easy to transfer to other substrates Useful in transparent electronic	Limited scalability potential, dictated by furnace and substrate sizes Not suitable for composite application High temperature processing Damage possibility during transfer Metal substrates impose high cost
Liquid phase exfoliation by sonication	High quality graphene Low process capital cost Scale up possibility Screening possibility to the range of sizes and thicknesses Environmentally friendly in case of using water/surfactant	Low throughput Low concentration dispersion Solvent recovery problem Small content of mono-layer Small flake size due to breakage with high power ultrasound
Graphite Oxidation-Reduction	Scalable liquid phase route High monolayer yield possible Water-processable graphene oxide intermediate High concentration (~10 mg/ml) Useful for composite application	Defected with holes and persistent functional groups Electronically altered Strong acid needs (Not sustainable) Non-trivial reduction step by reducing chemicals or high temperature

2.13. Photocatalysis enhancement in Carbon nanotube/TiO₂

Carbon nanotubes (CNTs) are tubular allotrope of carbon composed of graphene sheet (single layer makes SWCNTs and multilayer makes MWCNTs) with entirely sp² bonds rolled at specific and discrete (chiral) angle which poses unique mechanical strength, electrical

conductivity, thermal conductivity, optical properties and chemical stability^{210,211}. Nowadays CNTs are playing an important role in developing new technologies for many applications such as electronics, energy storage, battery and supercapacitors, LEDs, flexible electronics, sensors, solar cells, nanocomposites and catalysis such as hydrogen production and storage²¹²⁻²¹⁷.

Due to its unique properties in addition to high surface area ($400\text{--}900\text{ m}^2\text{g}^{-1}$), CNT is an interesting material for photocatalytic enhancement of TiO_2 through providing high quality active sites, retardation of electron-hole recombination and driving visible light catalysis by modification of band-gap and/or sensitization. Owing to high metallic-like electrical conductivity, CNTs can accept TiO_2 's photo-generated electrons when they are in direct contact with each other, resulting in slowing down the recombination rate²¹⁸⁻²²⁰. In addition, very high surface areas of CNTs make them a suitable material for immobilisation of TiO_2 as a catalyst support using chemical methods and functionalization²²¹. CNTs have unique adsorption properties toward organic molecules with aromatic rings via π - π interaction with sp^2 free electrons of CNT which in the case of TiO_2/CNT composite enhances photocatalysis degradation of the pollutants on the surface of composite²¹². Carbon nanotubes can also act as a photosensitizer when in contact with TiO_2 , absorbing more visible light, extending TiO_2 's band gap into the visible region and thereby enhancing the efficiency of the photocatalytic reactions under solar light irradiation^{222,223}.

Like other TiO_2 composites, TiO_2/CNT can be synthesised by different methods, including sol-gel, CVD, hydrothermal treatment or mechanical mixing followed by annealing step at $300\text{--}500^\circ\text{C}$ in an inert atmosphere like Ar or N_2 to crystallize amorphous TiO_2 without burning CNTs^{224,225}. Degradation of different varieties of organic pollutants such as pesticides, pharmaceuticals, dyes and aromatic pollutants had been studied extensively focusing on several parameters including the molecule structure of target pollutants, UV intensity, catalyst dosage, catalyst surface area, etc. One of the most important keys in $\text{TiO}_2/\text{carbonaceous}$ composite is the mass loading of TiO_2 ; for example, it was found that the optimum percentage of CNT for mixed TiO_2 : CNTs is around 20 wt.% CNT²²³. The main mechanism proposed for photocatalysis enhancement is formation of a Schottky barrier at the CNT/ TiO_2 interface. Generally TiO_2 is an n-type semiconductor, but in the presence of CNTs, photogenerated electrons may move freely towards the CNT surface which has a lower Fermi level. Thus CNT acts as an electron sink which leaves an excess of holes in the valence band of the TiO_2 . These holes migrate to the surface for oxidation reaction and makes TiO_2 to behave more like a p-type semiconductor²²⁶.

Numerous studies have confirmed the importance of the morphology, configuration and fine dispersion of TiO_2 on CNTs. They found that fine, well-dispersed TiO_2 coating produced via sol-gel on CNT surface shows higher photocatalytic activity than those produced by a

hydrothermal route, which tended to lead to TiO_2 particle agglomeration at CNT junctions²²⁷. Yao et al. studied the effect of synthesis method, size of TiO_2 particles (5nm and 100 nm), the type of nanotube (SWCNTs and MWCNTs) and its interface with TiO_2 on photo-reactivity of the composite (Figure 2-13). They found optimal activity in SWCNTs wrapped around on 100 nm TiO_2 , suggesting that this morphology and the use of SWCNTs provides optimal dispersion and inter-phase contact²²⁸. Considering the similarities of graphene and carbon nanotubes, this strategy and mechanism can be applied to the current research which leads to identify an appropriate method which is able to produce highly dispersed fine TiO_2 coating on graphene surface with optimum interface and maximum photocatalysis efficiency under UV and visible irradiation.

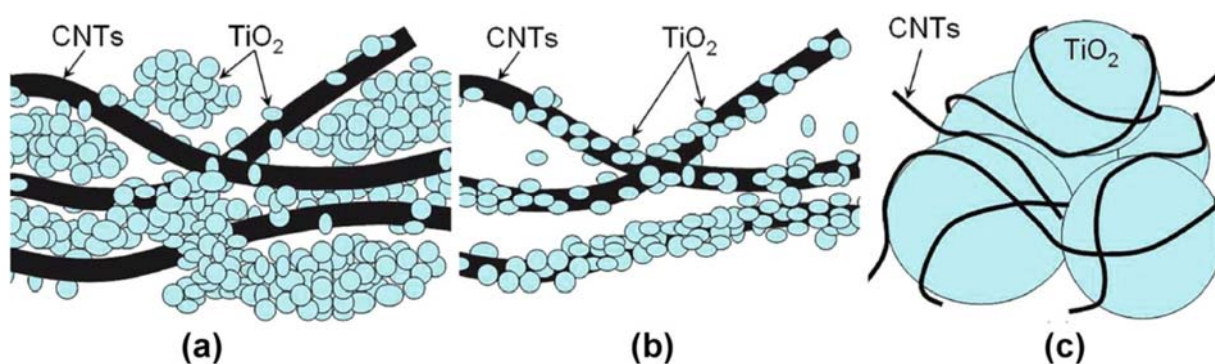


Figure 2-13: TiO_2 /CNT morphologies and inter-phase contact. (a) Random mixture of TiO_2 nanoparticles and CNTs, (b) TiO_2 coated CNTs, and (c) CNTs wrapped around large TiO_2 nanoparticles²²⁸

2.14. Graphene- TiO_2 composite

Recently Graphene is used as a two-dimensional mat for photocatalyst support owing to its excellent properties reviewed in section 2.9. Graphene has very high electron transfer rate, making it potentially ideal electron sink or electron transfer bridge and its high transparency of one-atom thick structure allows efficient light penetration through the composite^{(208,229,230}. Having delocalized electron behaviour in the conjugated π - π interaction of TiO_2 with graphene results in rapid photo-induced charge separation and slow charge recombination in the electron transfer process^{231,231}. Graphene narrows down the bang gap of TiO_2 from 3.2 eV to the range of 2.66–3.18 eV, depending on the graphene content from 0.25 to 10 wt.% which extend the absorption edge of TiO_2 to the long-wavelength light of the visible region^{208,232,233}. The synthesis and physiochemical characterization of TiO_2 /GO and TiO_2 /rGO composites were reviewed in few literature emphasized on the different synthetic strategies for the preparation of different morphologies of this composite for water splitting, solar cells, lithium-ion battery

electrodes and photocatalysis applications²³⁴⁻²³⁷. There are four common methods that has been reported so far for producing G/rGO/GO-TiO₂ composites:

1. *Hydrothermal/solvothermal methods*: Generally, precursors (GO or rGO, dispersed in an organic solvent or water and a titanium organometallic compound or TiO₂ powder) are loaded into a pressure vessel and treated at high pressure and temperature for several hours. Depending on pH and other growth conditions, rod-shaped TiO₂²³², nitrogen-doped rGO/ TiO₂²³⁸, nanoparticles²³⁹ and other morphologies can be obtained.
2. *Solution mixing*: This process involves ultrasonic-assisted mixing pre-synthesised TiO₂ with GO or rGO in water or organic solvent followed by UV-assisted photocatalytic reduction of GO²⁰⁸. Using this method layer-by-layer rGO/TiO₂ can be obtained by spin-coating, dip-coating or Langmuir-Blodgett self-assembly of rGO/GO and TiO₂ consecutively²⁴⁰.
3. *Sol-gel*: In this process generally a titanium precursor is injected drop-wise into rGO/GO dispersed in an organic solvent under controlled hydrolysis condition. The mixture is then aged to induce TiO₂ growth and resulting powder is calcined in order to crystallise amorphous TiO₂²⁴¹.
4. *Self-assembly (direct growth from salt)*: In this method TiO₂ particles with different morphology is hydrolyse on the surface of GO directly by drop-by-drop addition of titanium chloride (TiCl₄) or fluoride (TiF₄) salt into GO dispersed in organic solvent or water-surfactant system^{242,243}

There are few papers also reported the combination of above methods such as sol-gel/hydrothermal or solvothermal method^{235,244}. It is remarkable that all the main production methods are based on rGO and not pristine graphene because rGO nanosheets still contain decent amount of functional groups and defects which are capable of binding uniformly to metal oxide particles and remain in suspension without aggregation.

Zhang et al. prepared chemically bonded TiO₂ (P25)-graphene nanocomposites using a hydrothermal method. The synthesized catalysts shows significant enhancement in the degradation of methylene blue compared to bare Degussa P25 and CNT-P25 composites²²⁹. It was also found that hydrothermal treatment not only reduces GO to rGO, but also plays an important role to strengthen the interaction between TiO₂ and rGO which results in increasing the efficiency of hydrothermally treated samples comparing solution-mixed rGO and Degussa P25 composite. Another study showed that photocatalytic activity of the TiO₂/graphene composite highly depends on graphene contents and calcination temperature. The highest photocatalytic activity was observed for the sample with 5% graphene sheets^{233,245}.

2.15. Photocatalytic degradation of Pollutants by rGO/TiO₂

One of the most important uses of graphene composites especially graphene/TiO₂ composite is the photo-degradation of ionic, organic and biologic pollutants from aqueous and gas phase. Kemp et al. reviewed the applications of graphene composites for water remediation, where rGO based TiO₂ composites turned out to be highly useful for removal of many organic compounds from water ²⁴⁶. Many papers reported different routes to synthesis various morphologies of TiO₂/graphene composites for photocatalysis application. However majority of them used dyes such as methylene blue as a pollutant model ^{175,247-252}. For example Zhang et al. ²⁵³ have used a hydrothermally prepared TiO₂/rGO composite for degradation of methylene blue and found that photocatalytic activity was higher than that of TiO₂ alone, or TiO₂/CNT composites with the same carbon content. The enhancement was attributed to the giant two-dimensional planar structure of graphene favouring dye absorption, suppressing electron-hole recombination due to the high electrical conductivity of rGO, extending light absorption to the visible range due to the high transparency and band-gap narrowing resulting from the presence of Ti-O-C bonds. Liang et al. synthesised TiO₂ nanocrystals on graphene oxide via hydrolysis followed by hydrothermal treatment to crystallise TiO₂ and reduce GO to rGO. The as-prepared composite exhibited an impressive three-fold photocatalytic rate enhancement over pure TiO₂ P25 and 2.5 times over graphene/TiO₂ mixture towards rhodamine-B dye degradation ²⁵⁴. In summary all reviewed research exhibited much higher photocatalytic activity for graphene/TiO₂ composite than bare TiO₂ and also reported an optimum ratio of graphene to TiO₂ for the best photocatalytic activity. The increase in photocatalytic activity was explained to be attributed to enhanced adsorption of pollutants on the composite surface, intensified light absorption, increased lifetime of electron hole-pair and extended light absorption range to the longer wavelength in solar spectrum.

2.16. Mechanism of Photocatalytic Enhancement in graphene/TiO₂

There are two main limitations concerning the use of TiO₂ as a photocatalyst especially for water remediation. First is very fast electron-hole recombination (10⁻⁹s) which provides very short chemical reaction response time of only 10⁻⁸–10⁻³ s. Second is wide band gap (3-3.2 eV) which requires UV light for activation ^{255,256}. There are four main parameter introduced to be responsible for enhancement in photocatalytic properties of graphene based TiO₂ comparing to pure TiO₂.

- (I) Trapping and shuttling electrons which enhances electron-hole separation and reduces charge recombination rates owing to very high electron mobility of graphene. It has been demonstrated that electrons flow from higher to lower Fermi

levels. Since the work function of graphene (4.42 eV) is higher than the conduction band of TiO₂ (4.21 eV) graphene could be used as an electron shuttle so that electrons will flow from graphene to TiO₂. Both electrons and holes react with O₂ and water to form superoxide and hydroxyl radicals, respectively which ultimately degrades organic molecules. ²³¹.

- (II) Enhancing light absorption via enlarging the absorption range to the visible region, by narrowing the band gap of the TiO₂ to 2.8 eV because of Ti-O-C bonds formation and nano-sized Schottky interfaces, acting as a sensitizer ²⁵⁷.
- (III) Enhancing the transportation of the photogenerated carriers via photothermal effect of rGO which is continuous generation of thermal energy in graphene under NIR irradiation ²⁵⁸.
- (IV) Increasing the adsorption of pollutants with TiO₂ via increasing the interaction surface area and creating a π - π interaction with the delocalized electrons of rGO especially towards pollutants with benzene ring ²⁵⁹.

A schematic of the main three mechanism is shown in Figure 2-14.

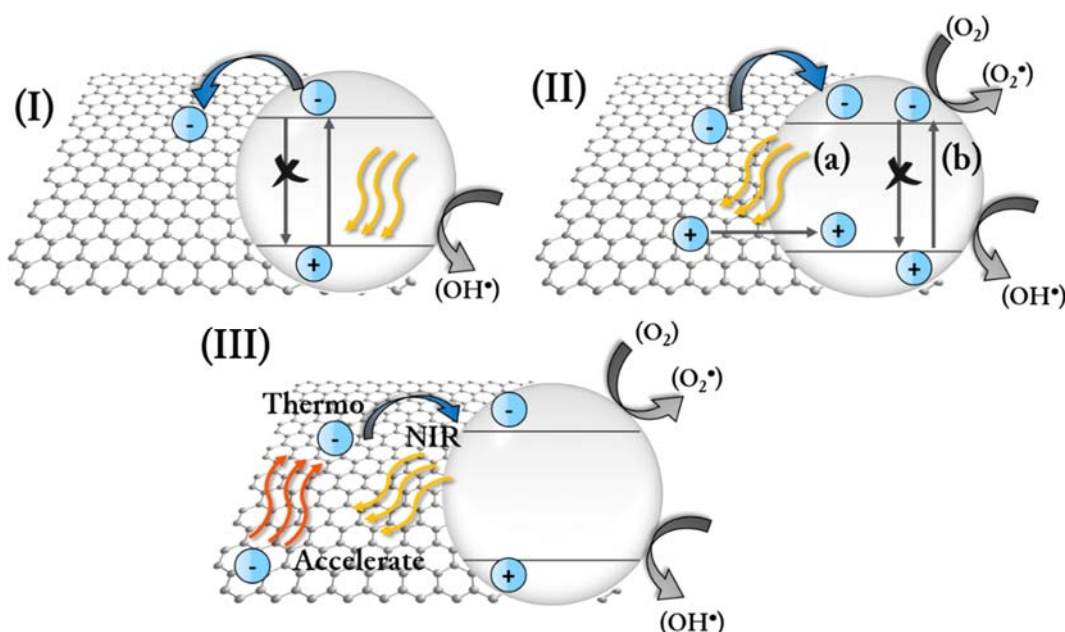


Figure 2-14: Proposed mechanism for photocatalysis enhancement in graphene/TiO₂ composites, (I) graphene act as an electron trapper and shuttle, (II) graphene act as a photosensitizer and produces charge carriers due to interacting with photons (a) and act as impurity and doping agent reducing the band gap of the TiO₂ due to the Ti-O-C bonds formation, (III) Surface Plasmon resonance under NIR irradiation leads to photothermal effect of rGO. Thermal energy promotes carrier mobility on rGO sheets and thus results in the improved photodegradation activity.

Through the first mechanism, valence band electrons of TiO_2 are excited by high energy photons and transferred to the conduction band. Photogenerated electrons are then transferred into the graphene and a hole remains in TiO_2 , with redox reactions occurring on the surface of TiO_2 . The second mechanism considers graphene as photosensitizers which photo-generated electrons from graphene transfer to the conduction band of TiO_2 , followed by formation of superoxide radicals from the adsorbed molecular oxygen. Meanwhile, the positively charged graphene takes an electron from the valence band of TiO_2 , leaving a hole. The positively charged TiO_2 then reacts with adsorbed water to form hydroxyl radicals (Figure 2-14II). In this mechanism also has been proposed that functional groups such as $-\text{OH}$ and $-\text{COOH}$ which are abandon on rGO basal plane and edges can make chemical bonds with TiO_2 and create Ti-O-C bond and function as TiO_2 dopant. This helps to extend the light absorption to longer wavelengths, potentially improving the photocatalytic activity.

CHAPTER 3: MATERIALS & METHODS

3.1. Introduction

This chapter discusses the main characterisation methods and experimental techniques used in this thesis. In this work, different types of TiO₂/graphene nanocomposites were prepared via different chemical routes and used for adsorption and photocatalytic degradation of selected drugs. All samples were separated from the liquid phase, washed and dried. For UV/Vis spectroscopy characterisation, small amount of each sample re-dispersed in water with ultrasonication and supernatant were transferred into the quartz cuvet for further spectroscopy characterisation. The remaining characterisations were carried out on solid material deposited or extracted from the liquid dispersions. Infrared and Raman spectroscopies were used to probe the chemical nature and composition of the produced materials. Transmission electron microscopy was extensively used to examine dimensions of as synthesised material and, their crystallinity. Scanning electron microscopy was used to study the morphology of TiO₂ nanostructure and their assemblies on graphene in the form composite deposited on different substrates. These various techniques will be now be discussed with reference to relevant literature as appropriate.

3.2. Materials and chemical reagents

All materials, chemicals and reagent used in current research can be divided in three categories: chemicals and precursors for material synthesis, solvents for HPLC analysis, and consumables such as filters, syringes and HPLC stationary phase (column). All the chemicals and consumables used in this study is listed in Table 3-1.

Table 3-1: Source and description of materials used

Materials and consumables	Supplier	Application
Graphite flakes	Asbury Carbon/USA	Graphene synthesis
Potassium permanganate	Sigma-Aldrich	Graphene synthesis
Hydrogen peroxide 30%	Sigma-Aldrich	Graphene synthesis
Sulphuric acid 97%	Sigma-Aldrich	Graphene synthesis
Nitric acid	Sigma-Aldrich	Graphene synthesis
Hydrochloric acid 37%	Sigma-Aldrich	Graphene synthesis
Titanium isopropoxide (TTIP)	Sigma-Aldrich	TiO ₂ synthesis
Iso-propyl alcohol, ethanol	Sigma-Aldrich	TiO ₂ synthesis
Acetic acid	Sigma-Aldrich	TiO ₂ synthesis
Ammonium hydroxide	Sigma-Aldrich	PH control
Sodium hydroxide	Sigma-Aldrich	TNT synthesis
N-Methyl-2-pyrrolidone (NMP)	Sigma-Aldrich	Graphite exfoliation
TiO ₂ powder Degussa	Evonik Industries/Germany	Photocatalyst
Dolomite granules	Queens University/Belfast	Adsorbant
VitraPOR® Porous Glass Beads	Robu Glassfilter Gerate/GMBH	Adsorbant
Silica gel granule	VWR Ireland	Adsorbant
Methylene blue dye	Sigma-Aldrich/Germany	Pollutant model
Famotidine	Astellas/Ireland	Pollutant model
Solifenacin succinate	Astellas/Ireland	Pollutant model
Diclofenac	Sigma-Aldrich	Pollutant model
Carbamazepine	Sigma-Aldrich	Pollutant model
HPLC grade water	Fischer Scientific Ltd	HPLC mobile phase
HPLC grade methanol	Fischer Scientific Ltd	HPLC mobile phase
Spectrometry grade formic acid	Fischer Scientific Ltd	HPLC mobile phase
Nylon syringe filters (0.22 µm)	Phenomenex	Filtration
Nylon filters (0.2 µm, 47 mm)	Pall/Ireland	Filtration
Amber HPLC vials	Fischer Scientific Ltd	HPLC sample storage
Quartz cuvette CXA-145-050W	Hellma GmbH & Co. K	UV/Vis spectroscopy
HPLC Column	Phenomenex	HPLC
Silicon wafer cuts	NCPST	Raman analysis

3.3. Apparatus

Apparatus are all the equipment that were used in material preparation and photocatalysis test excluding analytical instruments and were briefly listed in Table 3-2.

Table 3-2: Apparatus and their application in this project

Apparatus	Model	Application
Ultrasonic cleaner	5510 E-Mt	exfoliation of GO, cleaning
Probe Sonicator	VibraCell, CVX 750 W	Graphite exfoliation
Carbolite Tube furnace	CTF 31 600	Calcination/ reduction
1L-Photo reactor	model 7841-06	UV Photocatalytic tests
29cm immersion well	model 7857	UV-vis Photocatalytic
Medium pressure Hg lamp	TQ 150 Heraeus Noblelight	UV source
Hydrothermal reactor		composite synthesis
Oven		Drying materials
Freeze-dryer	Labconco	GO sponge preparation
Shaker		Adsorption rests
Microwave oven		Graphite expansion

3.3.1. UV irradiation experimental set-up

Photodegradation studies using suspensions of TiO₂ composites with water spiked with selected pharmaceuticals were conducted in 1 L borosilicate glass photo-reactor manufactured by Ace Glass (model 7841-06) and a quartz immersion well (model 7857), 290 mm in length with water cooling (Figure 3-1). On the central axis, the 125W medium pressure mercury lamp (TQ 150 Heraeus Noblelight, emission between 248 and 579nm, λ_{max} 366nm) is placed in a jacketed quartz cylinder as the UV light source (thermo-regulated with cooling water to remove lamp and reaction heating) encasing the lamp with a Pyrex reactor vessel to ensure filtration of light below 300 nm outside of the vessel for the safety. Three necks are used for sampling, purging air, and measuring temperature. The internal wall of the box hosting the reactor is covered with aluminium foil which prevents the penetration of any parasitic radiation coming from the outside environment within the reactor. The solution is stirred with a magnetic stirrer continuously and purged with air in order to increase the circulation of the composite between the reactor walls also provide enough oxygen for the photoreaction. Air purging was undertaken with standard air pumps throughout the reaction (Hagen Elite aquarium pumps). A sparger at the air inlet allowed generation of a consistent flow of small air bubbles.

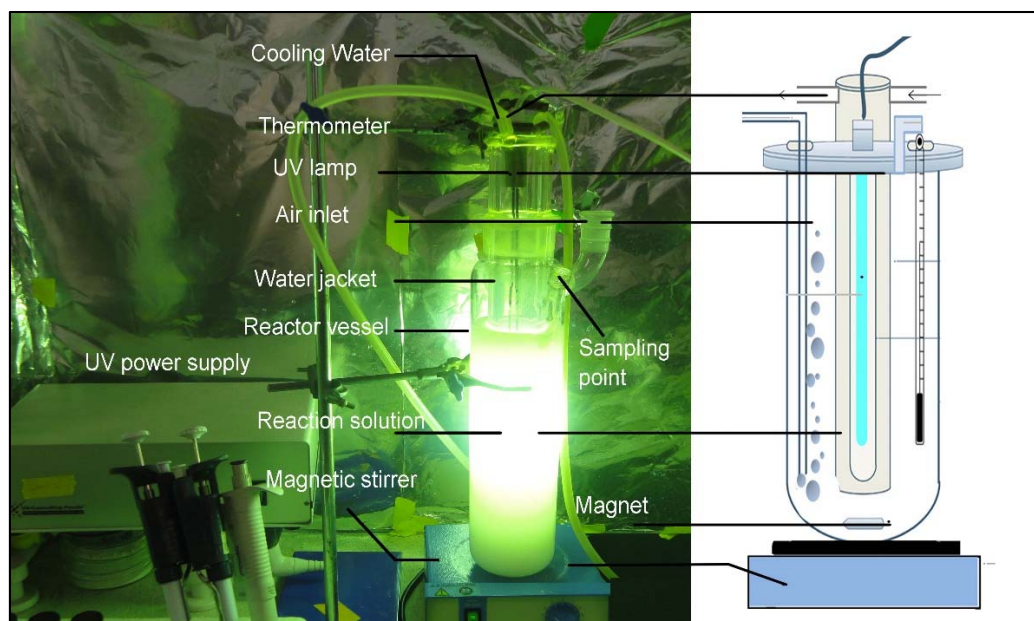


Figure 3-1: photograph and schematic of photochemical reactor with labelled components

3.3.2. General method for UV-photocatalysis studies

For photodegradation studies different as-synthesised TiO_2 /graphene composites described in chapter 5, 6 and 7 were mixed with water containing certain concentrations of selected pharmaceuticals ranging from 10 to 100 ppm. In each photodegradation experiment a catalyst concentration of 0.3 g/L as the optimum catalyst dosage were used. A 100mg/L initial concentration of Famotidine, Solifenacin, and diclofenac and a 15 mg/L initial concentration of carbamazepine were used for photodegradation experiments. Each photocatalytic experiment includes two sequential successive processes: adsorption then oxidation.

- **Adsorption step:** 1L of distilled water spiked with pharmaceutical models in certain concentration as mentioned earlier, was poured inside the reactor then a known mass of the photocatalytic materials (as stated previously) was added. The solutions were then magnetically stirred inside the box in dark without any light irradiation at 25°C for 1 hour to allow adsorption equilibrium to be reached. During the adsorption, one sample was taken immediately and four samples were taken every 10 min and filtered for analysis either by HPLC or UV-Vis spectrophotometry.
- **Oxidation step:** After the adsorption step, the UV lamp was switched on and a stream of air was supplied to provide more agitation, faster mass transfer and enough oxygen

for the reaction. During the oxidation step, samples were taken regularly and then analysed either by HPLC or UV-Vis spectrophotometry.

The change of the substrate concentration during adsorption and UV/visible light irradiation was measured by withdrawing 3 mL samples of the solution from the reactor. These samples were syringe filtered with 0.22 μm nylon filters to remove any particles in the sample and then analysed with HPLC which is described in the following section of 3.3.6. Degradation profiles are plotted with reaction (illumination) time on the x-axis (in minutes) and concentration on the y-axis in the form of: C_t/C_0 where C_t is the concentration of pharmaceutical at time t , divided by the concentration of pharmaceutical at 0 minutes, C_0 . Kinetic of the reaction modelled with Pseudo-first-order model subsequently.

3.3.3. Visible irradiation set-up

The set-up for study the visible light activity of TiO_2 composites as shown in includes a 300 mL Pyrex schlenk flask, a 500 W Halogen lamp (IQ Group), a Pyrex cold finger and a Hagen Elite air pump. The schlenk reaction vessel was clamped to a stirring plate and 250 mL of selected pharmaceutical with certain concentration and calculated amount of composites were added to the flask and stirred for one hour to reach the adsorption equilibrium and samples were taken regularly as described in previous section. Then the cooling cold finger inserted and the halogen lamp, located by 30 cm distance from the vessel, was turned on to initiate visible light photodegradation, while the reaction was purging with air bubbles. Sample concentrations were monitored by HPLC chromatography.

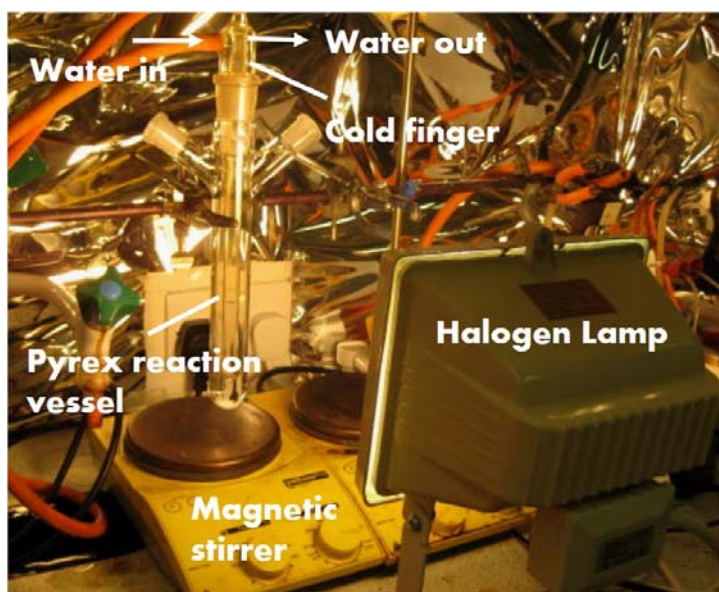


Figure 3-2: Indoor visible light photocatalytic reaction set-up irradiated by a Halogen lamp.

3.3.4. General method for visible-photocatalysis studies

The general process of Visible light photocatalytic degradation of famotidine, solifenacin, diclofenac and carbamazepine were followed as outlined previously (3.3.2) with the incorporation of a Halogen lamp instead of Hg UV lamp. The reactor volume was also 300 mL in this case. Generally 250 ml of spiked water containing the same concentrations as UV experiments described in section 3.3.2 was added to the schlenk flask (Figure 3-2) along with a previously weighed amount of photocatalyst (0.3 g/L) (or none for photolysis experiments). Prior to irradiation the reaction solution were stirred in dark for 60 min, and 2ml samples were taken every 10 min. Then the air purging tube was inserted and lamp was turned on. Samples from both adsorption and photocatalysis step were filtered using Nylon filter membranes straight into vials for HPLC analysis. Degradation profiles are plotted with reaction (illumination) time on the x-axis (in minutes) and concentration on the y-axis in the form of: C_t/C_0 where C_t is the concentration of pharmaceutical at time t, divided by the concentration of pharmaceutical at 0 minutes, C_0 .

3.3.5. Control experiments

Control experiments were performed with a drug concentration of 100 ppm and were conducted as follow: (i) Photolysis (UV only), (ii) Pure TiO_2 in dark, (iii) TiO_2 /UV/visible light, (v) P25/UV/visible light, (vi)GO/rGO in dark and (vii) GO/rGO/UV/Visible. The general procedure, as outlined previously in sections 3.3.2 and 3.3.4, and 3.3.6 was then followed.

3.3.6. HPLC-UV chromatographic methods

The concentrations of pharmaceuticals used for this study were measured using a high performance liquid chromatography (HPLC) system consisting of an Agilent 1100 (Agilent Technologies, Palo Alto, Ca, USA) low-pressure gradient pump equipped with a UV-Vis detector. Stock solutions of 100 ppm were prepared in Millipore distilled water and dilutions were made with Millipore water with laboratory auto-pipettes in order to make 8 standard with known concentrations. All freshly made standards were analysed by HPLC method and calibration curve was derived to calculate the unknown concentrations. Table 3-3 contains method development conditions with the methanol solvent phase system which were optimized from methods developed by A. Deegan detailed in a PhD Research Thesis previously undertaken in our group ²⁶⁰. The LOD (limit of detection) and LOQ (limit of quantification) for FAM, SOL and DIC were 0.2 and 1mg/L respectively. A 150 x 4.6mm, 3.5 μm particle Luna

pentafluorophenyl propyl reverse phase column was used for separation of FAM and SOL analytes and a C18, Luna 25 cm×4.6 mm with 5 μ m particle size was used for separation of DIC. The mobile phases used for FAM analysis consisted of 15% methanol to 85% water with 0.1% formic acid. The mobile phase used for SOL analysis was 70% methanol to water with 0.1% formic acid. The mobile phases used for DIC was 80% methanol to 20% water and pH was adjusted to 3 by addition of ortho-phosphoric acid to the MeOH/H₂O mixture. These solvents were filtered by 0.22 μ m nylon filters and degassed by ultrasonication for 30min. For FAM, SOL and CBM the eluent flow rate was 1mL/min and for DIC was 0.75 mL/min with the injection volume of 50 μ L.

Table 3-3: Chromatographic conditions for pharmaceutical pollutant models

Eluent	Mobile phase	Inj. Vol. (μ L)	Flow rate (ml/min)	WL (nm)	Column	LOD mg/l	LOQ mg/l
Famotidine (FAM)	15% MeOH: H ₂ O (0.1% formic acid)	50	1	205	150×4.6mm, 3.5 μ m, Luna PFP	0.2	1
Solifenacin (SOL)	70% MeOH: H ₂ O (0.1% formic acid)	50	1	205	150×4.6mm, 3.5 μ m Luna PFP	0.2	1
Diclofenac (DIC)	80% MeOH: H ₂ O pH:3 phosphoric acid	50	0.75	277	25 cm×4.6 mm, 5 μ m Luna C18	0.2	1
Carbamazepine (CBZ)	ACN:6MeOH: 4H ₂ O	50	1	230	25 cm×4.6 mm, 5 μ m Luna C18	0.2	1

3.4. Material synthesis and experimental section of chapter 4

3.4.1. Chemicals

Expandable graphite flakes (1721, Asbury Graphite Mills, US) with flake size average >500 μ m were used as starting material for GO synthesis. All the HPLC grade solvent such as water, methanol, acetonitrile and spectroscopy grade formic acid and ortho-phosphoric acid were purchased from Fischer Scientific Ltd. Three different substrates including dolomite, porous glass, and silica were employed as porous substrates immobilization of graphene oxide nano-

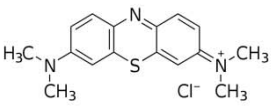
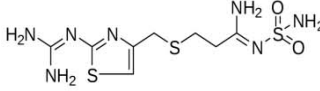
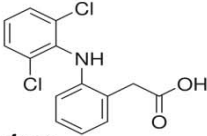
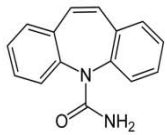
sheets. Physico-chemical properties of each material are summarized in Table 3-4. The grounded dolomite, donated by Queens University Belfast, was mined from the dolomite deposits found in Co. Fermanagh, Northern Ireland and calcined at 800 °C for 8 hours to increase the porosity of the powder. Porous glass bead (VitraPOR® ROBU) was donated by ROBU-GLASFILTER-GERÄTE Germany and the silica gel was supplied by GeeJay Chemicals Ltd., UK. All substrates were initially washed several times with distilled water and dried at 60 °C overnight.

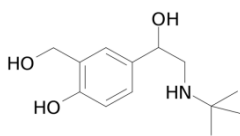
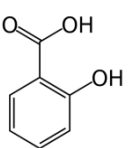
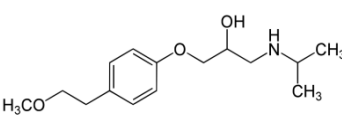
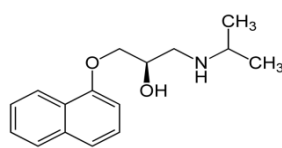
Table 3-4: Physical properties of the substrates for GO immobilisation

Properties	Dolomite	Porous glass	Silica gel
Formula	$\text{CaMg}(\text{CO}_3)_2$	USP-class I borosilicate	SiO_2
Crystal structure	Trigonal rhombohedral	Amorphous	Amorphous
Density g/cm^3	0.75	2.23	2.21
Particle size (mm)	0.3-0.5	4	2-4
Surface area (m^2/g)	6.1	1.6	800
Pore size (nm)	63.3	40000-100000	0.5-4
Chemical composition	CaCO_3 , CaO, MgO	SiO_2 80.60%	SiO_2

Diluted solutions of methylene blue (MB), famotidine (FAM), diclofenac (DIC), and a mixture of salbutamol, salicylic acid, metoprolol, propranolol, carbamazepine and diclofenac (MIX) were used as adsorbate to model pharmaceutical rich wastewater. The test solution was prepared using ultra high purity water.

Table 3-5: Molecular structure and physical properties of methylene blue and pharmaceuticals used as pollutant models

			
Methylene Blue	Famotidine	Diclofenac	Carbamazepine
Molar Mass (g)	319.85	337.50	236.2
Solubility in water (g/l)	43.6	1.1	0.0177
Density (g/cm ³)	1.757	7.1	1.296
Pka	3.8	4.15	13.94

			
Salbutamol	Salicylic acid	Metoprolol	Propanolol
Molar Mass (g)	239.31	267.36	259.34
Solubility in water (g/l)	0.03	16.9	0.07
Density (g/cm ³)	1.443	9.68	9.5
Pka	5.9	2.97	

The properties of the adsorbates are shown in Table 3-5. All chemicals and solvents used for chromatography were HPLC grade and purchased from Fisher Scientific Ltd.

3.4.2. Synthesis of GO film and GO sponge

Large GO sheets were prepared by modified Hummers' method using expandable flake graphite with a size of 500–600 μm as raw materials. As shown in Figure 3-3, graphene synthesis procedure simply be divided in three step: expansion, oxidation/exfoliation and reduction.

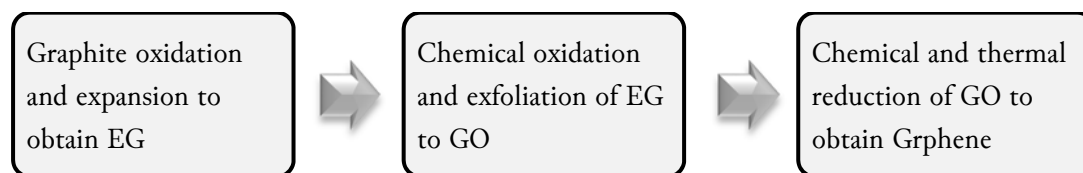


Figure 3-3: Graphene synthesis procedure via oxidation-reduction method

In a typical procedure, graphite flakes were heated in 100 W microwave for 15 sec to produce expanded graphite (EG) as the precursor for graphene oxide (GO) synthesis. Then 4 g of EG and 500 ml of sulphuric acid were mixed and stirred in a three neck flask for 2 hrs. Next 20 g of KMnO_4 was gradually added to the mixture. After 24 hrs of stirring at room temperature, the mixture was then transferred into an ice bath and 500 ml of deionised water and 100 ml of H_2O_2 were poured slowly into the mixture resulting in a colour change to golden brown. Having

stirred for another 30 min, the resulting oxidised EG particles were washed and centrifuged with HCl solution (9 H₂O:1 HCl %Vol.) three times, then centrifuged again and washed with deionized water. Repeated centrifugation washing steps with deionised water were carried out until a solution pH ≥ 5 was achieved. In Figure 3-4 step-by-step procedure of making GO is shown graphically.

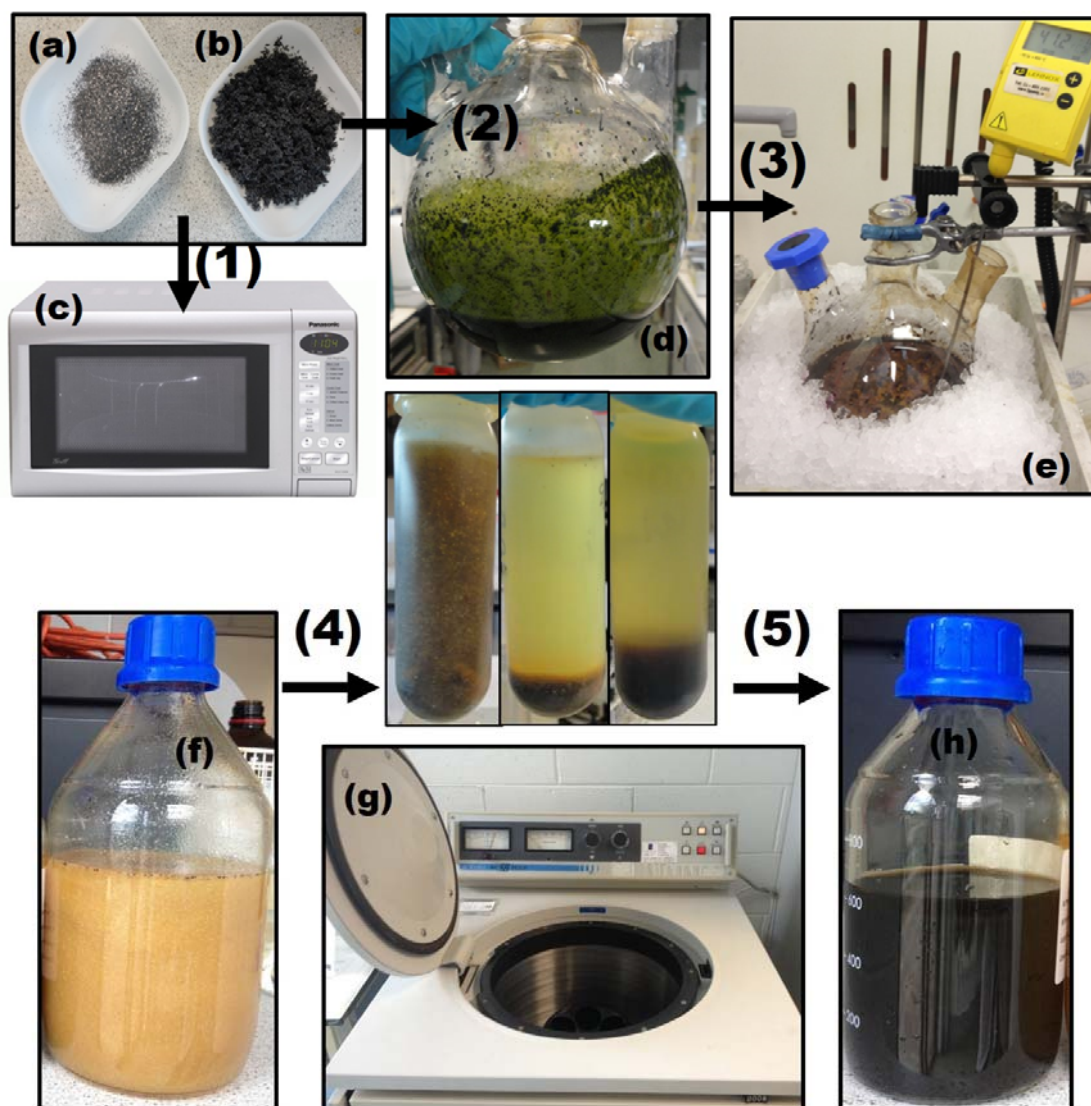


Figure 3-4: Experimental procedure for making graphene oxide: (1) Microwave assisted expansion of graphite (a) to EG (b); (2) Oxidizing with sulphuric acid and KMnO₄ to form a green paste (d); (3) Adding water and H₂O₂ gradually under controlled temperature using ice bath (e) to obtain golden yellow suspended graphite oxide flakes (f); (4, 5) Washing with 1 L of HCl solution and water using repeating centrifuge and discarding the supernatant, this will cause gradual exfoliation of graphite oxide into paste like GO solution (h)

During washing process, oxidised EG particles were exfoliated to GO sheets resulted in a highly viscos honey like solution with concentrations up to 10 mg.ml⁻¹. In order to produce GO

sponge, the resulting concentrated solution were transferred into 500 ml bottle and frozen at -80 °C. The solidified GO aqueous solution was then placed in freeze-dryer under vacuum for 2 days until the water was removed completely and light porous GO sponge was obtained. To prepare GO composites certain amount of GO re-dispersed in water by sonication for 60 min. To produce GO film, the GO concentrated solution was poured onto a Teflon plate or mould and was dried in the oven at 50 °C for two days. The GO paper was then peeled off the Teflon surface, cut into desired sizes and were stored in dry place. In order to study the effect of GO reduction on adsorption properties, thermal reduction of GO to obtain reduced graphene oxide (rGO) was performed at 450 °C for 2 hours. The images of these three form of graphene is shown in Figure 3-5.

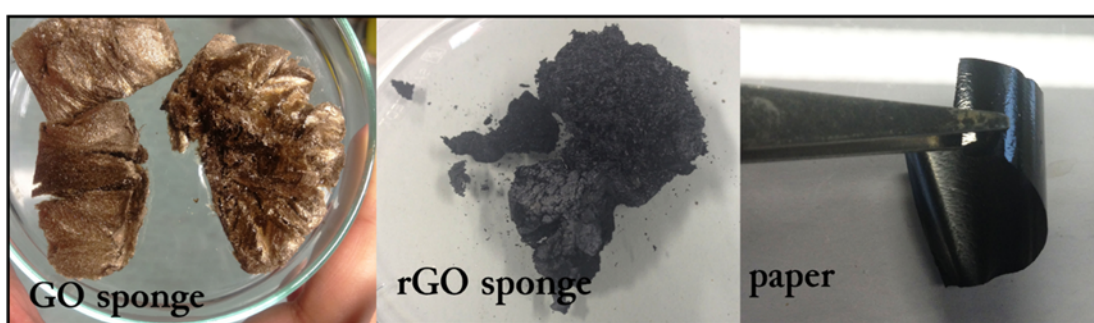


Figure 3-5: Photograph of freeze-dried GO foam, rGO foam and GO paper

3.4.3. Immobilisation of GO on the surface of porous substrates

Immobilisation of GO on the surface of porous materials is an approach to produce engineered adsorbent with higher adsorption capacity and easier post recovery of GO from water after the adsorption process. In this experiment, three different porous supports as mentioned in Table 3-4, including porous glass beads, dolomite powder (charred at 800 °C for 8 hrs), and silica gel granules were chosen as a substrate for GO immobilization. The as synthesised GO solution with the concentration of 3.37 mg/ml, as a source of GO, and 15 g of each substrate after washing and drying were used to make composite containing 2.2 %wt. of GO. Generally 100 ml of GO solution with pH 4.5-5 divided in to three parts and were added to the substrate in three steps, stirred for 30 min and dried at 60°C before adding the next GO part in order to obtain uniformly coated substrates containing 2.2 wt% GO.



Figure 3-6: GO coated substrate: porous glass/GO (1), dolomite/GO (2), silica/GO (3), bare substrates (a), coated with GO (b)

3.4.4. Synthesis of Dolomite/GO composite

Three different types of dolomite were examined in order to find the most efficient form of dolomite to make GO composite. As shown in Figure 3-7(a-c) dolomite with average grain size of 2-2.5 mm and 1 mm as received and 200-250 μm charred at 800 $^{\circ}\text{C}$ for 4 h were used as substrate. 50 g of these substrates were mixed with 300 ml of GO with the concentration of 6.4 mg/ml and as a result of increased pH as well as water absorption by dolomite, the dispersion was turned into viscous gel as shown in Figure 3-7(e). The resulting gels were dried at 70 $^{\circ}\text{C}$ overnight to obtain black to grey composites (a_1 - c_1) containing 3.6 %wt. GO. They were stored in sealed vials for further adsorption experiments.

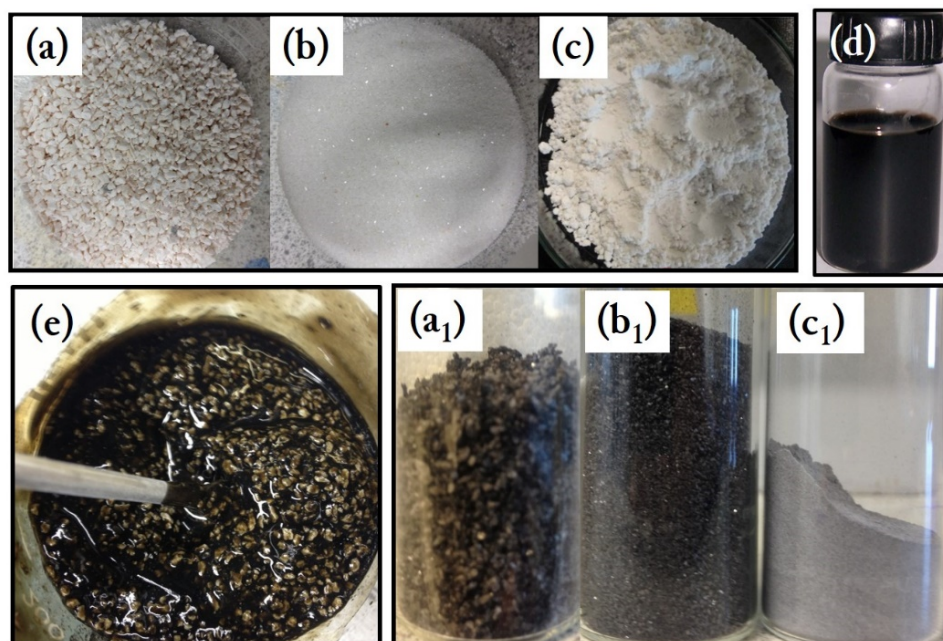


Figure 3-7: Process of making dolomite/GO adsorbent using three different meshes of dolomite before coating (a-c), after mixing GO solution (d) with bare dolomite they create a gel which holds dolomite particle stable (e) and makes uniformly GO coated dolomite after drying the gel (a₁-c₁)

3.4.5. Adsorption experiments: Graphene oxide

All adsorption experiments were conducted using a batch equilibration technique at 23 ± 1 °C. TO evaluate the adsorption capacity pharmaceuticals on GO and the optimum GO concentration, adsorption of 200 mg/l of diclofenac, famotidine and solifenacin were carried out by mixing a certain amount of GO sponge (0.1 to 1 g.L^{-1}) in 100 ml sealed flask and were shaken for 4 hours in dark to reach the equilibrium and prevent any possible photodegradation of the adsorbate. The suspension then was centrifuged at 10000 rpm for 15 min to separate liquid from solid phases and the liquid phase was filtered with the $0.22 \text{ }\mu\text{m}$ nylon syringe filter and stored in amber HPLC vials for concentration measurement.

In order to investigate the functionality of the GO adsorbent in real condition which is the presence of variety of drugs in water, the adsorption experiments of a mixture of five different pharmaceutical (Salbutamol, Salicylic acid, metoprolol, propranolol, carbamazepine and diclofenac at three initial concentrations (50 , 10 , 5 mg.L^{-1}) and three GO concentration (0.1 , 0.05 and 0.01 g.L^{-1}) were carried out in 100 mL solution with constant shaking under ambient conditions. After the adsorption studies were completed, the samples were taken at regular intervals then centrifuged and filtered in the same procedure. The concentration of the adsorbate in the solution was determined using Beer–Lambert law by monitoring absorbance at wavelength of 284 nm which is the maximum absorbance of the mixture obtained from the UV-Vis scan of the solution.

The adsorption kinetic study was carried out with an initial diclofenac and famotidine concentration of 200 mg.L⁻¹ at 296 K, GO concentration of 0.025 g.L⁻¹ in 200 mL and pH 4.0 to determine the minimum time required for adsorption to reach the equilibrium. Samples were taken every 10 min for the first hour then every 30 min for the next two and half hours and were analysed based on the HPLC method described in section 3.3.6. To study the effect of pH on adsorption of diclofenac and famotidine 0.05 g.L⁻¹ of GO sponge were added to 20 mL of the two analyts at the concentration of 100 mg.L⁻¹ and pH was adjusted ranging from 2 to 11 by addition of 0.1 M NaOH and HCl aqueous solution. The adsorption isotherms were carried out by stirring of 20 mL aqueous solution with 1000, 500, 200, 150, 100, 50, 10, 5, and 1 mg.L⁻¹ of diclofenac and famotidine and the GO concentration of 0.05 g.L⁻¹ and the pH was adjusted at 4. The samples were taken after 60 min and prepared via the same procedure. HPLC samples for the concentrations above 200 were diluted 10 times to be able to obtain accurate data. The effect of adsorbent concentration on removal rate and amount of adsorption was studied using graphene sponge concentration at 1, 0.5, 0.2, 0.1, 0.075, 0.05 and 0.01 g.L⁻¹ in 20 mL of 100 mg.L⁻¹ of diclofenac and famotidine during one hour of adsorption through the same procedure. In adsorption graphs C_e (mg.L⁻¹) denotes the equilibrium concentrations in aqueous phase after the adsorption of tetracycline on GO. The equilibrium adsorption capacity or the uptake of the adsorbate (q_e , mg.g⁻¹) is the variation between the initial (C_0) and equilibrium concentration (C_e) caused by per unit weight of the adsorbent which can be calculated by $(C_0 - C_e)/C_{GO}$. The removal efficiency is calculated by $[(C_0 - C_e)/C_0] * 100$.

3.4.6. Adsorption experiments: GO/Dolomite and other substrates

3.4.6.1. Batch mode adsorption experiment

Adsorption on GO and GO coated materials were initially carried out in a batch system to determine their removal capacity. A desired amount of each adsorbent ranging from 0.01 up to 3 g/l was added to the flask containing 100 ml of water with the known concentration of pollutants. As mentioned in Table 3-5, two classes of pollutant models were chosen for adsorption experiments, pharmaceuticals and methylene blue dye. The initial concentration of pharmaceuticals, depending on the solubility, was set between 2 to 10 mg/l for carbamazepine and 10 and 100 mg/l for other compounds. Methylene blue concentration was varied between 10 to 1000 mg/l. The glass bottles were sealed and then were placed on a shaker in the dark. The adsorption experiments were carried out at 180 rpm for 12 hrs to ensure that equilibrium is reached. The temperature was maintained between 21 and 23 °C. Upon equilibration, the water sample was filtered through a 0.45 µm nylon syringe filter to remove the adsorbent and collected in HPLC vials. Finally the concentration of pharmaceuticals in water samples were

measured by HPLC and the concentration of MB were measured by UV spectrophotometer. The amount of adsorbed pollutants on GO (q_e) and water sample (C_e) for equilibrium condition at respective adsorbent dosage was calculated for each experiment using:

$$\text{Equation 3-1} \quad q_e = \frac{V(C_0 - C_e)}{m}$$

Where q_e is the adsorbed amount; V is the volume of the liquid phase (l); C_0 (mg/l) is the initial concentration of pollutant; C_e is the concentration after equilibrium; and m is the mass of the adsorbent.

3.4.6.2. SPE column adsorption experiments

In order to examine the adsorption properties of the composites in continuous flow and to examine the life time of adsorbent before reaching the saturation also to prevent the post separation of composite in batch adsorption experiments, a special adsorption column was designed based on solid phase extraction method. As shown in Figure 3-8, the adsorbent was placed in SPE cartridges between two frits and attached to the stopcock fitting which is switchable. For adsorption experiments methylene blue at a concentration of 0.2 μM were used. For each experiment, 5 ml of each solution was injected and a vacuum applied to keep the pressure at -254 mmHg. Water samples were collected accordingly at the bottom in a vacuum manifold for each cartridge and were analyzed with UV spectrophotometer to determine the concentration. This process were repeated 10 times for each cartridge to find out the exhaustion time for each adsorbent.

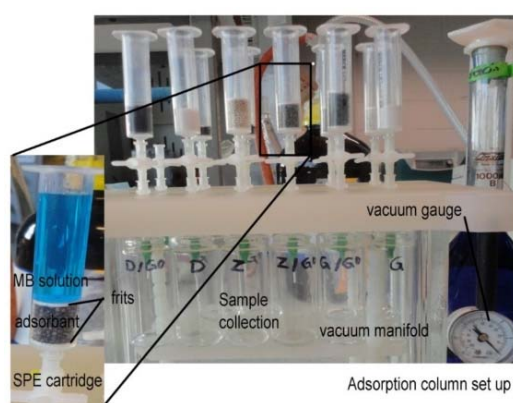


Figure 3-8: Adsorption column set up for adsorption test of bare and GO coated substrates

3.5. Material synthesis and experimental section of chapter 5

3.5.1. Chemicals

Titanium (IV) Isopropoxide 97%, also called Titanium Tetraisopropyl orthotitanate (TTIP), were used as TiO_2 precursor in sol-gel synthesis. Anhydrous Isopropyl alcohol (IPA) and sulphuric acid purchase from Sigma were used without any further purification. The chemical structure of TTIP and IPA, the two main compound involved in sol-gel process is shown in Figure 3-9. Graphene oxide dispersion with certain concentration were synthesised according to section 3.4.2. The commercially available Degussa P25 TiO_2 powder under the trade mark of AEROXIDE[®] was purchased from Sigma Aldrich.

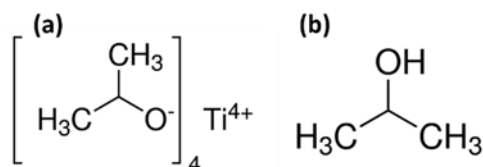


Figure 3-9: Chemical structure of TTIP and IPA

3.5.2. Sol-gel synthesis of TiO_2 nanoparticles

TiO_2 nanoparticles were derived via sol-gel hydrolysis of titanium isopropoxide, followed by calcination or hydrothermal treatment in order to increase crystallinity of the as-synthesised powder. Generally 15 ml of TTIP was dissolved in 150 ml of anhydrous IPA gentle stirring in order to avoid hydrolysis of TTIP with the moisture present in the air and labelled as solution A, as illustrated in Figure 3-11. Separately 300 ml deionised water was mixed with 30 ml IPA (solution B). Then, the former solution (A) was added dropwise to the latter (B) under vigorous stirring and the pH was adjusted to 0.5 by adding required amount of 1 M nitric acid and stirred for 1 h at room temperature to obtain the homogenous TiO_2 sol. Small amount of white precipitates of hydrous oxides were produced instantly which was dissolved after adding acid and stirring for 3 h and the resulting sol was aged at 40 °C overnight. The amorphous sol were then subjected to either calcination or hydrothermal treatment to promote TiO_2 crystallisation. In the former, the sol were first dried at 70 °C followed by calcination at 450 °C for 2 h in air circulated furnace for removal of volatile and organic species and formation of crystalline oxides. In the hydrothermal route, the as-synthesised sol was transferred to a sealed Teflon-lined stainless steel autoclave (70% filled), and treated at 170 °C for 20 h. The hydrothermally treated

suspension was then centrifuged at 5000 rpm; the powder recovered was washed with deionized water, and dried at room temperature.

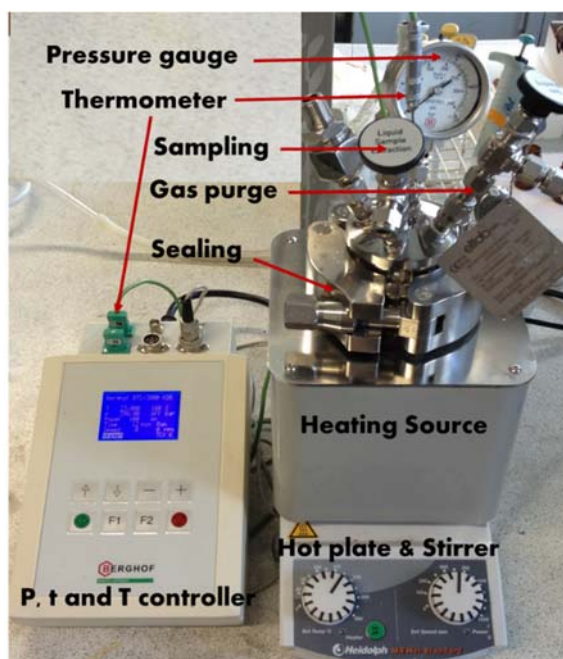


Figure 3-10: BERGHOF hydrothermal reactor with controlled time, pressure and temperature equipped with magnetic stirring

3.5.3. In-situ synthesis of TiO_2 nanoparticles on GO

As illustrated in Figure 3-11, sol-gel derived GO/ TiO_2 composite was produced via exactly same process as describe in previous section. The only difference in these two process was the addition of GO dispersion to the solution B (solution B*) before adding TiO_2 precursor (Solution A). The amount of GO was adjusted in order to make GO/ TiO_2 composites with 1, 2, 5, 10, and 20 %wt GO. To be able to adjust GO mass in the composite, it was necessary to know the total mass of TiO_2 particles in sol. In a typical procedure certain volume of TiO_2 sol were dried and calcined at 450 °C as described in previous section and weighed after drying. Concentration of the TiO_2 was estimated around 10 mg/ml with the total mass of 5 g TiO_2 in every 500 ml batch of TiO_2 sol.

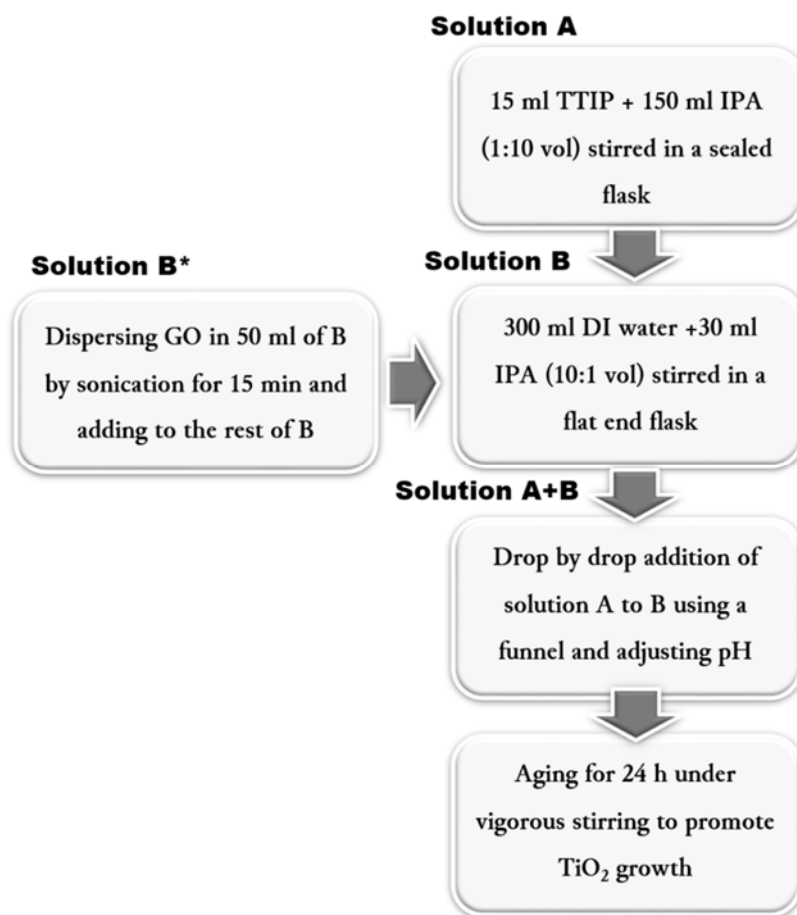


Figure 3-11: Flow chart of TiO_2 and TiO_2 nanoparticle sol-gel in-situ synthesis on GO

To make each GO/ TiO_2 composite with different weight percent GO, one batch of TiO_2 were synthesised based on the recipe explained in Figure 3-11 and accordingly the required amount of GO were taken from the previously synthesised GO batch with the concentration of 4.9 mg/ml and dispersed in water/IPA mixture before adding to the solution B. After aging all samples showed cloudy whitish brown ranging from very light for the 1 % wt GO sample to very viscous and dark brown for the 20% wt GO sample. Then each batch of composites were divided into two parts. One part dried at 40 °C overnight and pulverised into fine powder using mortar and pestle and calcined at 450 °C for 2 h in controlled atmosphere furnace under flow of 99.999% pure nitrogen to avoid burning graphene to CO and CO_2 in presence of oxygen during crystallisation of TiO_2 . The second part of sol was loaded into the Teflon lined stainless steel directly and treated hydrothermally at 170 °C for 24 h. The hydrothermally treated suspension was then centrifuged at 5000 rpm; the powder recovered was washed with deionized water, and dried at room temperature. The colour of the powder changed from brown to light navy blue to dark blue and black which was the sign of the GO reduction to rGO due to

hydrothermal treatment. All samples were labelled as GO-PS-X where X=1, 2, 5, 10, 20 wt% and stored for further characterisation and photocatalysis experiments. The colour contrast of GO-PS-X wt% composites with increasing the weight percent of GO is shown in Figure 3-12.

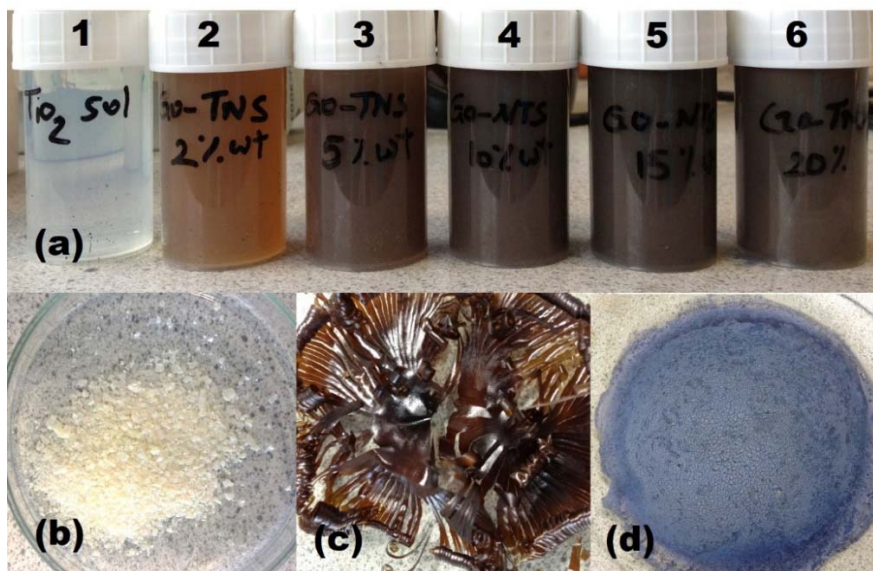


Figure 3-12: photographs of (a): TiO₂ sol and sol-gel synthesised GO/TiO₂ composite with 2, 5, 10, 15 and 20%wt (1 to 6), (b): Pure TiO₂ nanoparticles, (c): 5% wt GO/TiO₂ composite after drying, (d): Sample GO-PS-5 (5% wt GO/TiO₂ after hydrothermal treatment at 170 °C for 24 hrs)

3.5.4. Immobilisation of pre-synthesised TiO₂ on GO

Through a different route, pre-synthesised crystalline commercial TiO₂ nano-powder, known as P25, were used in order to study the effect of in-situ growth of TiO₂ nanocrystals via sol-gel on the surface of graphene comparing with dispersing pre-synthesised TiO₂ nanopowder on the surface of GO. P25 is a photocatalyst manufactured commercially and sold under the trade mark AEROXIDE[®] P25. P25 is a mixture of anatase and rutile in the region of 70-90% anatase and is manufactured by flame synthesis. P25 has an average particle diameter of 35–40nm and a specific surface area of 44–50 m²g⁻¹.

GO/P25 composites were prepared by ultrasonic assisted mixing method. The ultrasound provides enough energy to break TiO₂ agglomerates and bind them to the GO surface through electrostatic interaction between negatively charged GO and positively charged P25 particles. First 1 g of P25 were added to 100 ml water and sonicated in ultrasonic bath for 1 h to obtain very homogeneous slurry. Next calculated amount of GO were added to each TiO₂ dispersion in order to obtain GO/P25 composites with the GO weight percent ranging from 1 to 20 %wt and were sonicated in bath for more 1 h until a uniform light brown dispersion was obtained.

All the dispersions were dried at 40 °C overnight and pulverised into fine powder using mortar and pestle, were divided into three parts and labelled as GO-P25-C-X% for further treatment. The first part is stored without any further treatment, the second part calcined at 450 °C for 2 h in controlled atmosphere furnace under flow of 99.999% pure nitrogen and the third part hydrothermally treated at 170 °C for 24 hrs.

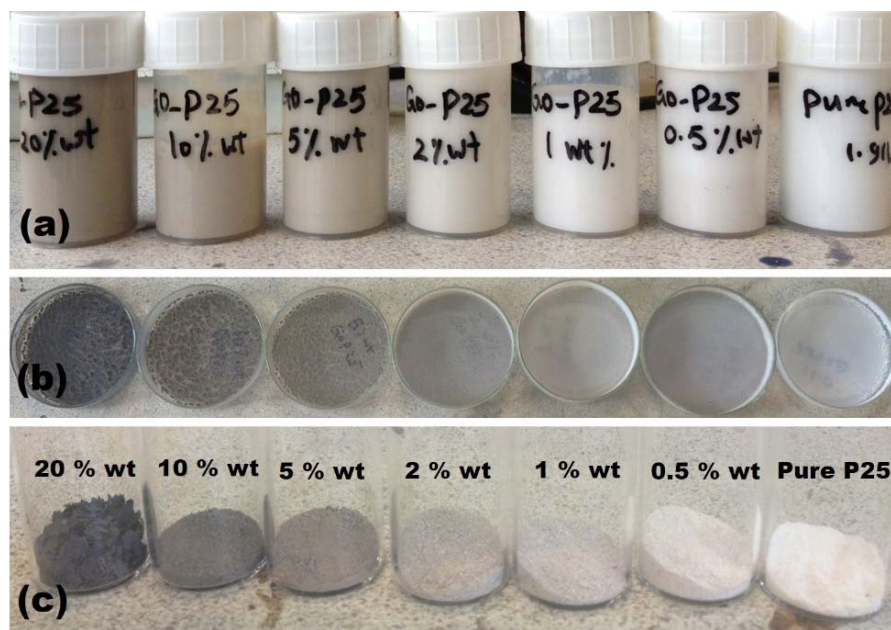


Figure 3-13: photographs of (a): GO/P25 TiO₂ dispersion with 0, 0.5, 1, 2, 5, 10, and 20%wt, (b) and (c): Pure TiO₂ and GO/P25 composites after drying

3.6. Material synthesis and experimental section of chapter 6

3.6.1. Chemicals

The major chemical to synthesis TiO₂ nanotubes are P25 AEROXIDE[®], sodium hydroxide (ACS reagent ≥97%) in pellets form and hydrochloric acid (ACS reagent 37%) from Sigma Aldrich.

3.6.2. Synthesis of TiO₂ nanotubes (TNTs)

Generally 4gr P25 TiO₂ particles was added to 120 ml of 10 M NaOH (48 g NaOH in 120 ml water) and dispersed by sonication for 30 min. The resulting TiO₂ slurry were hydrothermally treated at different temperature (110, 130, 150, and 180 °C) and time (5, 24, 40 and 80 hrs), followed by calcination at different temperature (300, 450, 550 and 700 °C) and time (1, 2, 5, and 7 hrs) in order to crystallize TNTs. After cooling the reactor naturally to the room

temperature, it was transferred to PTFE tubes and centrifuged at 3000 rpm for 30 min to remove NaOH from the supernatant. Then washed with 0.1 molar HCl to reach the pH 7. Finally the resultant milky slurry was washed with 1 litre of deionised water to removed NaCl residue and dried at 70 °C overnight. The white TiO₂ powder was grinded with mortar and pestle to obtain uniform and smooth powder, labelled and stored in sealed glass vials for further characterisation. Among all the TiO₂ -TNTs the one hydrothermally treated at 150 °C for 24 hrs and calcined 2 hrs at 450 °C shows highest surface area, more porosity, longer tubes, smallest diameter and well defined tubular structure. This sample labelled as TNT-150-24 and were used for photocatalytic experiments and making graphene composite.

3.6.3. Synthesis of TNTs/rGO

The synthesis of TNTs/rGO composite was achieved via three different routes. For all three methods, the optimised TNT sample TNT-150-24 was chosen as the standard TiO₂ nanotubes based on its high surface area and nanotube quality as the optimised sample.

- **Method A:** 1 g of previously synthesised TNT-150-24 dispersed in 50 ml of deionised water then mixed with calculated amount of GO dispersed in 20 ml water in order to make 5 and 10 wt% TNT/GO composite. Finally the dispersion were dried and calcined in nitrogen flow furnace at 450 °C for 2 h for reduction of GO to rGO and also crystallisation of TiO₂ nanotubes. This sample labelled as rGO-TNC-X (X=5 and 10 %)
- **Method B:** 1 g of previously synthesised TNT-150-24 dispersed in 50 ml of 25:75 ethanol: deionised water mixture and mixed with calculated amount of GO dispersed in 20 ml water in order to make 5 and 10 wt% TNT/GO composite. The dispersions then were loaded into Teflon lined autoclave for the second hydrothermal treatment at 170 °C for 10 h in order to reduce GO to rGO also crystallise TiO₂ nanotubes and were labelled as rGO-TNH-X (X=5 and 10 wt%).
- **Method C:** In third method TiO₂ nanotubes were synthesised on GO surface in one pot. First 3.6 g P25 powder was added to 120 ml of 10 M NaOH and dispersed by sonication for 30 min. Then 0.4 gr of freeze dried GO were added to the TiO₂ slurry and sonicated for another 30 min to make 10 wt% GO containing composite. The resulting homogeneous light brown dispersion were hydrothermally treated at 150 °C for 24 hours. After cooling the solution to the room temperature, the resulting navy blue dispersion was centrifuged to remove NaOH, washed with 0.1 M HCl to the pH 7, washed with deionised water, filtered and dried at 60 °C overnight and labelled as rGO-TNP-10 wt%.

3.6.4. Synthesis of rGO/TiO₂ nanofiber composite (TNFs/rGO)

The procedure to make TiO₂ nanofibers are quite similar to procedure of making TiO₂ nanotubes but hydrothermal treatment was performed at 200 °C for 48 hrs. After washing and drying, 1 g of the resulting powder was dispersed in 50 ml of deionised water then mixed with 10 wt% GO, dried and calcined in nitrogen flow furnace at 450 °C for 2 h. This sample labelled as rGO-TNF-10 wt%.

3.7. Material synthesis and experimental section of chapter 7

3.7.1. Chemicals

Hexadecylamine (HDA, 90%), potassium chloride pellet (ACS reagent ≥85%), titanium (IV) isopropoxide (TTIP) and absolute ethanol (ACS reagent ≥99.8% Fluka) were purchased from Sigma-Aldrich and used without any further purification.



Figure 3-14: Chemical structure of Hexadecylamine

3.7.2. Synthesis of TiO₂ beads (TBs)

Mesoporous TiO₂ beads were prepared from a combined sol-gel and solvothermal process based on the method reported by Caruso et.al.²⁶¹. In a typical synthesis 10.6 g HDA was dissolved in 1200 mL ethanol, followed by the addition of 6.5 mL 0.1 M KCl solution. Then 30 ml of TTIP were added to this solution drop wise under vigorous stirring at ambient temperature. The resulting white TiO₂ suspension statically ages overnight, then the TiO₂ beads were collected on whatman filter paper, washed with ethanol three times and dried in air at room temperature. In order to increase porosity and crystallinity of TiO₂ beads, a solvothermal method was used. Typically 4 g of as synthesised amorphous TiO₂ beads was dispersed in 35 ml water and 70 ml ethanol and were hydrothermally treated at 160 °C for 16 h. The solid products were collected by filtration, washed with ethanol, and dried in air at room temperature. The resultant powders were calcined at 450 °C for 2 h in air to burn HDA and other organic compounds from TTIP and produce the final mesoporous crystalline TiO₂ micro beads. This

sample was labelled as TBs. The schematic of synthesis process is shown consecutively from 1 to 3 in Figure 3-15.

3.7.3. Synthesis of rGO/TBs

TiO₂ beads/rGO composites was synthesised by dispersing 4 g of TBs beads in 70 ml of ethanol and was added to 35 ml of water containing 0.44 g of GO finely dispersed with sonication aid and stirred for an hour to make a homogeneous GO/TBs composite containing 10 wt% GO (Figure 3-15). The final slurry then was loaded into autoclave and heated at 170 °C for 10 h in order to reduce graphene oxide and enhance TiO₂/graphene binding. After cooling to room temperature the slurry were filtered and washed three times with ethanol, dried overnight.

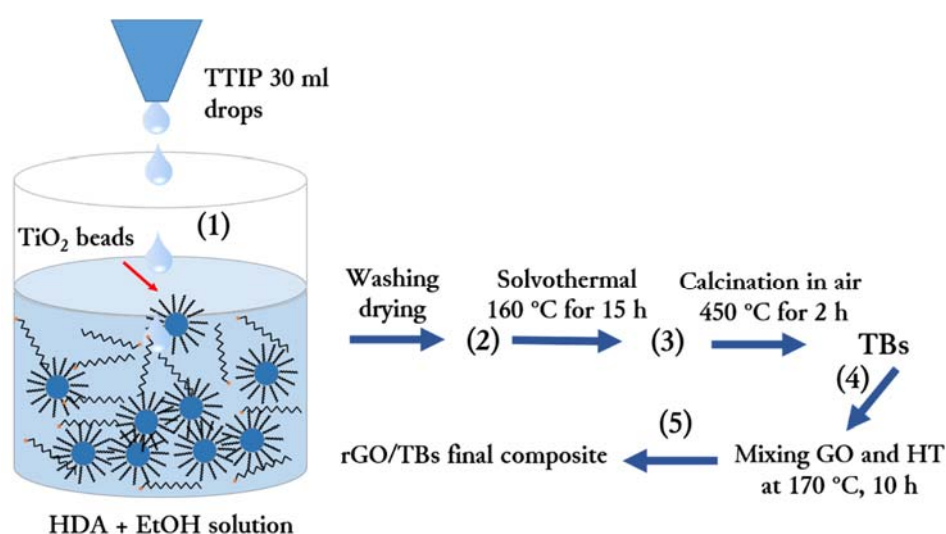


Figure 3-15: schematic process of synthesising TiO₂ beads (1-4), and two different routes for synthesising graphene wrapped TiO₂ beads (a and b)

3.8. Analytical methods

3.8.1. High performance liquid chromatography (HPLC)

Reversed-Phase Chromatography were used in this study to quantify the amount of residual pharmaceuticals in water after removal by adsorption and photocatalysis. The separation is based on analytes' partition coefficients between the polar mobile phase (H₂O:MeOH) and the hydrophobic (nonpolar) stationary phase which is octadecyl (C18) bonded groups, on silica support. The polar analytes elute first while nonpolar analytes interact more strongly with the hydrophobic C18 groups. Thus in chromatograph the more polar compounds are located in less retention time than the non-polar ones.

The HPLC system used for this study is an Agilent 1100 (Agilent Technologies, Palo Alto, Ca, USA) consisting of low-pressure gradient pump equipped with a UV–Vis detector. This is a typical HPLC system consists of a pump, an injector, a column, a detector, and a PC-based data handling workstation which is integrated with the Agilent Chem-Station software B.02.01SR1. (see schematic diagram in Figure 3-16). The UV/Vis absorbance detector monitors the absorption of UV or visible light in the HPLC eluent since all pharmaceuticals used have the highest UV absorbance in specific wavelength which were identified from their UV/vis spectrum.

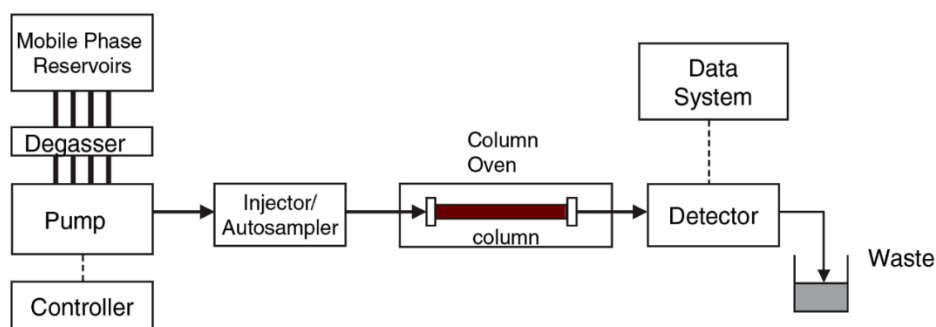


Figure 3-16: schematic diagram of HPLC system with different modules

3.8.2. UV/Vis Spectroscopy and Beer-Lambert

The ratio of the intensity of light transmitted through a medium, I , to the incident intensity, I_0 , at a given frequency is called the transmittance, T . It has been shown empirically²⁶² that the transmitted light varies with the length, l , of the sample and the concentration, C , of the absorbing species according to the Beer-Lambert law:

$$I = I_0 10^{-\alpha Cl} \quad \text{Equation 3-2}$$

Where α is known as the extinction coefficient (or the molar absorption coefficient). The attenuation of light beam passing through a cuvette, due to absorption as outlined by the Beer-Lambert law.

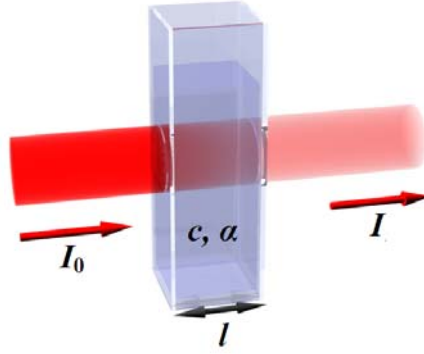


Figure 3-17: Representation of Beer-Lambert law, showing the various components as outlined in Equation 3-3 ²⁶³

The absorbance, A , can be defined as:

$$A = \log \frac{I_0}{I} \quad \text{Equation 3-3}$$

So the Beer-Lambert law takes its usual form:

$$A = \alpha Cl \quad \text{Equation 3-4}$$

It shows the absorbance in a sample is to be reliant on the concentration of the sample and the thickness of the sample that the light is transmitted through. In this work Beer-Lambert law was used to calculate the concentration of methylene blue dye after adsorption experiments.

3.9. Characterisation techniques

Material characterizations in this work include measurements of crystallographic information, identification of chemical functional groups, characteristic images, surface structure and morphology, surface areas and porosity etc. The characterization techniques being mostly used in the present work are described in this section.

3.9.1. Field Emission Scanning Electron Microscopy (FESEM)

The Scanning Electron Microscopy (SEM) is a technique of electronic microscopy based on the electrons-material interactions, capable of producing images of the sample surface. The principle of the SEM is based on the fact that an electron beam bombards the surface of the sample to be analysed which re-emits certain particles. These particles are analysed by various detectors which give a three dimensions image of the surface. Due to the excited state of the atoms present in the material by interaction with the incidental electrons, photons are emitted (de-excitation process). The emission volume of photons depends upon the energy of the

incidental electrons, the atomic number of the sample and the level energy initially ionized. The chemical analysis by EDX (Energy Dispersive X-ray analysis) consists of a detection of these photons by using a detector (detection by energy dispersion). The energy of these photons is characteristic of its atoms; which can be used for elemental analysis. The detectors allow to FESEM, high resolution FEI SEM, Quanta 650 FEG, equipped with Oxford Instrument EDS, X-MAX20 SDD detector, is used in the present thesis which can provide characteristic images and is useful for judging the surface structure and morphology of all samples. Depending on the type of materials, electron voltage was adjusted between 5–15 keV. For graphene samples voltage should be set as low as possible to prevent sample damage and chamber pollution. Compared to commonly used SEM, FESEM is a type of electron microscope which is able to produce the highest resolution and less electrostatically distorted images. Besides sample images, FESEM can also provide information on the elemental composition of materials imaged with EDX. Samples were adhered on stainless steel stubs using carbon tabs and coated with thin layer of gold (2–4 nm) by plasma sputtering method in order to prevent charge accumulation on the surface of non-conductive samples. Considering that graphene is highly conductive, graphene and graphene composites were not coated with gold.

3.9.2. Transmission Electron Microscopy (TEM) and SAED

JEOL 2100 HRTEM under conventional bright field conditions operated at 80 keV for graphene and up to 200 keV were used to study the structure and crystallography of graphene and graphene/TiO₂ composites. TEM is an imaging technique whereby a beam of electrons is transmitted through a specimen, then an image is formed, magnified and directed to appear on a fluorescent screen. Sample preparation is very crucial for TEM analysis as it should be very thin to let the electron beam pass through the specimen. Graphene is a thin sheet of carbon which is conductive and transparent. As a result there is no need to electron milling for sample preparation and samples can be easily deposited on lacy carbon conductive TEM copper grids from solution. During the specimen preparation, around 5 mg of sample powder was dispersed into 10 mL of ethanol, isopropyl alcohol or water followed by ultra-sonication for 15 minutes to obtain a better dispersion of particles in the suspension and a few drops of such solution were spread on the carbon coated grid for analysis. Depending on beam selection, there are four common types of TEM image: bright field (BF) image; dark field (DF) image; selected area diffraction (SAD); and lattice or high-resolution TEM (HRTEM) imaging.

High resolution transmission electron microscopy (HRTEM) is an imaging mode of TEM that allows the imaging of the crystallographic structure of a sample at an atomic scale. In HRTEM, several beams scattered by the crystal in different directions interfere to form a

“lattice image”, which is formed by the interference between the diffracted beam and un-scattered beam. In practice, a larger objective aperture is selected to allow both types of beam to pass. Furthermore, all the diffracted beam and un-scattered beam are brought together again in the objective lens and the Fourier transform (analysis) creates a diffraction pattern of the object in the back focal plane. The inverse Fourier transform (synthesis) is performed subsequently, making the interference of diffracted beams back to a real space image in the image plane as a lattice image and at present, the highest resolution realised is 0.8 Å.

Selected Area Electron Diffraction (SAED), crystallographic technique that can be performed inside a TEM, is obtained when a special aperture namely SAD aperture is inserted. It encloses a small area through which both un-scattered and diffracted electrons contribute to the image formation. The periodic structure of a crystalline solid acts as a diffraction grating, scattering the electrons in a predictable manner. Working back from the observed diffraction pattern, it can deduce the structure of the crystal producing the diffraction. SAED is similar to X-ray diffraction, but unique in that areas as small as several hundred nano-meters in size can be examined, whereas X-ray diffraction typically samples areas several centimetres in size. If a large number of randomly orientated crystallites are covered, ring patterns will be obtained. With fewer crystallites present in the selected aperture, the “rings” lose their continuity and a spotty ring pattern results. Furthermore, a single crystal will give rise to a regular and ideally symmetrical arrangement of diffraction spots, each of which has a different value of crystallographic planes. In current research SAD pattern were used to estimate crystallinity and orientation of graphene crystallites.

3.9.3. Powder X-Ray Diffraction (XRD)

XRD is a technique used to characterize the crystallographic structure, crystallite size, and preferred orientation in polycrystalline or powdered solid samples also to identify the presence of inorganic phases in nano-composites. For current project XRD studies were conducted at room temperature using a Bruker D8 Advance GX002002 X-ray diffractometer with NaI scintillator detector configured with 0.6mm solid slot. A 0.6mm slit was placed in front of the 2.2 kW Cu-K α ($\lambda = 1.5406$ Å, 60 kv and 20 mA) X-ray radiation source. The samples are prepared in the form of fine homogeneous powder and a thin smooth layer of the samples mounted on a substrate is held in the path of X-rays. Powder samples were adhered onto borosilicate glass slides using two sided pressure sensitive adhesive tape. The glass slides and adhesives were analysed separately to provide controls for all samples. The XRD patterns with diffraction intensity versus double diffraction angle (2θ) are recorded from 10° to 80° at a step size of 0.02° and step time of 0.01 seconds. The interlayer space (d) of the crystal planes

can be obtained from Bragg's equation ($\lambda = 2d\sin\theta$). Data processing used Diffrac-plus XRD commander version 2.6.0 and EVA Application 8,0,0,2 software. The unknown substances were identified by comparing diffraction data against a database (JCPDS cards).

Principally in X-ray diffractometer, the X-ray source is produced in an X-ray tube where the high speed electrons collide with a metal target. By passing the X-ray beam through a filter which absorbs undesirable components, a monochromatic X-ray with strongest $K\alpha$ characteristic line is obtained and used for diffraction purpose. In principal, the phase identification is based on the fact that when a beam of monochromatic X-rays passes through a crystal containing of atoms arranged periodically in three dimensions, it can be scattered by the atoms in all directions. If there exists a large number of crystallites involved, then the chances of a crystal plane diffracting the beam is high. In addition, diffraction will take place only when the coherently scattered rays mutually reinforce each other in certain directions and fulfil the Bragg's Law ($n\lambda = 2d \sin\theta$). Where n is order of diffraction, λ is the wavelength of monochromatic X-rays, d is the inter-planar spacing of particular (hkl) crystal plane and θ is the angle between the incident X-rays and diffraction plane. By fixing the wavelength λ of X-rays and measuring θ , therefore the d -spacing of various planes in a crystal can be determined. The direction of diffraction is related to the shape and size of the unit cell, while the positions of atoms with the unit cells of the crystal determine the intensity of a diffracted beam. The principal of XRD is shown in Figure 3-18.

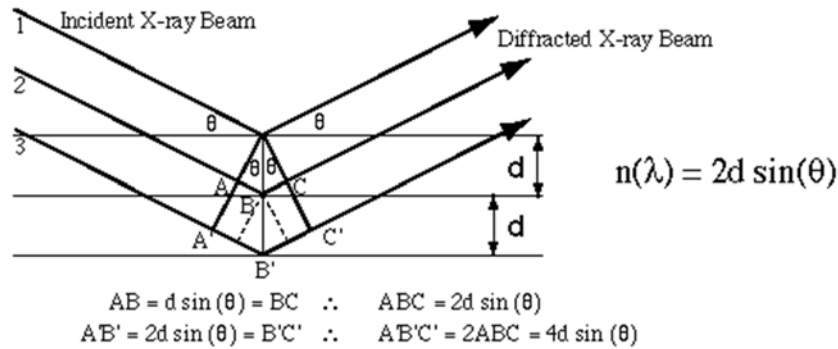


Figure 3-18: Interaction of x-ray with crystallographic plane in specimen according to Bragg's Low

For selected samples, crystallite sizes of TiO_2 in nano-composite were estimated using the Scherrer's equation ²⁶⁴:

$$t = \frac{0.89 \lambda}{\beta \cos \theta} \quad \text{Equation 3-5}$$

where t is the average crystallite size, λ is the Cu- $K\alpha$ X-ray wavelength, θ is the Bragg's diffraction angle and β is the integral breadth of peak or peak broadening (full-width at half maximum (FWHM) in radians). For proper calculation, other aspects such as the broadening due to strain in the sample should be considered. Therefore, the crystallite sizes determined from XRD was compared with those derived from the transmission electron microscopy (TEM) analysis.

3.9.4. Attenuated Total Reflectance Fourier Transform Infrared

Spectroscopy (ATR -FTIR)

FTIR is an absorption spectroscopy for collecting infrared spectra and analysing the chemical bonding information. It works because chemical bonds have specific frequencies at which they vibrate corresponding to energy levels. Thus a particular bond type can be deduced from the frequency of the vibrations. Typically FTIR needs sample preparation including dilution down to more than 100 times and making tablet. Attenuated Total Reflectance (ATR) is today's most widely used FTIR sampling tool. ATR generally allows qualitative or quantitative analysis of samples with little or no sample preparation, which greatly speeds sample analysis. The main benefit of ATR sampling comes from the very thin sampling path length and depth of penetration of the IR beam into the sample. This is in contrast to traditional FTIR sampling by transmission where the sample must be diluted with IR transparent salt, pressed into a pellet or pressed to a thin film, prior to analysis to prevent totally absorbing bands in the infrared spectrum. This encourages faster analysis with the higher resolution.

In this study the infrared spectra of the graphene oxide and reduced graphene oxide were obtained using an ATR-FTIR (Perkin-Elmer Spectrum 100 with ATR) averaging 10 recorded scans at a resolution of 2 cm^{-1} in mid infrared range ($2.5\text{--}50\text{ }\mu\text{m}$ or $4000\text{--}400\text{ cm}^{-1}$). The resulting infrared spectrum is presented as the absorbance versus wavenumber.

3.9.5. Raman Spectroscopy

Another useful technique in characterizing carbonaceous materials is Raman spectroscopy. The Raman Effect arises when the incident light excites the molecules in a sample which subsequently scatters the light. The scattered light consists of two types; *Rayleigh scattering*, which is strong and has the same frequency as that of the incident beam, and *inelastic Raman scattering*, which is very weak and scattered at different wavelengths due to phonon losing or gaining. The difference in frequency between the scattered light and the incident light is known as the *Raman shift*, the intensity of which can be measured and illustrated as a Raman spectrum. Measurements of the Raman shifts enable the identification of the scattering

compounds and further analysis of peak intensities can provide useful information related to stoichiometry, stress and the degree of crystallinity of the material under investigation. These advantages have made Raman spectroscopy as one of the very sensitive and important technique to analyse the structure and electronic transitions of carbonaceous materials such as carbon nanotubes, fullerene and recently graphene and graphene oxide.

Raman can be used to determine the number of graphene layers as well as the nature of their defects, regardless of the substrate and preparation methods. In graphene, there are three prominent bands in the characteristic Raman spectrum of graphene: the D-band due to lattice defects in graphene, the G-band due to in-plane vibration of the sp^2 bonded carbon atoms, and the $G'/2D$ -band due to the double resonant condition in graphene as it shown in Figure 3-19.

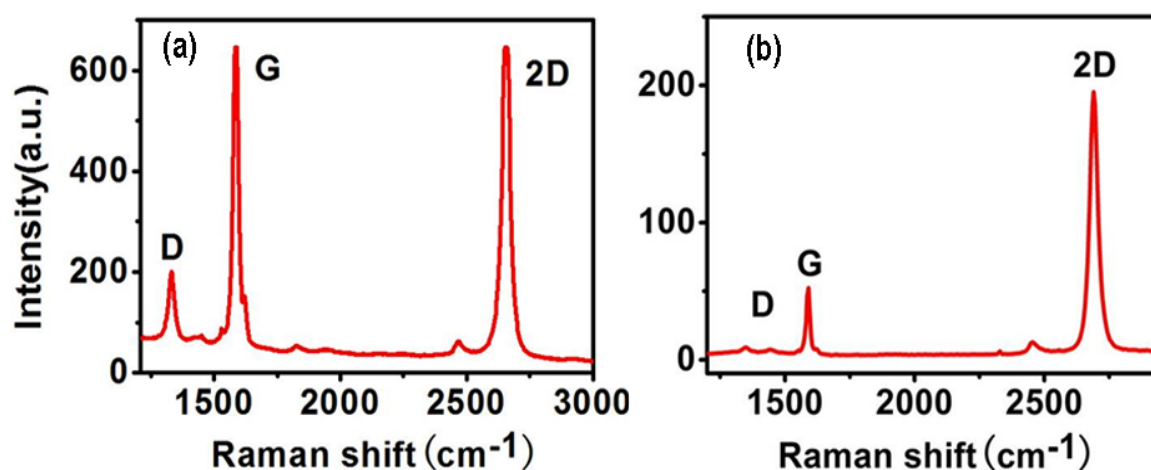


Figure 3-19: Raman spectra of (a): multilayer, (b): single layer graphene

The intensity of the G-band essentially increases linearly with the increasing number of graphene layers with greater quantity of carbon atoms measured. The low intensity G-band, the sharp and symmetrical 2D-band, and the large intensity ratio of 2D-band over G-band (I_{2D}/I_G) serve as unambiguous identification of monolayer graphene^{265,266}. As shown in Figure 3-20, the 2D peak of a single layer is sharp and symmetric compared with other Raman spectra which is hence widely used to identify single layer graphene. In addition to the difference of the 2D peak, the intensity of the Raman G peak increases almost linearly with the layer number²⁶⁷.

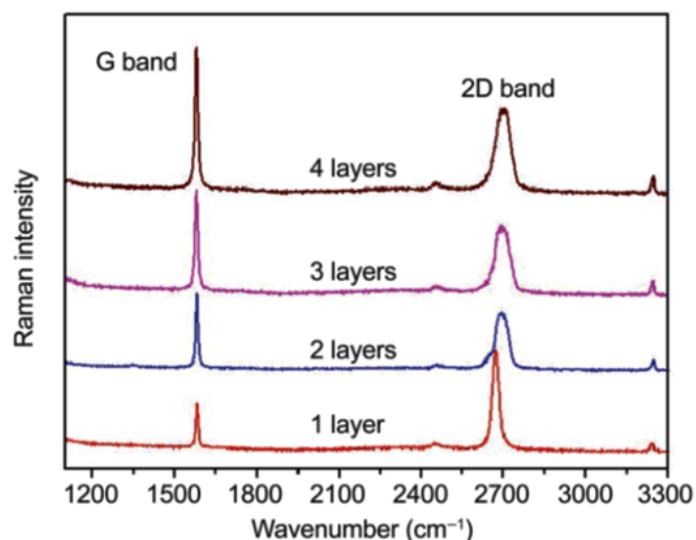


Figure 3-20: Comparison between Raman spectra of increasing layers of graphene

In this work, the Raman measurement was carried out in back scattering configuration using micro-Raman system (Jobin-Yvon Horiba LabRam HR800) equipped with a Synapse Air Cooled CCD detector using a 488 nm (Uniphase 2014) argon ion visible laser with a maximum output power of 20mW. The excitation power were adjusted low at 10 mW in order to avoid the undesired heating effect on the sample or sample damage. The spot size of the laser was adjusted 1 μ m approximately with the acquisition time of 1 second. The spectral resolution of the apparatus is estimated to be approximately $^{-1} \text{ cm}^{-1}$.

3.9.6. UV-Visible Spectroscopy

Ultraviolet–Visible (UV–Vis) spectroscopy measures the wavelength and intensity of absorption of near-ultraviolet and visible light by a sample. The transition alters the configuration of the valence electrons in the molecule and the radiation is generated by the ultraviolet-visible portion of the electromagnetic spectrum 160 to 780 nm. The absorption generally results from excitation of bonding electrons from the ground state to higher energy levels. The mechanisms involved can be categorized into: (i) absorption by species containing π , σ and n electrons; (ii) absorption involving d and f electrons; and (iii) absorption by charge-transfer electrons. The first mechanism is the most common one for organic molecules where the absorption in the conventional spectral region (200–700 nm) is dominated mainly by n to π^* and π to π^* transitions involving the electrons in s and p orbitals. During such a transition in a molecule, electrons are promoted from the highest occupied molecular orbital (HOMO) to the lowest unoccupied molecular orbital (LUMO). On the other hand, most inorganic

compounds with transition-metal ions absorb ultraviolet and visible light due to second and third mechanisms, which involve transitions with d and f orbital electrons as well as electron donor-acceptor characteristics. In TiO₂ nano-structures as a semiconductor, the transitions occur between the valence band (VB) and conduction band (CB). To some extent, the VB and CB can be considered as the solid state analogue of the HOMO and LUMO of an organic molecule. For composites containing TiO₂ nanoparticles, the UV-Vis spectrum can provide a correlation between the fundamental absorption edge and the respective photon energy required to excite the electrons from valence band to higher energy conduction band. The band gap energy can be calculated from

$$(\alpha_0 h\nu)^n = A(h\nu - E_g) \quad \text{Equation 3-6}$$

Where α_0 is linear absorption coefficient; $h\nu$ is the incident photon energy; A is the edge-width parameter; and E_g is the optical band gap energy, respectively. The absorption coefficient at the higher energy side of the absorption edge can be used to fit to obtain the optical band gap E_g of TiO₂ nanotubes and graphene/TiO₂ composites in chapter four by extrapolating the plotted $(\alpha_0 h\nu)^n$ as a straight line towards an intersection with the $h\nu$ axis. The value of n can be assumed to depend on the nature of electronic transitions responsible for the absorptions (n is equal to 1/2 and 2 for indirect and direct band gaps, respectively). UV-Vis spectrometer used in this work to measure properties of composites was Perkin Elmer UV-VIS Spectrometer with the wavelength between 190-1100nm. UV-Vis spectroscopy used for identifying the maximum absorption wavelength for methylene blue and pharmaceuticals was a Beckman Du520 general purpose UV/Vis spectrophotometer with the wavelength between 190-1100nm with the samples placed in quartz cuvette.

3.9.7. BET Gas adsorption Isotherm

Surface area and porosity were measured using a Nova 4200 High Speed, Automated Surface Area and Pore Size Analyser from Quantachrome Instruments. Samples were prepared by outgassing in vacuum at 120-200 °C for 2 hours under 10⁻³ torr vacuum to remove adsorbed contaminants (especially water and carbon dioxide) which were acquired from atmospheric exposure. The mass of the degassed sample is then measured to calculate the final specific surface. The samples were then cooled at -196 °C under vacuum. Nitrogen was dosed to the samples in controlled increments and quantity adsorbed was calculated. The quantity of gas required to form monolayer on the external surface was determined from adsorption isotherm. The isotherm is determined by both the sequential introduction of known gas pressure in the

cellular unit and the measure of the adsorbed gas quantity according to the pressure in the system. The temperature of the system remains constant and equal to that of the liquid nitrogen.

To calculate the specific surface, it is necessary to analyse the experimental adsorption isotherm which leads to the adsorbed gas quantity on the complete monolayer, then to calculate the layer area and thus the specific surface of the solid, further increase of gas pressure will form multi-layer coverage (see Figure 3-21). The general equation for the physical adsorption of a gas on a solid is:

$$V = \frac{V_m \cdot C' \cdot \left(\frac{P}{P_0}\right)}{\left(1 - \frac{P}{P_0}\right) \cdot \left(1 + (C' - 1) \cdot \frac{P}{P_0}\right)} \quad \text{Equation 3-7}$$

Where p is the adsorption equilibrium pressure (Pa);

P_0 - the vapour pressure of adsorbate at adsorption temperature (Pa);

V - Volume of the adsorbed gas (m^3);

V_m - volume of the gas necessary to form a complete monolayer on the surface (m^3);

C' - the adsorption constant of gas used

The BET Equation may be given under a linear shape for relative pressure values $\left(\frac{P}{P_0}\right)$ ranging from 0.05 to 0.20:

$$\frac{P}{V \cdot (P_0 - P)} = \frac{1}{V_m \cdot C'} + \left(\frac{C' - 1}{V_m \cdot C'}\right) \cdot \frac{P}{P_0} \quad \text{Equation 3-8}$$

This equation is called transformed linear BET of the adsorption isotherm. The values of V_m and C' are obtained from the slope $\frac{P}{V \cdot (P_0 - P)} = f \cdot \left(\frac{P}{P_0}\right)$ and the intercept. If the area of a gas molecule, A_m , is known (16.2 \AA^2 for nitrogen), the specific surface of the solid (S_{BET}) is obtained according to the following equation:

$$S_{BET} = \frac{N_A \cdot A_m \cdot V_m}{V_{mol} \cdot m_s} \quad \text{Equation 3-9}$$

Where:

V_m is the volume of the monolayer;

A_m is the cross-sectional area occupied by each adsorbate molecule;

N_A is the Avogadro's number (mol^{-1});

V_{mol} is the molecular volume of gas ($\text{m}^3 \cdot \text{mol}^{-1}$);

m_s is the mass of solid sample (kg).

With increasing pressure, gas was condensed on small pores (smallest diameter) first and continue until saturation pressure was reached at which all pores filled with liquid. The gas pressure was then reduced incrementally to allow evaporation of the condensed gas. The Kelvin equation (see the Equation 3-10) was used to calculate the relative pressure of nitrogen in equilibrium with the solid. The pore size distribution was determined from the desorption data using the Barrett, Joyner, and Halenda (BJH) model. A relative nitrogen pressure step, ranges from 0.98 to 0.37 was used.

$$\ln \frac{P}{P_0} = -\frac{2\gamma V_L}{rRT} \cos \theta \quad \text{Equation 3-10}$$

Where

P is the equilibrium vapour pressure of a liquid in a pore of radius r

P_0 is the equilibrium pressure of the same liquid on a plane surface

γ is surface tension of the liquid

V_L is the molar volume of the liquid

θ is the contact angle with which the liquid meets the pore

R is the gas constant

T is the absolute temperature

The value of the total pore volume is based on the measurement of the nitrogen volume adsorbed until $p/p_0 = 0.98$.

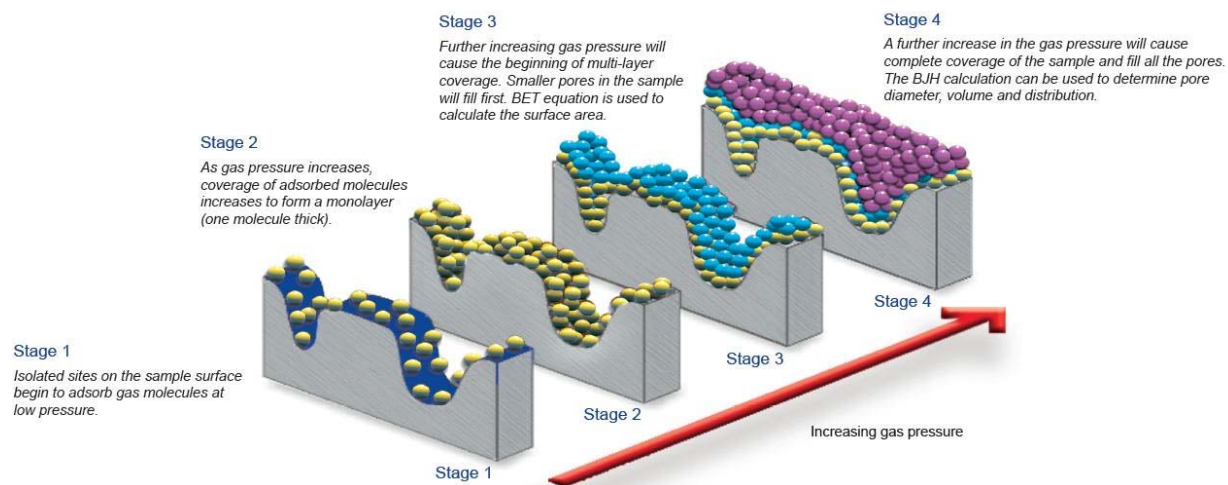


Figure 3-21: Gas adsorption mechanism to measure the specific surface area (200 Micromeritics Instrument Corporation)

CHAPTER 4: GRAPHENE AND GRAPHENE OXIDE AS AN ADSORBENT

4.1. Introduction

Pharmaceuticals which are used extensively worldwide in human therapy and the farming industry, have recently attracted increasing concern as a new class of pollutants^{268,269}. Because most of pharmaceuticals are partially metabolized and absorbed by the treated humans and animals, large fractions are excreted intact through urine and faeces to agricultural runoff and municipal wastewater treatment plants becoming a source of contamination for soil, surface water, groundwater, and even drinking water^{4,270}. Recently, tremendous attention has been devoted to improve the efficiency of pharmaceutical removal from water and wastewater because of their detrimental effect on aquatic environment and human health^{30,268}. Different technologies such as adsorption, membrane filtration, biological treatment, and photocatalytic degradation has been explored for pharmaceutical removal from water^{58,271-273}. However photocatalysis and adsorption are the two important methods that we have been working on extensively in recent years^{135,136,274}. Despite of advantages of each method, they suffer from number of drawbacks in use which has been challenging for water purification in industrial scale. For instance adsorption is the most effective and widely used one so far because of its relatively low cost and simplicity of the operation, however the adsorption efficiency is highly pH dependant and not effective for many harmful organic substances. The other limitation is the regeneration need after adsorbent saturation which can be done chemically or thermally. However both of regeneration methods are not environmentally friendly since they transfer the pollutant from solution phase into concentrated form in other solvents in chemical regeneration or into the air in thermal regeneration. Also the regeneration causes considerable weight loss and reduction in efficient life cycle of the adsorbent^{51,275}. In contrast the other interesting technique, photocatalysis, breaks down the organic pollutants to smaller intermediate molecules and finally to the H₂O and CO₂ using a semiconductor nanomaterial (typically TiO₂ nanoparticles) irradiated by UV light²⁷⁶. But the major problems in photocatalysis are low

quantum efficiency and poor adsorption property of pollutant on TiO_2 surface which can be attributed to the low specific surface area of TiO_2 ²⁷⁷. In addition the post recovery of the catalyst from water considering their small size, ranging from 25-100 nm, is also challenging²⁷⁸. Comparing these two approaches revealed combination of adsorption and photocatalysis method in the form of adsorbent-photocatalyst composite can omit the regeneration step of the adsorbent along with enhancing photocatalysis and post recovery efficiency.

Many efforts have been made by designing various type of adsorbent with chemical stability and large surface area which increase the adsorption amount of pollutant on the surface of catalyst but do not deteriorate the photocatalytic activity or light transmittance. The porous nano-carbons such as carbon aerogels, carbon nanotubes (CNTs), fullerenes, nanoporous carbon and graphene are some of the most extensively investigated and most promising materials water treatment owing to their lightweight, nonpolar, nonreactive and nontoxic nature of carbon materials and the easy separation of the materials from water are attractive in wastewater treatment²⁷⁹⁻²⁸¹.

Recently graphene has attracted tremendous attention as a new class of adsorbent for highly efficient removal of different organic and inorganic pollutants owing to its unique two dimensional honey comb structure of sp^2 -hybridized carbon atoms which imposes an exceptional physicochemical properties such as huge adsorption capacity, transparency, conductivity, unique pore geometry and large surface area (theoretical specific surface area of $2630 \text{ m}^2.\text{g}^{-1}$)^{194,282}. However, hydrophobicity and tendency to re-stacking into graphite hinders graphene from being an ideal adsorbent for removal of water soluble organic compound²⁸³. By contrast, GO, the oxidized form of graphene, is rich in oxygen-containing groups, such as hydroxyl and epoxide (mostly located on basal plane), and carboxyl and carbonyl (mostly at the sheet edges)^{152,154}. This chemistry makes GO water soluble, hydrophilic, positively charged and acidic, which can consequently improves the accessibility and affinity of GO to adsorbate molecules¹⁹⁰. GO can be produced on a large scale and at low cost by chemical exfoliation of graphite. Reduced graphene oxide (rGO) could obtain from subsequent reduction of GO which restores the sp^2 carbon structure via various methods such as annealing²⁰⁰, solvothermal/hydrothermal processes²⁸⁴⁻²⁸⁶, chemical reduction^{198,287-289} or UV-assisted reduction^{207,208}.

According to the these explanations we decided to select GO as a platform to immobilize our catalyst on the surface, hence we needed to study the adsorption properties of the GO adsorbent separately before combining with the catalyst. Based on literatures graphene-based adsorbents have been applied to remove various organic pollutants, such as dyes^{290,291}, naphthalene and 1-naphthol²⁹², bisphenol A²⁹³, tetracycline antibiotics¹⁹⁵, and oil^{194,294} from aqueous solutions.

Yang et al.²⁹⁵ demonstrated methylene blue removal by GO with a large adsorption capacity, as high as 714 mg.g⁻¹. Other studies reported the adsorption capacity of 1939 mg.g⁻¹²⁹⁶ and 397 mg.g⁻¹¹⁹⁶ of MB on GO. Sun et al.²⁹⁷ reported maximum adsorption capacity of 1400 mg.g⁻¹ for acridine orange by GO and 3300 mg.g⁻¹ for modified rGO. Wu et al.²⁹⁸ reported the maximum adsorption amount of 1430, 1460 and 1520 mg.g⁻¹ by graphene nanosheets for p-toluenesulfonic acid, 1-naphthalenesulfonic acid and methyl blue respectively.

According to all literature that summarised above, five possible interactions including van der Waals type interactions, π - π bonds (cation- π bond), hydrophobic effect, covalent and electrostatic interactions and hydrogen bonds are believed to be responsible for the adsorption of organic molecules on the surface of GO and rGO²⁹⁹. However they are not still able to justify the extraordinary adsorption capacity of GO towards different types of non-aromatic organic molecules and the difference between adsorption behaviour of GO and rGO. In this study, we aim to study the possible phenomena behind the extraordinary adsorption capacity of GO using different type of pharmaceuticals with different physicochemical properties and methylene blue as a cationic dyes to study the effect of electrostatic interaction in adsorption characteristic of GO and rGO in aqueous solution under different experimental conditions. For this investigations GO sponge was obtained by chemical exfoliation of graphite according to the modified Hummers method and freeze-drying. Then GO sponge was reduced to rGO chemically using hydrazine mon-hydrate named HrGO, thermally in vacuum at 300 °C for 20 h named VT-rGO and in Ar atmosphere furnace at 450 °C for 2 h named rGO. In order to study the role of functional groups in adsorption mechanism, thermally reduced rGO was obtained by annealing of GO sponge in Ar atmosphere furnace at 450 °C was used. The effect of benzene ring on adsorption process has been studied using diclofenac as a pharmaceutical molecule model containing aromatic functionality and famotidine as benzene free linear molecule. These findings may open up many possibilities for the use of graphene oxide in water decontamination, drug recrystallizations and catalysis in organic molecule synthesis.

In order to study the adsorption mechanism, the graphene oxide sponge, rGO sponge and dolomite/GO composite were selected for further characterisation. The structure and morphology of rGO, GO and processing steps towards GO synthesis were characterised by SEM and high resolution TEM. The crystallinity of both rGO and GO was obtained from SAD patterns and XRD. Raman spectroscopy was used to measure the D and G bands of graphitic structures. The ratio of the intensities of the two bands (D/G) was used for evaluating the efficiency of the reduction and the 2D band was used to estimate the number of layers. The porosity characteristics and surface area were measured through N₂ sorption analysis. The surface area of rGO and GO was also calculated based on MB adsorption. FT-IR spectra were conducted

for studying the degree of the reduction and functional group types. The optical properties of GO were measured by a UV–Vis spectrophotometer using the normal incident transmittance. More detail on instruments, sample preparation and working parameters were described in chapter two.

4.2. Result and Discussion

4.2.1. Morphological study

Exfoliation of graphite into graphene oxide sheets through oxidation and washing processes with the omission of sonication step resulted in a stable brown suspension. Fabrication of large GO sheets depends on the size of starting graphite flake and avoiding strong reactions promoted by vigorous ultrasonic force. However the use of large graphite flakes as a starting material does not necessarily guarantee large-size GO final products. Therefore the sonication process was omitted by using exfoliated graphite and pre-exfoliation with microwave to ensure minimum possible breakage of GO sheets during the process. Without the sonication step, a high yield of large size single GO sheets was obtained. The SEM images of the starting expandable graphite flakes is shown in Figure 4-1. This product contains a distribution of sizes but they mainly (more than 80% of flakes) fall between 300-600 μm across their largest dimension as shown in size distribution diagram in Figure 4-2. Based on the image processing with *ImageJ* software, the average length of flakes is about 500 μm with the average area of 0.3-0.4 mm^2 and thickness of 10-50 μm . These dimensions are similar to those reported by the supplier. As can be seen in higher magnification in Figure 4-1(b), each graphite flake is composed of smaller sheets with different shapes highly stacked on top of each other.

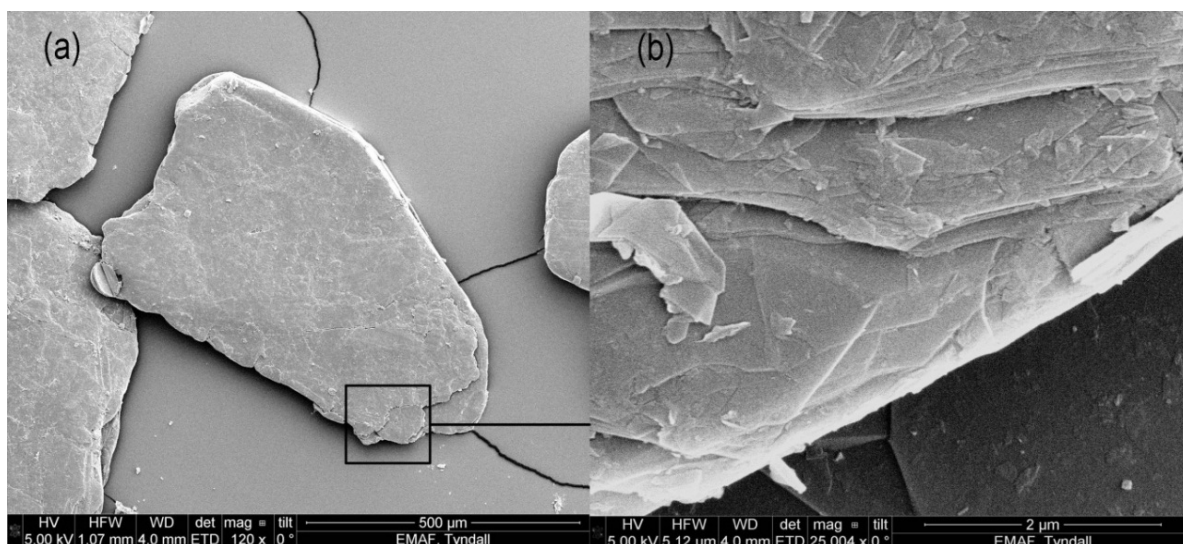


Figure 4-1: SEM images of expandable graphite flakes before expansion. In higher magnification image (b) steps which shows layered structure of graphite are visible

Our source of expandable graphite is known as a sulphate intercalated graphite which sulphate molecules were introduced between layers by treating highly crystalline natural flake graphite with a mixture of sulphuric acid. Expandable flakes were heated by microwave for about 10 seconds to provide enough heat to initiate foaming reaction. During the time in the microwave, the intercalated compounds vaporize and create pressure between sheets. This high pressure caused by the rapid heating of intercalant compounds, result in its decomposition and the conversion of intercalate and decomposed compounds from liquid or solid phase to gas phase. The pressure generated by the gas phase forced adjacent graphene layers to separate along the c crystallographic axis (Figure 4-3), resulting in the expansion observed ³⁰⁰.

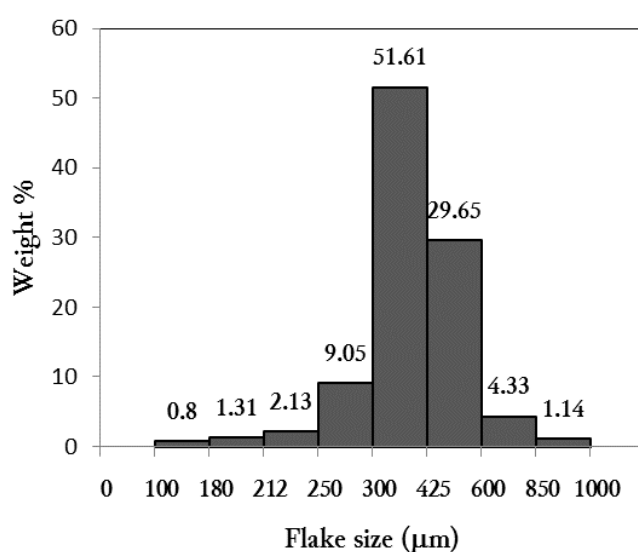


Figure 4-2: Graphite flake size distribution diagram

As illustrated in Figure 4-3 expansion of a single graphite flake results in layering graphite into hundred thousands of graphene sheets parallel with the "c" crystallographic axis of the graphite flake due to the internal pressure induced by gas evolution. The expansion of [0002] planes of graphene parallel with the "c" axis is leads to the formation of accordion morphology or worm-like structure which can be seen in SEM micrograph shown in Figure 4-4.

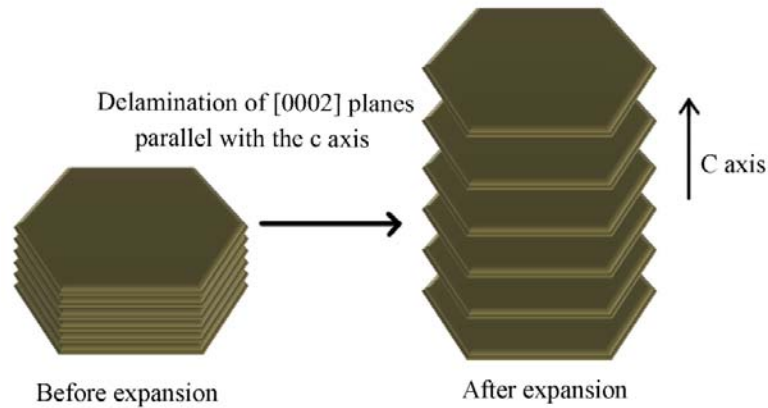


Figure 4-3: Schematic illustration of expansion of expandable graphite

The expansion rate of the graphite is of 290:1 cc/g which exhibits a 1000 times increase in volume. Compared to the compact structure of normal flaked graphite, this expanded porous structure is more suitable to produce GO in larger scale with higher efficiency and less un-exfoliated waste.

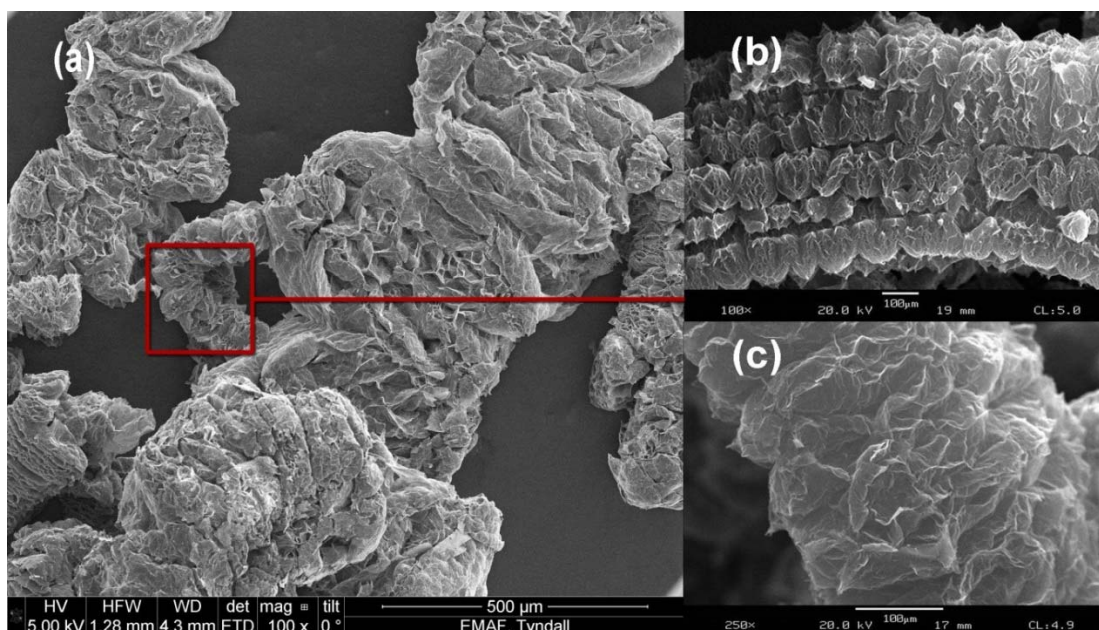


Figure 4-4: SEM images of worm like expanded graphite (EG)

Considering interlayer spacing of graphite which is 0.34 nm, the thickness of a single graphene sheet which is 0.23 nm and the average thickness of each flake (30000 nm) as indicated in Figure 4-5, each flake can be exfoliated into 80000 single layer sheets of graphene.

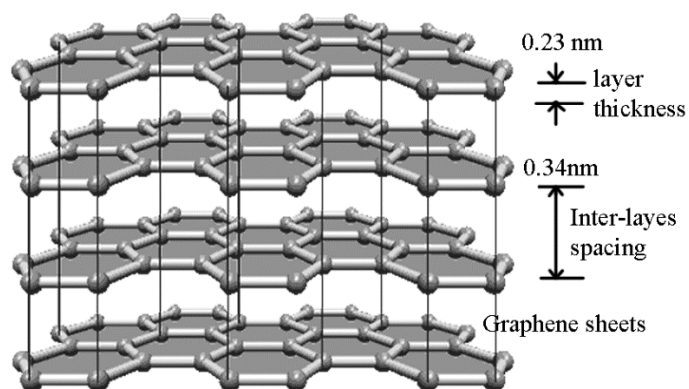


Figure 4-5: Schematic structure of graphite and graphene building blocks³⁰¹

As shown in Figure 3-4 from experimental chapter, during the washing process of oxidised expanded graphite, the GO sheets were exfoliated without any external force such as sonication and a highly stable brownish aqueous dispersions with difference concentrations were obtained. The As-prepared GO dispersions contain large monolayer GO sheets predominantly in the order of 40-50 μm . It is widely believed that the electrostatic repulsion of the edge carboxylic acid

groups allows graphite oxide to be fully exfoliated and form stable single layer GO aqueous dispersions. Another driving force to form stable and well dispersed GO in water is proposed as very strong interactions between the water and the GO mainly hydrogen bonding network formed between oxygen functionality on GO and water molecules. The neutron scattering studies confirmed that water is strongly bound to the basal plane of GO through hydrogen bonding interactions with the oxygen in the epoxides of the GO which can be responsible for hydrophilicity and dispersability of GO in water ^{190,302}. The as-synthesized GO suspensions are very stable and did not form any aggregation even after several months of aging time.

GO adsorbent foams necessary for adsorption experiments were produced by freeze drying. The concentrated suspension of GO solution (5 mg/ml) were converted to 3D self-assembled, binder free foam like material (see Figure 4-6(h)) by freeze-drying method. SEM images (Figure 4-6(a and b)) of GO sponge clearly shows ultra-hollow porous framework with large sheets which wrinkled and connected to each other by twisted graphene fibre like morphology (Figure 4-6(e)) formed due to the pressure imposed by ice crystals during the freezing process. These wrinkled GO sheets interconnected with fibre like GO possess relatively homogeneous pores around 10 μm between them.

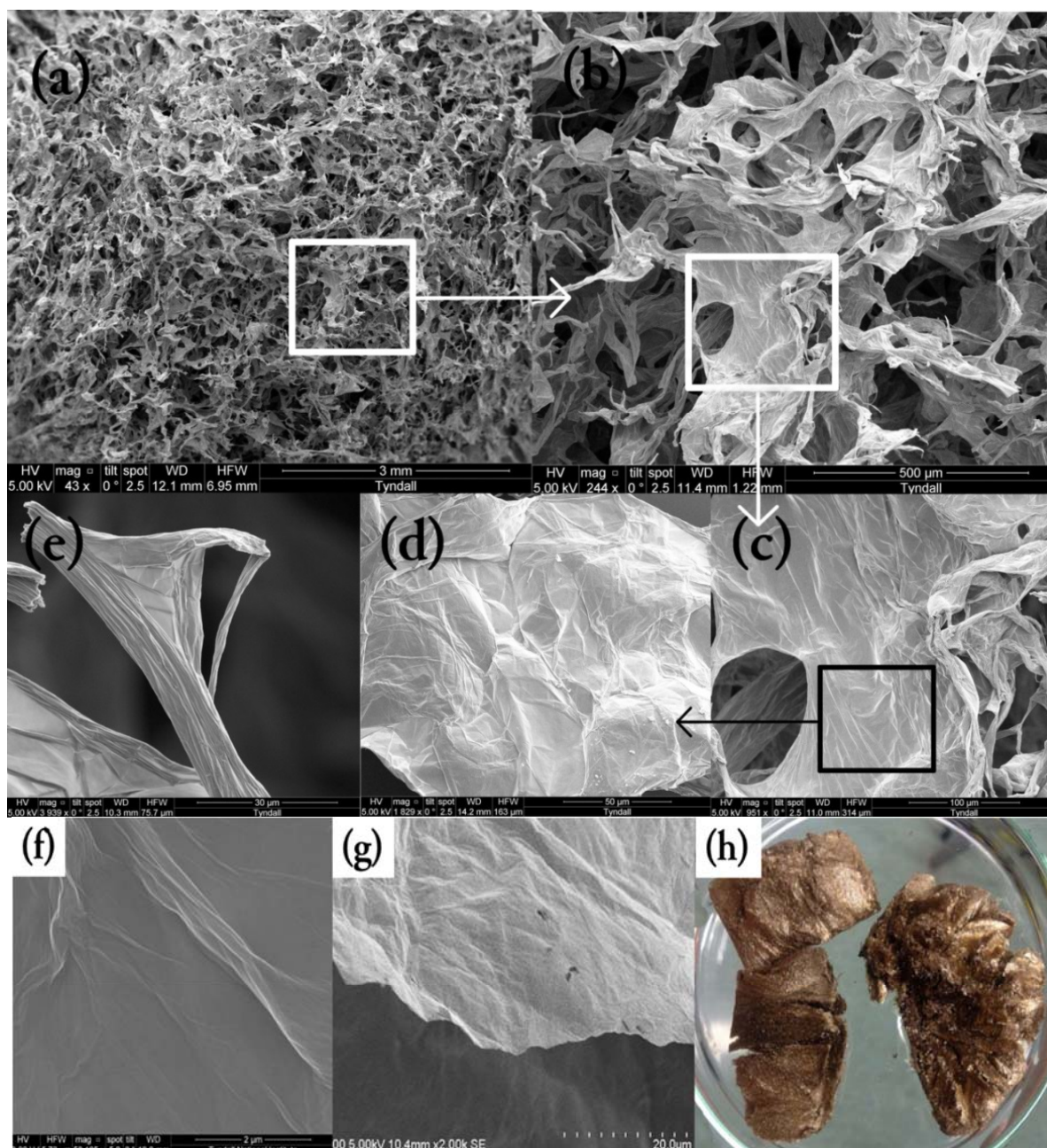


Figure 4-6: SEM micrograph of (a-e) GO sponge in different magnifications, (f) GO sheet surface, (g) GO single sheet edge, (h) photograph of GO sponge

The lateral cohesion of the adjacent GO sheets is attributed to the strong van der Waals interactions (from the hydrophobic polyaromatic nanographene domains remaining on the basal planes) and the formation of hydrogen bonds (mediated by the oxygenated functional groups and water molecules). The drying of the GO foams also prevented the GO sheets from agglomerating and forming compact lumps which are difficult to be re-dispersed. The resultant GO sponge with shiny brown colour and soft layered morphology was easily obtained with the same size of the drying container. This porous structure of the GO sponge provides a high

accessible surface area for contamination adsorption. The layered structure and long range order of sheets which is related to the liquid crystallinity of the GO can be seen clearly. A higher magnification view inside GO sponges reveals that individual GO sheets larger than 40 μm in lateral dimensions are mainly single later and have the wrinkled feature of GO on the surface and very smooth edge as shown in Figure 4-6 (f) and (g).

The freeze dried GO sponges and vacuum dried GO film were sonicated for 30 min in water in order to recover individual monolayer GO sheets and to examine the re-dispersability of the sponge compared to GO dried in the oven. It was observed that the GO sponge disperses more quickly and the re-dispersed solution is more stable than the re-dispersed GO film. An explanation for this is that the bonding between neighbouring GO sheets are relatively weaker than their bonding in the GO film ³⁰³. This approach can be suitable to produce reduced graphene from GO sponge since the strong bonding between GO sheets in GO paper promotes re-stacking of graphene sheets to graphite after reduction as shown in cross-section SEM image in Figure 4-7. These results demonstrate that after reduction of GO sponge simple sonication process can disconnect the rGO network to produce a single-layered graphene. The rGO sponge also presented better dispersability in water compared to rGO films. So the reduced GO sponges can be a source for monolayer graphene with less sonication time which reduces the lateral size of graphene sheets.

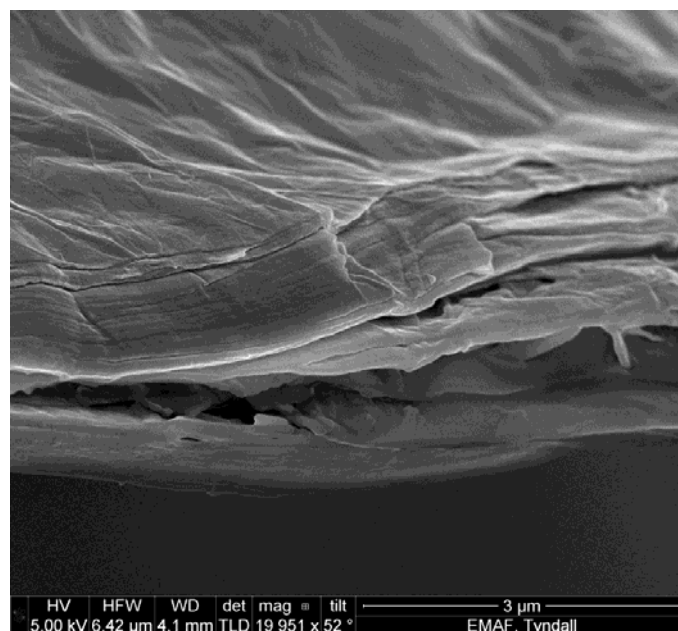


Figure 4-7: Low magnification side view SEM micrograph of an rGO paper cross section prepared by vacuum drying of GO solution followed by hydrazine reduction

However semi-transparent sheets in SEM images were observed, which is a sign of single layer or few layer GO, but the conclusive proof of single-layer exfoliation of GO sheets requires transmission electron microscopy (TEM) or atomic force microscopy (AFM). High-resolution TEM (HRTEM) was then used to image the GO and rGO sheets. The HRTEM micrograph of an isolated GO sheet on lacy carbon grid is shown in Figure 4-8. As shown in figure a, GO sheets are larger than few micron in size and are atomically transparent to electrons which is an evidence that GO sheets are indeed consist of single layers.

A selected area electron diffraction pattern (SAED) image in Figure 4-8c shows the typical six-fold symmetry expected for graphite and graphene. Although the GO structure mostly contains distorted and oxidized sp^3 domains, SAED results showed some crystallinity due to the existence of un-oxidized polyaromatic nano-graphene domains which remain on the basal planes of GO. This suggests that that GO still has the ordered structure of graphene related to the sp^2 areas that was not destroyed completely by the oxidation process. Also according to Miller–Bravais ($hkil$) indices, the relative intensity of the inner spots $\{1100\}$ of six-fold symmetry diffraction pattern is more intense than the outer $\{2110\}$ spots, which confirms that the re-dispersed GO sponge is indeed composed of single layer GO ¹⁸⁰.

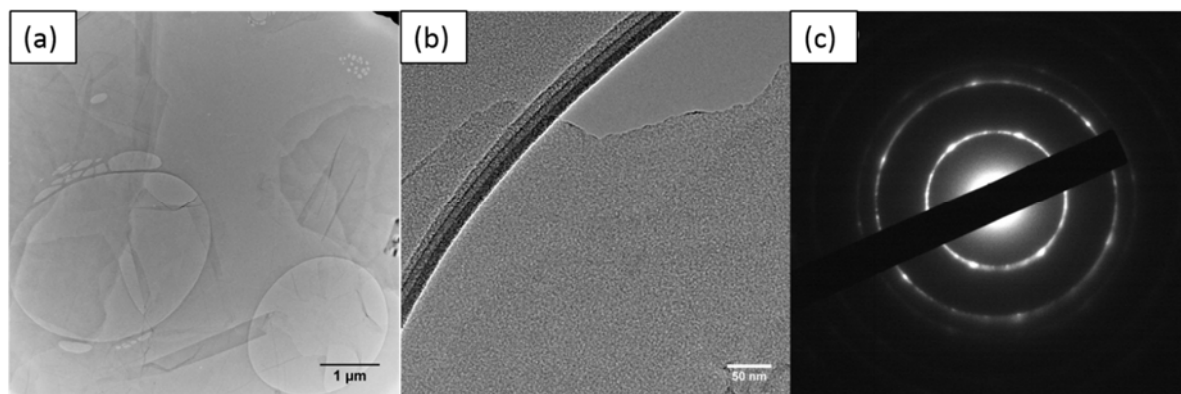


Figure 4-8: TEM image of atomically transparent and thin GO sheets (a), HETEM of single layer GO sheet (b), SAED pattern of GO (c)

AFM image of GO dispersion deposited on SiO_2/Si substrate is shown in Figure 4-9(a). GO sheets are expected to be around 1 nm thick due to the presence of covalently bonded oxygen and the displacement of the sp^3 hybridized carbon atoms slightly above and below the original graphene basal plane ³⁰⁴ which is also responsible for wrinkles observed on the GO surface. Figure 4-9 confirms that GO sheets are flat and wrinkled with the average thickness of ~0.8 nm according to the height profile in Figure 4-9(b) consistent with the thickness of a

single-layer graphene^{305,306}. This is in complete agreement with the literature and calculated inter layer spacing (d) value obtained from XRD results (0.82 nm) shown in Figure 4-16.

The wrinkles observed on the surface are normal for large size GO sheets. These wrinkles were also observed in GO sheets shown in Figure 4-6(b). They are important characteristic of GO causing the increase in surface area and susceptible sites to attach functional groups and inorganic particles as they represent the highest concentration of chemical functions and electron density³⁰⁷. From the AFM profile in Figure 4-9(b) it is also apparent that the thickness of individual wrinkles is in the range of 0.5 to 5 nm. There are different explanations for the origin of these wrinkles. It is widely believed that it originates from the chemical structure of graphene oxide but the precise chemical structure of GO is still the subject of considerable debate and currently, there is no unambiguous model for GO plane. The main reason for this is the nonstoichiometric atomic composition and the lack of precise analytical techniques for characterizing such materials¹⁹⁰.

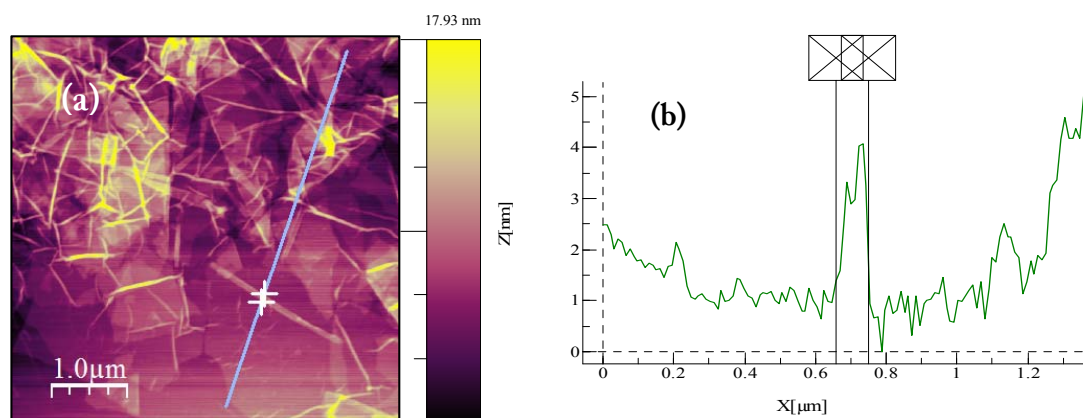


Figure 4-9: AFM image of GO sheets (a), height profile along the blue line (b)

Many structural models were proposed for GO physical and chemical structure and they are mostly agreed on regular lattices composed of discrete repeat units. However Ruess for the first time proposed a variation of this model which incorporated hydroxyl groups into the GO basal plane, accounting for the hydrogen content of GO. Ruess's model also modified the basal plane structure to a sp^3 hybridized system instead of sp^2 . A model suggested by Scholz and Boehm proposed substituting regular quinone species in GO backbone instead of epoxide and ether groups³⁰⁸.

The latest model by Dékány modified the Ruess and Scholz–Boehm models and suggested that GO basal plane is composed of two distinct domains: *trans*-linked cyclohexyl species interspersed with tertiary alcohols, ethers, and a corrugated network of quinone species (Figure

4-10). However, potentiometric acid–base titrations indicated the presence of acidic sites on the basal plane of GO ³⁰⁹. No carboxylic acids are believed to be present in these models of GO. So it is widely believed that carboxylic acids are created after further oxidation by destruction of alkenes of the quinones through formation of 1, 2-ethers and aromatic domain that were persistent during the initial oxidative conditions ³¹⁰. It is also proposed that the quinone's domain introduce rigidity to the planes and are a possible source of the macroscopic wrinkling of the GO sheets observed in TEM and AFM images ³⁰⁸. A recent study has also suggested that the hydrogen bonding between the as created carboxylic acid edge groups with water might be responsible for the wrinkling behaviour ^{153,190}.

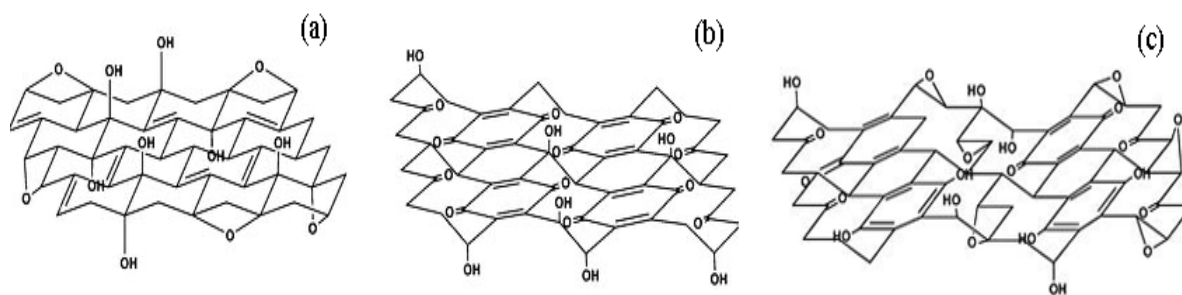


Figure 4-10: Structure of GO proposed by Ruess (a), Scholz-Bohem (b) and Dékány (c) ³⁰⁸

All these functional groups cause massive rupture in the sp^2 basal plane of graphene and acid oxidation create lots of pores and holes on the GO surface which destroyed electronic structure and electrical conductivity of graphene as proved by four point probe conductivity measurements. Therefore chemical reduction using hydrazine mono-hydrate was chosen to reduce GO and partially restore the damaged structure of GO and eliminate functional groups as much as possible. The reduction process previously described in chapter 3. Figure 4-11 shows the HRTEM image of chemically reduced GO using hydrazine (HrGO). As indicated by arrows, small domains of graphitic sp^2 surrounded by sp^3 disordered domains can be distinguished. It is also illustrated schematically in inset image.

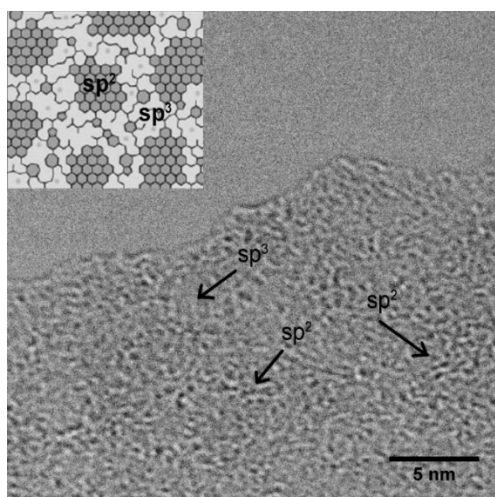


Figure 4-11: TEM micrograph of HrGO and schematic inset showing the restoration of sp^2 domains after reduction (inset image adopted from ref¹⁹³)

Figure 4-12(a) shows a TEM image of reduced graphene oxide sheets, where the low contrast of the image, wrinkles and folding indicate thinness of the single layer graphene sheets. Figure (a) confirms that rGO sheets are quite large (few micron), atomically thin and free from agglomerates and inorganic contaminants. In the corresponding SAED pattern shown in Figure 4-12(b), the ring patterns along with point patterns of hexagonal symmetry are clearly seen. Ring patterns indicate various orientations of graphene plane which is related to the wrinkles and folds of a graphene layer or overlapping of diffraction patterns of different graphene sheets. The point patterns reflect the presence of a main single crystalline domain composed of sp^2 -hybridized carbons arranged in a hexagonal lattice. As can be seen, the intensity of the $\{1100\}$ sets of planes which corresponds to the inner spots are stronger than that of $\{2110\}$ planes in the outer ring which identifies single layer rGO.

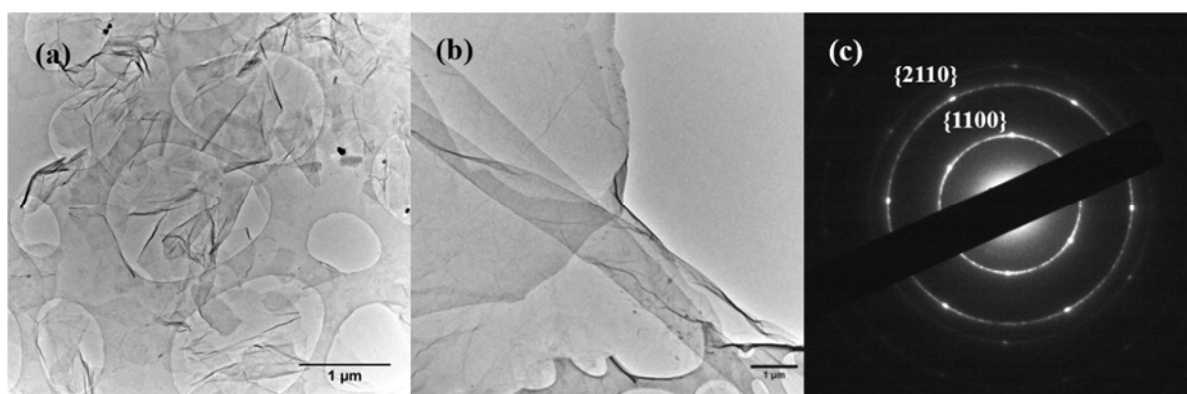


Figure 4-12: TEM image of HrGO (a,b), SAED image of HrGO (c)

Figure 4-13 is the SEM images of HrGO. It can be seen that rGO sheets are agglomerated and created an orientated bundles of sheets aligned parallel with their basal plane. As mentioned before, a reduction process is responsible for the agglomeration of the rGO sheets and obtaining a stable and homogeneous solution at high concentrations without any surfactant becomes a challenge. This stacking is related to the π - π interaction between restored sp^2 domains and also the hydrophobic character of rGO layers.

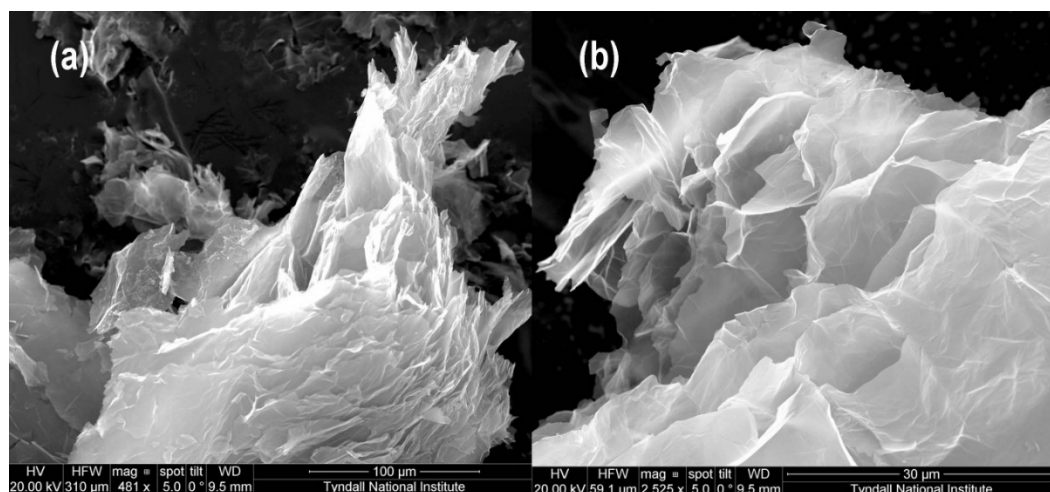


Figure 4-13: SEM images of chemically reduced GO (HrGO)

Although chemical reduction by hydrazine is one of the most effective reduction methods, however it is indeed a toxic chemical which is not environmentally friendly especially for our application in water treatment. Therefore we considered developing a thermal reduction method as replacement for chemical reduction. It had been reported that annealing GO at temperatures higher than 220 °C removes basal plane functional groups to some extent depending on temperature and heating time. Most of the literature reported so far are focused on thermal reduction of GO for electronic application which demands high quality graphene with lowest sheet resistance. For this reason annealing had been carried out normally at temperature higher than 800 °C to encourage graphitisation or two step reduction method composed of chemical reduction followed by thermal reduction or vice-versa was applied^{206,311-313}. For the first time we considered a new low temperature annealing method which may not be suitable for electronic application but quite suitable for making composite and rGO adsorbent for our application. In this method GO sponge or GO paper was heated in vacuum oven at 280 °C overnight. This temperature is slightly above the required temperature to remove functional groups, however prolonged heating time for 24 h makes this method quite efficient for GO reduction.

4.2.2. FTIR characterisation of GO and rGO

FTIR spectroscopy was used to examine the effectiveness of the different reduction processes. In order to obtain an overview about the chemistry of GO and the type of functional groups on the GO planes an FTIR spectrum was collected and oxygen-containing groups on the surfaces of GO nano-sheets were identified by comparing the vibrations from collected spectrum with the FTIR database (Figure 4-14(a)).

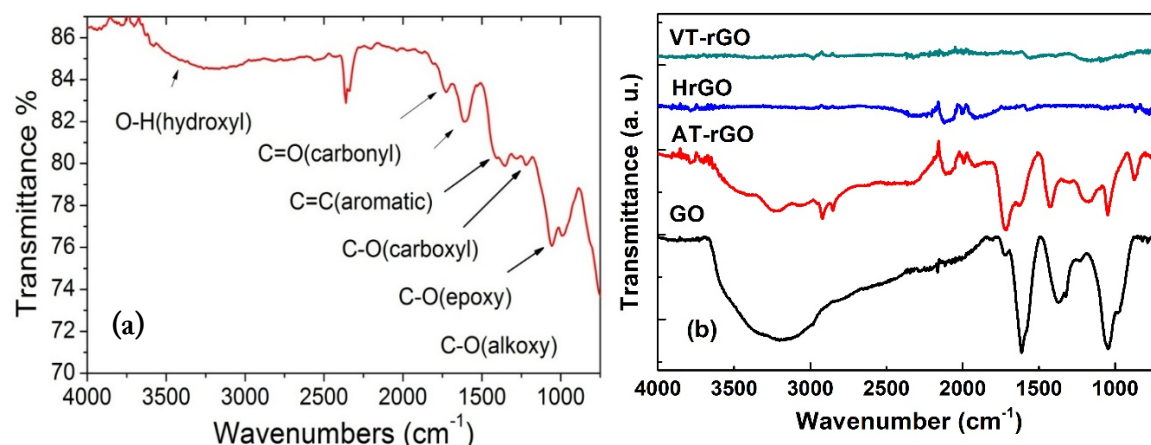


Figure 4-14: (a) FTIR spectrum of GO sheets and corresponding vibrations, (b) FTIR spectrum of GO in comparison with thermally reduced GO in air (AT-rGO), chemically reduced GO with hydrazine (HrGO) and vacuum reduced GO (VT-rGO).

In the FTIR spectrum a broad vibration related to the O-H bonding can be seen in the range of 3500-3700 cm⁻¹. This corresponds to water or the O-H groups on the surface of GO. Two vibrations related to the carbonyl and aromatic C=C which is related to the sp² domains of graphene basal plane can be distinguished in the spectrum. This is well in agreement with the Scholz-Bohem and D  k  ny's model described earlier. Other vibration related to carbonyl, carboxyl and epoxy functional groups were also indicated in Figure 4-14(a). The high dispersability of GO in aqueous and most of non-aqueous solvents, strong complex bonding with different substrates such as dolomite, and uniform coverage and bonding with TiO₂ nano-structures can be related to strong interaction with this surface oxygen- functional groups.

Figure 4-14(b) is comparing FTIR spectra of graphene oxide and reduced graphene oxide prepared via thermal reduction in vacuum chamber and air with the one reduced chemically by hydrazine. From this spectrum thermal reduction in vacuum can be introduced as the most effective reduction method as no oxygen containing functional group appeared in

the spectrum (VT-rGO) in contrary to annealing in air which not only did not reduce GO but also introduced additional functional groups to it.

Although annealing at low temperature in vacuum oven successfully removes functional groups from GO however, it is not applicable for sol-gel synthesised GO/TiO₂ composites. As described in chapter three, after in-situ synthesis of TiO₂ nano-particle on the surface of GO, they need to be annealed at 450 °C for 2 h in order to convert amorphous TiO₂ into crystalline form. Therefore it is necessary to check if GO is reduced in this process as well. In Figure 4-15 (a) the FTIR of the rGO sponge reduced at 450 °C for 2 h comparing with GO film and sponges clearly confirms the effective removal of oxygen containing functional groups. Since adsorption experiment was carried out on GO sponge and GO film as well as rGO, so it was necessary to collect their FTIR as well. As it can be seen there is no difference between GO film and sponge except their morphology.

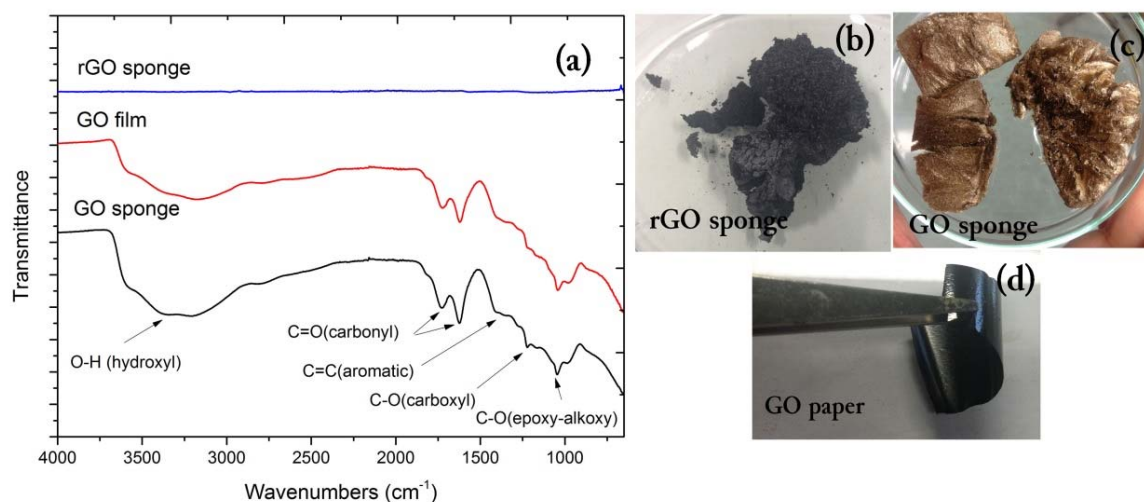


Figure 4-15: FTIR spectra of GO sponge, film and rGO (a) and images of each material (b-d)

4.2.3. XRD characterisation of GO and rGO

When the as-synthesized GO sponges were reduced, the brown colour of GO sponges turned black and the porosity of the GO sponges was diminished as the functional groups on the GO planes were removed and the aromatic structure of graphene was restored. This causes the restacking of graphene sheets into few layers in order to reduce the energy of the system to graphite state which has the least energy state and the most stable form of graphene sheets. Hydrophobicity of the rGO sheets also is the other reason of the re-stacking. The XRD results and TEM images of this study also confirm this re-stacking after reduction.

Figure 4-16 shows the X-ray diffraction patterns of both graphene oxide and thermally reduced graphene oxide samples. It can be seen that as-prepared GO shows a distinct peak at 10° attributed to the (002) plane and corresponding to a layer-to-layer distance (d-spacing) of about 0.82 nm. This d-spacing is related to single layer of water molecules trapped and presumably hydrogen-bonded between the graphene oxide sheets ³¹⁴ and is in well agreement with AFM results previously discussed. The crystallite size of graphene oxide sheets is about 7.5 nm based on the calculations from the half width at maximum (HWHM) of the X-ray diffraction peak using the Scherrer's equation (see methods in chapter 2). In contrast the rGO sample showed a considerable decrease in interlayer spacing ($d = 0.36$ nm), in XRD pick at $2\theta = 25.6$ which is in accordance with the diffraction peak of normal graphitic planes in graphite precursor at $2\theta = 26.40^\circ$ ($d = 0.34$ nm).

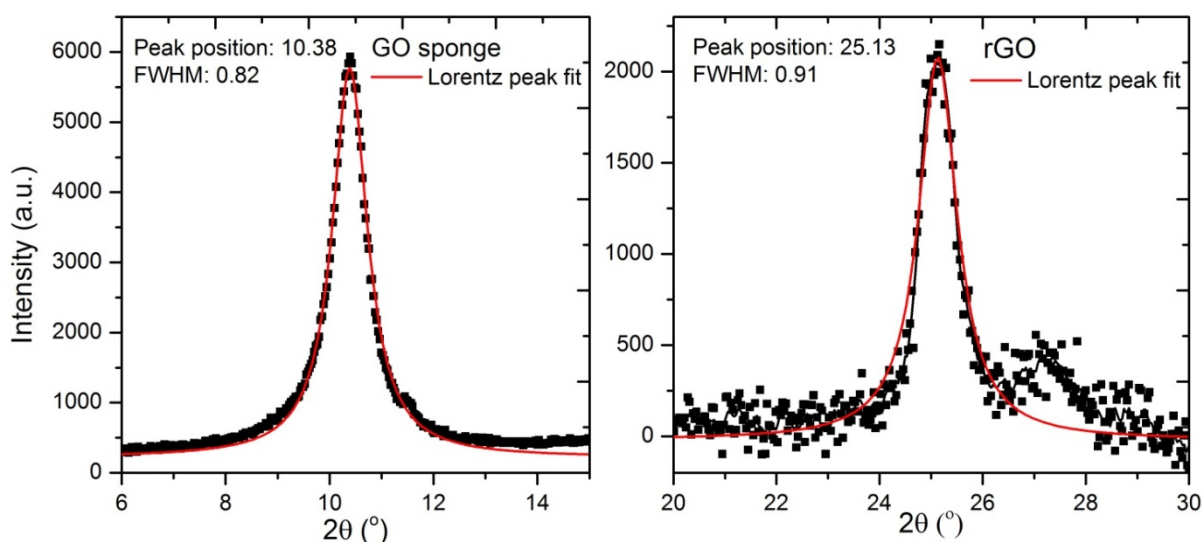


Figure 4-16: XRD pattern of GO and thermally reduced rGO

Table 4-1: GO and rGO XRD peak information

Sample	Peak ($2\theta^\circ$)	FWHM	d spacing (\AA)	L_a (nm)
GO	10.38	0.82	8.5	18.8
rGO	25.13	0.91	3.54	17.34

The decrease of interlayer spacing (c-axis spacing) from 0.82 nm to 0.36 nm after reduction is due to the loss of the oxygen-containing functional groups on GO basal plane and the restoration of sp^2 aromatic domains which implies strong π - π attractions between the basal planes of rGO sheets and promotes the restacking of rGO sheets into semi-graphitic structure. Since the larger interlayer spacing and the more functional groups are ideal for adsorption of

pollutant and attachment of inorganic particles on the surface and between the layers, it was concluded that reduction of GO to rGO deteriorate its functionality as an adsorbent. Hence pure was used for adsorption experiments and starting material for developing graphene based photocatalyst composites. However GO suffers from low electron conducting properties which has negative impact on transferring the electrons generated by TiO_2 when used as adsorbent platform for making TiO_2 composites. Our strategy to solve this problem was synthesis of TiO_2 on the surface of GO or mixing TiO_2 with GO, then reducing it at the same time while crystallising TiO_2 at 450 °C. Therefore in one annealing treatment GO partially reduced to rGO and amorphous TiO_2 crystallised simultaneously. Also, an advantage of TiO_2 /GO composites is that GO will reduce to rGO more via photochemical process while illuminating with UV light during photocatalysis experiments which will be discussed in chapter 5. Photochemical reduction of GO by TiO_2 has the added benefit of keeping rGO sheets from restacking³¹⁵ because of the intercalation with TiO_2 nanoparticles.

4.2.4. Surface area measurements of GO and rGO

In order to use GO as an adsorbent, open pores and carbon sp^2 sites on the surface of GO layers should be accessible when the GO layers are packed together when dried normally. By increasing the space between the GO sheets by freeze-drying, the available accessible pores and carbon sites to adsorb pollutant molecules is increased substantially leading to the superior performance of GO network as an adsorbent especially for molecules with the benzene ring. As mentioned before the reduction process causes the decrease in interlayer spacing and also agglomeration of the rGO sheets which consequently decrease the surface area and pore volume of the rGO compared to that of the GO sponge. This phenomenon can be described clearly from the N_2 adsorption isotherms shown in Figure 4-17.

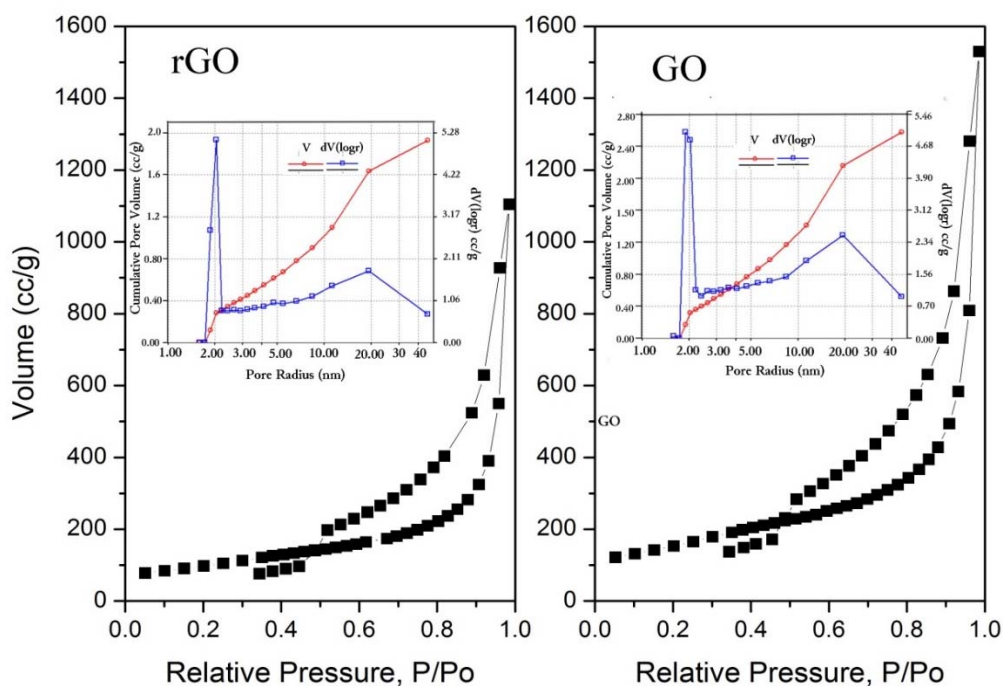


Figure 4-17: N₂ adsorption-desorption isotherm and BJH accumulative pore size distribution (inset) of GO and rGO sponges

Both isotherms were identified as type III which is indicative of micro-porous (pore size $0.5 < R < 2$ nm) and meso-porous solids ($2 < R < 50$ nm) with the multilayer formation and a cylindrical meniscus pore filling mechanism. The observed hysteresis loop is another indicative of multilayers formation in meso-porous materials which is as a result of the differences in the pore filling and emptying processes. This class of isotherm is a characteristic of weak adsorbate-adsorbent interactions. The weak interactions between the nitrogen molecules as an *adsorbate* with rGO and GO as *adsorbent* lead to low uptake at low relative pressures. However, after adsorption of the first layer, accelerated uptake at higher relative pressure observed. These isotherms also confirm that there are large quantities of open pores in the structure which causes the hysteresis loop. The GO isotherm shows that 1550 cc of nitrogen were taken to fill the pores of 1 g of GO. However this is 1100 cc per g for rGO which shows a less porous structure of rGO compared to that of the GO sponge which is quite in agreement with the XRD and TEM data from this study. The BJH pore size distribution shown in Figure 4-17 insets confirms the meso-porosity of the both samples. However in the GO sample majority of pores have a diameter around 1.5 nm and for 2 nm for rGO. This finding is not consistent with the XRD results where rGO showed less interlayers spacing compared to the GO sample. However, this finding can be explained as the restacking of the rGO planes decreases the accessible small pores, so that the pore size distribution shifts towards the larger pore radius as shown in the pore size

distribution diagram. A summary of pore properties such as surface area, pore size and pore volume is reported in Table 4-2. According to the surface area and pore volume, BET data also confirms that the rGO is less porous than GO which is in accordance with XRD and SEM data.

Table 4-2: Surface characteristic of GO and rGO obtained from N₂ adsorption isotherms based on BET and BJH models

Properties	GO	rGO
BET surface area (m ² /g)	547.37	345.92
Pore volume cc/g (size< 66nm)	2.366	1.7
Average pore radius nm	8.64	9.87
BJH desorption pore radius nm	1.89	2.039

However the surface area obtained from adsorption isotherm using BET model is very different from the theoretical surface area (2630 m²/g)^{306,316,317}. This means that N₂ adsorption is not suitable for surface area measurements for GO and rGO for two reasons. Firstly, all samples need to be degassed at high temperatures to make sure the entire surface is available and no water molecule present inside the pore. For this experiment samples were degassed at 100 °C for 10 hours in vacuum which obviously reduced GO partially. This was observed visually as the colour of GO changed from brown to black. Secondly, the pores in GO and rGO are mainly open pores but BET model is more suitable for closed microspores. Therefore in order to obtain the actual surface area, another technique which is the absorption of methylene blue (MB) molecules from solution onto the GO and rGO surface was used.

MB dye (formula C₁₆H₁₈ClN₃S), with a corresponding molecular weight of 319.87 g/mol is a cationic dye, C₁₆H₁₈N₃S⁺, which absorbs in large amounts onto the surface of negatively charged GO and rGO. The specific surface area of samples was calculated from the amount of absorbed MB. The surface area covered by one methylene blue molecule is typically assumed to be 130 Å²³¹⁸. The value of specific surface is derived from the point of complete cation replacement determined on the titration curves shown in Figure 4-18. For this experiment 0.2 g of adsorbents were poured into a flask and 20 ml of 1 g/L of MB solution were added at regular intervals and the remnant concentration of MB in the solution was measured with UV-vis spectrophotometer at 665 nm after removing the adsorbent using high speed centrifugation (12000 rpm for 15 min). Then the amount of MB added versus the amount of absorbed MB was plotted to identify complete cation replacement point (CRP shown in Figure 4-18 plots). The specific surface is calculated from the amount of absorbed MB at CRP point using:

$$S_s = \frac{m_{MB}}{319.87} A_v A_{MB} \frac{1}{m_s} \quad \text{Equation 4-1}$$

Where m_{MB} is the mass of the absorbed MB at the point of complete cation replacement, m_s is the mass of GO and rGO samples, A_v is Avogadro's number ($6.02 \times 10^{23}/\text{mol}$), and A_{MB} is the area covered by one MB molecule (assumed to be 130 \AA^2).

A summary of the surface areas obtained by the BET and MB adsorption techniques is presented in Table 4-3. There is a considerable difference between the surface area values reported by the two methods. The MB surface area for GO is 4 times higher and for rGO is 6 times higher than the ones reported from BET model. The specific surface area of both samples are in agreement with the theoretical surface area of graphene around $2630 \text{ m}^2/\text{g}$.

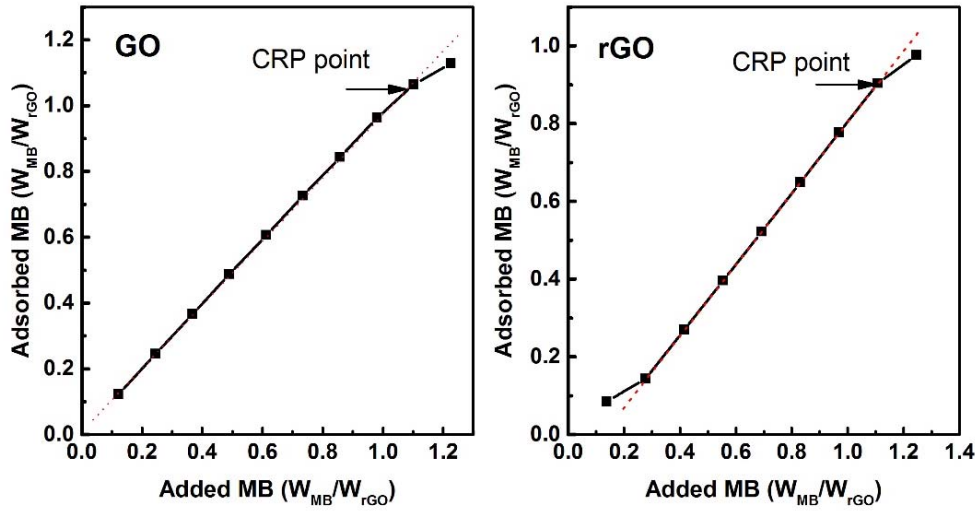


Figure 4-18: Titration plots to determine complete cation replacement point

Both techniques involve the sorption of an adsorbate (MB and nitrogen gas). The methylene blue technique involves high bonding energy (ionic Columbian attraction-chemisorption) and it is generally limited to a monolayer. In the nitrogen gas absorption, N_2 molecules are neutral and attracted to the surface by van der Waals forces (physi-sorption), and multiple layers may form. This is schematically shown in Figure 4-19. The MB absorption method renders higher values of specific surface because of the strong bonding between MB and adsorbent surface and strong hydrogen bonding between water molecules and graphene plane in the aqueous solution (which creates swelling of the sample) can delaminate GO layers and more interlayer surfaces can be reached by exchangeable ions after hydration.

Table 4-3: Surface areas determined by N₂ adsorption (BET) and MB adsorption

Sample	BET surface area (m ² /g)	MB surface area (m ² /g)
Graphene oxide	547.37	2605.5
Reduced graphene oxide	345.92	2210.2

Another disadvantage of the N₂ adsorption method is imposed by heating and degassing the specimen at high temperatures which can chemically alter the chemistry of the materials including the functional groups which causes dehydroxylation of the GO. Therefore for this study, it is concluded that the MB adsorption method is more accurate and reliable technique to measure the actual surface area of not only GO and rGO but also for all carbonaceous materials including carbon nanotubes and activated carbon.

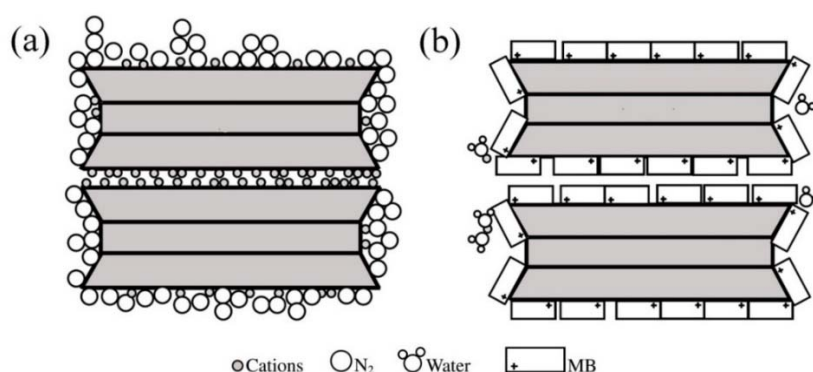


Figure 4-19: schematic illustration of MB wet adsorption and N₂ dry adsorption mechanism

4.2.5. UV/Vis spectroscopy of GO and rGO

Considering our application of GO and rGO as a platform for TiO₂ photocatalyst immobilisation which is subjected to the UV and visible light irradiation for photocatalysis experiments, it is important to study the interaction of GO and rGO nano-sheet with UV and visible light. It is also important that they transmit UV light to the TiO₂ with high efficiency. As illustrated in UV/vis spectrum (Figure 4-20) there is an absorption peak for GO at 232 nm due to the $\pi \rightarrow \pi^*$ transition or the C=C bonding, which is similar to the reported value in the literature^{319,320}.

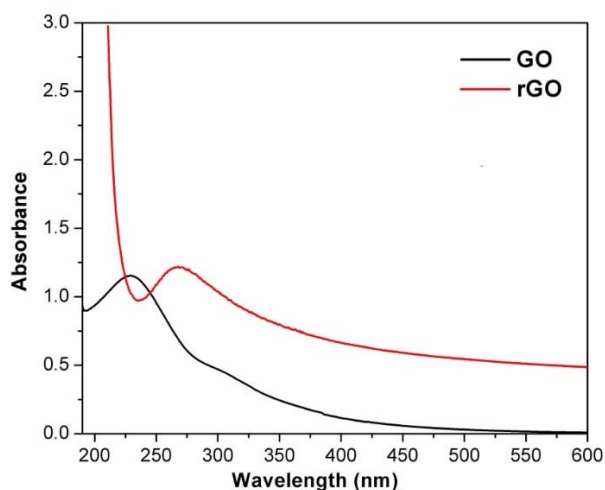


Figure 4-20: UV/vis spectra of GO and rGO suspension

The peak position exhibits the lowest wavelength, indicating that the sample has a lower amount of remaining conjugation (thus requires higher energy for the electronic transition). Therefore the red shift from 232 to 270 in rGO suggests that the sp^2 area within the graphene sheets is restored by hydrazine reduction, i.e. this shows a lower degree of oxidation, with less functional groups on the GO basal plane and a higher amount of conjugation. For GO sample also a small shoulder appears around 300 nm which is attributed to the carbonyl groups. This shoulder has not observed for the rGO which is further evidence of a high degree of reduction. However both GO and rGO can transmit UV light with higher wavelength than 270 nm quite efficiently which matches with the UV light used in photocatalytic experiments.

4.2.6. Raman spectroscopy characterisation of GO and rGO

Although UV/Vis spectroscopy can provide information about the efficiency of reduction, to determine the order of crystallinity, number of layers and quality of the graphene Raman spectroscopy is the key analysis not only for graphene but also for every carbonaceous material. It can provide useful information about the relative position of carbon atoms within the lattice and the nature of their bonding to one another. Another important feature of Raman spectroscopy which has been used in this work is the ability to differentiate between graphene and graphite since many studies in the literature have reported graphitic structure instead of graphene because of the similarities in the Raman spectra. In this section first we studied the efficiency of our method to exfoliate and reduce GO comparing to graphite and commercial graphene nano-platelets provided by Haydale Company UK. Then investigate the degree of reduction by thermal and chemical method comparing with the as-synthesised GO.

The theory of Raman spectroscopy for carbon nano-materials was explained briefly in chapter three. Generally graphene is characterized by three prominent features: a G band at 1587 cm^{-1} arising from first order Raman scattering of the E_{2g} phonon due to the bond stretching of all pairs of sp^2 atoms in both rings and chains, a weak D band at 1357 cm^{-1} arising from A_{1g} phonons or breathing modes of sp^2 atoms in rings which renders the small size of the ordered graphene (small sp^2 domains) or defects and functional groups in basal plane or carbon atom located on the edges of nano-sheets. Another feature of graphene is the 2D band ($\sim 2680\text{ cm}^{-1}$) arising from Raman scattering of hexagonal lattice. The obvious difference between the Raman features of graphene and graphite is the 2D band. The 2D peak can reflect the stacking order of graphene and the number of layers. For single layer graphene, the 2D band is a sharp and symmetric peak. Adding successive layers of graphene causes the 2D band to split into several overlapping modes which arises from symmetry lowering due to increasing the layers of graphene^{265,266,321-323}. In this work the 2D band analysis has been used in order to examine whether we obtained graphene.

As shown in Figure 4-21 Raman spectroscopy of starting graphite flakes showed features at: 1350 cm^{-1} (D-band) which corresponds to the breathing mode of sp^2 carbon atoms, and it should be absent without the presence of defects or edges detected by Raman laser; 1580 cm^{-1} (G-band), associated with the doubly degenerate phonon mode at the Brillouin zone centre, which are associated with in-phase vibrations of the graphite lattice; and the relatively wide 2D band at 2730 cm^{-1} , an overtone of the D-band. The Raman spectrum of rGO (thermally reduced at $450\text{ }^\circ\text{C}$ for 2h in Ar) shows both features of graphene, D and G bands, however the intensity of the D band dramatically increased relative to the G band and 2D band became very broad and hard to detect. All these differences are related to the defected structure of the GO and distortion of the graphite lattice due to strong oxidation with acid which is mostly irreversible. However with chemical and thermal reduction, oxygen containing groups attached to the edges and defected basal plane can be removed (as confirmed with the FTIR spectra in Figure 4-14) which improves the electron conductivity of the reduced graphene flakes.

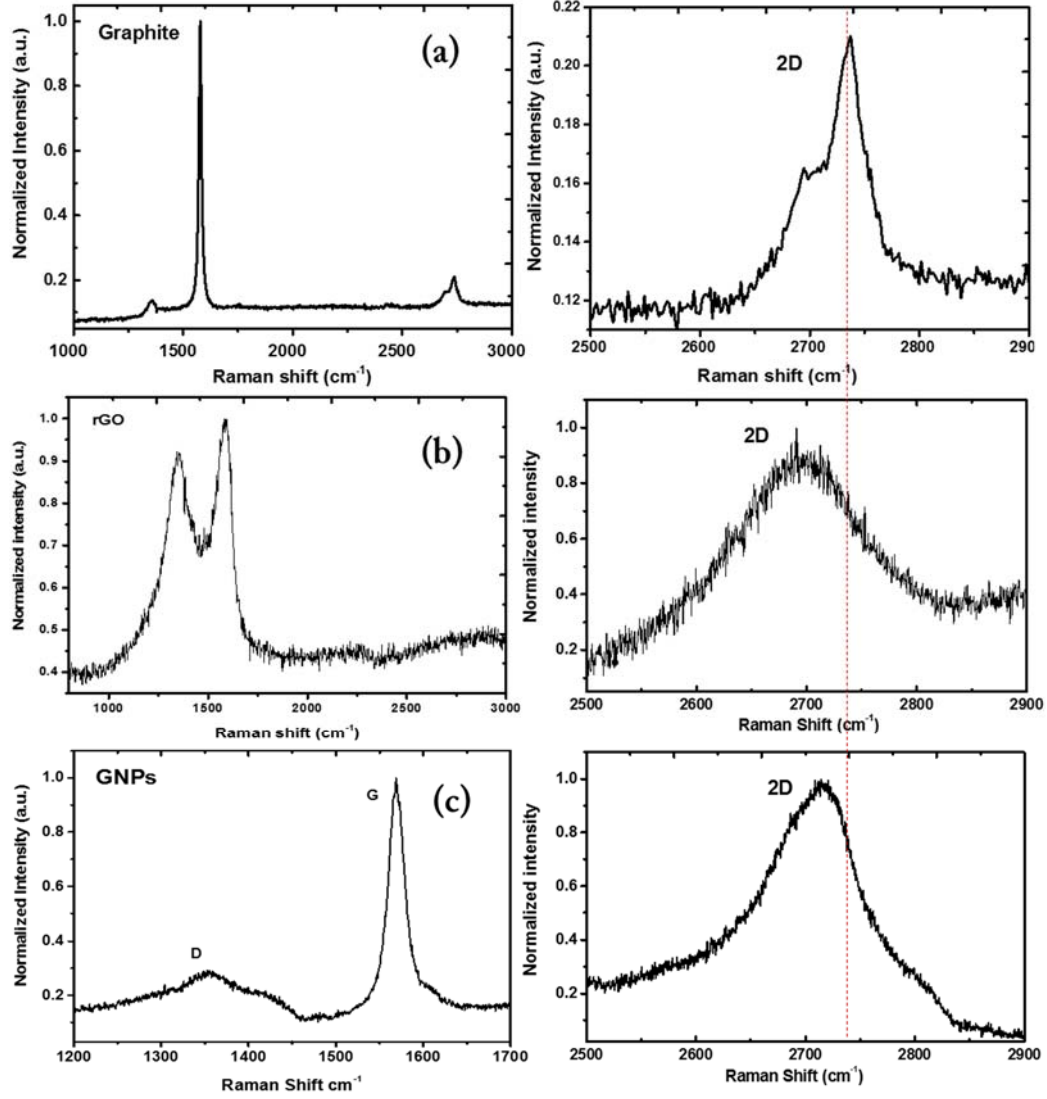


Figure 4-21: Raman spectra for graphite, thermally reduced GO (our method) and commercial graphene nano-platelets. Spectra are normalised to [0, 1] and numerically averaged over 10 measurements for each sample. Their magnified 2D bands are shown in right panels.

Comparing the 2D band of graphite with rGO shows that our method has a good degree of exfoliation since the doublet 2D peak is replaced by the broad symmetric peak which is characteristic of graphite exfoliation. The ratio of D band to the graphitic G band (I_D/I_G) for our rGO is 0.92 while the commercial graphene shows the intensity ratio of about 0.28. It could be concluded that the commercial sample is composed of a high quality graphene, however further investigation of the asymmetric shouldered 2D band (deconvoluted in Figure 4-22) which will be discussed later, revealed that the sample might be defected graphite or stacked layer of defected graphene and not single or few layer graphene.

According to the isolated 2D band of rGO shown in Figure 4-21(b), our thermally reduced graphene oxide shows a symmetric 2D band without any shoulder on the left tail of the peak (which is the characteristic of graphite as shown in 2D band of graphite source in Figure 4-21(b)) but the 2D band of the graphene nano-platelets exhibits an asymmetric shoulder. It should be noted that 2D band of single layer graphene normally shows 50 cm^{-1} red shift comparing with the 2D band of graphite which is matched with 43 cm^{-1} red shift for our rGO. In contrast GNPs shows only 20 cm^{-1} red shift which confirms the graphitic structure of the GNPs. Both characters of the peak are the evidence of having graphite instead of graphene which necessitated further investigation. In order to study the stacking of the commercial graphene, the 2D band was plotted in Figure 4-22 separately and fitted with three Lorentzian peaks centred at $2660\text{ (G}^*_{3\text{DA}})$, $2680\text{ (G}^*_{2\text{D}})$ and $2726\text{ (G}^*_{3\text{DB}})$, respectively. The 2D or G^* peak of the graphene is mostly composed of the $\text{G}^*_{2\text{D}}$ peak but graphite has a strong $\text{G}^*_{3\text{DA}}$ peak ²⁶⁷.

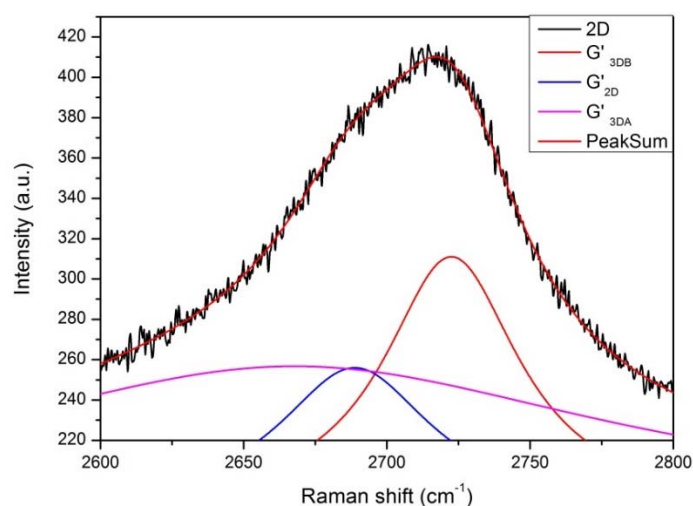


Figure 4-22: 2D band of commercial graphene nano-platelets fitted with Lorentzian equation which confirms Bernal stacking of graphene layers

Comparing the positions and the intensity ratios of these peaks revealed that the commercial graphene exhibited high intensity of G band and less defect although it poses Bernal stacking ²⁶⁷ which is characteristic of graphite. Hence it was concluded that it mostly composed of un-exfoliated graphite as it mainly composed of $\text{G}^*_{3\text{D}}$ peaks rather than $\text{G}^*_{2\text{D}}$. Comparing our graphene with commercially available graphene one can be concluded that although the reduced graphene oxide produced in this study has more defects and smaller sp^2 domains compared to the commercial graphene, however single layer graphene with acceptable quality which is suitable for future applications was produced in larger quantity and lower cost.

To investigate the efficiency of the reduction process in order to generate the highest quality of graphene, Raman analysis was used. The Raman spectra of graphene oxide (GO), hydrazine reduced graphene oxide (HrGO), thermally reduced graphene oxide in vacuum (VT-rGO) and thermally reduced GO at 450 °C, 2h in Ar, are shown in Figure 4-23. The Raman spectrum of GO displayed a strong D band at 1357 cm^{-1} (which matched the D band of graphite) and a broad G band at 1597 cm^{-1} . The perfect matching of the G peak positions for both reduction processes (1586 cm^{-1} for both methods) clearly indicates the efficient healing of sp^2 conjugated electrons during the reduction. After reduction of GO, the position of G band in all reduction methods is red shifted from 1597 which exactly matches with G band position of graphene (1587 cm^{-1}). The intensity ratio of D band to the G band (I_D/I_G) of GO is about 0.9 to 1.0 (comparing with single layer low defect CVD grown graphene about 0.1-0.2) which is due to the defects introduced by strong oxidations and presence of various functional groups³²³. At first glance by looking at the intensity of the D and G bands it seems that after reduction the I_D/I_G ratio increased from 0.9 for GO to 1.0 and 0.92 for HrGO and rGO respectively. This increasing in I_D/I_G ratio according to the literature is not necessarily related to increase in defect densities²⁰¹. However it might be due to the small size of the newly formed nano-graphene like sp^2 domains which are smaller than the domains which had been present in the initial sample before reduction^{324,325}. But interestingly we found out that all the Raman spectra can be deconvoluted to three Lorentzian peaks (with adj. R-Squared $\geq 92\%$) and not only 2 peaks of D and G. Based on the intensity of deconvoluted D and G peaks shown in inset spectra in Figure 4-23, I_D/I_G was recalculated and noted as fitted I_D/I_G in Table 4-4. This shows that I_D/I_G decreased from 1.27 for GO to 1.02 for all reduced graphene oxides which equals to almost 20% increase in density of sp^2 nano-graphene domains due to restoration of graphene defected structure during the reduction process.

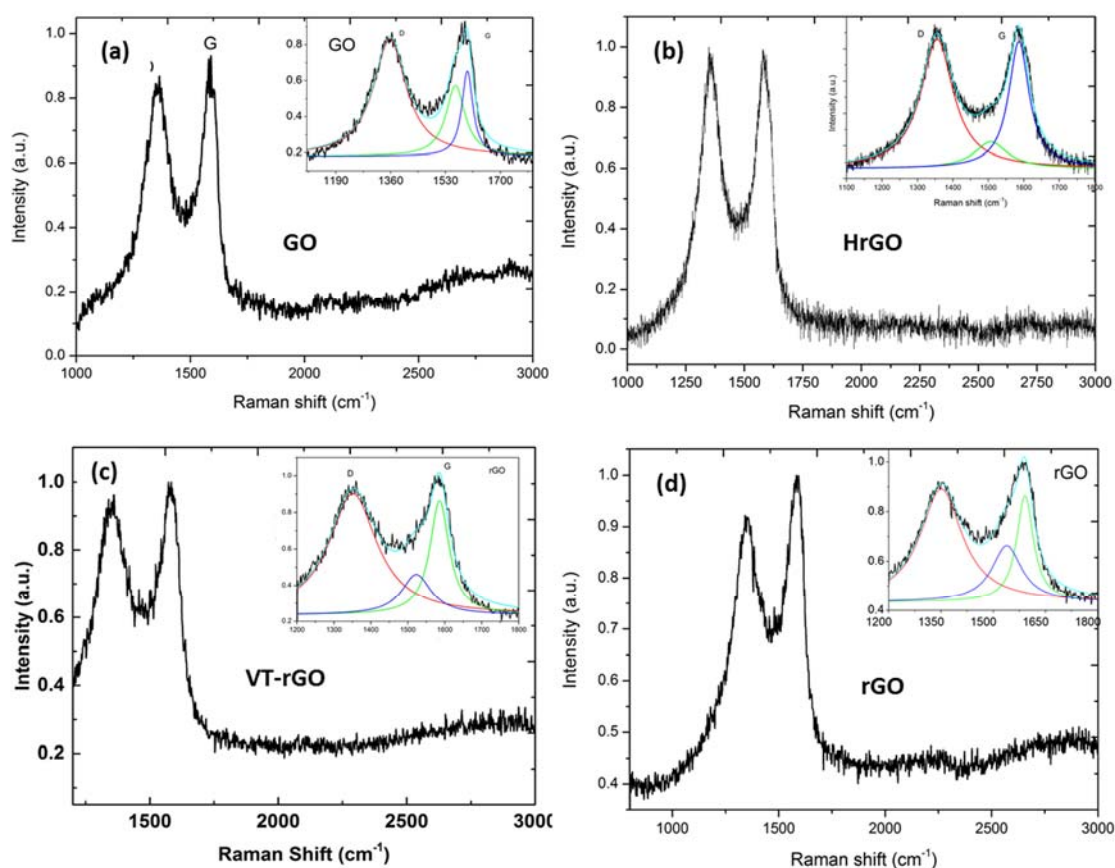


Figure 4-23: Raman spectra of GO, thermally reduced graphene oxide in vacuum (VT-rGO) and hydrazine reduced graphene oxide (HrGO)

Table 4-4: Raman band position and ratio of GO and rGO

Sample	D band (cm ⁻¹)	G band (cm ⁻¹)	I _D /I _G	I _D /I _G (fitted)
GO	1357	1597	0.90	1.27
HrGO	1355	1586	1.0	1.02
VT-rGO	1344	1590	0.90	1.02
rGO	1350	1590	0.92	1.02

Based on all the characterisation methods described so far such as Raman, FTIR, XRD and electron microscopy we concluded that the quality of graphene for all the three evaluated methods are very similar therefore thermal reduction is preferred to the chemical one because it is simpler, more controllable, and straightforward with less impact on the environment.

4.2.7. Liquid phase exfoliation of graphene (LPE)

In order to examine the chemical exfoliation method to produce high quality graphene sheets in comparison with oxidation-reduction method, graphite flakes were bath sonicated in N-Methylpyrrolidone (NMP) for 20 hours and the supernatant of the solution was collected

after centrifuging at 3000 rpm for 60 min. The Raman spectra of rGO and exfoliated graphene are shown in Figure 4-24. The two G band and 2D band positions exactly match the characteristic peaks of graphene with very little I_D/I_G intensity ratio which confirms the production of high quality of defect free graphene. The 2D band data fitted with three Lorentzian peaks (Figure 4-24(c)) shows that graphene lost the typical Bernal stacking of the initial powder and attains the turbostratic stacking typical of disordered graphite²⁶⁷. It can be concluded that high quality mainly single layer graphene was produced via exfoliation by sonic waves in NMP.

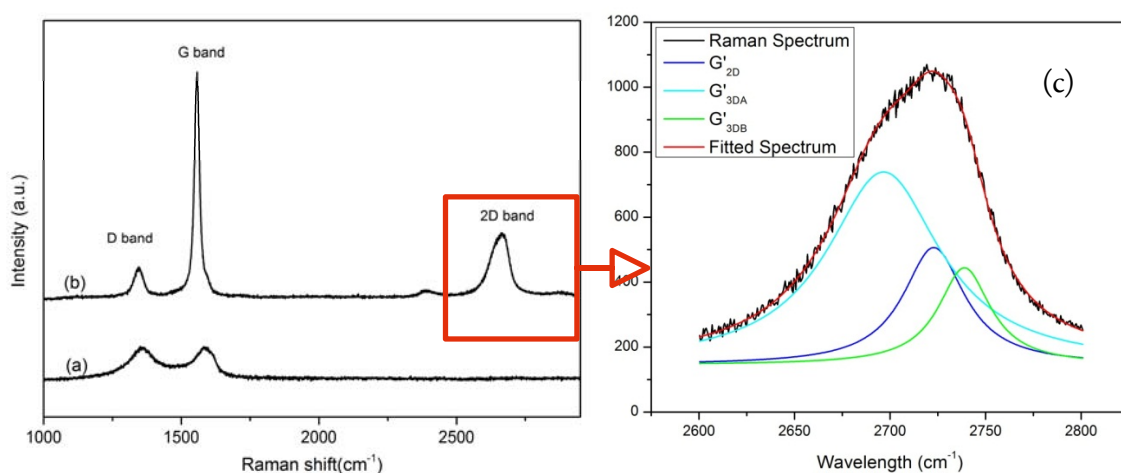


Figure 4-24: Raman spectra of liquid-phase exfoliated graphene (b) comparing with HrGO (a), the 2D band of exfoliated graphene nano-sheets (c)

Although the as-produced graphene made by sonication-assisted LPE (Liquid Phase Exfoliation) possess characteristic of low defect pristine graphene, however because of the following limitations this method was not considered to produce graphene for our application in this study. The first limitation is difficult washing process to remove the NMP completely which is a toxic solvent therefore not suitable for water treatment. The second reason is that the as-produced graphene is highly hydrophobic which is not desirable for the application in water since it will affect dispersibility of the composites and adsorption of the water soluble pollutants on the surface. It also does not have functional groups and defects which are favourable sites for TiO₂ attachments therefore there is a need to pre-functionalization of the graphene flakes to be able to immobilise TiO₂ on its surface which imposes more complex chemical treatments. However the most important limitation is the very low efficiency or production yield of this method (0.05 to 0.1 mg/ml) which make it difficult to produce graphene in high concentrations and large masses for adsorption experiments. Therefore oxidation-reduction were selected as the main method to produce graphene as an adsorbent and a substrate for TiO₂ immobilisation in current research.

4.3. Graphene oxide integrated adsorbents

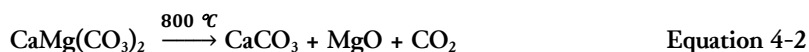
As described in materials and methods section 3.4.3 page 59 in order to reduce the amount of GO dosage for adsorption experiment and facilitate post recovery of the adsorbent after adsorption experiments a series of adsorbent substrates were examined for GO immobilisation including porous glass beads, dolomite and silica gel. Among these substrates as will be discussed in next section, only dolomite exhibited promising properties such as cyclability and adsorption capacity. In case of glass beads, the small surface area of the substrate ($1.6 \text{ m}^2/\text{g}$), large pore sizes 40-100 μm and lack of functional groups on the surface, introduced it as an inapplicable substrate for GO immobilisation. It was observed that large amount of immobilised GO detached from the surface during the batch adsorption experiment which destroyed the cyclability of the composite.

Silica gel possessing high surface area ($800 \text{ m}^2/\text{g}$) and small pore size (0.5-4 nm) should be a favourable substrate for GO immobilisation however it was found that it only absorb small amount of GO on its surface non-uniformly which detached during batch experiments too. Further investigation showed that it might be due to the strong hydrogen bonding between the silica's surface oxygen groups with water which makes it difficult for any other molecule except water to approach to the silica surface. In contrary dolomite has reasonably high surface area ($65\text{-}85 \text{ m}^2/\text{g}$) and small average pore size (60 nm). In addition it is positively charged due to alkaline dissociation in water which interact with positively charged GO very strongly. Also dolomite has a layered structure which can swell in water and provide more surface for GO incorporation between the layers. This structure depicted in Figure 4-26. Further adsorption studies confirmed that Dolomite/GO composite is a promising adsorbent especially for dye removal from wastewater which has the potential for the commercialisation and large scale industrial textile manufacturer wastewater treatment plants considering dolomite abundance and low price. Therefore in the following sections first we will characterise dolomite and dolomite/GO composite and study their physical and morphological properties then adsorption properties of all the integrated adsorbents towards dye removal will be discussed briefly.

4.3.1. Characterisation of dolomite/GO integrated adsorbent

Dolomite powder with an average particle diameter size of 200-500 μm was used as a substrate to coat graphene oxide. The raw dolomite was charred in a furnace at 800 $^{\circ}\text{C}$ for 8 hours with an air atmosphere to produce a porous body for GO immobilization. The SEM images of the charred dolomite powder are shown in Figure 4-25. Dolomite is a calcium and magnesium carbonate compound ($\text{CaMg}(\text{CO}_3)_2$) which possess a non-porous rhombohedra

layered crystalline structure Figure 4-26. However in the inset image of Figure 4-25 small pores between dolomitic grains on the surface of the charred dolomite can be distinguished. According to the literature ^{326,327}, dolomite calcination at temperatures between 780 and 840 °C produces a porous calcite-magnesium oxide structure based on the following chemical reaction:



The as-calcined sample in Figure 4-25(b) shows the presence of discrete round shaped grains and the layered structure with sharp edges is shown in Figure 4-25(a). The step like features confirms the layered structure of dolomite and shows an apparent preferential orientation of crystals growth along c-axis. This layered structure is possibly responsible for the instant reaction of GO with dolomite in water as a result of swelling and delamination. The presence of spherical particles with small pores between them can be explained by the decarbonation of MgCO_3 associated with dolomite as shown in Equation 4-2. The CO_2 release leads to a more porous structure ^{328,329}.

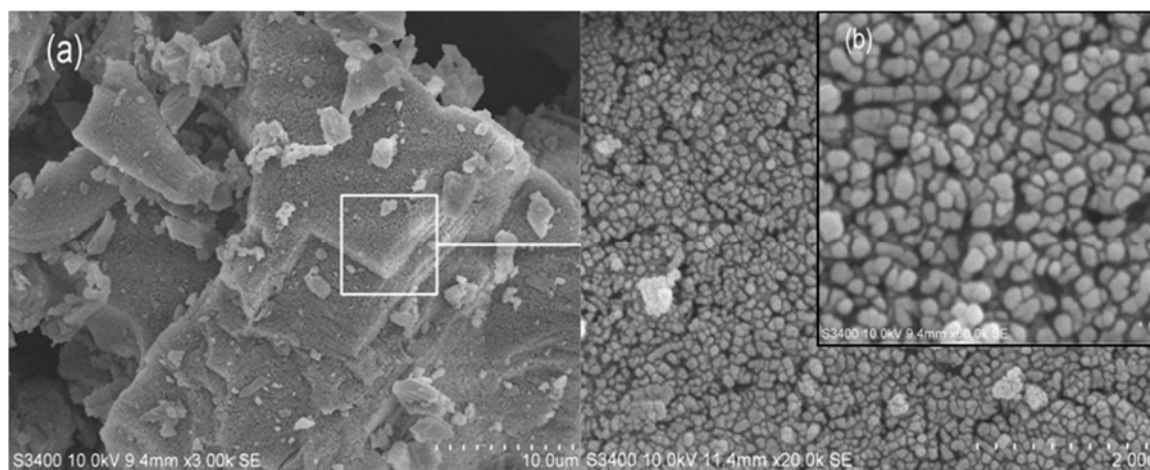


Figure 4-25: SEM micrographs of charred dolomite

The layered structure of dolomite is based on the calcite structure. The calcite group structure is layered with alternating carbonate layers and metal ion layers as shown in Figure 4-26. These layers start to delaminate when they dispersed in water and create a positively charged suspension. When dolomite disperses in GO aqueous solution, a strong exothermic reaction occurs, which is as a result of the interaction between negatively charged graphene oxide and positively charged dolomite in water media. This reaction might be the reason for the hierarchical morphology as shown in Figure 4-27.

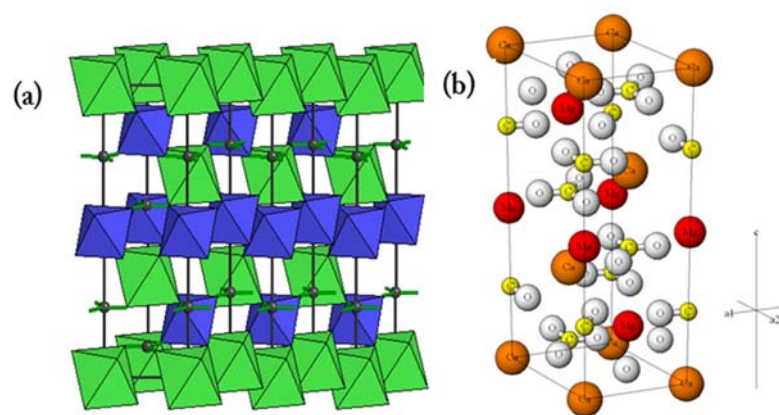


Figure 4-26: Dolomite trigonal crystal structure (a), atom's position in each unit cell

In the proposed mechanism in this research, the electrostatic interactions between negative GO and positive layers of carbonate encourages the nucleation and growth of dissolved $\text{Ca}(\text{OH})_2$ into a pillar hollow structure based on the orientation of the adjacent GO sheets. GO sheets can be seen on the surface of the pillars and between the routes of the flower like structure. Another interesting morphology in this composite is the open structure of the pillars or open cap pillar which will be investigated further with BET analysis. This type of morphology possibly is the reason for the extraordinary adsorption capacity of the dolomite/GO composite compared to bare dolomite. In order to investigate the crystal structure of this new morphology and determine if it exhibits different crystalline structure compared to bare dolomite, samples were analysed using X-ray diffraction (XRD) and the resultant scans are presented in Figure 4-28.

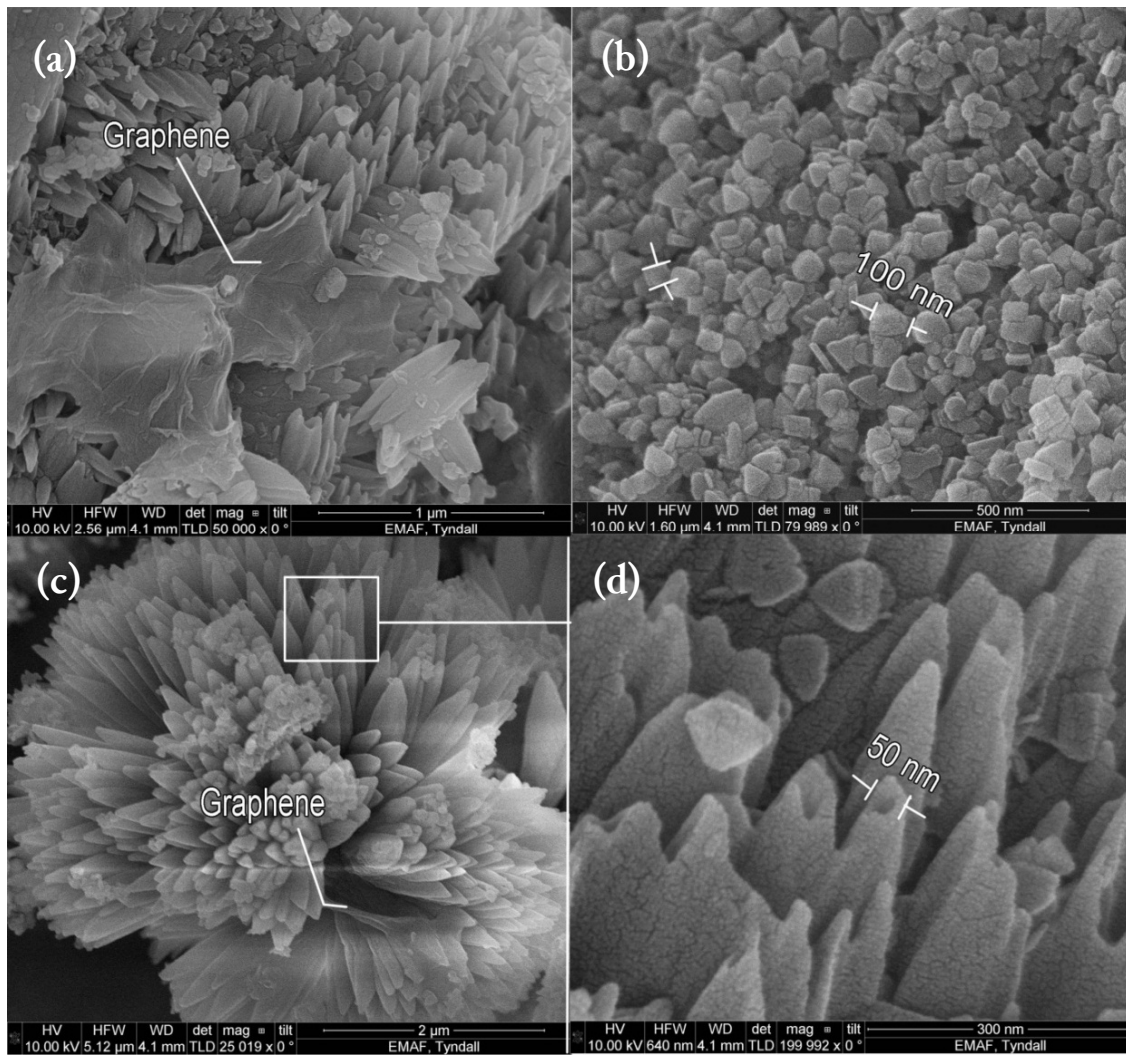


Figure 4-27: SEM images of Graphene oxide/dolomite composite. Graphene oxide covers dolomite partially (a), high magnification of dolomite surface showing granular morphology of dolomite (b), dolomite recrystallized flower-like morphology (c) and in higher magnification (d)

The XRD scan of bare dolomite suggests that the main components of the both samples are calcite (CaCO_3 strong peak at $2\theta=29^\circ$ and small peaks at 39° and 49°), magnesium oxide ($2\theta=36^\circ$ and 43°) which shows similar patterns in both samples. The other similar feature is related to the calcium oxide that rehydrates into calcium hydroxide once removed from the furnace in contact with the moisture in the air at 23° and 47° . Although both samples follow the same trend, the dolomite/GO composite shows more features related to the Ca(OH)_2 at 34° , 51° , 18° and 19° that is possibly related to the acidic nature of the GO solution which caused dissociation of calcite into calcium hydroxide. This is confirmed by the drop in calcite peak intensity at 29° and the increase of calcium hydroxide peaks compared to the similar peaks in dolomite sample.

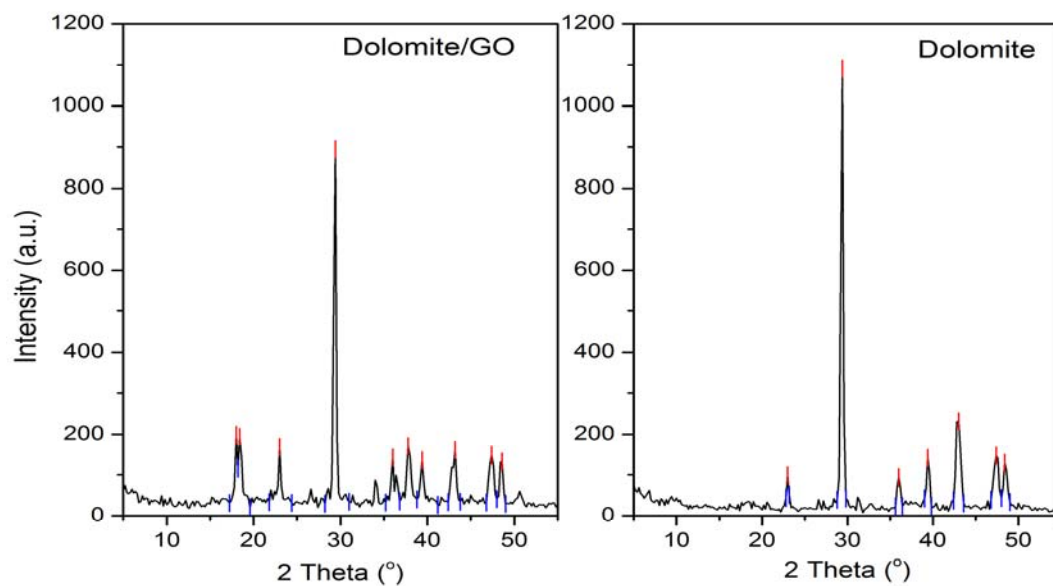


Figure 4-28: XRD spectra of bare dolomite and Dolomite/ graphene oxide composite

According to the XRD spectra, the needle like structure could be related to the formation of $\text{Ca}(\text{OH})_2$ in the solution. In order to investigate the effect of this new structure on the surface area of the composite, N_2 adsorption isotherm was used to obtain more information about the surface, pore size and pore volume of the dolomite and dolomite/GO composite. The isotherm is shown in Figure 4-29. The sample presented the isotherm type III which shows weak interaction between adsorbent and adsorbate without large meso-pores available in the structure. The BET model was used to measure the surface area and the BJH model to study pore size. The results are listed in Table 4-5.

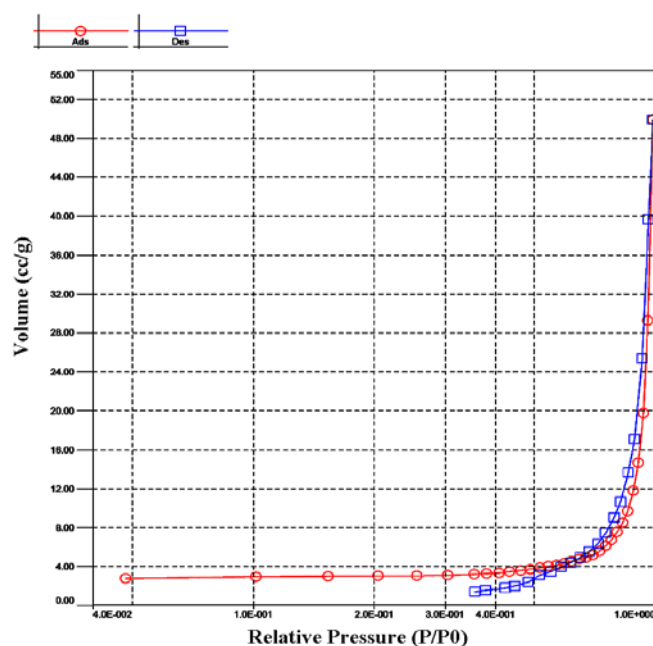


Figure 4-29: N_2 adsorption isotherm of Dolomite/GO composite

Table 4-5: Surface area and porosity of Dolomite/GO and dolomite composite

Sample	BET surface area	Total pore volume	Average pore Radius
Dolomite/GO	8.97 m ² /g	0.07 cc/g	17.3 nm
Dolomite	6.21 m ² /g	0.04 cc/g	63.3 nm

These results indicate that the rise in specific surface area of the composite is not significant when compared to the bare dolomite; however the average pore radius of the composite dramatically decreased from 63.3 to 17.3 nm which could be as a result of the small pores on the top of pillars observed in SEM images in Figure 4-27 and covering some of large pores by GO sheets. This possibly increases the pore volume of the composite from 0.04 to 0.07 cc/g. In conclusion on reviewing the data from XRD and BET it was found that the observed hierarchical morphology does not imply significant difference on the structure and porosity of the material compared to the bare substrate. Therefore the extraordinary adsorption of the composite towards dyes could be as a result of interaction with GO intercalated in the lamellar structure of the dolomite.

4.3.2. Adsorption Studies

Adsorption experiments were carried out for MB dye via column studies and batch studies, after which the most efficient adsorbents were selected for adsorption of pharmaceuticals in a series of batch adsorption experiments. These experiments were described in more detail in Chapter 3.

4.3.2.1. Fixed bed column studies

Methylene blue solution with an initial concentration of 30 mg/L was filtered through syringes containing compact adsorbents to evaluate the ability of fast removal of pollutants by adsorbents. The effect of the number of cycles of the solution through column is illustrated in Figure 4-30. The data show that the dye concentration decreases with increasing the number of cycles indicating that dye removal is not completely successful after the first cycle. However for all of the adsorbents the first filtration is the most efficient and after that the adsorption rate decreases. It also clearly indicates that all of the GO integrated adsorbents are more efficient than their bare substrate. Among all the filters dolomite/GO shows promising adsorption and it removes almost 100% of MB after the first filtration. Considering the characteristic of MB which is a cationic dye and negative charges on GO as a result of various functional groups like carboxyl at the edge planes, epoxy, and hydroxyl groups in the basal plane of graphene sheets, the electrostatic interaction plays an important role in adsorption of MB. The increase in

negative charges on GO may increase the adsorption efficiency of MB which is a positively charged dye molecule. According to the literature the zeta potential of graphene and graphene oxide shows that they stay negatively charged between the pH range 2-11^{157,320}. However with the increase in the pH of GO containing solutions the negative charge associated with GO increases thereby increasing the extent of adsorption of cationic dye from the solution phase is expected. Measuring the pH of the effluents confirm the hypothesis of the relation between adsorption extent and pH. The pH of the dolomite/GO adsorbent was between 11 and 12 which favours the negative charge accumulation on the GO surface. However the pH of the silica/GO and silica was 3.67 and 4.68 respectively which is in contradiction with the high adsorption efficiency of the composite. This can be related to the porous nature of the silicon and the high adsorption ability of silica on its own and is not related to the GO coating since there is no significant difference between GO coated silica and bare silica. Although the silica/GO exhibited considerable adsorption ability, the GO coating did not present the strong bonding with the silica surface and leached out to the solution which can be as a result of affinity of silica to adsorb water rather than another compound. Hence silica/GO was not considered for any further investigation.

Despite the fact that there are less functional groups on the surface of HrGO compared to GO, it showed a higher adsorption rate. Measuring the pH of the both solutions confirmed that rGO has the higher pH which can be responsible for the higher adsorption efficiency. The porous glass and GO/glass showed poor adsorption that could be related to the large size of beads that encouraged channelling of water among the beads instead of having contact with the surface features. In summary the data suggested a rapid removal rate higher than 80% for dolomite, dolomite/GO and rGO within the first filtration experiment and dolomite/GO adsorbent showed promising application toward the adsorption of MB. In order to find out the capacity of the adsorbents by time and number of cycles, syringes were used 6 times in separate experiments and the concentration of MB in the filtrate was measured.

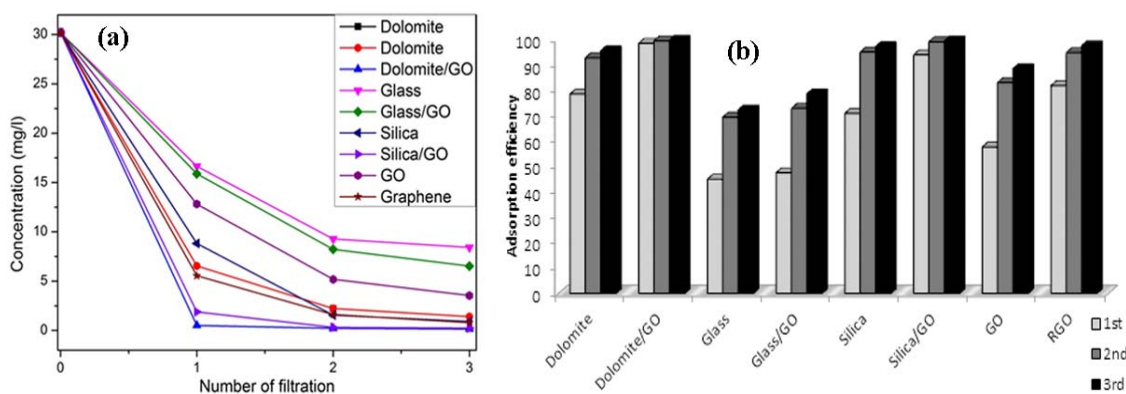


Figure 4-30: Concentration of MB solution after 3rd filtration (a), removal efficiency of filters (b)

As illustrated in Figure 4-31 the adsorption efficiency of all adsorbents except dolomite/GO decreased by repeating the number of filtrations. This reduction could be as a result of the saturation of the MB on the surface of adsorbents. However the considerable difference in GO and HrGO could not be explained by saturation or the difference in electrostatic charges on the adsorbent surface only. The agglomeration of the GO during the experiments to form a compact film which is not accessible for the dye molecules, was recognised as the reason of this decrease. Reaching a constant efficiency value after the second run is another proof for this conclusion.

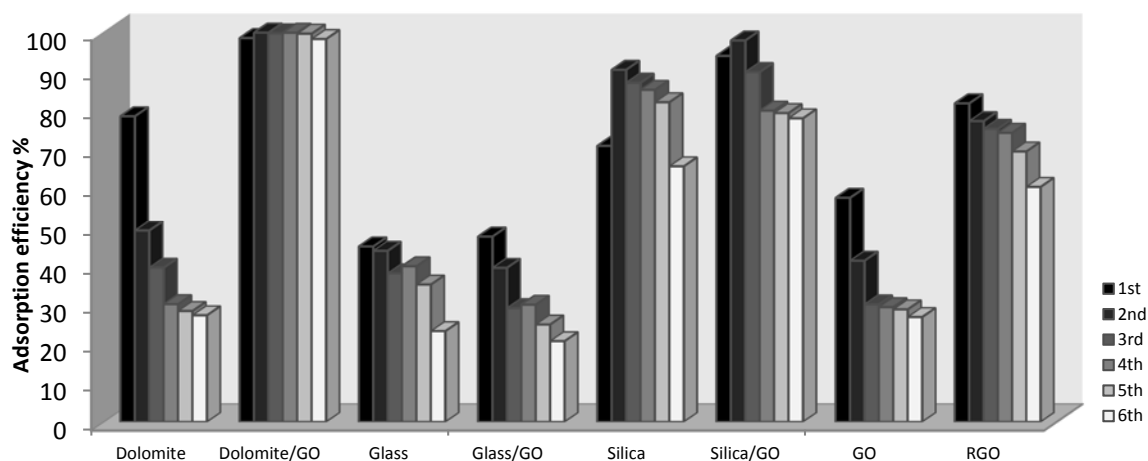


Figure 4-31: Adsorption efficiency of different GO integrated adsorbents within six adsorption experiments

Comparing the adsorption data of bare dolomite and dolomite/GO confirmed that the high adsorption capacity of the composite is not related to the dolomite substrate since it has shown a dramatic decline after the first adsorption run. In contrast, dolomite/GO offers almost 100% of adsorption at the first run which stayed constant even after using it over time. The image shown in Figure 4-32 visually shows the difference in adsorption efficiency of the bare

dolomite and the GO coated dolomite in the first and sixth filtrations. After the first filtration cycle, dolomite/GO filtrate is quite clear compared to the filtrate of the dolomite. In addition after six cycles the adsorption ability of the dolomite decreased while the filtrate of the dolomite/GO is still quite clear.

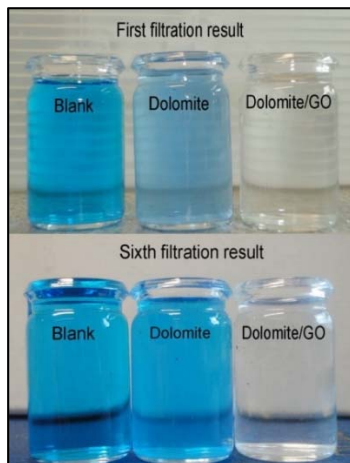


Figure 4-32: MB solution after first and sixth filtration through dolomite and dolomite/GO adsorbents

In conclusion, dolomite/GO was introduced as a promising adsorbent for the removal of a cationic dye. It offers some advantages such as high adsorption capacity, fast adsorption process, easy recovery compared to pure GO and rGO and low cost as the main body of the adsorbent composed of dolomite which is cheap and abundant mineral. The adsorption ability of this material towards the different types of pollutants will be investigated further.

4.3.2.2. Batch adsorption experiments

4.3.2.2.1. Methylene blue adsorption

The result of 1 hour MB batch adsorption experiments using 0.2 g of different GO integrated adsorbents is shown in Figure 4-33. It can be seen that dolomite/GO, rGO and GO have the highest amount of adsorption from all the adsorbents. Also the difference in the amount of adsorption by dolomite with dolomite/GO is evident. Therefore the high adsorption efficiency of the dolomite/GO is more related to the integration with GO since bare dolomite offered less than 10 mg/g compared to 40 mg/g for the dolomite/GO adsorbent. However this is not the highest capacity of the adsorbent because the volume of the solution was limited and the time of adsorption was short. In order to study the effect of contact time on adsorption a new set of experiments for GO, RGO and dolomite/GO were conducted. The results indicate almost no time dependency of GO and RGO samples as the adsorption takes place on their

surface instantly and no considerable decrease in the concentration was observed for samples taken after 1 and 6 hours contact time. In contrast, the adsorption equilibrium for dolomite/GO was achieved after 3 hours contact (Figure 4-35). When this adsorption equilibrium time for GO and dolomite/GO at three hours is compared with the performance of commercial activated carbon which varies between 8 hours to one day, depending on the type and level of the pollution, it can be seen that this new material is a fast and efficient adsorbent for dye removal from industrial effluents^{330,331}. The GO foam and rGO powder offered the highest amount of adsorption at around 50 mg/g of adsorbent compared to dolomite/GO with 40 mg/g amount of adsorption. However these results do not illustrate the maximum capacity of the adsorbents. Based on a new experiment which offers a regular addition of MB solution to the adsorption batch, the adsorption capacity of 1128 mg/g, 978 mg/g and 232 mg/g was measured for GO, HrGO and dolomite/GO respectively (Figure 4-36). These results show the very large capacity of GO and GO integrated composite for dye adsorption when compared to activated carbon with the adsorption capacity of 500 mg/g³³².

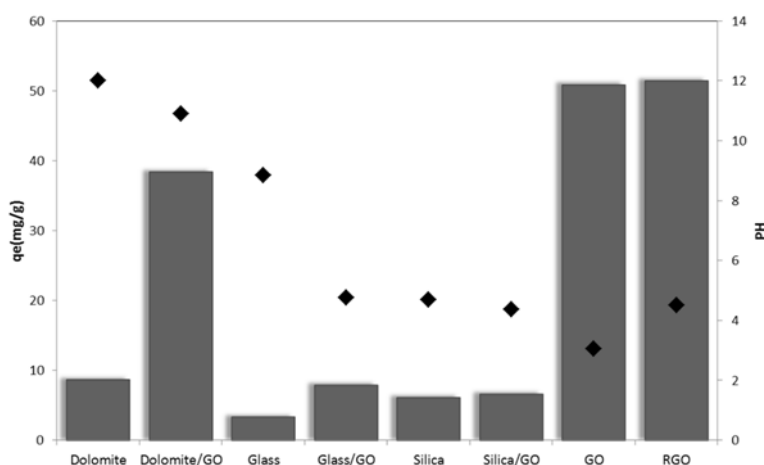


Figure 4-33: The amount of adsorption (bars) and pH (black dots) for GO integrated adsorbents

Figure 4-34 also indicates the high removal rate of GO, HrGO (indicated with RGO) and dolomite/GO adsorbent since the concentration of MB declines to less than 1 mg/L after one hour. In another words GO, HrGO and dolomite/GO have very high removal efficiencies and they reach 99.4%, 98.4% and 80.2% removal after the first hour of adsorption respectively. The q value for GO and HrGO is similar as depicted in Figure 4-33, however Figure 4-36 shows about 150 mg/g difference between the two q values. The difference in q value for GO and HrGO might be related to the difference in pH of the solution since the pH of GO and HrGO solutions are 3.04 and 4.5 respectively in the first experiment. Hence in order to exclude the effect of pH in the second experiment, the pH of both solutions was adjusted to 5 by adding 4 molar NaOH solution. As a result the two different q values (1128 mg/g and 978 mg/g for GO

and HrGO) were obtained which can be purely related to the differences in chemical and physical properties of nano-sheets. However it is strongly believed that the differences between the q values is more related to the configuration of the columns and size and shape of adsorbents which determines the contact efficiency between adsorbent and adsorbate.

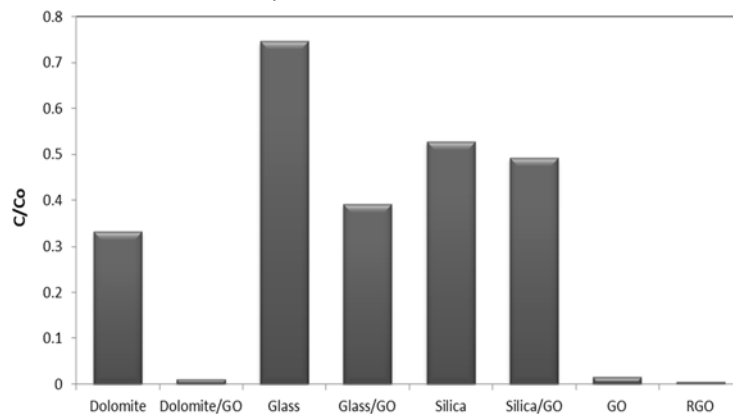


Figure 4-34: Final concentration of MB in solutions containing GO integrated adsorbents

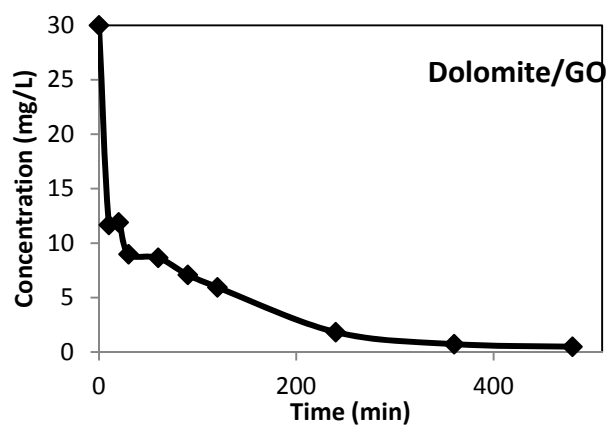


Figure 4-35: The variation of the concentration versus time for dolomite/GO composite

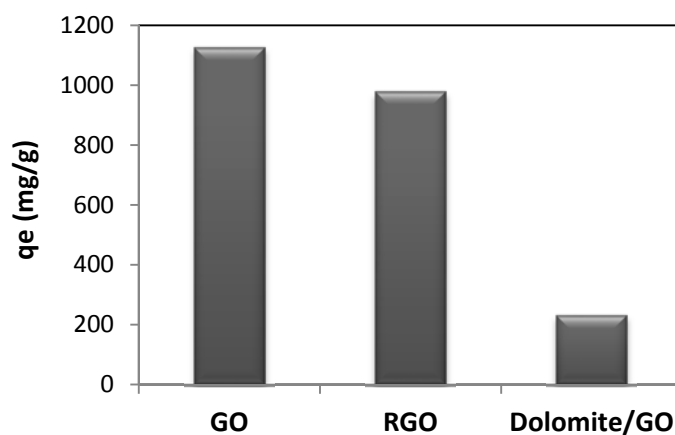


Figure 4-36: Maximum adsorption capacity of MB for GO, rGO and dolomite/GO

Effect of pH

The pH of a solution is an important parameter affecting the adsorption process. A change in the pH alters the charge profile of adsorbate species which consequently influences their interactions with the adsorbent. The effect of pH on the adsorption of MB onto GO sponge was investigated in pH range from 1-12 (Figure 4-37). The top photo shows the GO sponge after mixing with the MB solution and the bottom photo shows the filtrate after removing the GO. The results show that the adsorption of MB onto GO is not drastically influenced by the pH of the solution, but is instead, related to the large negative zeta potential of GO in pH wide pH range³²⁰. The negatively charged surfaces can enhance the adsorption properties of the positively charged MB cations by the adsorbents through electrostatic forces of attraction. However further investigation of dolomite/GO, rGO and GO indicate that the adsorption by graphene integrated adsorbents is not affected by pH significantly.



Figure 4-37: GO mixed with 100 mg/L of MB at different pHs (top photo) and MB solution after removing GO comparing with the blank MB (left side of bottom photo)

As depicted in Figure 4-38 a similar trend was observed for dolomite/GO composite and increasing the pH did not change the adsorption significantly.



Figure 4-38: effect of pH on adsorption of MB on dolomite/GO adsorbent

Effect of initial concentration

Another important parameter that can affect the adsorption is the initial concentration of the adsorbate. This is important because the adsorption efficiency of the most common adsorbents declines at very high or very low pollutant concentration. However because of the high adsorption uptake of GO integrated adsorbent no significant efficiency was observed at various range of concentrations which is an advantage for GO based adsorbents for dye removal. Figure 4-39 shows that the final concentration is independent of the initial concentration of MB.

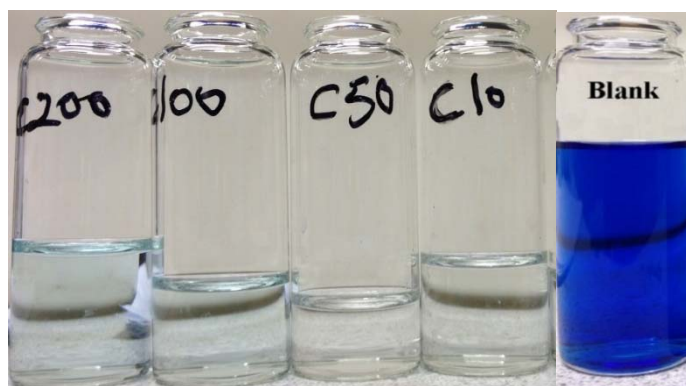


Figure 4-39: The effect of initial concentration of MB on the final concentration

The outstanding adsorption properties of GO towards MB can be due to the availability of a large surface area caused by its unique single atom layered structure. Another reason for the high adsorption capacity of MB onto GO integrated adsorbents can be attributed to π - π electron donor acceptor interactions with graphene surfaces. MB has C=C double bonds and contains π electrons. These π electrons can easily interact with the π electrons of benzene rings on GO surfaces through π - π electron coupling²⁹⁸. On the other hand, MB is a cationic dye and will exist as positively charged ions in aqueous solution. In contrast GO and rGO are negatively charged in a wide range of pHs. Therefore, the electrostatic attraction also plays a key role for MB adsorbed by GO integrated adsorbents. However the effect of oxygen containing functional groups on the basal plane of GO and rGO could not be ignored. In order to examine the possibility of functional group involvement in the adsorption process, an adsorption experiment with rGO and commercial graphene was carried out (Figure 4-40). The result was significant since the commercial graphene did not show significant adsorption of MB. Based on FTIR studies this can be related to the absence of functional groups and defects on the basal plane of pure defect free commercial graphene. Another reason for low adsorption ability of commercial graphene can be as a result of graphitic structure and not having graphene as it

proved by Raman spectroscopy shown in Figure 4-22. Therefore it can be concluded that along with the π - π interactions and electrostatic attraction, functional groups and defects on the surface of GO and rGO play a crucial role on the adsorption properties of GO.

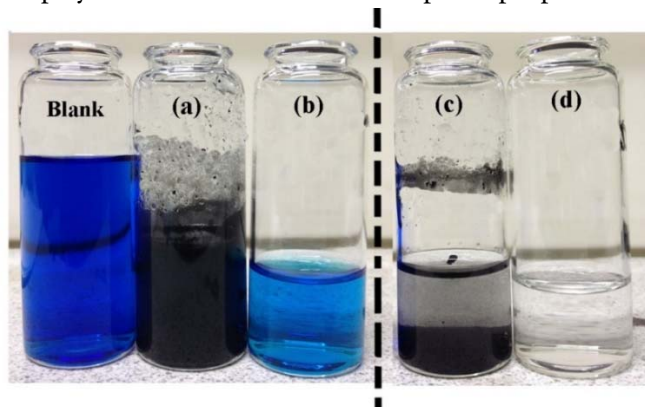


Figure 4-40: Adsorption of MB by commercial graphene (a mixture and b infiltrate) comparing with the chemically reduced graphene oxide (a mixture and d infiltrate)

4.3.3. Batch adsorption experiments of pharmaceuticals

4.3.3.1. Diclofenac and Carbamazepine adsorption

Graphene oxide showed a high affinity towards diclofenac since 100% adsorption of diclofenac was observed after 30 min of stirring. According to the calculations based on the weight of GO (0.002 g), the concentration of diclofenac (100 mg/L) and the volume of the solution (10 ml), the total amount of adsorption was obtained around 5000 mg/g which is the highest capacity of any adsorbent and adsorbate reported to date. In addition to the massive adsorption capacity of GO towards diclofenac, reaching the adsorption equilibrium rapidly in less than 30 min is another outstanding adoption properties of GO. In order to study the effect of pH and initial concentration of diclofenac, a series of experiments were conducted. However because of the fast adsorption of 100% of diclofenac, no comparable data was achieved since all of them demonstrated zero mg/L at the final concentrations. According to the chemistry and structure of diclofenac it can be related to the benzene ring and hydroxylic and carboxylic groups of the molecule Figure 4-41.

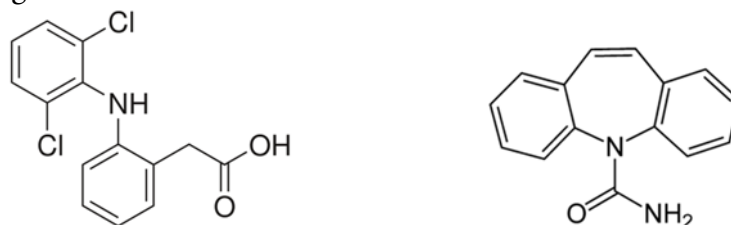


Figure 4-41: Molecular structure of Diclofenac (right) and carbamazepine (left)

A similar trend was also observed for carbamazepine. At GO concentrations higher than 0.05 g/L no comparable data was obtained and for 0.0015 g/L of GO more that 40% of carbamazepine was adsorbed instantly and 100% was adsorbed after 30 min of adsorption (Figure 4-42).

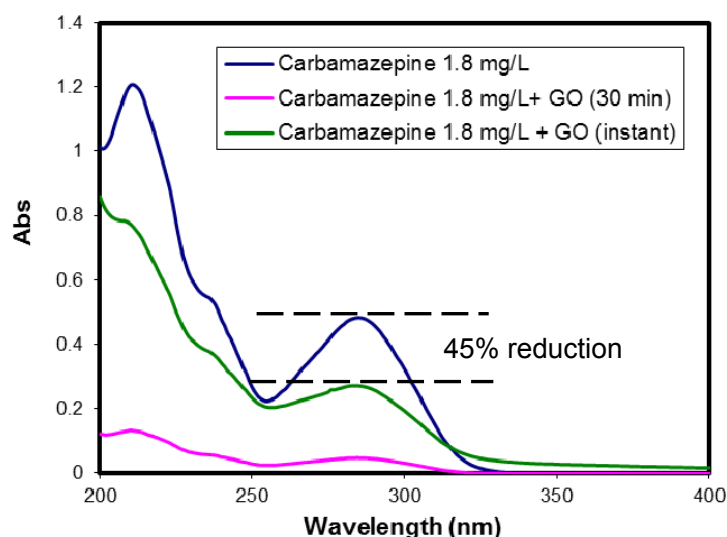


Figure 4-42: UV-Vis absorption spectra of carbamazepine adsorption by GO

4.4. Adsorption Kinetic study

4.4.1. Pharmaceutical adsorption by GO

Adsorption kinetics of diclofenac and famotidine were investigated in order to understand the mechanism of adsorption, evaluate the maximum amount of adsorption and determine the optimum equilibration time. The concentration of remaining Fa and Di (C_t) versus time (t) and the effect of contact time on the amount of adsorption (q_t) are plotted in Figure 4-43 (a,b). As stated in the graph the concentration of GO is very small (0.025 g.L^{-1}) however it has removed 15% of Fa and 35% of Di in less than 30 min. Based on the plot of q_t versus t (Figure 4-43b) the adsorption capacity of GO increased quickly in the first 30 min and then rose slowly until the adsorption equilibrium was reached within 4 h. On the basis of the above result, a contact time of 1 h was selected as an adsorption equilibrium in further adsorption studies. Two conventional kinetic models (pseudo-first-order and pseudo-second-order) were applied to analyse the experimental data and calculate the adsorption constants.

The pseudo-first-order model can be expressed as:

$$\ln(q_e - q_t) = \ln q_e - k_1 t \quad \text{Equation 4-3}$$

where q_e and q_t are the amount of adsorption at equilibration time and various time respectively and k_1 is the adsorption rate constant (1/h) based on this model. The values of q_e and k_1 were calculated from the intercept and slope of the linear plot of $\ln(q_e - q_t)$ versus t . The pseudo-second-order model which is more accurate and detailed model can be described as

$$\frac{t}{q_t} = \frac{1}{k_2 q_e^2} + \frac{t}{q_e} \quad \text{Equation 4-4}$$

where k_2 is the rate constant of the pseudo-second-order model of adsorption ($\text{g.mg}^{-1}.\text{h}^{-1}$). The q_e and K_2 constants were calculated from the slope and intercept of the linear plot of t/q_t against t . The kinetic parameters and coefficients for the diclofenac by graphene are summarized in Table 4-6. According to the R squared (R^2) value the data is fit with the pseudo-second-order model exceeded with the R^2 value of above 0.99. In addition, the calculated amount of adsorption based on the pseudo-second-order model ($q_{e,\text{cal}}$) is very close to the experimental adsorption capacity ($q_{e,\text{exp}}$) reported for the both pharmaceutical. So these results showed that the adsorption kinetic of pharmaceutical on GO can be described with the pseudo-second-order kinetic model with a fast adsorption equilibrium rate.

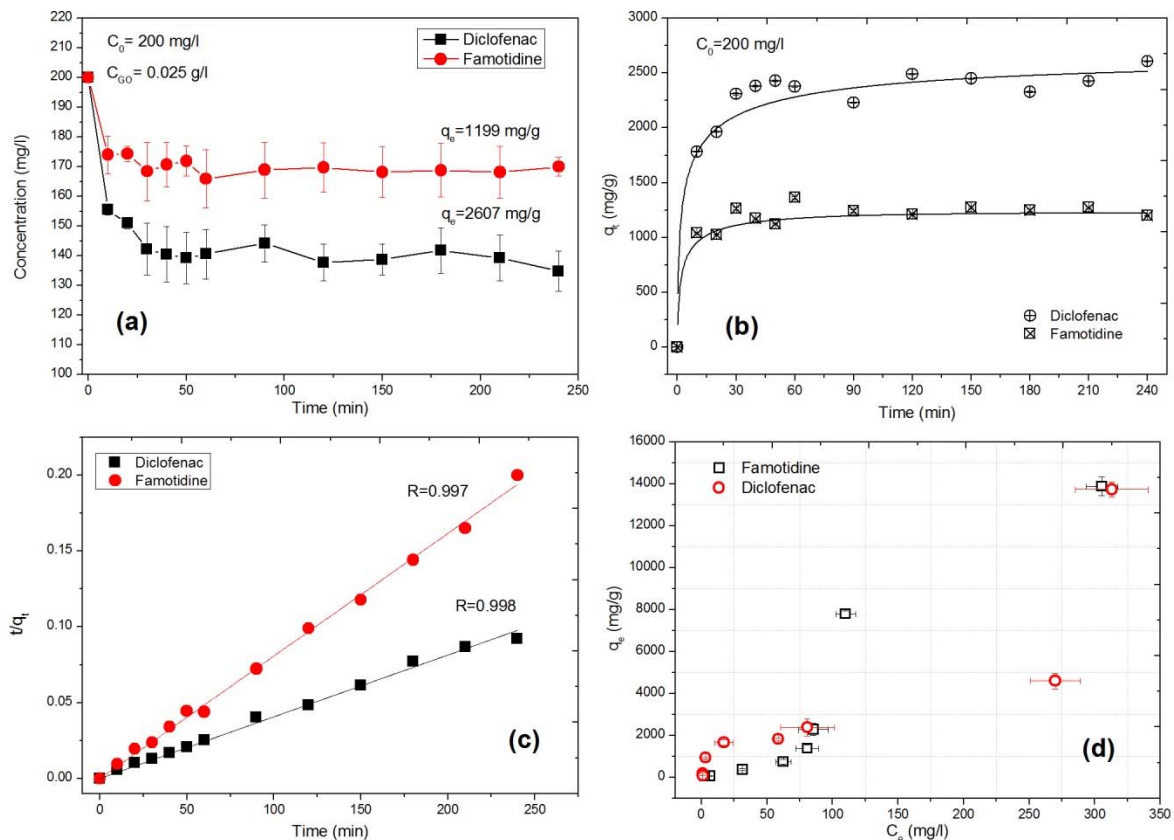
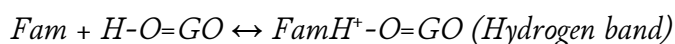
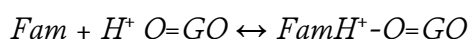
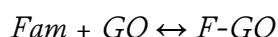
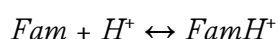


Figure 4-43: Concentration versus time (a), adsorption capacity versus time (b), pseudo-second-order kinetic fit (c) and the adsorption isotherm for diclofenac and famotidine

Table 4-6: Kinetic Parameters for the Adsorption of diclofenac and famotidine by GO

Model	pseudo-first-order				pseudo-second-order		
Parameter	$q_{e,exp}$ ($mg \cdot g^{-1}$)	k_1 (1/h)	$q_{e,cal}$ ($mg \cdot g^{-1}$)	R^2	k_2 ($g \cdot mg^{-1} \cdot h^{-1}$)	$q_{e,cal}$ ($mg \cdot g^{-1}$)	R^2
Diclofenac	2607	0.45	595.5	0.50	0.0048	2538	0.998
Famotidine	1199	0.89	281.3	0.31	0.0007	1246	0.997

The pH of a solution is one of the most important parameters affecting the adsorption process by changing the net charge of the adsorbent and adsorbate in the solution. A change in the pH alters the charge profile of adsorbate species and adsorbent which consequently influences their mutual interactions. Figure 4-44a shows the effect of initial pH ranging from 2 to 11 on the adsorption capacity and removal of diclofenac and famotidine by GO sponge. For diclofenac the adsorption decreased slightly from 100% removal to 80% and adsorption amount reduced from around $2000 \text{ mg} \cdot \text{g}^{-1}$ to $1600 \text{ mg} \cdot \text{g}^{-1}$ under investigated pH range. The adsorption of famotidine rapidly decreased over pH 2.0–6.0, stayed constant over pH 6.0–8.0 and rapidly increased to the adsorption capacity in acidic range over the basic conditions (pH > 6.0). So clearly the adsorption of famotidine is the lowest at the neutral pH and with receding from the neutral region the amount of adsorption is acceding quickly. At the acidic pH, GO possess the highest amount of negative charge (–44 mV) which decreases with increasing the pH up to natural pH around 6, leading to the decrease in amount of adsorption of famotidine. In the other side, pH dependant dissociation (pKa) of famotidine can affect the adsorption through the interaction of negatively charged GO and positively charged dissociated famotidine.



The transition of Fam to FamH⁺ is dependent on pH, with a maximum amount of FamH⁺ occurring at low pH (pH_i ≤ 4), which results in the highest adsorption of FamH⁺ onto the negatively charged surface of the GO. With increasing the pH (pH_i ≥ 4), the Fam molecules are neutral in charge however the surface charge of GO also decreasing. So the observed increasing in the amount of adsorption could not be interpreted by the electrostatic interaction. It has been observed that in pH ≥ 8.5 the GO sheets dispersed in water become unstable and create a netlike structure and settle down in the flask. Therefore we propose that the adsorption is promoted by a process similar to flocculation. In this process famotidine molecules which has been located between sheets through physical interaction or by hydrogen bonding between

hydroxyl group of GO and N-H groups of famotidine were trapped. Therefore GO has the minimum affinity to famotidine at $6 \leq \text{pH} \leq 8$ and the maximum adsorption were observed at the highly acidic pH when GO has the highest amount of negative charges and famotidine has the highest amount of positive charges due to the dissociation.

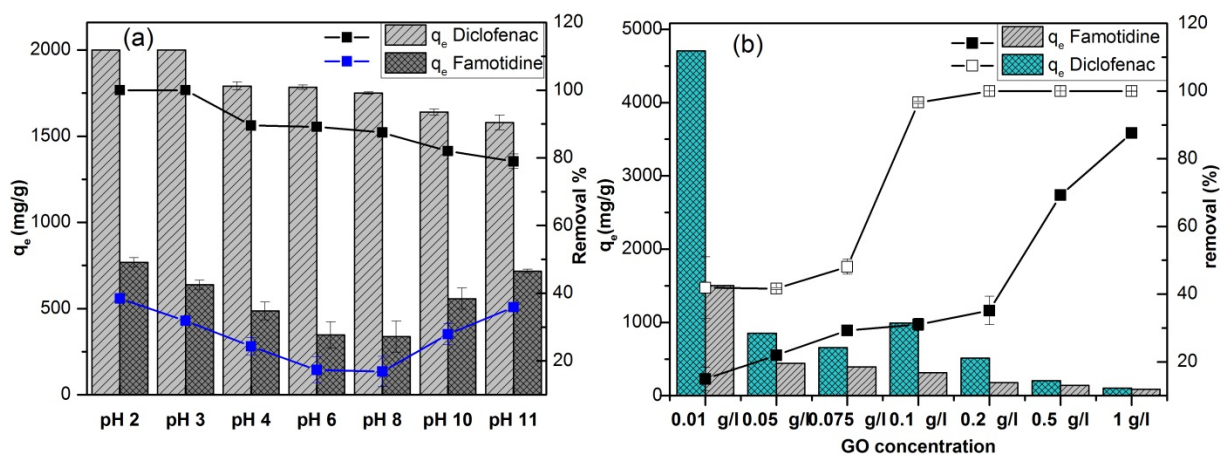


Figure 4-44: effect of pH (a) and adsorbent concentration (b) on amount of adsorption (q_e) and the removal efficiency

However as shown in Figure 4-44a, adsorption of diclofenac on GO is not highly pH dependant from pH 4.0–11.0. However the maximum amount of diclofenac adsorption of about 2000 mg.g^{-1} for diclofenac was observed at acidic pH. Diclofenac sodium salt dissolves in water and creates the molecule shown in Figure 4-45 which is protonated at acidic pH. The protonation reduces the amount of repulsive electrostatic forces between negatively charged GO and dissociated diclofenac which results in the more π - π interaction between the aromatic groups of diclofenac and benzene ring of GO and therefore the higher amount of adsorption. With increasing the pH, the amount of protons adsorbed by diclofenac is reducing which increases the negative charge of the adsorbate.

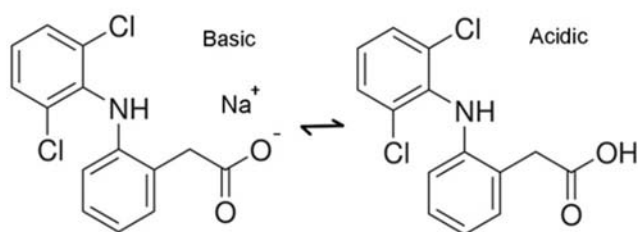


Figure 4-45: The structure of dissolved diclofenac and the adsorption mechanism on GO

As a result of the repulsive interaction of both negatively charge GO and diclofenac the amount of adsorption is reduced. However this reduction is not very significant because on the

other side the negative charge of GO is decreasing due to the pH increase which reduced the amount of adsorption drop. This value of adsorption has not reported so far for any type of adsorbent. Therefore more investigation had been conducted to identify different aspects of the adsorption phenomena occurring on the surface of GO adsorbent which is discussed in next section. Figure 4-44b also confirms the extraordinary adsorption of diclofenac by GO which is about 4500 mg.g^{-1} at lowest concentration of adsorbent. As expected with the same initial concentration of adsorbate, the amount of adsorption is decreasing with the increase of adsorbent concentration. This graph shows that the removal of famotidine had not been completed and even at high concentration of GO, the maximum adsorption of 87% had achieved. However for diclofenac the 100% removal has been achieved at GO concentration of 0.1 g.L^{-1} and the maximum adsorption capacity of 4600 mg.g^{-1} is obtained at the GO concentration of 0.01 g.L^{-1} . This data also confirmed the difference between the mechanism of diclofenac adsorption by GO.

In order to visually observe the difference between adsorption of pharmaceuticals with difference chemical functionality, the adsorption of diclofenac, famotidine and solifenacin with the initial concentration of 200 mg.L^{-1} were conducted with the GO concentrations ranging from 0.1 to about 1 g.L^{-1} . As shown in Figure 4-47 using 0.1 g.L^{-1} of GO considerably reduced the concentration of diclofenac in supernatant (60 % removal) which exhibit nearly 1000 mg.g^{-1} of adsorption capacity. However only 10% of famotidine and 25% of solifenacin were adsorbed by 0.1 g.L^{-1} of GO. To determine the minimum GO adsorbent that can completely remove the three pollutant, the amount of GO were increased gradually to 1 g.L^{-1} but even at the highest adsorbent concentration only 50% of famotidine is removed. Although the removal efficiency of famotidine by GO is much less than diclofenac and solifenacin however the adsorption capacity of GO is still higher than common adsorbent. For example 0.2 g of GO removed 25% of famotidine showing the amount of adsorption of about 300 mg.g^{-1} which is considerable value for the adsorption comparing most of common adsorbents.

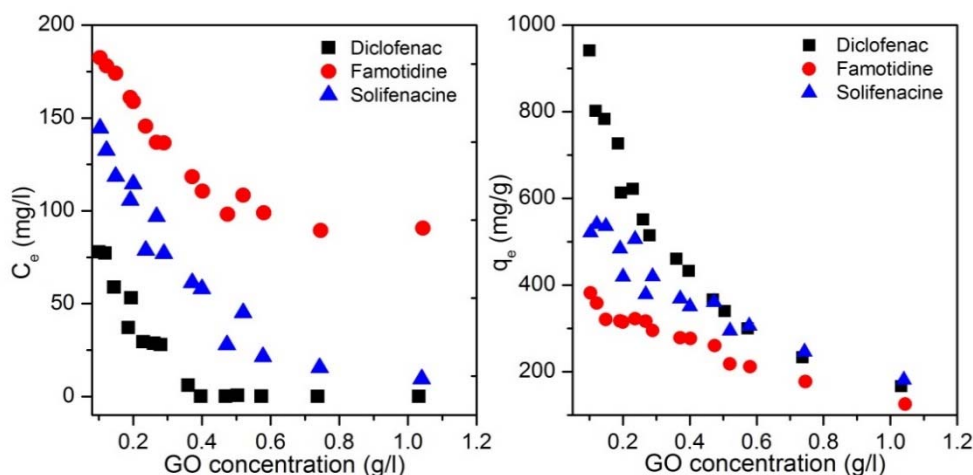


Figure 4-46: equilibrium concentration (C_e) and adsorption capacity (q_e) versus GO concentration for diclofenac, famotidine and solifenacin

4.4.2. Mechanism of adsorption

In order to study the adsorption mechanism the chemical structure of diclofenac, solifenacin and famotidine as well as the digital photo of GO behaviour in solution is illustrated in Figure 4-47. As shown diclofenac and solifenacin both have two aromatic rings which are favourable for adsorbing on the GO surface through π - π stacking. Due to the hydrophilic property of GO and 3D compact framework, the GO sponge are well dispersed in an aqueous phase and remove pollutants efficiently during mixing. While mixing GO with aqueous solution of solifenacin and famotidine the morphology of GO sponge was changed from compact lump into millimetre sized GO globular connected network structure which were precipitated and easily and quickly collected through a simple vacuum filtration or low speed centrifuge (Figure 4-47b). In pure water GO sponge will be dispersed into GO sheets and create brown homogeneous solution which is difficult to collect however in the presence of trace amount of positively charged organic molecules they tend to restack and agglomerate. This agglomeration is not observed in the presence of diclofenac even though it has two aromatic ring which is favourable for restacking of GO. The main reason for this phenomena can be related to the ionic interaction due to the acidic dissociation constant (pK_a) in experimental condition. In this experiment the pH was about 4 which is natural pH of the solution after dispersing GO in water. In this experimental pH solifenacin which is weakly basic (pK_a 8.5) and famotidine which is weakly acidic (pK_a 6.9) are mainly positively ionized (cationic). When negatively charged GO exposed to water due to the hydrophilicity, hydrogen bonding between GO functional groups with water and their repulsive electrostatic charges between sheets they start to disperse. At the same time because of the pH reduction due to GO dispersion solifenacin and famotidine ionized

and became positively charged. The interaction between negative charges of GO and positive charges of drugs neutralized the GO sheets and initiated the coagulation and agglomeration of GO sheets into particulates which will be followed by enhanced π - π stacking of GO resulting in easy post separation of adsorbent.

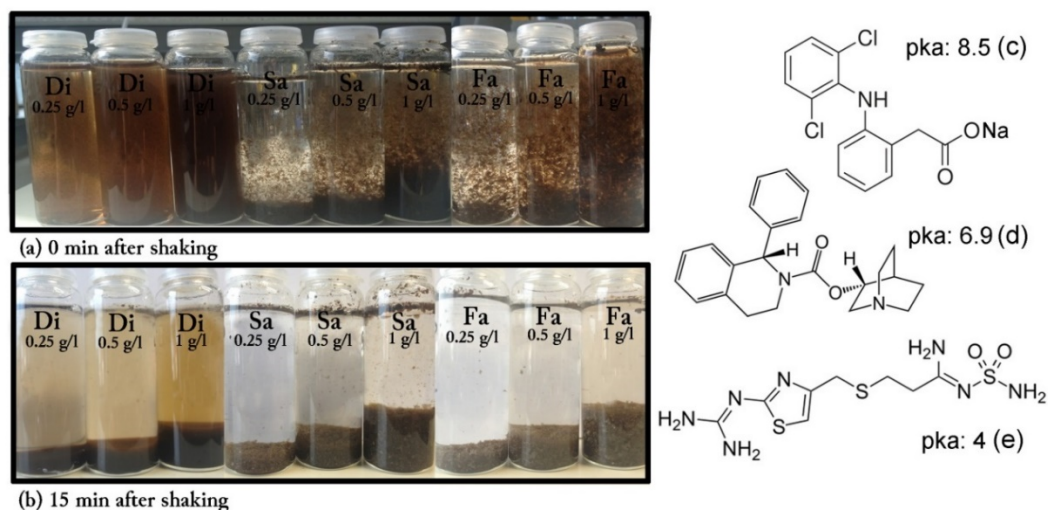


Figure 4-47: Image of three different GO concentration mixed with diclofenac, solifenacin and famotidine (a) and the mixture after settling for 15 min (b). Chemical structure of diclofenac (c), famotidine (d) and Solifenacin (e)

In summary the different maximum adsorption of famotidine and solifenacin values could be explained by the different pKa values and number of aromatic rings. The pKa values of solifenacin (pKa 8.5) which is higher than famotidine (pKa 6.9) so under the experimental condition of pH 4, the proportion of cationic form of solifenacin is higher than that of famotidine, which facilitates the adsorption. Also solifenacin has two benzene ring in the structure comparing to famotidine which enhances the adsorption through π - π interaction of these groups with the intact sp^2 areas remaining in basal plane of graphene oxide.

In contrast this explanation could not be applied to explain the extraordinary adsorption of diclofenac by GO because diclofenac sodium is a salt which dissociated in water into Na^+ and hydrated negative diclofenac molecule. The negative charges on diclofenac is not favourable for adsorption by negatively charged GO because of the electrostatic repulsion. The data obtained from measuring the zeta potential is also confirmed the increase in negative charge of the system. The GO solution in experimental condition had the potential of -36.91 mV while mixing GO with diclofenac decrease the potential down to -53.24 mV. The zeta potential data explains why the agglomeration of GO in solution was not observed. However the GO dispersion changed to a swelled gel like instead while still many GO sheets stayed stable in the top solution which made the post separation more difficult. To investigate the actual mechanism involved in

diclofenac adsorption, the GO sponge were collected by centrifuge after adsorption and were dried in vacuum oven 6 hrs, sputter coated with gold to avoid charging the samples by electron and were analysed by SEM in low voltage. As shown in Figure 4-48(a) large particles were observed on the surface of the GO also from the contrast around the wrinkles and the topography of the surface particles could be recognised under GO sheets.

Figure 4-48b in higher magnification confirmed the existence of crystals wrapped by thin layer of GO sheets. These crystals are different in size and shape with preferable growth direction towards the GO surface. In some areas of the samples they create interesting flower shape all wrapped with a transparent blanket of GO as shown in Figure 4-50c. TEM images in very low voltage and short exposure time verified that these particles are highly ordered crystalline organic material which was burning quickly under electron beam exposure. As shown in Figure 4-49 the as grown diclofenac are highly crystalline and they burn under the electron beam quickly.

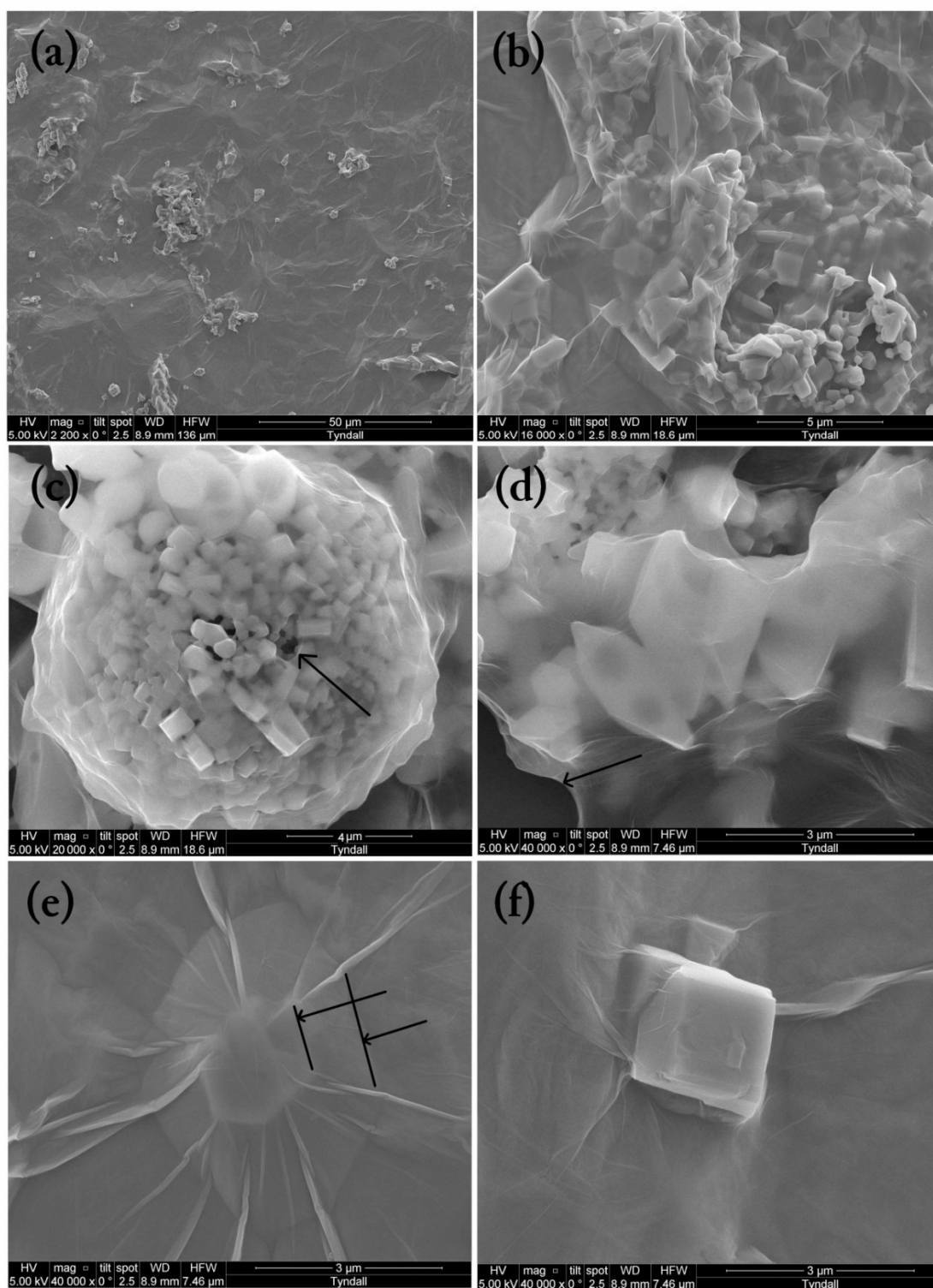


Figure 4-48: SEM images of GO sponge after adsorption of diclofenac with different magnification (a-d), growth mechanism (e,f)

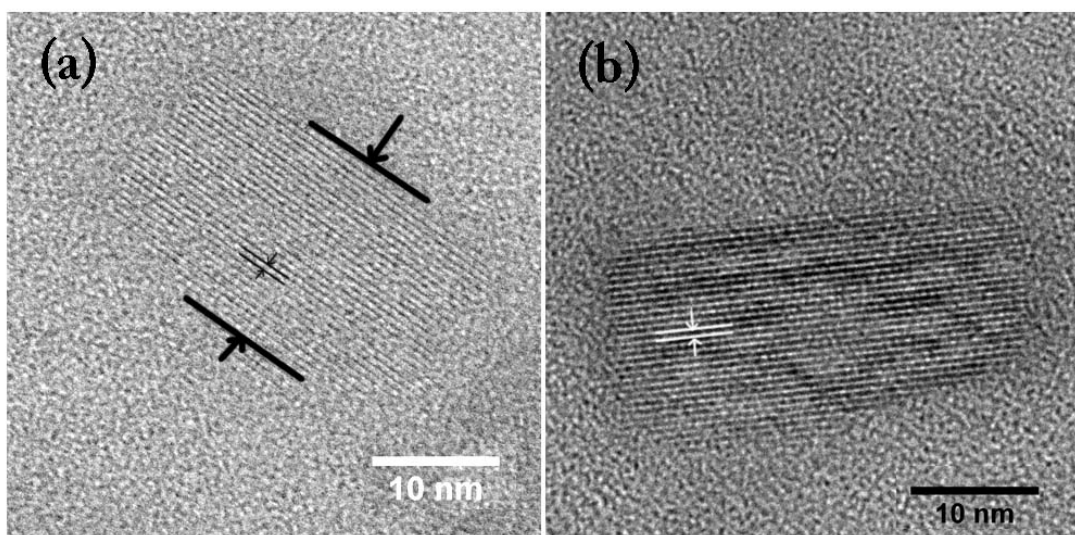


Figure 4-49: TEM images of diclofenac crystals grown on the surface of GO sheets first shot (a) and second shot after few second electron beam exposure

To confirm that the observed crystals are actually diclofenac the EDX spectra was collected in SEM chamber from two different spot on GO sponge after diclofenac adsorption (Figure 4-50). The both spectra showed highest amount of carbon and oxygen which is common in both GO and diclofenac and presence of Na, S, and Cl which are the elements of diclofenac and Au which is from the sputter coating. However the spectra 2 which was collected from the surface of a crystal shows higher amount of carbon, oxygen, sulphur and sodium due to the direct exposure to the beam.

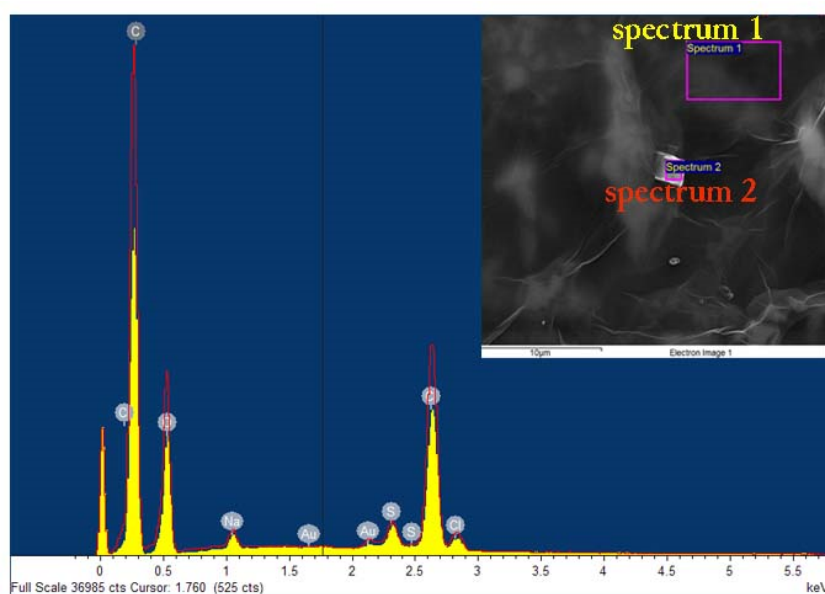


Figure 4-50: EDX spectra of GO sponge after adsorption of diclofenac

To study the size and polymorph type of as grown crystals, diclofenac with different initial concentration were prepared and certain amount of GO paper were introduced to the solution. In this case GO paper was used because they were not dispersed without shaking and ultrasonic force, therefore crystals that were formed in the solution were separable without traces of GO in their structure. The crystal formation were started immediately after introducing the film into the solution and clear solution became cloudy and white. The paper was taken out and dried for SEM analysis and crystals precipitates were collected from the bottom of beaker using filtration. According to the literature, diclofenac salts exhibit a variety of hydrates and polymorphs³³³⁻³³⁵. In particular, the crystal structure of some diclofenac salts prepared with hydroxyl amines revealed that these salts exist as ion pairs in the solid state, where the hydroxyl groups participate in a network of H-bonds, in some cases together with water molecules of crystallization, that keep anion and cation in a close association: these structural aspects suggested it would be better to define these compounds as complexes rather than simple salts. The complexity of the structures observed made it possible to preview a frequent occurrence of polymorphs among these diclofenac salts as a function of the extent of hydration and/or the nature of the crystallization solvent.

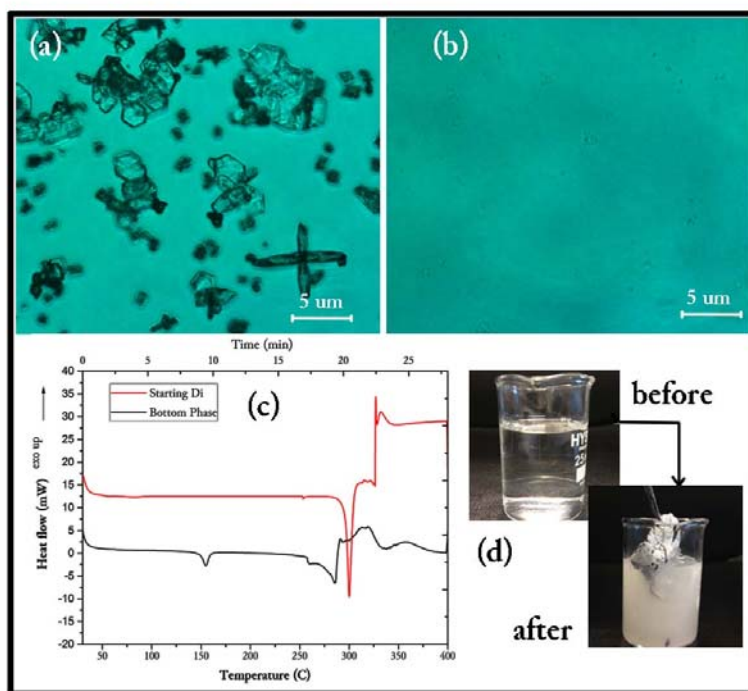


Figure 4-51: Optical microscopy image of collected diclofenac precipitate (a), and original source of diclofenac (b), DSC data of original diclofenac comparing the as grown precipitate (c), digital image of 500 mg.L⁻¹ diclofenac solution before and after introducing the GO paper

DSC results also confirms that the grown crystals are hydrate form of diclofenac as a result of contacting with water. However the driving force of this transformation is not still clear since the similar phenomena were not observed using rGO instead of GO. SO we concluded that it might be related to the acidic nature of GO and its high surface energy which make it a perfect substrate for nucleation of new crystals. Also as shown in Figure 4-51(a, b) the hydrate crystals are much larger than the original form of diclofenac powder. They also exhibit different shapes and geometry which is in accordance with the SEM images of Figure 4-48.

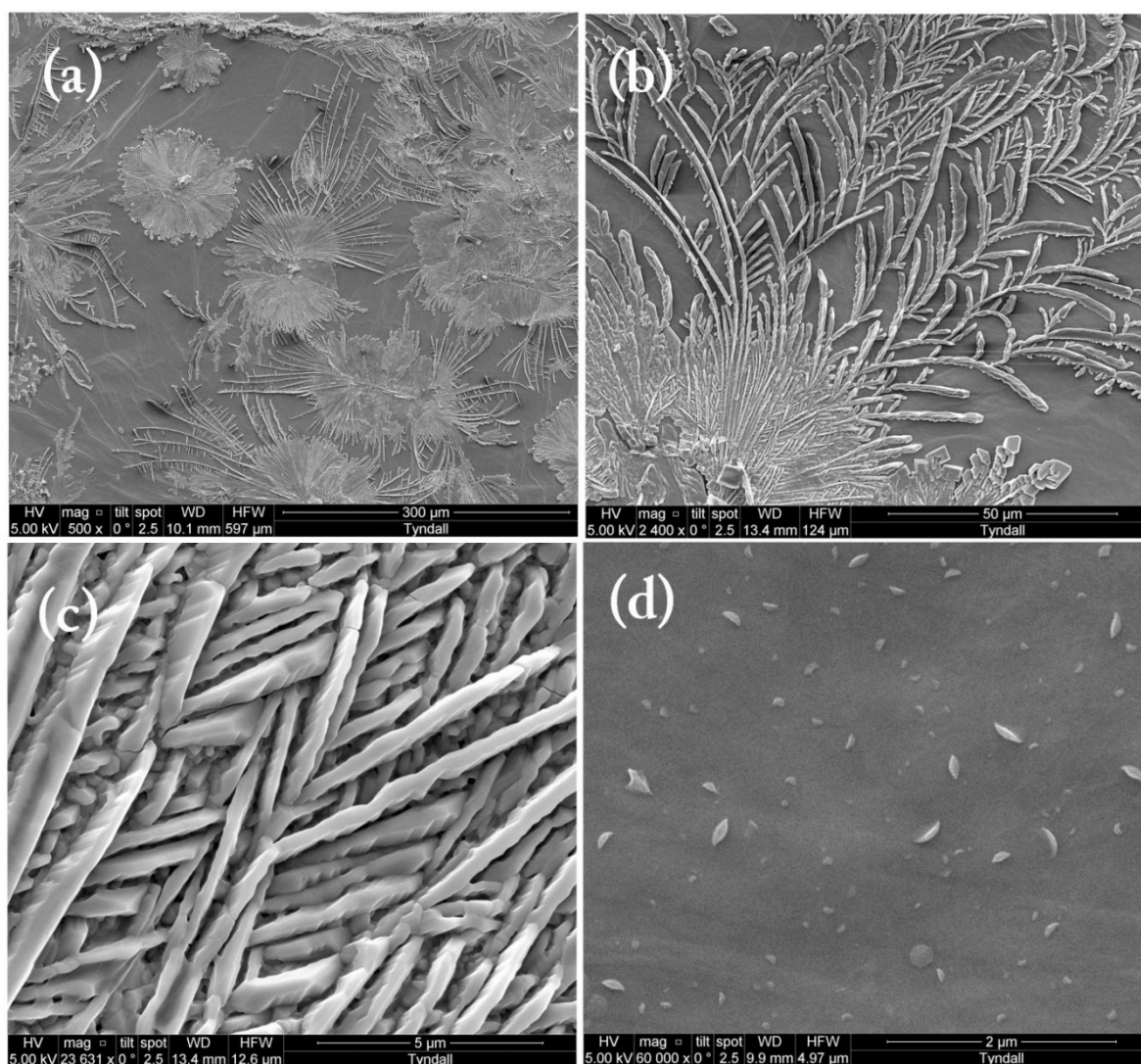


Figure 4-52: SEM image of as-grown diclofenac crystals on the surface of GO paper at different magnifications

SEM images of as-grown diclofenac crystals on the surface of GO paper revealed interesting nucleation and instant growth of the well-shaped crystals on its surface. As shown in Figure 4-52(a) the crystallisation initiated at different spots on the surface and growth

centrically into a peacock feather morphology. Looking closer in image b shows that the growth was started from the centre of the zone or peacock tail and spread directionally in the area of a circle. The SEM image (d) shows the growth mechanism clearly. We proposed that diclofenac started to be saturated on the surface of GO and then the nucleation happened in certain spots which might be defected areas of GO. With increasing the concentration of diclofenac the feather like structure grew instantly in the form of large crystals.

Contact angle data which is shown in Figure 4-53 confirmed that the surface energy was decreased as a result of diclofenac growth on its surface. The average of 6 point on the surface of both samples showed contact angle of 67.5 degrees for GO paper and 32.3 degrees for GO/diclofenac paper which can be related to the free surface energy of the films. The considerable decrease of 50% in contact angle confirms the energy loss in the system after growing crystals which is favourable for formation of crystals based on nucleation-growth mechanisms.

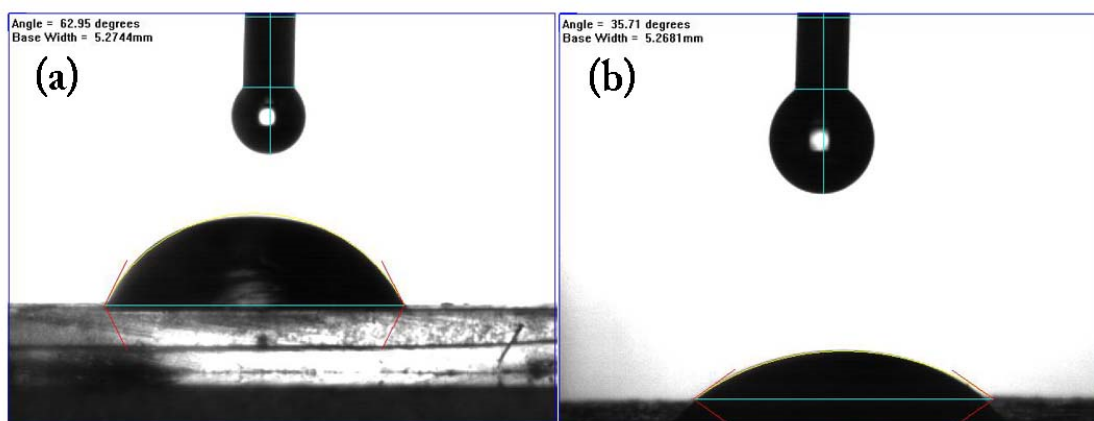


Figure 4-53: Contact angle of GO film (a) and GO film after diclofenac adsorption (b)

Studying the recovered GO sponge after adsorption of famotidine and solifenacin were not exhibited the similar phenomena. As shown in Figure 4-54 there are some crystals of famotidine on the surface of GO however only small numbers of crystals were found by searching all over the surface. They also do not have an ordered pattern of growth direction. We assume that these crystals were created after drying of the remaining solution after centrifuge on the surface. No crystal were also found on the surface of GO adsorbed solifenacin as shown in Figure 4-54b.

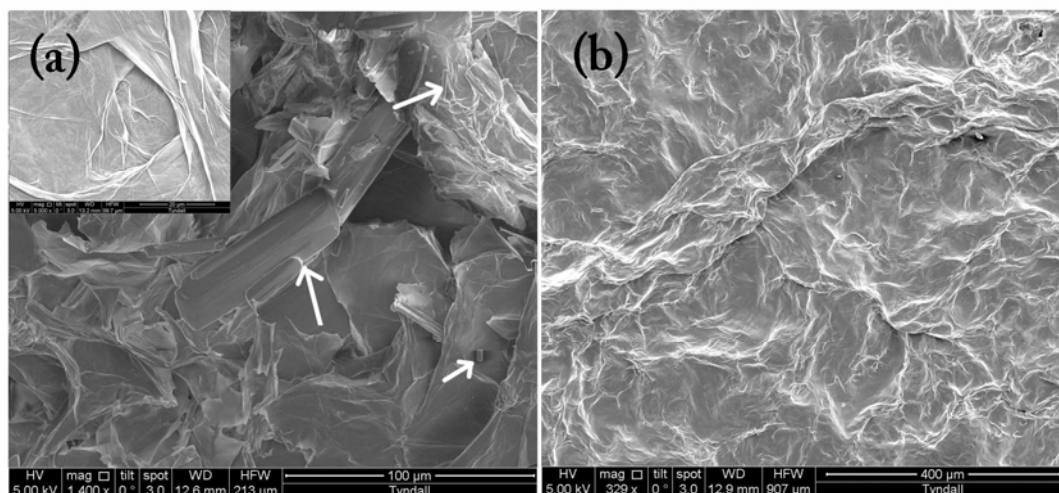


Figure 4-54: SEM images of GO sponge after adsorption of famotidine (a) solifenacin (b)

4.4.3. Pharmaceutical cocktail adsorption

In order to study the synergistic effect of different pharmaceuticals on the adsorption process, adsorption of a pharmaceutical cocktail containing six different drugs (salbutamol, salicylic acid, metoprolol, propranolol, diclofenac and carbamazepine) with the total concentration adjusted to 100 mg/L was conducted. Figure 4-55 indicated the fast adsorption of 50% of the substrate in only 1 min and more than 80% after 30 min of contact time. Therefore high adsorption capacity it is not only related to the type of pharmaceutical analyte which can be very useful in real application of treating wastewater containing many different organic pollutant that affect adsorption process. In following section we studied kinetic of adsorption and examined the effect of adsorbent dosage on adsorption efficiency.

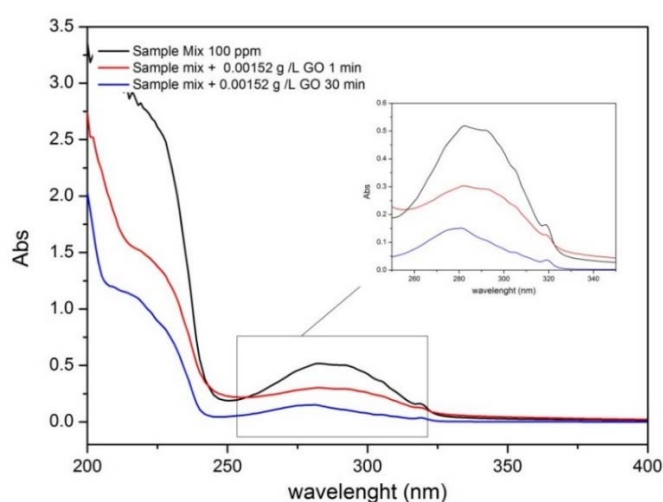


Figure 4-55: UV-vis adsorption spectra of six drugs before and after adsorption

4.4.3.1. Adsorption Kinetic Studies

In order to study the kinetic of adsorption we studied the effect of GO concentrations and initial concentration of pharmaceuticals on adsorption efficiency, final concentration and the amount of adsorption is demonstrated in Figure 4-56. It can be seen that adsorption on 0.01 g of GO at 50 ppm of drug mixture has the highest amount of adsorption at around 3000 mg/g which correlates well with the results of diclofenac adsorption. However the adsorption efficiency of GO declined dramatically at low concentration of the substrate since the final concentrations by different GO dosage did not make significant decrease in the final concentrations and increase the amount of adsorption. This is because at low concentration is less probable that pharmaceutical molecule get in contact with GO surface especially at short adsorption times. The kinetic of adsorption were fitted with pseudo-second-order model (Figure 4-56B) as described previously.

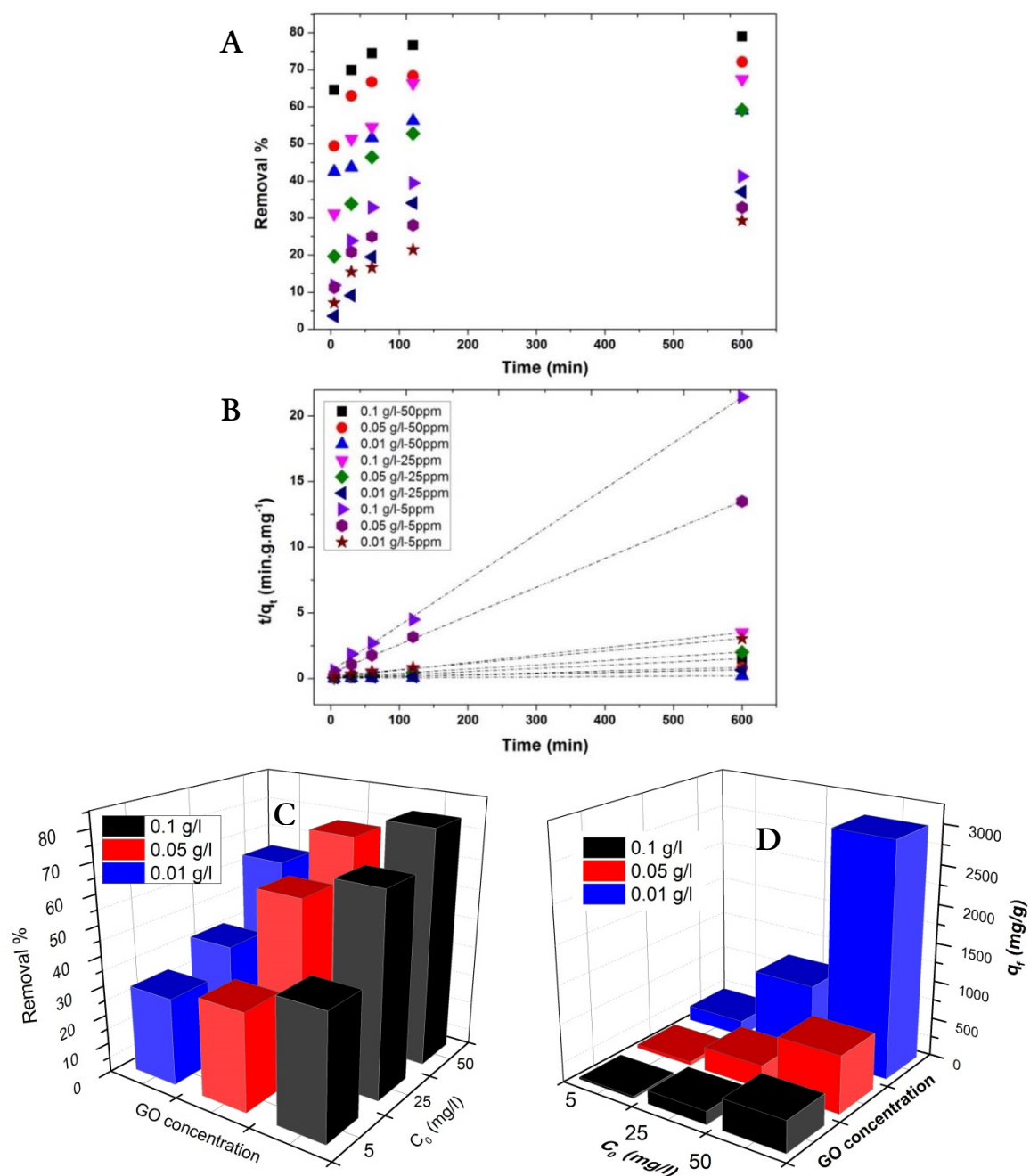


Figure 4-56: Pharmaceutical cocktail removal with initial concentration of 5, 25 and 50 mg/l by GO dosage of 0.01, 0.05 and 0.1 g/l by time of adsorption (A) pseudo-second order kinetic plot of adsorption (B) bar charts summarizing amount of adsorption and removal efficiency versus initial concentration and graphene oxide dosage (C and D)

Table 4-7: Kinetic parameters of 5, 25 and 50 mg/L of diclofenac using three dosage of GO

GO concentration	Parameters	Concentration (mg/l)		
		50	25	5
0.1 g/l	$q_{e,exp}$ (mg/g)	401.08943	172.07317	27.9626
	q_e (mg/g)	403.22	174.82	28.74
	K ($g\ mg^{-1}min^{-1}$)	0.00075746	0.00064296	0.002193405
	Adj. R-Square	0.99996	0.99959	0.99938
0.05 g/l	$q_{e,exp}$ (mg/g)	733.07317	301.86992	44.54309
	q_e (mg/g)	740.74	310.55	45.76
	K ($g\ mg^{-1}min^{-1}$)	0.000277398	0.00018128	0.00120984
	Adj. R-Square	0.99992	0.9995	0.99937
0.01 g/l	$q_{e,exp}$ (mg/g)	2998.69919	944.30894	198.3252
	q_e (mg/g)	3039.5	1054.8	209.2
	K ($g\ mg^{-1}min^{-1}$)	4.44E-04	1.47E-05	1.31E-04
	Adj. R-Square	0.99975	0.98205	0.99507

The results of fitting parameters by this models are listed in Table 4-7 where k ($g\ mg^{-1}h^{-1}$) is the rate constant of sorption, q_e ($mg\ g^{-1}$) is the calculated amount of adsorption at equilibrium as well as fitting coefficients of determination (Adj. R^2). In most of the cases R^2 is above 0.99 and the calculated adsorption capacity (q_e) values estimated by the pseudo-second-order model shows good consistency with the detected values in experiment ($q_{e,exp}$). As discussed above, the pharmaceutical adsorption on GO can be well described by the pseudo-second-order kinetic model. Since the kinetic data of adsorption at high initial concentration fit pseudo-second-order kinetics model best, the initial rate (kq_e^2) from this linear fitting was calculated to be $4064\ mg\ g^{-1}h^{-1}$ and the rate constant of sorption (k) is $0.0004\ g\ mg^{-1}h^{-1}$. By comparing this results (initial rates and q_e) with the literature^{195,291,293,297,336,337} our results shows higher adsorption capacity in order of magnitude. However isotherm data shown in Figure 4-57 did not fit well with Langmuir and Temkin models with are the ideal model for monolayer physical adsorption and chemical adsorption based on strong electrostatic interaction between positive and negative charges respectively. Only Freundlich model which is an empirical widely used in the field of chemistry can be applied to obtain a reasonable fitting as shown in Figure 4-57 inset graph with $R^2 = 0.98$.

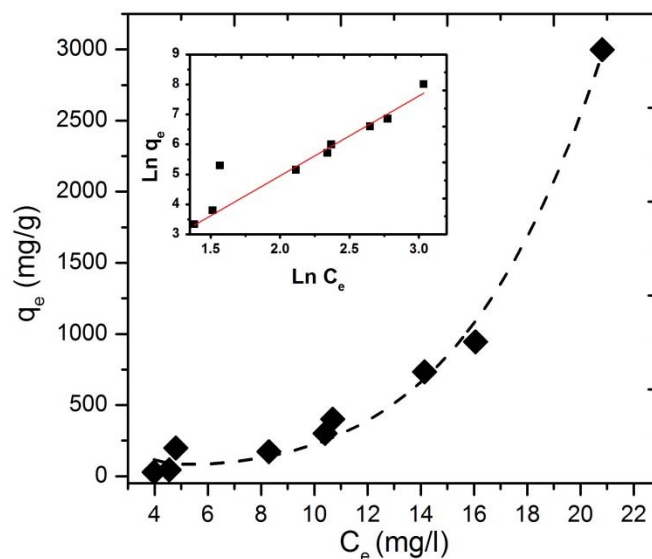


Figure 4-57: Adsorption isotherm of pharmaceutical mixture and Freundlich adsorption isotherm (inset graph)

Table 4-8: Freundlich adsorption isotherm parameters calculated from the inset graph of Figure 4-57

Freundlich model	Temperature (K)	K_F	$1/n$	R^2
$\ln q_e = \ln K_F + (1/n) \ln C_e$	298	1.677	2.32	0.90

The mechanism for strong adsorption of drugs on graphene oxide is not clear. Yet π - π stacking interaction reported as a dominant driving force to explain the mechanism of aromatic adsorbate to graphene surface^{338,339}. However we showed that GO also has high affinity to adsorb non-aromatic compounds such as famotidine. In another proposed mechanism the cation- π bonding could also be responsible for adsorption. The cation- π bonding is dominated by the cation-induced polarization and electrostatic force between the cation and the π -electron-rich aromatic structure or another word electrostatic interaction between negatively charged GO and positively charged species^{195,291,340,341}. However, since some of our tested drugs such as diclofenac dissociate in water and contain a negatively charged group in their structure, most likely electrostatic interaction between opposite charges is not responsible for high adsorption efficiency of the graphene oxide towards pharmaceutical. We showed that GO is very effective adsorbent which not only can remove pharmaceutical from water via normal adsorption process but also via other mechanism such as crystallisation or precipitation. Therefore we believe that combination of π - π interaction, cation- π bonding and drug crystallisation due to low surface energy of graphene oxide can be described as involved mixed mechanism of adsorption.

4.5. Summary

Briefly in this chapter:

- Single layer Graphene oxide sheets were synthesised via modified Hummers method and fully characterised by different techniques such as Raman, Uv/Vis and FTIR spectroscopy, AFM, SEM and TEM, XRD and N₂ adsorption methods to study morphology, structure, efficiency of exfoliation, size of nano-sheets, degree of oxidation and defects, surface area and chemistry of graphene oxide nanosheets
- Reduction of graphene oxide to reduced graphene oxide was studied via chemical and thermal reduction and the efficiency of reduction were examined by XRD, Raman and FTIR spectroscopy.
- High concentration of graphene oxide dispersion were used to create 3D structure of graphene oxide foam via freeze drying which was used as an adsorbent for methylene blue dye and various type of pharmaceuticals from water
- Graphene oxide immobilised on the surface of different type of substrate in order to obtain an engineered adsorbent which is efficient and easy to recover after adsorption process
- Kinetic of pharmaceutical adsorption on graphene oxide foam were studied

4.6. Conclusion

It may be concluded that graphene oxide foam resulting from graphite oxidation and freeze drying of high concentration of GO dispersion is a very efficient and fast adsorbent for adsorption of organic contaminant from water. We observed high adsorption capacity of up to 3000 mg of drugs per gram of GO with a high rate of adsorption about 4064 mg g⁻¹ h⁻¹ which is one of the highest numbers reported so far. This can be attributed to the following reasons:

- Planar 2D structure of GO which provides both side of GO sheets available for adsorption of organic molecules on its surface via different interactions such as π - π interaction between aromatic groups and electrostatic interaction between positively charged molecules and negatively charges GO
- Open macro-pore structure of GO which reduces the diffusion path length of adsorbate molecules to reach the surface of GO
- Abundancy of defects on basal plane of GO and functional groups on edges and basal plane are suitable sites for adsorption via chemical interaction

- Crystallisation of diclofenac and maybe some other drugs that observed on the surface of GO might be responsible for extraordinary adsorption capacity which is related to the low surface energy of graphene oxide as a suitable site for nucleation of organic and inorganic soluble species

We also found that nitrogen adsorption isotherms and BET model is not suitable method to identify pore structure and surface area of graphene oxide porous material which might be due to partial restacking of graphene oxide during vacuum heating of GO foam for degassing process. We for the first time used Methylene Blue dye solution to measure actual surface area of GO and obtained 2600 m²/g which is very close to the theoretical surface area of graphene whereas BET gave 547 m²/g that was not able to verify the high adsorption capacity of GO. We also assembled GO sheet on the surface of different inorganic substrates and found that Dolomite/GO engineered adsorbent has great capacity towards dye adsorption and can be an efficient and cheap adsorbent for industrial wastewater treatment.

One interesting outcome of the current research is that very special surface chemistry of graphene oxide makes this material a suitable platform for range of chemical reactions, adsorption and physical phenomena such as crystallisation and growth of organic and inorganic materials. We observed that dissolved dolomite re-crystallised on the surface of GO to form hierarchical morphologies. This also happened for organic drug diclofenac which might be related to low surface energy of graphene oxide as a suitable sites for nucleation and growth of other organic and inorganic materials in aqueous solution.

CHAPTER 5: TiO₂ nanoparticle/Graphene nano-composite Synthesis and Photocatalytic Properties

5.1. Introduction

In recent years variety types of pharmaceuticals are being detected in the aquatic environment and common sewage treatment plants are not able to remove these compounds completely as described in chapter 1. The most common approach for removal of these trace pollutants which is adsorption by carbonaceous materials such as activated carbon or new class of nanomaterials such as graphene oxide was described in chapter 4. Heterogeneous photocatalytic using TiO₂ semiconductor nanoparticles as catalyst is one of the most promising advanced oxidation processes which is based on the generation of very reactive species such as hydroxyl radicals (.OH) that can oxidize a broad range of organic pollutants quickly and non-selectively^{88,276,342,343}. Most organics can be mineralized to water, carbon dioxide and mineral acids by successive hydroxyl radical attack and fragmentation³⁴⁴⁻³⁴⁶.

We designed new Graphene based TiO₂ nano-composite which combines photocatalytic properties of TiO₂ with excellent adsorption capacity of graphene oxide (GO) and reduced graphene oxide (rGO) to achieve the highest removal efficiency of pharmaceuticals. As a new form of carbonaceous material, graphene and graphene oxide (GO) are promising adsorbent owing to their planar structure, abundant functional groups and defects, light weight, large surface area, and hollow geometry. The aim of this study is to find the most efficient TiO₂ /graphene nano-composite which is easy to process and able to purify water under solar light irradiation and investigate photocatalytic activity; kinetics and efficiency of graphene/TiO₂ catalyst to remove commonly found pharmaceuticals in water. The combination of TiO₂ and graphene oxide and/or graphene which possess excellent adsorption, transparency and conductivity is predicted to generate a synergistic effect that simultaneously enhance pollutant adsorption and charge transportation to facilitate photodegradation of the pollutants. Few reports related to the synthesis of such graphene-based composites with TiO₂ photocatalyst have been published³⁴⁷⁻³⁵². For example it has been shown that P25-graphene composites

exhibit higher adsorptivity and photocatalytic activity towards methylene blue dye than P25 and P25-carbon nanotube composites^{229,353}. Manga et al.³⁵⁴ monitored the ultrafast electron transfer between TiO₂, graphene oxide and graphene sheets in femtosecond transient absorption spectroscopy, reflecting the higher separation efficiencies of photo-induced charge carries. They also determined that the photo-reductions in the transformation of graphene oxide to graphene created a continuous electron conducting network through cross-surface charge percolation and allowed graphene to function as an efficient electron sink. However to do so, graphene oxide needs to be reduced to some extent to recover its electronic structure partially.

In TiO₂/GO composites reduction can be achieved via chemical reduction, thermal annealing, photocatalytic reduction and hydrothermal dehydration route^{236,285,355-357}. The photocatalytic reduction of graphene oxide in the presence of TiO₂ suspension developed by Kamat's group²⁰⁸ is based on the reduction of GO by accumulated UV generated electrons if the holes are scavenged by ethanol. Hydrothermal dehydration method means that supercritical water serves as the reducing agent to achieve the reduction from exfoliated graphene oxide to graphene²⁸⁵.

In the present study two different approaches were applied to make TiO₂/graphene oxide composite. First method is in-situ synthesis of TiO₂ nanoparticles from the Ti organic precursor on the surface of GO via sol-gel method and the second method is a simple one-step colloidal blending of graphene oxide with commercial and commonly used P25 TiO₂ powder both followed by a reduction step. The photocatalytic activity of this new composite was evaluated by degradation of pharmaceuticals in the immersion well photoreactor presented in chapter three. The studied process is composed of two sequential batch steps: every cycle alternates a step of adsorption and a step of photocatalytic oxidation in the presence of UV, at 22 °C and atmospheric pressure. The role of graphene oxide content adsorption capacity and photocatalytic activities under both UV and visible irradiations was investigated and the optimum GO weight in composites was identified. Then the effect of thermal annealing and hydrothermal reduction on morphology and structure of composite and their resulting photocatalytic activities were studied.

5.2. Result and Discussion

5.2.1. Sol-gel synthesis of TiO₂ nanoparticles on GO

TiO₂/GO composite were prevalently obtained by in-situ hydrolysis of TiO₂ precursor on the surface of GO. The amount of GO were adjusted from 0 to 100 wt% in the mother sol (GO-PS-X, X=0-100 %wt). TiO₂ sol was prepared based on the sol-gel method described in section 3.5.2. SEM images of as-synthesised composite are shown in Figure 5-1. Clearly the morphology

of TiO_2 particles are quite different in pure TiO_2 and TiO_2/GO composite. As shown in Figure 5-1A in vicinity of GO, TiO_2 powder is composed of agglomerated poly-crystalline spherical TiO_2 particles with the average particle size of $2\ \mu\text{m}$ which is expected to have low surface area which confirmed by BET analysis. On the other side as shown in Figure 5-1F, graphene oxide powder is a network of large GO sheets with a layered and porous structure and large amount of pores between sheets which can provide large surface area for immobilisation of TiO_2 .

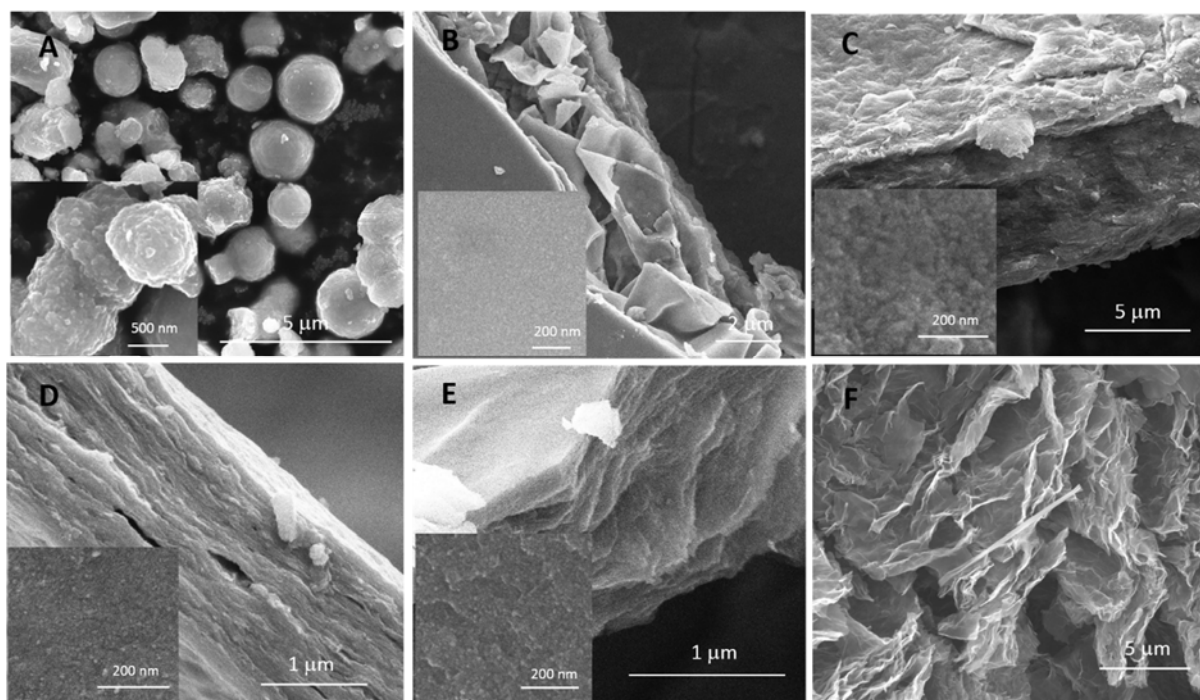


Figure 5-1: SEM images of TiO_2/GO composite with (A) 0 wt% GO; (B) 2 wt% GO; (C) 10 wt% GO; (D) 15 wt% GO; (E) 20 wt% GO; (F) 100 wt% GO

In the presence of 2 wt% GO (Figure 5-1B) the TiO_2 nanoparticles preferentially hydrolyse on GO surface which forms uniformly coated TiO_2 /graphene oxide nano-sheets after condensation step rather than forming large agglomerated TiO_2 particles (A). This was confirmed by closer look at the surface of each nano-sheets at inset SEM images which showed very smooth and fuzzy morphology representing the amorphous nature of TiO_2 nano-structure. With increasing the amount of GO from 2 to 20% the amount of available surface for TiO_2 nucleation increases leading to more layered-porous morphology observed in cross section of the deposited composite films in SEM images of Figure 5-1 (C, D and E). The mechanism of TiO_2/GO composite formation with such a unique structure is relied on the mechanism of sol-gel process. Generally in sol-gel, TiO_2 alkoxide precursor is added at controlled rate to the water/IPA mixture when hydrolysis of the precursor happens and TiO_2 nucleation starts. In acidic environment hydrolysis is being catalysed by acid which leads to fast and uniform

nucleation with control over the growth of the particle resulting in a sol with nano sized TiO_2 particles which later during the condensation grow to larger spherical particles. Depending on the temperature and aging time of the sol this particles grow larger and precipitate. This process is shown in Figure 5-2.

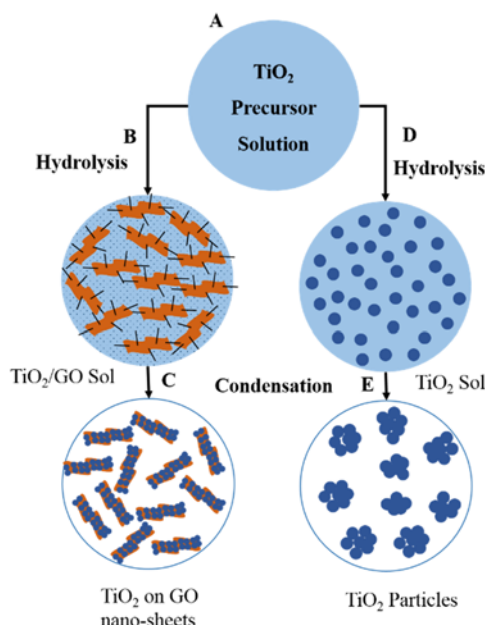


Figure 5-2: Proposed mechanism for TiO_2/GO composite formation via sol-gel process. TTIP in IPA as TiO_2 precursor (A) is added to water/IPA under controlled pH which initiates hydrolysis of the precursor (D) yielding a clear homogeneous TiO_2 sol. TiO_2 agglomerate particles formation after condensation and drying the sol (E). In the presence of GO in water/IPA during the hydrolysis, GO regarding to abundant functional groups acts as a substrate which encourage uniform nucleation on its surface (B) and hinders growth during condensation (C)

However when TiO_2 was added to water/IPA mixture containing graphene oxide nano-sheets, hydrolysis of TTIP starts from the GO surface as preferential sites which upon condensation leads to formation of small and uniform TiO_2 particles on the surface of GO. In another words graphene oxide acts as a nucleation platform which prevents growth of TiO_2 particle. We believe this is as a result of low surface energy of the GO (which was also the reason of diclofenac crystallisation on GO surface during the adsorption experiments described in section 4.4.1) and abundant functional groups which get involve in hydrolysis reactions. In order to support this hypothesis, very pure pristine (defect-free graphene) graphene synthesised by Jonathan Coleman's group in Trinity College Dublin was used instead of graphene oxide to synthesis $\text{TiO}_2/\text{graphene}$ composite following the same procedure. This pristine graphene was made by ultrasonic assisted liquid-phase exfoliation of graphite in suitable solvent^{181,185}. The Raman spectra of the single graphene flake shown in Figure 5-3A confirms the absence of any

defect in graphene basal plane since the D band related to the defects around 1350 cm^{-1} is not present.

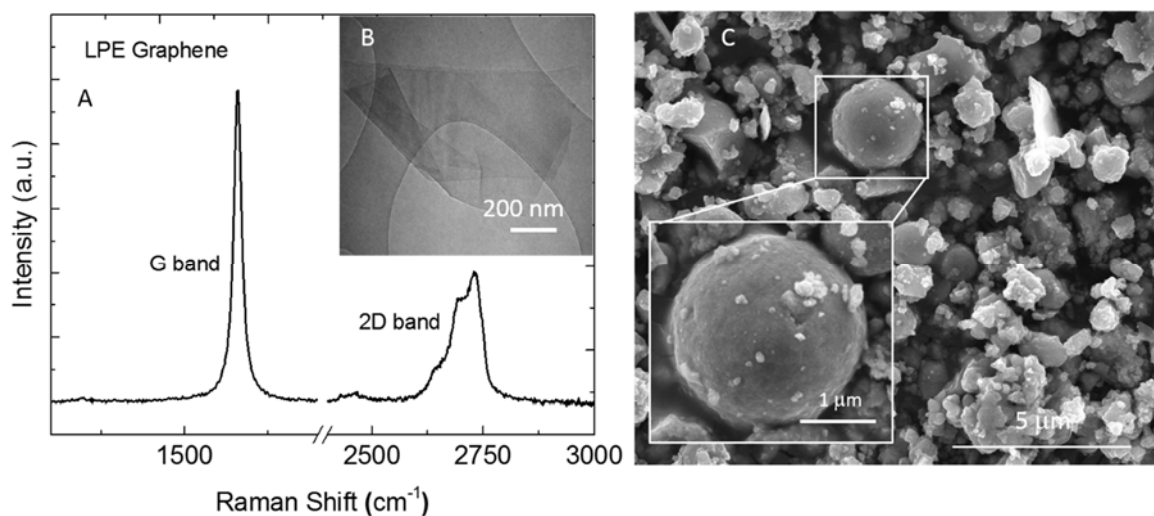


Figure 5-3: Raman spectra of liquid-phase exfoliated pristine graphene (A) with the representative TEM image of a single graphene nano-sheet (B). SEM image of TiO_2 synthesised via sol-gel process in pristine graphene dispersion.

The TEM image also shows the electron transparency of the graphene which is the evidence of few layer graphene. As shown in SEM image in Figure 5-3C, the morphology of the resulting TiO_2 /graphene is quite similar to the pure TiO_2 powder synthesised in the absence of graphene via sol-gel. This means that TiO_2 nano-particle were not hydrolysed on graphene surface and as if graphene was not existed in the system which led to emerging growth rather than nucleation. This supports our hypothesis about the importance of the functional groups and defect on formation of nano-sized TiO_2 coating on GO surface and building a layered structure nano-composite. We suggest that graphene without functional groups and defects exhibit weaker chemical interactions (van der Waals) with coating species on the surface which is in favour of growth to decrease the surface energy of graphene sheets in aqueous media of the chemical synthesis media. However GO interacts via stronger chemical interaction with oxygen functional groups including carboxylic, hydroxyl, and epoxy groups and the coated species, providing pinning forces to the small particles to hinder diffusion and recrystallization and results in smaller and more uniform coating of inorganic species.

This is important to grow TiO_2 nanocrystals on graphene surface to facilitate the electron transport via conducting graphene efficiently. Although decoration of different nanoparticles on graphene oxide has been shown^{230,231,358-360} in numerous researches, however synthesising inorganic materials especially TiO_2 with controlled morphology on the surface of highly

conducting pristine graphene with high conductivity yet remains unexplored. For the future work studying the relation between the morphologies of the as synthesised TiO₂ nanocrystals via sol-gel/hydrothermal two-step process and the degree of oxidation of underlying graphene sheets, and rationalize the nanocrystal growth behaviour is highly recommended.

Dai et. al grew nickel and cobalt hydroxide on graphene oxide and graphene with two degrees of oxidation and observed drastically different nanocrystal growth behaviours on low-oxidation graphene sheets and highly oxidized GO in hydrothermal reactions. While large single crystalline platelets with defined shape formed on the surface of pristine graphene with few oxygen-containing surface groups, small nanocrystals without recrystallization were obtained on the surface of Go with large amount of oxygen groups and defects³⁶¹.

So based on our results and Dai's study we suggest that by tuning the chemistry of graphene by controlling the concentration of the functional groups and defects on basal plane of graphene the nucleation and growth of inorganic materials can be controlled leading to a new approach to synthesis hierarchical structures with engineered properties. Graphene's functional group and defects concentration can be tuned by the degree of oxidation which can be obtained by exfoliation-intercalation-expansion and reduction methods method^{206,284,312,362,363}.

In summary based on these experiments our strategy to make graphene modified TiO₂ nano-structures for this thesis is first to make different morphologies of TiO₂ composite with graphene oxide followed by a reduction process (thermal and hydrothermal reduction) to convert graphene oxide to partially reduced graphene in order to increase the conductivity and efficiency of graphene.

As shown in SEM images in Figure 5-1 the TiO₂/GO composite has a layered structure but the shape and morphology of TiO₂ could not be identified due to the small size and also is not quite clear if nanoparticles are actually covered the surface of the GO. Therefore high-resolution TEM imaging was used to first confirm the underlying GO sheets and second identify the shape and crystalline structure of TiO₂. Typical high-resolution TEM images of TiO₂/GO with 5 wt% GO sample in different magnification and the corresponding SAED pattern are shown in Figure 5-4(A-E).

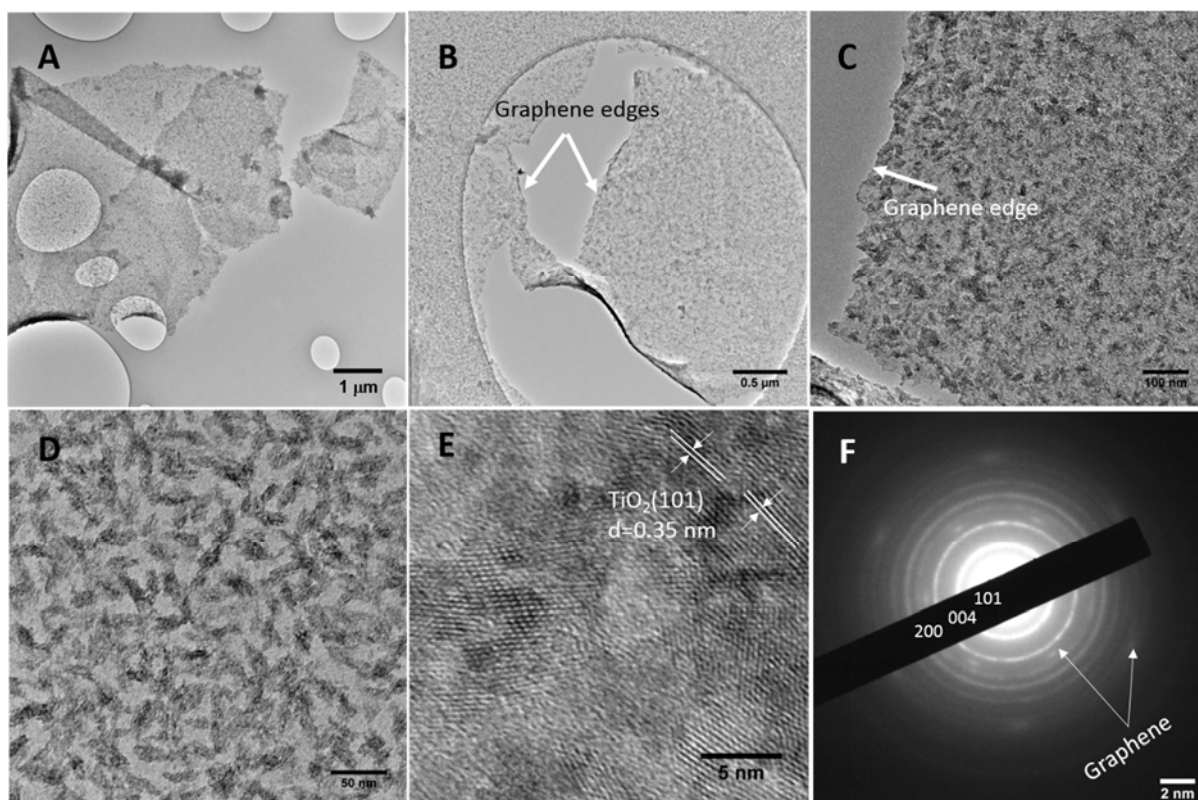


Figure 5-4: High-resolution TEM images of in-situ synthesised TiO_2 on graphene oxide sheets (TiO_2 with 5 wt% GO) (A-E) showing the morphology of the composite and also the shape and crystallinity of TiO_2 particles. The corresponding SAED pattern assigned to (101), (004) and (200) lattice planes. Two sets of 6 dot can be distinguished in this pattern which is related to crystalline pristine areas of underlying graphene oxide

From Figure 5-4A, the large GO sheets can be identified without any agglomerated TiO_2 on the surface. The electron transparency of the composite confirms very well exfoliation of GO and uniform single layer coating of TiO_2 . In higher magnification shown in Figure 5-4B, the edges of GO can be seen clearly and still no free TiO_2 particle could be found in image. In Figure 5-4C TiO_2 particles are observed more profoundly due to the contrast which might be related to the crystallinity of the particles. The surface coverage is quite uniform without any unattached particle covered all over the GO surface up to the sharp edges. This well-dispersed coverage is attributed to the functional groups on graphene oxide basal plane which acts as surfactant and promotes the individualization of the particles as were described previously. The different TEM images of our study are consistent with a well-dispersed suspension of nanoparticles on GO surface. The higher resolution image shown in Figure 5-4D revealed that the TiO_2 particles are not actually spherical but they have spindle morphology and some particles are more crystalline which results in darker contrast in TEM image. From the image analysis the average length of spindle-shape TiO_2 is 25 ± 5 nm. However higher resolution image in Figure 5-4E shows that each spindle is composed of a mixture of small TiO_2 crystallites and

amorphous phase with the average crystallite size of between 5 and 10 nm. This can explain the fuzzy image in lower magnification and wide variety of contrast in TEM images. The corresponding selected area electron diffraction (SAED) pattern (Figure 5-4E) showed a concentric-continuous ring pattern, suggesting that TiO_2 were polycrystalline with a mixture of amorphous and crystalline structure. However a closer examination revealed that there are two different type of patterns: one fringe type (rings) which exhibits polycrystalline nature of the as-synthesised TiO_2 . The three most distinguished rings were assigned to (101), (004) and (200) lattice planes with the inter-layer (d-spacing) of 3.5, 2.3 and 1.8 angstrom respectively which was calculated by measuring the distance of each ring from the central spot of the image and microscope constant as described in methods section with more detail. The second type of pattern is two set of individual dots each composed of 6 dot which is attributed to the underlying graphene lattice in some pristine and defect-free areas.

This shows partial oxidation of the graphene basal plane and confirms that GO sheets are composed of small patchy sp^2 areas (pristine graphene) which are connected by disordered sp^3 oxidised GO. This might be the main reason for the formation of spindle-shape TiO_2 because of the tendency of the growth along the pristine area to cover them and decrease the surface energy of the whole system. In summary this TEM study validates our synthesis approach towards synthesising a stable suspension containing individual homogeneously covered TiO_2/GO composite.

For real world application of nanoparticles such as TiO_2 , immobilising it on a suitable substrate to prevent agglomeration of the particles is a very critical challenge. When reduce the dimension of materials to nano size the new surfaces will be created which increases free energy of the system. Therefore they always tend to agglomerate (in case of nano-particles or re-stack in case of two dimensional layered materials such as graphene)^{183,364}. In-situ sol-gel synthesis of TiO_2 nanoparticles on the surface of GO has three advantages. First of all it prevents graphene from restacking after reduction process because of TiO_2 coating between each graphene single sheets. Second it forms very uniform TiO_2 nanoparticles on GO surface without any free particles in dispersion or agglomeration which effectively increases the active surface area of the catalyst in contact with electrolyte or organic pollutants. The third and the most important advantages of in-situ hydrolysis of TiO_2 nanoparticles on GO surface is the strong chemical and physical interaction between TiO_2 particles and the underlying graphene substrate which facilitates charge transfer between the two materials and prevents the recombination of the charge carries due to the conductivity of graphene.

5.2.2. Immobilization of pre-synthesised TiO₂ P25 nanoparticles on GO

In order to examine the effect of chemical bonding between graphene and TiO₂ we prepared TiO₂/GO through another strategy which was explained in section 3.5.4 precisely. Briefly we mixed pre-synthesised calcined commercial P25 Degussa TiO₂ powder with average particle size of 35 ± 5 nm which was dispersed in water via sonication and was centrifuged to remove un-exfoliated particles. Because GO is negatively charged and TiO₂ P25 is positively charged so they tend to mix together quite effectively. After drying the composite powder also looks quite uniform and depending on the weight percentage of the GO the colour varies from very light brown to dark navy. In Figure 5-5 SEM images of P25 TiO₂/GO composite labelled as GO-P25-X which X is the weight percentage of graphene oxide varying from 2 to 20 wt%. Top images are in lower magnification to get an overall view about the morphology of the composite however the higher resolution images (second row) from the surface of the composite shows the coverage of TiO₂ on GO surface.

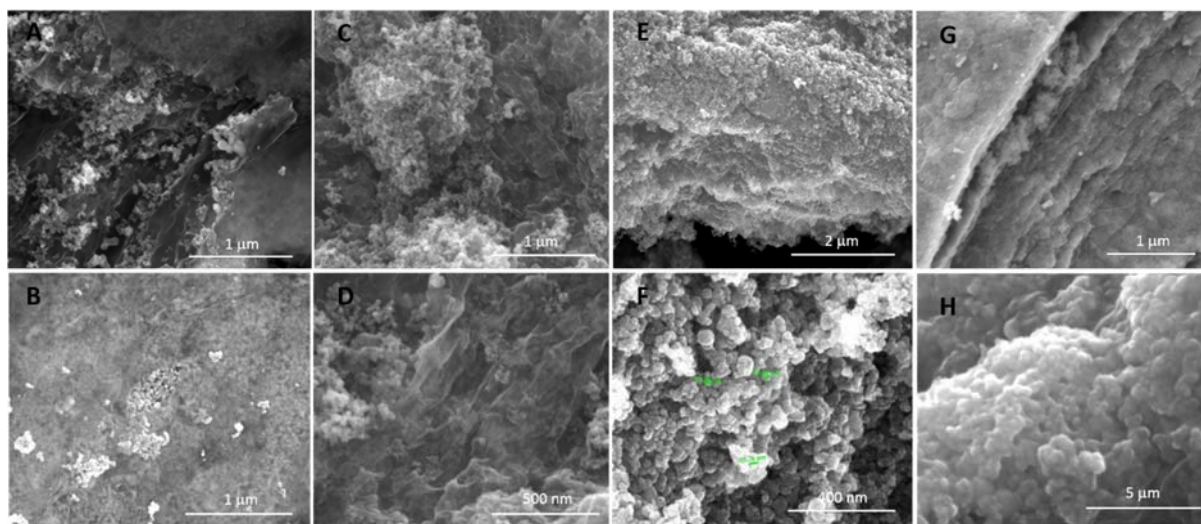


Figure 5-5: SEM images of P25 TiO₂/GO (GO-P25-X wt% X=2, 5, 15, 20) composite prepared by simple mixing of previously dispersed P25 powder with GO dispersion. A and B: tilted image and top surface image of GO-P25-2 wt% respectively. C and D: GO-P25-5 wt%. E and F: GO-P25-10 wt% G and H tilted image and high magnification image of GO-P25-20 wt%

In composite with 2 wt% GO (Figure 5-5A) very thin GO transparent film can be seen on top part of the image and TiO₂ particles are dispersed between GO layers which creates a sandwich-like structure. However TiO₂ is mostly agglomerated all over the GO surface and the coverage is very poor. In lower image B, TiO₂ nanoparticles can be observed under a transparent blanket of GO which is torn in the middle and TiO₂ particles are appeared from underneath. However with increasing the amount of GO to 5 and 10 (Figure 5-5C-F) the composite forms

more uniform morphology and less agglomerates were observed in samples. While still some area in GO remained uncovered (Figure 5-5C) in composite sample with 5 wt% GO but further increasing the concentration of GO to 15 wt% the homogeneity of the composite increases and no free GO surface can be distinguished in higher resolution SEM image (Figure 5-5F). We propose that GO plays a role as a surfactant which facilitates dispersing TiO_2 in aqueous solution through electrostatic interaction between opposite charges on GO and TiO_2 . Therefore like every other surfactant there is an optimum concentration which the surfactant is the most efficient function which in the case of GO/P25 system is between 10 and 15 wt% GO. With additional amount of GO to 20 wt% the composite become more compact and less homogeneous as shown in Figure 5-5G and H.

In order to investigate the composition of GO-P25-20 wt% composite powder and see how well-dispersed TiO_2 is in the composite, EDX elemental mapping was collected from 4 different spots of sample (corresponding inset SEM image) as shown in Figure 5-6.

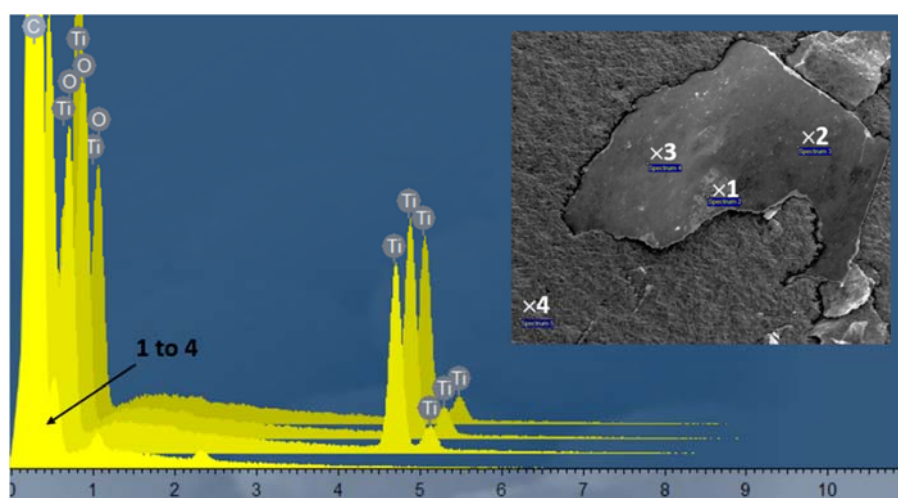


Figure 5-6: EDX elemental mapping of 4 different spots on GO-P25-20 wt% composite

As shown in inset SEM image three spots are located on a large GO flake covered with TiO_2 and forth spot is located on an area which is more uniform without flake feature. Comparing the intensity of the Ti peak in spots 1 to 3 revealed that the spots 2 and 3 which are located in the middle of Go sheets almost have similar TiO_2 content however spot 3 which is close to GO edge contains less TiO_2 and the spot 4 outside the flake show no TiO_2 at all (contains carbon only). This confirm that the optimum dispersion of TiO_2 happens on GO weight less than 15 wt%.

Transmission electron microscopy (TEM) was performed in order to determine the nature of TiO_2 adsorption on graphene sheets. Very diluted sample of P25 containing 20 wt%

GO (GO-P25-20) nanocomposite were placed on holey carbon grid and dried. Although large amount of small unbound TiO_2 nanoparticles pass through the relatively large holes in the TEM grid, however still large amount of TiO_2 agglomerated lumps can be identified in TEM image shown in Figure 5-7A as well as poor coverage of the GO surface.

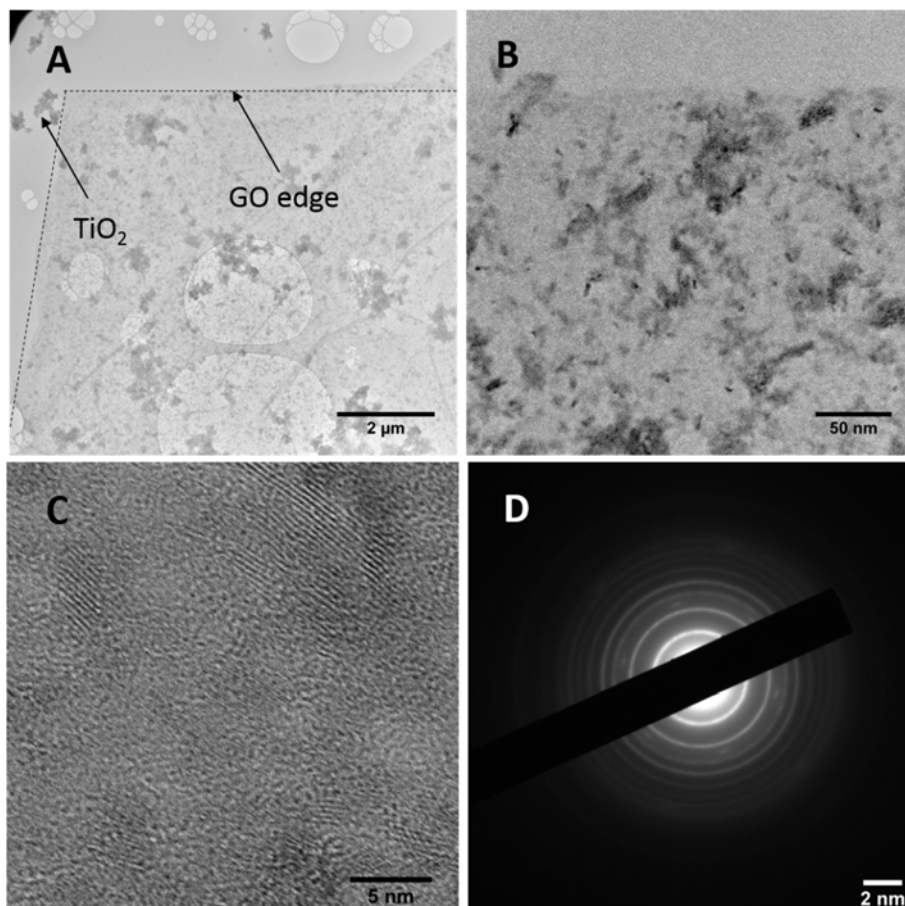


Figure 5-7: A and B: Bright-field TEM images of TiO_2 P25 with 5 wt% GO composite (GO-P25-5). C: high resolution TEM image of TiO_2 particles on GO surface. D: corresponding SAED pattern of GO-P25-5 composite showing the poly-crystallinity of TiO_2 .

Large TiO_2 agglomerate all over the surface of large GO sheet can be clearly seen also in phase image shown in Figure 5-7B. This strategy of making TiO_2 /graphene composite might be suitable for solid state application where electrodes are made by depositing thin or thick layer of composite material for battery or water splitting electrocatalysis or photo- electrocatalysis which graphene role is to interconnect TiO_2 particles and enhances charge transfer from TiO_2 to the supporting electrode^{237,365-367}. However for our application which is photocatalysis based on powder and water mixture performing under vigorous stirring is not suitable for two reasons. First, agitation provides shear forces which detach particles mechanically from the GO surface. Secondly unbound TiO_2 particles moving around in water would have no interaction with

graphene which makes the composite inefficient. However in further study we examined the effect of hydrothermal treatment and thermal treatment on strengthening TiO₂/graphene interaction along with GO reduction to rGO. The high-resolution micrograph of individual P25 TiO₂ nanoparticles on graphene oxide is shown Figure 5-7C with the interlayer spacing match with anatase TiO₂ as it also confirmed with selected area electron diffraction pattern (SAED) in Figure 5-7D. In SAED pattern 6 ring related to diffraction of electrons by graphene crystallite can be identified as well. It also exhibits reciprocal lattice spacing characteristic of anatase TiO₂ and graphene.

Degree of crystallinity plays an important role in photocatalysis activity because catalytic active sites are TiO₂ crystals and the smaller the crystals are the higher photocatalytic activity they exhibit. This is because the band gap is inversely relates to the crystal size and the smaller the crystallite size are the higher the bang gap is, which results in decreasing the rate of electron-hole recombination and therefore higher photocatalysis activity. Decreasing the crystallite size also increases the total surface area of the photocatalytic active sites. In order to study the difference between the degree of crystallinity of as-synthesised TiO₂ on the surface of GO and pre-synthesised commercial P25, X-ray diffraction of both composites with 5 wt% graphene oxide (Figure 5-8) were measured and the main anatase diffraction peak (101) located around $2\theta=25^\circ$ were fitted with Lorentzian equation (Figure 5-9) and fit parameters were used to calculate the crystallite size from Scherer formula as described in characterisation methods. Generally the intensity of the peaks corresponds to the crystallinity and particle size. Comparing these two pattern suggested that both composites are composed of irregular polycrystalline TiO₂. However the sol-gel synthesised TiO₂ contained a mixture of crystalline and amorphous phases which can be interpreted from low intensity and broader peaks.

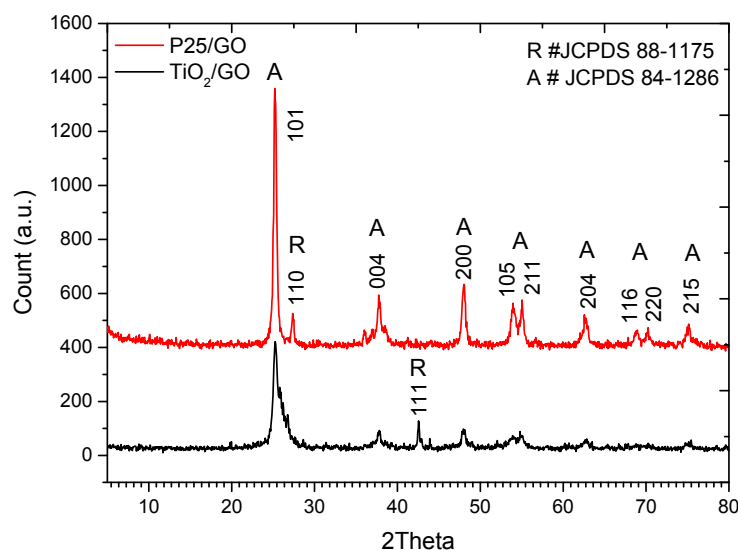


Figure 5-8: X-ray diffraction pattern of sol-gel as-synthesised TiO_2/GO composite versus commercial P25 TiO_2 immobilised on GO surface and their corresponding lattice indices and polymorph structure (A=Anatase, R=Rutile)

In both samples, TiO_2 crystal structure mainly composed of anatase phase which is indexed to tetragonal body-centered space group with lattice parameters $a = b = 3.7842 \text{ \AA}$, $c = 9.520 \text{ \AA}$. The structure comprised TiO_6 octahedra sharing two adjacent edges with the two other octahedra so that planar double chains are formed^{256,368}. Diffraction patterns of both TiO_2/GO and P25/GO composites show the characteristic peaks corresponding to anatase TiO_2 with a small (110) reflection of rutile phase located at 27.4° . Anatase peaks are located at 25.2° , 37.7° , 48.0° , 54.03° , 55.0° , 62.7° , 68.9° , 70.1° , and 75.1° which is indexed to (101), (004), (200), (105), (211), (204), (116), (220), and (215) crystal planes of anatase TiO_2 . The small peaks at 27° in P25/GO and 26° and 42.5° are assigned to (110) and (111) reflection of rutile phase. No typical diffraction peaks of GO are observed in these patterns which means that TiO_2 particles quite successfully adsorbed between GO lamellar structure so that the interlayer spacing is not matched with GO anymore.

Crystallite size is determined by measuring the broadening of anatase (101) peak at 25.2° in both diffraction patterns. It is inversely related to the full width at half maximum (FWHM) of fitted peak, the narrower the peak, the larger the crystallite size. Based on our calculations the average crystal size of commercial TiO_2 in P25/GO composite is about 22.5 nm whereas it is about 15 nm for TiO_2 which were synthesised in-situ on GO surface by sol-gel. This is reasonably match with the crystal size observed from high-resolution TEM image shown in Figure 5-4.

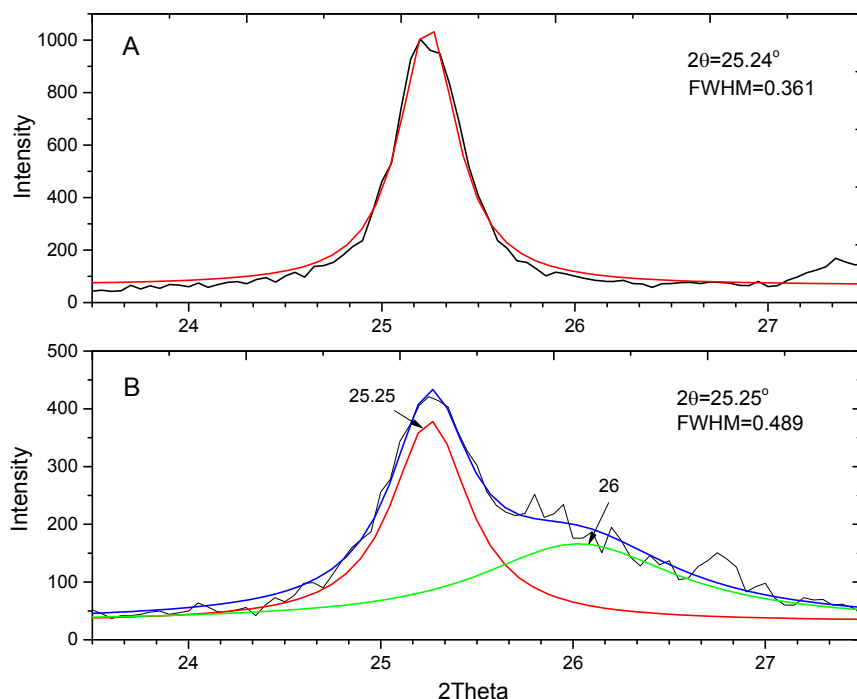


Figure 5-9: Anatase (101) diffraction peak with the corresponding Lorentz peak fitting for (A) P25/GO (sample GO-P25-5 wt%) and (B) TiO₂/GO synthesised by sol-gel (sample GO-PS-5 wt%). The (101) peak for as-synthesised TiO₂ by sol-gel is a shouldered peak which was de-convoluted into two peaks which small peak on the shoulder represents very small amount of (110) rutile shifted and broadened due to very small size.

Therefore based on all of these XRD and TEM data we concluded that TiO₂ nanoparticles crystallise on the surface of GO mainly in anatase form which is the most effective TiO₂ polymorph for photocatalytic applications. However base on the literature synthesising crystalline TiO₂ at room temperature is quite challenging and usually the as-produced TiO₂ powder through sol-gel is amorphous and needs a suitable post treatment such as thermal treatment at temperature above 400 °C or hydrothermal treatment above 120 °C in order to increase the crystallinity of the resulting powder³⁶⁹⁻³⁷². This could mean that graphene oxide provides a low surface energy which encourages nucleation of TiO₂ crystals on its surface. To justify this hypothesis we prepared TiO₂ sol in the absence of graphene oxide in exactly same manner. Then the sol was dried and grounded into the power and half of the powder was calcined at 450 °C. The as-synthesised TiO₂ powder and the calcined powder were analysed by XRD as shown in Figure 5-10 in comparison with the sol-gel synthesised TiO₂/GO composite (sample GO-PS-5 wt%).

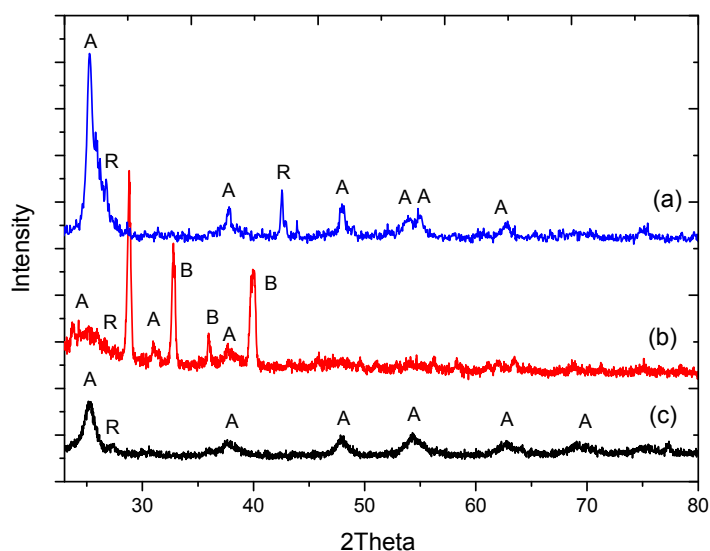


Figure 5-10: X-ray diffraction of sol-gel synthesised TiO_2 powder comparing with (a) GO-PS-5 wt%, (b) as-synthesised TiO_2 without any treatment, (c) TiO_2 powder calcined at 450 °C for 2 hours

As it can be seen from Figure 5-10(b) the as-synthesised TiO_2 sol only shows very weak peaks corresponding to anatase crystals however three strong peaks at 29, 33 and 40° are related to Brookite phase which is an unstable polymorph of TiO_2 and a common product of room temperature sol-gel process. After annealing at 450 °C brookite completely re-crystallised into anatase phase as shown in Figure 5-10C.

As described earlier when GO or rGO incorporated into TiO_2 nano-composite the diffraction of (002) plane which is normally located at °12 and °25 degree for GO and rGO (see Figure 4-16) are no longer visible in XRD pattern. In Figure 3, the (002) peak at 27° for pristine graphite indicates an interlayer spacing of 0.34 nm. The disappearance of these peaks can be attributed to the exfoliation of layered structures of GO and randomly distribution within the composite. Another reason is that comparing high intensity TiO_2 sharp peaks, graphene oxide's (002) peak is very broad and weak which can be masked in the background especially at low GO content composites. The (002) peak of rGO is located at °25 which is overlapped by reflection of (101) plane of anatase TiO_2 . Therefore although XRD is a useful technique to study micro-structure and crystalline phase of TiO_2 however it does not provide enough information about TiO_2 /GO composites since any signal from GO and rGO could not be distinguished in XRD pattern.

In contrast Raman spectroscopy is a powerful tool to characterize structure of both TiO_2 and graphene derivatives in same sample. The important advantages of Raman spectroscopy to study TiO_2 /graphene composite is that the Raman active modes of TiO_2 and graphene are quite

segregated since 5 Raman vibrations of TiO_2 located at the very beginning of the spectra (100 to 650 cm^{-1}) while D and G band modes of graphene are located at the tail of spectra (1300 to 1500 cm^{-1}). We recorded the Raman spectra of sol-gel synthesised TiO_2 on graphene oxide (GO-PT-5 wt%) and pure sol-gel TiO_2 without addition of GO (GO-PT-0 wt%) as a control as shown in Figure 5-11. The results were compared with the Raman spectra of commercial P25 powder.

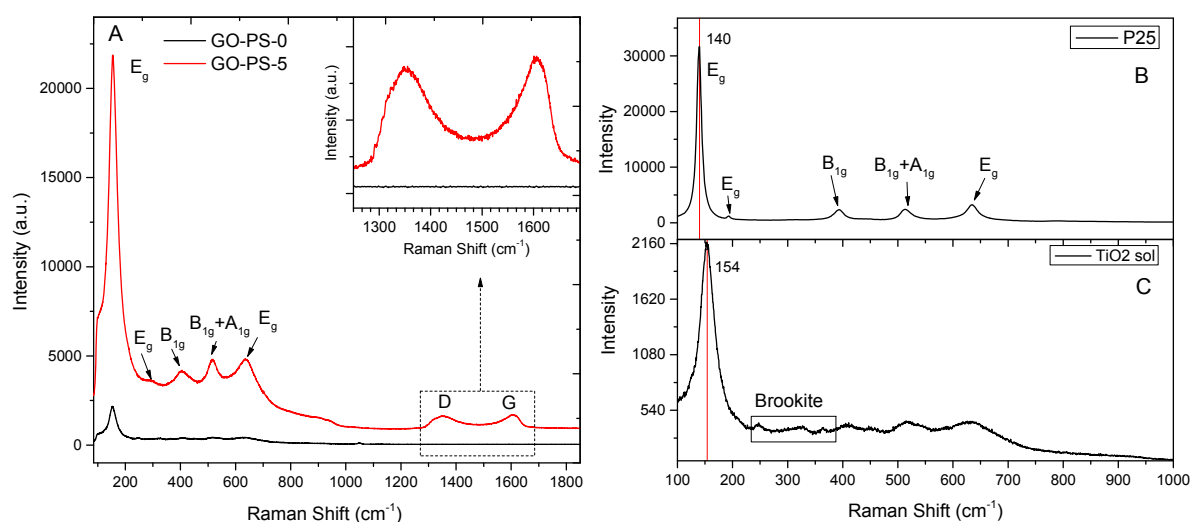


Figure 5-11: (A): Raman spectra of sol-gel synthesised TiO_2 and TiO_2/GO composite (inset: enlarged area of graphene's D and G band modes). (B) Raman spectra of commercial P25 TiO_2 powder with assigned vibration modes. (C): Raman spectra of as-synthesised TiO_2 powder in comparison with P25

Standard single crystalline Anatase has a space group $D4h$ with six Raman active vibrational modes, $A_{1g} + 2B_{1g} + 3E_g$. The six allowed bands in the first-order Raman spectrum are located at 144 (E_g), 197 (E_g), 399 (B_{1g}), 513+519 ($A_{1g}+B_{1g}$), and 639 (E_g) cm^{-1} . For commercial P25 TiO_2 , six Raman active modes appear at 140 cm^{-1} (E_g), 193 cm^{-1} (E_g), 393 cm^{-1} (B_{1g}), 513 cm^{-1} ($A_{1g}+B_{1g}$), and 634 cm^{-1} (E_g) which is close to single crystalline anatase Raman spectra²⁸¹. While, TiO_2 powder synthesised via sol-gel method shows all 6 anatase vibration modes respectively at 154, 203, 407, 517 and 632 cm^{-1} in addition to a set of very weak Raman bands located at 245, 321 and 362 cm^{-1} which matches with Brookite Raman modes. However when TiO_2 was synthesised in presence of 5 wt% of graphene oxide it shows stronger Raman bands comparing to as-synthesised TiO_2 powder but weaker than P25 with the Raman bands located at 154, 287, 405, 518 and 638 cm^{-1} which is in accordance with the band structure of anatase polymorph without any other phase such as Brookite. The massive increase in intensity of Raman peaks in TiO_2/GO sample compared to pure as-synthesised TiO_2 , confirms the role of graphene oxide in engaging TiO_2 crystallisation as discussed by XRD data earlier.

The other two peaks in GO-PT-5 wt% appeared at 1350 and 1600 cm^{-1} are assigned to D (disordered sp^2 carbons) and G (stretching mode of graphite) band of graphene oxide respectively.

This results indicated that TiO_2 was crystallise into anatase form with higher degree of crystallinity when synthesised in presence of 5 wt% graphene oxide nanosheets while pure as-synthesised TiO_2 powder contains brookite and exhibits less crystallinity. Raman modes of brookite polymorph is quite similar to anatase however the shape of peaks are different with two additional Eg modes at 245 and 325 cm^{-1} ³⁷³. In addition TiO_2 peaks in TiO_2 powder and TiO_2/GO composites are slightly broadened and shifted as compared to P25 TiO_2 . As the size of TiO_2 nanomaterials decreases, the featured Raman scattering peaks become broader. The size effect on the Raman scattering in nanocrystalline TiO_2 is interpreted as originating from phonon confinement. As the particle size decreases, the Raman peaks show increased broadening and systematic frequency shifts ³⁷⁴⁻³⁷⁷. The most intense E1g mode shows the maximum blue shift and significant broadening with decreasing crystallite size ^{256,374}. We found that the all Raman peaks of GO-PT-X wt% composites are blue-shifted compared with P25, more strongly for first and second Eg modes and B1g+A1g modes (between 10 to 14 cm^{-1} blue shift) and less pronounced for second B1g and third Eg (2 to 5 cm^{-1}). For example the strongest Raman mode (first Eg and at 140 cm^{-1}) of as-synthesised TiO_2 and TiO_2/GO composite is blue-shifted by 14 cm^{-1} and considerably broadened comparing with similar peak in P25. Such a peak broadening and blue shift is contributed to the decrease in average crystallite size which is indeed consistent with observations from XRD and TEM images.

5.2.3. Adsorption Properties of GO/TiO_2 Nano-composites

Considering the superior adsorption properties of graphene oxide (chapter 4), performing adsorption studies of the composites in dark prior to photocatalytic experiments seems necessary in order to first be able to differentiate between adsorption of pollutant molecule and photocatalytic degradation and second to investigate the effect of adsorption on their photocatalytic activity. Comparing the adsorption capacity of pure graphene oxide with pure TiO_2 as sorption baseline with GO/TiO_2 composites provides us very useful information about the kinetic of the reactions and mechanism of photocatalysis improvement.

Taking diclofenac as a pharmaceutical model, 0.06 mg of GO, GO/TiO_2 (GO-PS-X, X=0, 1, 2, 5, 10, 20) and $\text{GO}/\text{P25}$ (GO-P25-X, X=0, 1, 2, 5, 10, 20) with various amount of graphene oxide was first put into a diclofenac solution (200 ml, $C_0=100$ mg/L), and was stirred at 22 °C and samples were taken in regular interval (see materials and methods). The amount of adsorption

q_t (mg/g) within time t (min), was calculated by $q_t = \frac{(C_0 - C_t) \times V}{m_{catalyst}}$ where C_0 and C_t (mg/L) are the initial concentration of diclofenac and concentration after t time (min), respectively, V is the volume of the solution (L) and $m_{catalyst}$ is the mass of solid adsorbent or catalyst. The adsorption of diclofenac is shown in Figure 5-12. Unlike porous carbonaceous materials such as activated carbon or char coal which reach the equilibrium after weeks or month, graphene oxide adsorbs organic molecules quite quickly and reached equilibrium within less than 2 hours. As shown in Figure 5-12A the diclofenac concentration dropped by 80% after only 40 min for pure graphene oxide and reaches the equilibrium capacity of 286 mg/g. The quick decrease in concentration at the beginning of experiment might be due to the fact that initially all adsorbent sites were vacant and the solute concentration gradient is high. Afterwards, the diclofenac uptake by the graphene oxide functional groups (chemisorption) and graphene oxide aromatic basal plane surfaces (Physisorption) decreased significantly due to the decrease in adsorption sites. After 50-60 min of stirring the solution, the concentration did not decrease. Therefore, on the basis of these results a 60 min optimum contact time was selected for other adsorption experiment and dark adsorption before photocatalysis experiments. The adsorption kinetic can be fit by pseudo-second-order model:

$$\frac{t}{q_t} = \frac{1}{k_{ads} q_e^2} + \frac{1}{q_e} t \quad \text{Equation 5-1}$$

Where t is time in min, q_t the amount of diclofenac adsorbed at t in mg/g, q_e the amount of diclofenac adsorbed at equilibrium in mg/g, and k_{ads} is the pseudo-second-order rate constant in min·g/mg. We obtained k_{ads} and q_e by plotting diclofenac adsorption data t/q_t versus t and fitting the data linearly based on above equation and calculated q_e from the slope and k_{ads} from the intercept of fitted curve. In this model, the rate-limiting step is the surface adsorption that involves chemisorption, where the removal from a solution is due to physicochemical interactions between the two phases^{378,379}. The model is usually represented by its linear form as shown in Figure 5-13 and fitted pseudo-second-order-model kinetic parameters for GO-P25-X and GO-PS-X are presented in Table 5-1 and Table 5-2 respectively. Where k_{ads} (g/mg.min) is the pseudo-second-order rate constant of adsorption and R^2 is adjusted R-squared representing the goodness of the linear fit. Figure 5-12 shows contact time curves and the kinetic results are also shown in Figure 5-13 as a plot of t/q_t against time for sorption of diclofenac compatible with the pseudo-second order model. The values of the correlation coefficients are all extremely high (>0.990). For all of the systems studied, chemical reaction seems significant in the rate-controlling step and the pseudo-second order chemical reaction kinetics provide the best correlation of the experimental data. The correlation coefficients (R-

squared) for the linear plots of t/q_t against time from the pseudo-second order rate law are greater than 0.996 for all systems. This suggests that this sorption system is the pseudo-second order model, based on the assumption that the rate-limiting step may be chemical sorption or chemisorption through sharing or exchange of electrons between sorbent and sorbate, provides the best correlation of the data.

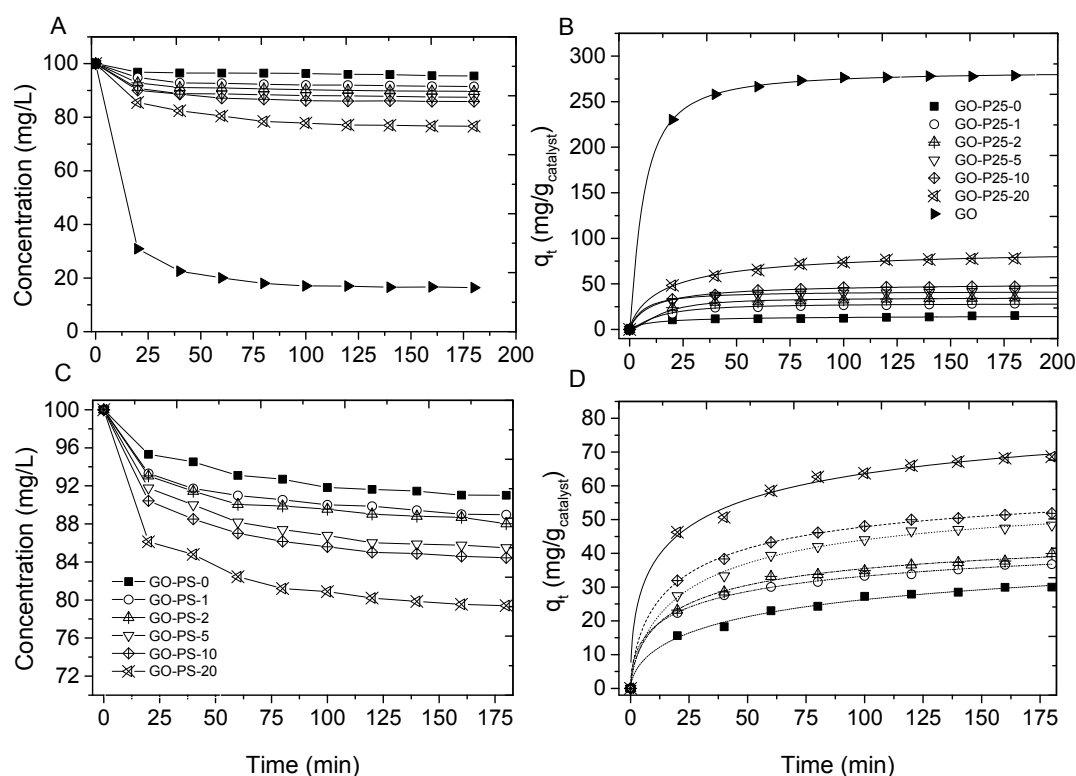


Figure 5-12: (A and C) The effect of graphene oxide content on adsorption of diclofenac by GO/P25 mixture (GO-P25-X wt%) and sol-gel synthesised GO/TiO₂ nanoparticles (GO-PS-X wt%) where X=0, 1, 2, 5, 10, 20, 100. The amount of diclofenac adsorption per gram of catalyst by time (B and D). GO-P25-0 and GO-PS-0 are TiO₂ samples without any graphene oxide and graphene oxide-only samples are included for comparison.

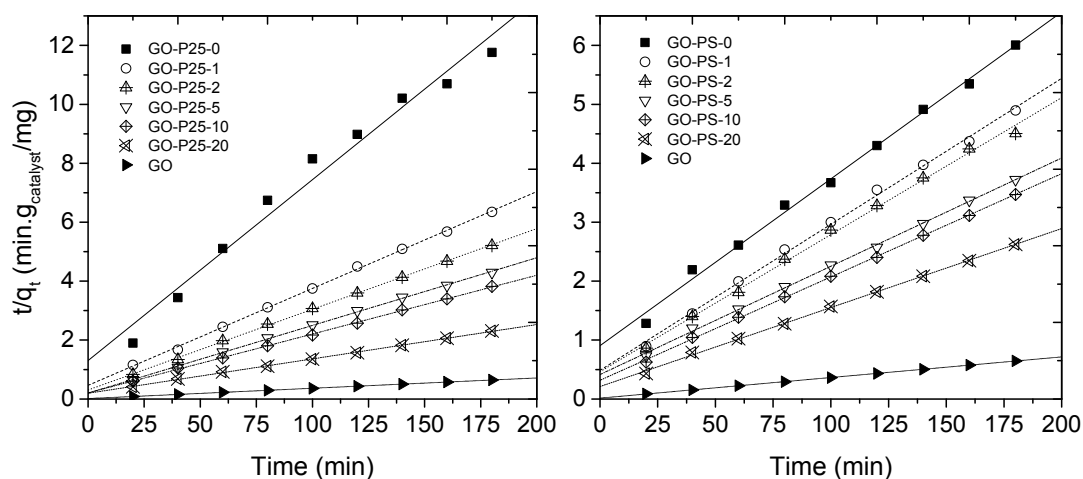


Figure 5-13: Second-order kinetic plots for the diclofenac adsorption by GO/P25 mixture and sol-gel synthesised GO/TiO₂.

Table 5-1: Adsorption kinetic parameters of GO/P25 composites

Sample	q_e (mg/g _{catalyst})	$k_{ads} \times 10^{-3}$	R^2
GO-P25-0	16.28664	2.89	0.974
GO-P25-1	30.4878	2.32	0.998
GO-P25-2	36.49635	2.46	0.999
GO-P25-5	43.66812	2.61	0.999
GO-P25-10	50.25126	1.89	0.999
GO-P25-20	86.2069	0.69	0.999
GO	285.71429	0.833	0.999

Table 5-2: Adsorption kinetic parameters of sol-gel synthesised GO/TiO₂ composites

Sample	q_e (mg/g _{catalyst})	$k_{ads} \times 10^{-3}$	R^2
GO-PS-0	35.31073	0.88	0.994
GO-PS-1	40.35513	1.27	0.997
GO-PS-2	43.01075	1.17	0.996
GO-PS-5	54.40696	0.815	0.998
GO-PS-10	57.01254	0.969	0.999
GO-PS-20	74.57122	0.854	0.998
GO	285.71429	0.839	0.999

In all cases, the adsorption reached a plateau after 30 min, indicating that adsorption equilibrium between diclofenac and GO containing composites takes place very fast. This can be due to the planar structure of GO which all pores are accessible and can be reached within very short adsorption time.

5.2.4. Photocatalytic properties of nano-particulate GO/TiO₂ composites

All of the photocatalytic experiments were carried out after adsorption of diclofenac in the dark for 60 min under stirring. Under ambient conditions, air bubbling and rigorous stirring to supply oxygen to the reaction, the reactor was exposed to the UV irradiation. Photocatalysis studies used unmodified TiO₂ to demonstrate how much substrate is removed by conventional photocatalysis. Also photolysis of the substrate without any catalyst were performed to determine the substrate photodegradation due to UV light. As shown in Figure 5-14(a,c) diclofenac concentration is plotted versus UV irradiation time along with a 60 min pre-dark adsorption. For a comparison P25 commercial TiO₂ powder and bare sol-gel synthesised TiO₂ nano-particles were tested for their adsorptivity and photocatalytic degradation of diclofenac using the same procedure and conditions described in materials and methods chapter. Photocatalysis degradation of diclofenac can be fitted by a pseudo first-order kinetic model described by Equation 5-2.

$$\log(C_t - C_0) = \log C_0 - \frac{K_{app}}{2.203} t \quad \text{Equation 5-2}$$

Where t is time in min, C_t is the diclofenac concentration after t min of irradiation in mg/L, C_0 is the equilibrium concentration reached after one hour of adsorption in dark which is initial concentration of the substrate for photo-degradation experiment. K_{app} is the first-order rate constant in min⁻¹. The simplified model of this equation can be written as:

$$-Ln \frac{C_t}{C_0} = k_{app} t \quad \text{Equation 5-3}$$

Where C_0 and C_t (mg/L) are the initial concentration which is the equilibrium concentration after dark adsorption experiment and concentration at time t (min), respectively. k_{app} (min⁻¹) is the pseudo-first-order rate constant for the kinetic model. By Plotting $-ln C/C_0$ versus irradiation time and linear fitting with zero intercept, the slope can give the k_{app} . The photocatalytic activities of the composite material can be quantitatively evaluated by comparing the first order reaction rate constants (k_{app}). Figure 5-14 shows the photocatalytic properties of GO/P25 and GO/TiO₂ with various amount of GO from 0 to 20 wt% of composite.

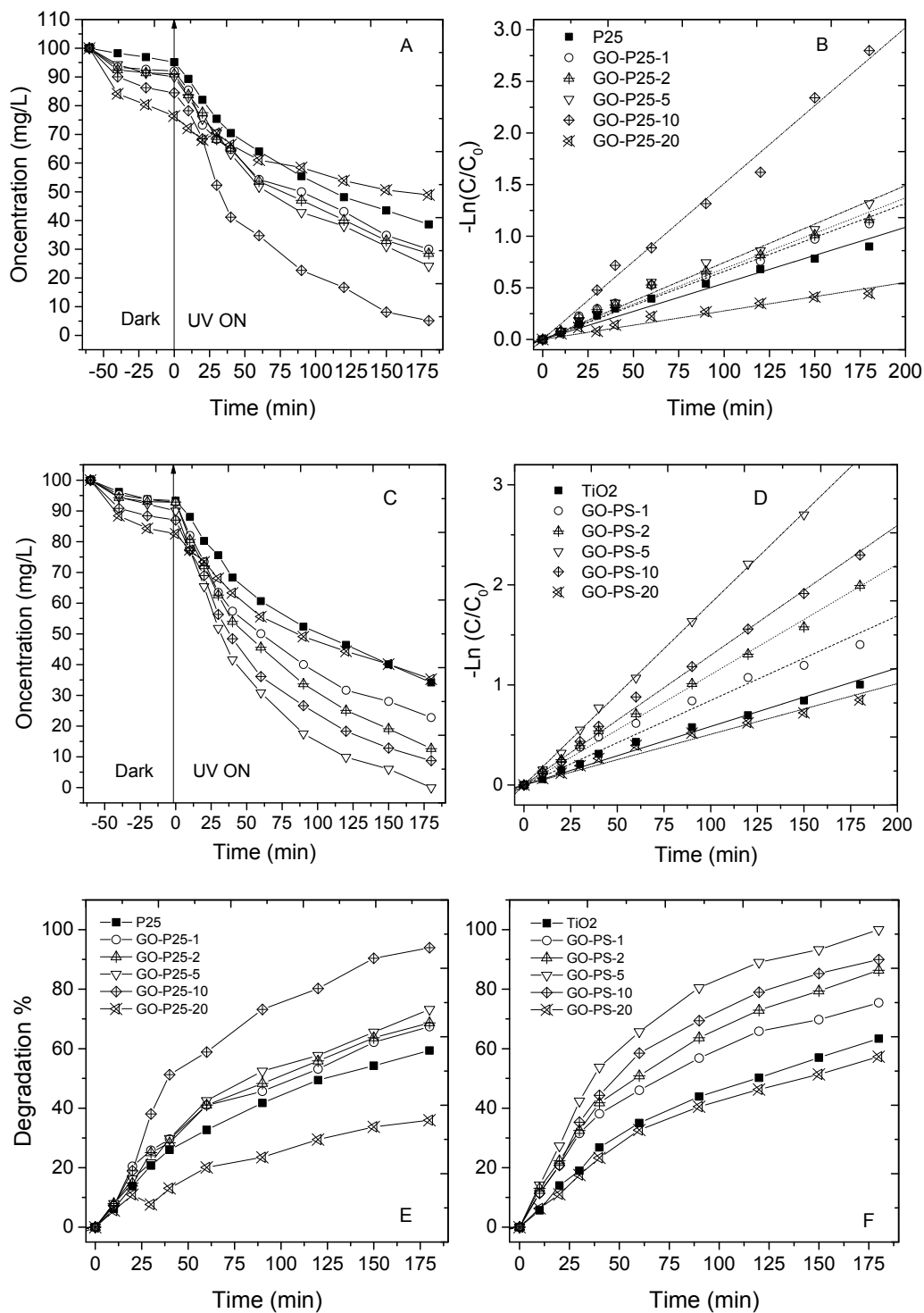


Figure 5-14: UV Photocatalytic activity of GO-P25-X and GO-PS-X (X=0 to 20 wt%). (A and C): Concentration of diclofenac versus dark adsorption time and UV irradiation time. (B and D): $-\ln(C/C_0)$ versus irradiation time and Pseudo-first order kinetic fitting. (E and F): Degradation efficiency of diclofenac versus time. In all experiments the initial concentration of diclofenac is 100 mg/L and catalyst mass loading of 0.3 g/L.

Table 5-3: Photocatalysis and kinetic parameter for GO/P25 composites

Sample	$K_{app} \times 10^{-3}$ (min^{-1})	C_0 (mg/L)	PC Removal %	Adsorption%	R^2
P25	5.43	95.15	59.36	4.85	0.987
GO-P25-1	6.61	92	67.40	7.96	0.984
GO-P25-2	6.68	91.02	68.67	8.98	0.991
GO-P25-5	7.41	90	73.19	9.95	0.995
GO-P25-10	15.12	84.44	93.91	15.56	0.95
GO-P25-20	2.7	76.39	35.94	23.61	0.979

Table 5-4: Photocatalysis and kinetic parameter for sol-gel GO/PS composites

Sample	$K_{app} \times 10^{-3}$ (min^{-1})	C_0 (mg/L)	PC removal%	Adsorption%	R^2
TiO₂	5.85	93.3	63.35	6.67	0.99
GO-PS-1	8.44	92.7	75.42	7.27	0.98
GO-PS-2	11	92.8	86.36	7.15	0.99
GO-PS-5	18.7	90.03	100	9.97	0.99
GO-PS-10	12.9	87.03	89.95	12.97	0.99
GO-PS-20	5	82.56	57.28	17.44	0.98

C_0 is the initial concentration when the adsorption-desorption equilibrium is reached

The results in general show that the photocatalytic properties of TiO₂ composite have great enhancement comparing pure TiO₂ standard samples. For these experiments the concentration of the substrate after 60 min of adsorption (adsorption equilibrium shown as C_0 in Table 5-3 and Table 5-4) is considered the initial concentration for photocatalysis experiments therefore the degradation percentage which is reported as PC removal % in parameter tables is only representative of photocatalysis efficiency. As can be seen from the table the amount of adsorption by both type of composites is increasing by increasing the amount of GO which is quite in agreement with the adsorption characteristic of graphene oxide. However adsorption by GO/P25 composite is greater than sol-gel synthesised GO/TiO₂ composite which confirms that the surface of GO is more efficiently covered with TiO₂ when synthesised via sol-gel rather than mixing P25 with GO. For example 23.6% of diclofenac was adsorbed by GO-P25-20 wt% while 17.4 % of diclofenac was removed by adsorption on GO-PS-20 wt% composite. After deducting the adsorbed diclofenac and using C_0 reported in parameter tables also the amount of substrate removed by photocatalysis increases by increasing the amount of graphene oxide from 0 to 10 wt% for GO-P25 composite and 0 to 5 wt% for sol-gel synthesised GO/PS TiO₂

composites. It means that optimum graphene oxide concentration for GO/P25 composite is about 10 wt% while it is only 5 wt% for GO/PS composites. This interesting results is quite in accordance with percolation theory of systems^{380,381}. For example this theory in case of non-conductor/conductor systems says the more homogenous a system is the less conductor is needed to increase the conductivity of the composite system few order of magnitudes and there is a point called percolation threshold which above that adding conductor will not improve conductivity of the system considerably³⁸⁰. Therefore this theory is very useful to find the optimum concentration of the second phase in composite system to achieve the highest performance with the least amount of second phase (usually a reinforcing phase or a conducting phase which are normally expensive materials). We can conclude that percolation threshold is 10 wt% for GO/P25 composite and 5 wt% for sol-gel synthesised GO/PS composites. Above this threshold the photocatalysis of both composites drops considerably which might be due to light scattering and UV penetration to the reactor because with increasing the amount of GO the composite becomes darker and the solution containing substrate and composite turns darker therefore reduces the amount of UV that penetrates to the reactor. Therefore, optimization of the carbon content should be considered in the preparation of TiO₂/GO photocatalysts.

Studying the kinetic of photo-degradation for both composite also confirms that the rate of photo-degradation K_{app} increases by increasing the amount of GO below the optimum GO weight percentage and higher than this threshold the photocatalysis rates drops considerably from 15 to 2.7 for GO/P25 and from 12.9 to 5 for GO/PS composites. This photocatalysis improvement of GO/TiO₂ composites over pure TiO₂ can be related to two factors. First, both type of TiO₂- Graphene Oxide composites have higher adsorption capacity than their pure TiO₂ powder (as summarized in Table 5-3 and Table 5-4) which provides higher concentration of diclofenac in contact with TiO₂ particles and higher probabilities for degradation by active species. Second, adding graphene oxide increases the surface area of the composite dramatically comparing their pure TiO₂ powder which is due to very high surface area of graphene oxide (~2600 m²/g). For example as shown in Table 5-5 adding 5wt% graphene oxide increase the surface area of P25 and sol-gel synthesised TiO₂ powder from 50 and 95 m²/g to 78 and 210 respectively. Also the average pore size of the composite were reduced considerably.

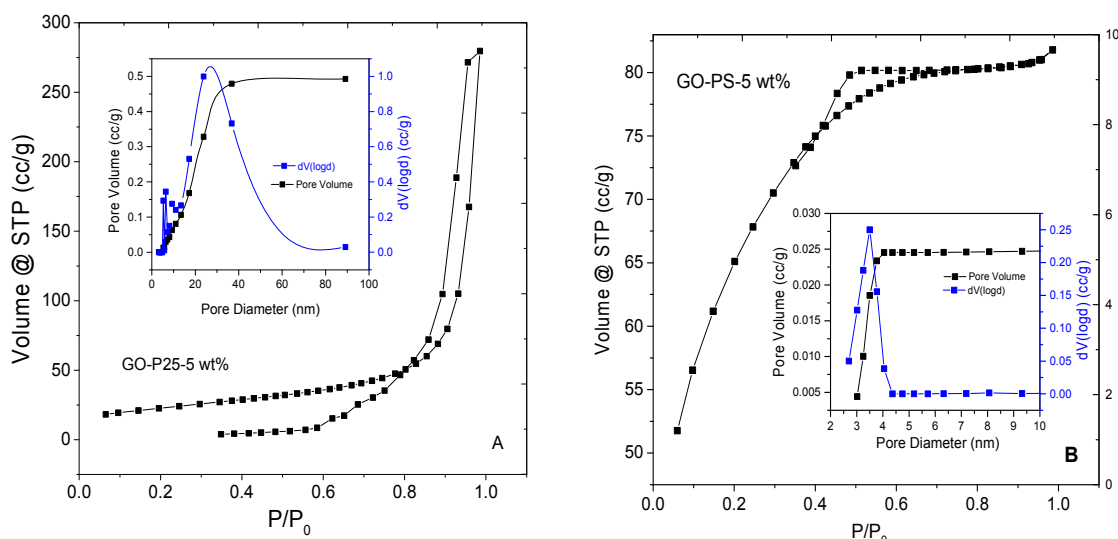


Figure 5-15: Adsorption isotherm of GO-P25-5 wt%, inset graph: BJH pore size distribution and cumulative pore volume with surface area and pore information extracted from BET and BJH plots

Table 5-5: N₂ adsorption data for GO/TiO₂ composites containing 5 wt% graphene oxide

Sample	BET surface area (m ² /g)	Total pore volume (cc/g)	Average pore size (nm)
GO-P25-5 wt%	78.63	0.493	5.28
P25	50	0.25	17.5
GO-PS-5 wt%	210.4	0.027	3.2
TiO ₂	95	0.01	10

Comparing photocatalytic activity of GO/P25 and sol-gel synthesised GO/TiO₂ composite shows that in all GO concentrations, GO-PS-X composites have higher activity. This can be described by considering surface area, morphology, TiO₂ crystallite size and pore size distribution of both composites. For example GO-P25-5 wt% and sol-gel synthesised GO-PS 5wt% exhibit the degradation rate constant (K_{app}) of 7.4 and 18.7 and removal percentage of 73 and 100 % respectively. This considerable difference in both type of composites which have same amount of TiO₂ photocatalyst and graphene oxide adsorbent can be described by higher surface area of the composite which were synthesised via sol-gel comparing the mixture of GO and P25. For example GO-PS 5wt% has 210 m²/g of active surface area comparing only 78 m²/g for GO-P25-5 wt%. This massive difference in surface area is obviously as a result of mesoporous structure and small particle size of TiO₂ when synthesised in-situ on the surface of GO which confirmed by TEM and XRD previously (see Figure 5-4, Figure 5-7 and Figure

5-9). The crystallite size of TiO₂ in GO-P25-5 wt% is 25 nm comparing 15 nm for GO-PS 5wt%. The crystallite size also is an important factor for catalytic activity of semiconductors. The smaller the crystallite of a particle, the higher is percentage of TiO₂ exposed to UV light. The homogeneous morphology of fine layered structure of the sol-gel synthesised composite is also another factor that can more contact between TiO₂ and organic substrate. Adsorption of diclofenac on graphene oxide can also decrease its diffusion path to TiO₂ nanoparticles by surface diffusion and increase photocatalytic activities for all samples.

In summary, we have synthesized graphene oxide/TiO₂ composite via two different route, in which TiO₂ is coated on both sides of planar GO sheets and forms a type of sandwich structure with graphene oxide core and TiO₂ wrapping. Reduced TiO₂ agglomeration, increased surface area, mesoporous morphology, reduced crystallite size, high adsorption capacity and reduced diffusion path length for the reactant and pore are responsible for the increased photocatalytic activity of the GO hybrid catalyst comparing their pure TiO₂ powder.

5.2.5. Photocatalytic reduction of GO to rGO in GO/TiO₂ composite

One interesting phenomena that observed during the photocatalytic experiments with graphene oxide/TiO₂ composite was changing the colour of the solution containing catalyst from light brown to grey and black depending the weight percentage of GO during the UV irradiation. This can be a sign of graphene oxide partial reduction to reduced graphene oxide or shortly rGO. It has been shown that carbon nanotube in combination of ZnO and TiO₂ shows electron accepting and storing capacity³⁸². Hence, it is reasonable to expect that GO sheets may play a similar role of accepting electrons when support semiconductor catalyst nanoparticles. This can cause partial reduction of graphene oxide and result in conductivity increase which can lead to photocatalytic enhancement. The ability of semiconductor nanoparticles to partially reduce GO samples when excited with UV light was demonstrated recently with TiO₂ and ZnO which opened up a new area of photocatalytic reduction method^{164,231,383}.

To examine how efficient UV-photocatalysis is in terms of enhancing photocatalyst performance 0.3 g of GO/P25 and sol-gel synthesised GO/PS containing 5 wt% GO recovered after first photocatalysis cycle of diclofenac degradation, washed with ethanol, dried at 25 °C overnight and reused with same procedure. The photocatalytic activity of the resulting catalyst were examined under both UV irradiation.

As shown in Figure 5-16 after first photocatalytic experiment the recovered sample performs better than the as-synthesised sample in terms of degradation rate and removal extent as summarized in Table 5-6. This is the case after second recovery which means 6 hours of

irradiation. By irradiating by 3 and 6 hours the photocatalytic apparent rate (K_{app}) increased from 7.9 to 13.3 and 24.2 respectively. Considering the reduction of adsorption percentage from 15.24 to 6.2 and 2.78 it can be concluded that this improvement in photocatalytic rate is not related to the adsorption. Since the adsorption main sites are GO functional groups the reduction in adsorption capacity can be representative of removal of some of the functional groups from GO basal plane. The observable change in colour of the solution during the test can be another evidence for partial reduction of GO to rGO. If this is the case then it is expected to observe improvement in conductivity of the composite. To examine this, solid thin films of each composite were made by filtration on cellulose membrane and transferring them on to non-conductive glass slides (see materials and methods). Then 4 electrodes were painted using silver paint and wired by silver wire. The following I-V curves were measured and sheet-resistance were calculated knowing the length and thickness of each sample and width of the electrodes gap.

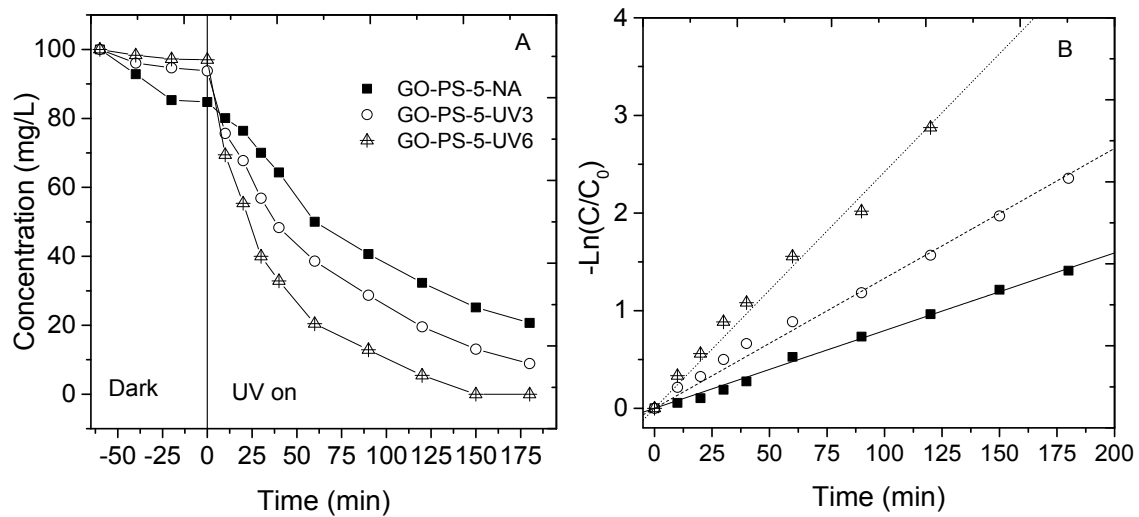


Figure 5-16: Plot of concentration vs adsorption and irradiation time (A) and Pseudo-first order kinetic plot (B) of sol-gel synthesised GO-PS-5 wt% (NA: as-synthesised with no processing, UV3: Recovered composite powder after 3 hours of UV irradiation, UV6: Recovered composite powder after 6 hours of UV irradiation).

Table 5-6: Photocatalytic, kinetic parameters and sheet resistance of GO-PS-5 wt% as-synthesised composite, recovered composite powder after 3 hours of UV irradiation and recovered composite powder after 6 hours of UV irradiation.

Sample	C_0 (mg/L)	Removal %	Adsorption %	$K_{app} \times 10^{-3}$ (min^{-1})	R^2	R_Ω ($\text{K}\Omega \cdot \text{sq}^{-1}$)
GO-PS-5-NA	84.67	75.57	15.24	7.9	0.99	$1.5 \times 10^3 \pm 500$
GO-PS-5-UV3	83.8	90.52	6.2	13.3	0.99	450 ± 10

GO-PS-5-UV6	97.22	100	2.78	24.2	0.99	210 ± 15
-------------	-------	-----	------	------	------	----------

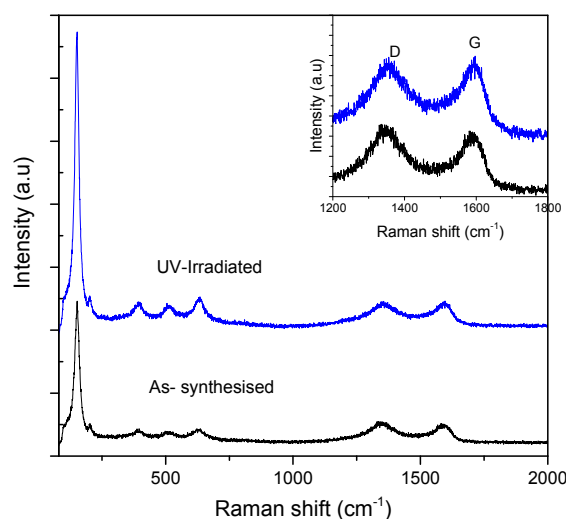


Figure 5-17: Raman spectra of as-synthesised GO-PS-5 wt% before and after 3 hours of UV irradiation

Resistivity measurements showed that as-synthesised GO-PS-5 wt% composite has very poor conductivity and can be classified as non-conductive ($R_{\Omega}=1.5 \times 10^3 \pm 500 \text{ K}\Omega/\text{sq}$). However following 3 hours of UV irradiation, the resistivity of the composite is dropped by three times which results in almost twice increase in degradation rate. Upon 6 hours of irradiation (sample recovered after being tested twice) the resistivity decreased to almost half of the 3 hours irradiated sample which resulted almost twice increase in photocatalytic rate (from 13.3 to 24.2 min^{-1}).

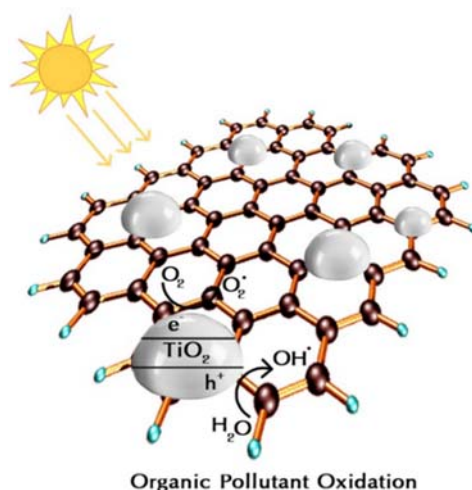


Figure 5-18: Excited-State Interaction between TiO_2 and Graphene Oxide leading to partial reduction of GO to rGO and photocatalytic degradation of organic pollutant at the same time

Raman spectra of the samples before and after irradiation (Figure 5-17) also confirms the reduction of GO to rGO by comparing intensity of the GO band to D band. Another

interesting results from Raman spectra is increasing the intensity of the TiO₂ vibration bands which can be attributed to increasing the crystallinity of TiO₂ during the irradiation.

The mechanism of reduction as shown Figure 5-18 is the electron transfer from excited TiO₂ nanoparticles to GO while hole are scavenged by water and organic molecules leading to degradation of organic pollutants. Using this method the photoconductivity of the composite and conductivity of graphene can be tuned for catalytic and photocatalytic applications such as water splitting, hydrogen production and environmental remediation.

In summary, all the evidences such as visual colour change, reduced adsorption capacity and reduced sheet-resistance (increased conductivity) confirms the partial reduction of GO to rGO in composite. This increase in conductivity facilitates charge transfer between TiO₂ and underlying reduced graphene and prohibit charge carrier recombination which results in dramatic increase in photocatalytic degradation rate. Therefore it seems critical to reduce graphene oxide in the composite to benefit from both adsorption properties of graphene and conductivity at the same time.

5.2.6. Thermal and Hydrothermal reduction of GO in GO/TiO₂ composite

Since photocatalytic reduction is not very practical way of reduction from energy consumption point of view and low yield as well as material loss during recovery therefore we tried thermal and hydrothermal reduction methods and compared their photocatalytic properties. We chose 5 wt% of both type of nanoparticle/GO composite and calcined one-half of it in inert atmosphere at 450 °C for two hours (samples with CA suffix) and another half was treated hydrothermally at 170 °C for 20 hours (HT suffix) which explained in materials and methods in detail. The photocatalytic degradation of diclofenac in presence or in the absence of the 8 composites with catalyst dosage of 0.3 mg/L and 100 mg/L diclofenac during the studied photoperiod (240 min) is presented in Figure 5-19. Under UV irradiation and absence of photocatalyst (photolysis), diclofenac underwent very slow dissipation as compared to the reaction rates in the presence of catalysts. The final diclofenac carry over in photolysis experiment is about 13.2 %. Photocatalytic degradation of Diclofenac follows the pseudo-first-order reaction kinetics as plotted in Figure 5-19 B and D. The results show that the apparent rate constant is remarkably enhanced by reducing treatment of the composite samples and for both type of composites, the hydrothermally treated sample shows the highest activity under UV irradiation. The apparent rate constant ($k_{app} = 37 \times 10^{-3} \text{ min}^{-1}$) for GO-PS-5 wt% composite catalyst which hydrothermally reduced is much higher than that of pure TiO₂ ($k_{app} = 4.32 \times 10^{-3} \text{ min}^{-1}$). Similar enhancement was observed for GO-P25-5 wt% sample as well.

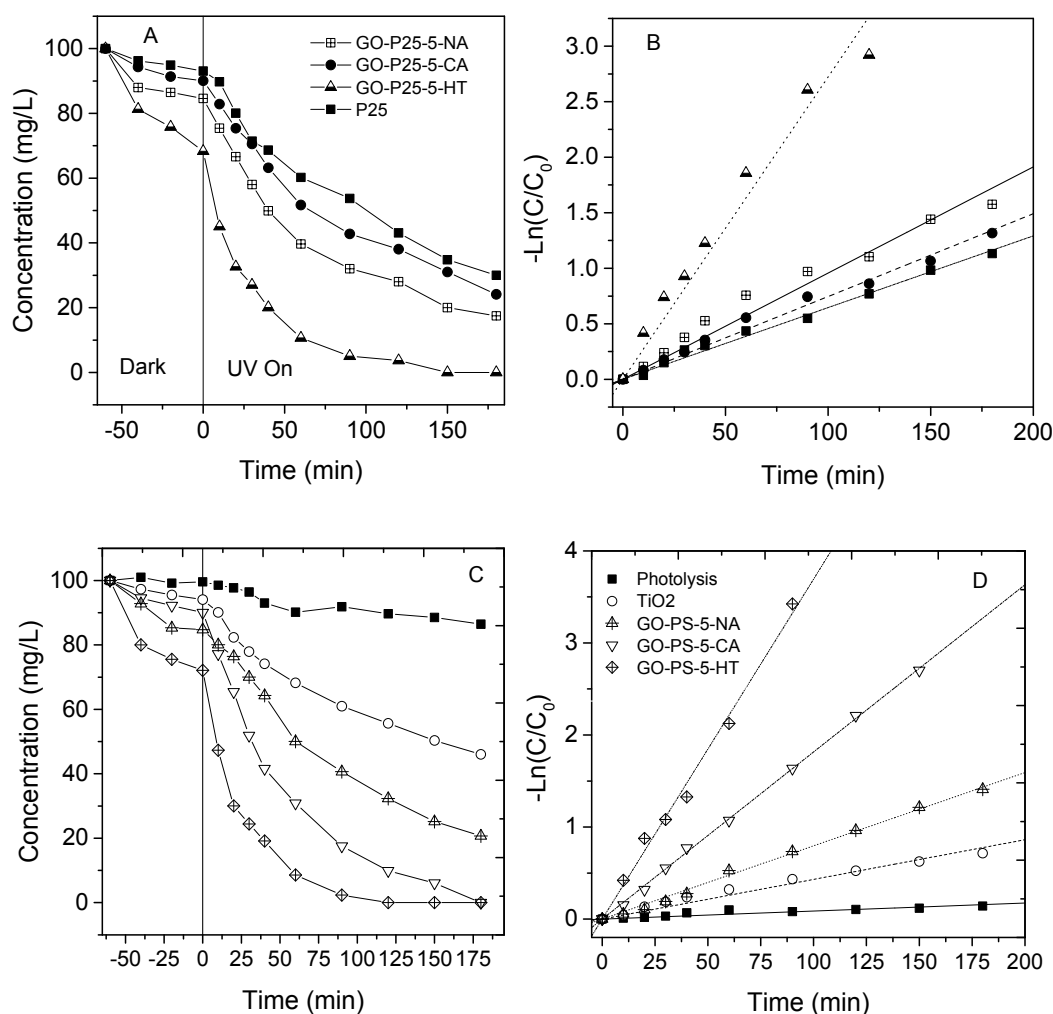


Figure 5-19: Dark and UV removal of 100 mg/l of Diclofenac (A, C) with degradation kinetic plots (B, D) for GO-P25-5 wt% and GO-PS-5 wt% as-synthesised composite compared with annealed and hydrothermally treated samples. Photolysis of diclofenac without any catalyst and pure P25 and TiO₂ synthesised powder as reference is also included.

However for the P25 composite the annealed samples has lower activity comparing the as-synthesised sample. This can be due to the particle growth since the initial P25 is crystalline therefore annealing cannot improve photocatalytic activity further. This deteriorates the rate of degradation even though graphene oxide reduced to graphene this still could not overcome the drawback of TiO₂ growth. Plotting the degradation efficiency versus time (Figure 5-20) shows that both composites which was hydrothermally reduced were reached 100% of degradation. Table 5-7 lists the photocatalytic kinetic parameters of diclofenac degradation such as apparent rate constants, r-squared and half-lives ($t_{1/2}$) for 5 wt% composites under different thermal treatments as well as their pure TiO₂ powder. Among all sample hydrothermally treated GO-PS-5 wt% composite with rate constant of $k_{app} = 37 \times 10^{-3} \text{ min}^{-1}$ is the most efficient composite

compared to its pure TiO_2 powder with rate of 4.32 min^{-1} . Although three composites including GO-P25-5-HT, GO-PS-5-HT and GO-PS-5-CA reached 100 % of removal within the experiment time however comparing their rate constant which are $27.2 \times 10^{-3} \text{ min}^{-1}$, $37 \times 10^{-3} \text{ min}^{-1}$ and $18.7 \times 10^{-3} \text{ min}^{-1}$ and their $t_{1/2}$ which are 19, 16 and 37 min respectively revealed that sol-gel synthesised composite which was reduced by hydrothermal treatment is the most active photocatalyst for degradation of diclofenac in shorter irradiation time. Therefore, the efficiency of the catalysts is arranged in the order: GO-PS-5-HT > GO-P25-5-HT > GO-PS-5-CA > GO-P25-5-NA > GO-PS-5-NA > GO-P25-5-CA > P25 > TiO_2 .

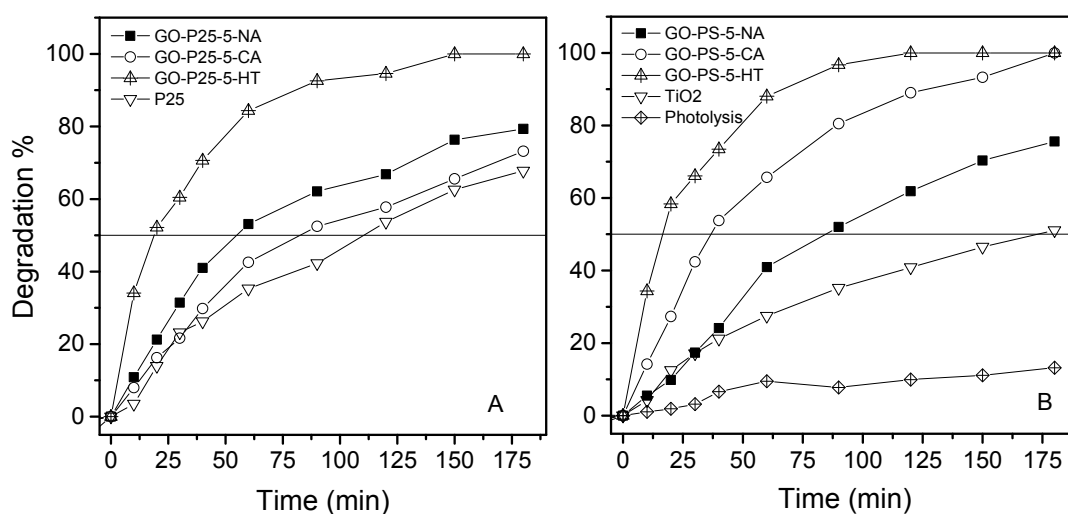


Figure 5-20: Degradation efficiency of as-synthesised GO-P25-5 wt% (A) and GO-PS-5wt% (B) comparing reduced composite by thermal and hydrothermal treatments. The straight line defines the $t_{1/2}$ which is the time that 50% of diclofenac is being degraded

Table 5-7: Surface area and Photocatalysis parameter of as-synthesised GO-P25-5 wt% and GO-PS-5wt% composite and reduced composite by thermal and hydrothermal treatment

Sample	C_0 (mg/L)	% Removal	$t_{1/2}$ (min)	$K_{app} \times 10^{-3}$ (min^{-1})	R^2
GO-P25-5-NA	84.8	79.3	55	9.5	0.985
GO-P25-5-CA	90.05	73.2	82	7.46	0.993
GO-P25-5-HT	68.3	100	19	27.2	0.985
P25	93.05	67.7	110	6.46	0.99
TiO_2	94.1	51.08	173	4.32	0.98
GO-PS-5-NA	84.67	75.57	85	7.96	0.99
GO-PS-5-CA	90.03	100	37	18.7	0.99
GO-PS-5-HT	72.11	100	16	37	0.998
Photolysis	99.6	13.2	NA	0.87	0.93

In order to investigate the reason why hydrothermal treatment is more efficient than thermal reduction we analysed the physical properties of each sample by N₂ adsorption isotherms as shown in Figure 5-21 and their BET specific surface area, pore volume and pore size were summarized in Table 5-8. It can be seen that GO-P25 samples are mainly contains large pores > 20 nm however sol-gel synthesised GO-PS is mesoporous with narrow pore size distribution < 4 nm before and after treatment. If arrange sample by the surface area (GO-P25-5-HT > GO-PS-5-NA > GO-PS-5-HT > GO-P25-5-NA > GO-PS-5-CA > GO-P25-5-CA) we observed that hydrothermally treated samples have higher surface area comparing to the annealed samples. This can be explained by the presence of water in the system during hydrothermal treatment which prevents re-aggregation of the samples. For sol-gel GO-PS-5 wt% sample the as-synthesised one has the highest surface area comparing to the hydrothermal and thermally reduced samples. This can be due to crystallisation and growth of TiO₂ during the treatment which reduces the surface area. However the extraordinary high surface area (338 m²/g) of GO-P25-5-HT could not be explained since both type of treatment are expected to reduced surface area to somewhat. Therefore we imaged both hydrothermally treated samples by TEM as shown in Figure 5-22. For GO-PS-5 wt% (A, B) TiO₂ particles are anchored to the surface of graphene quite uniformly without any free TiO₂ particle in image. The shape of these particle are spherical with the average size of 10 nm. If we compare this with the TEM image of the as-synthesised GO-PS-5 wt% without any treatment (Figure 5-4) we see that particles are slightly larger and spherical instead of spindle morphology observed for the as-synthesised material. This can be due to recrystallization of the particles under hydrothermal pressure which can be resulted to the smaller surface area. However hydrothermal treatment of GO-P25-5 wt% sample (C, D) comparing the as-prepared mixed sample (shown in TEM images of Figure 5-7) resulted considerable changes in the morphology and structure of both TiO₂ and composite. Firstly in contrast with the as-prepared sample we did not observe any free TiO₂ particle in the image which was not attached to the surface of graphene. So one good aspect of hydrothermal treatment is strengthening the bonding between TiO₂ and underlying graphene sheet via applying heat and pressure. Therefore, beside the reduced resistivity due to hydrothermal reduction of graphene oxide, the significantly enhanced photocatalytic performance of hydrothermally treated samples can be attributed to the strong coupling between TiO₂ and graphene.

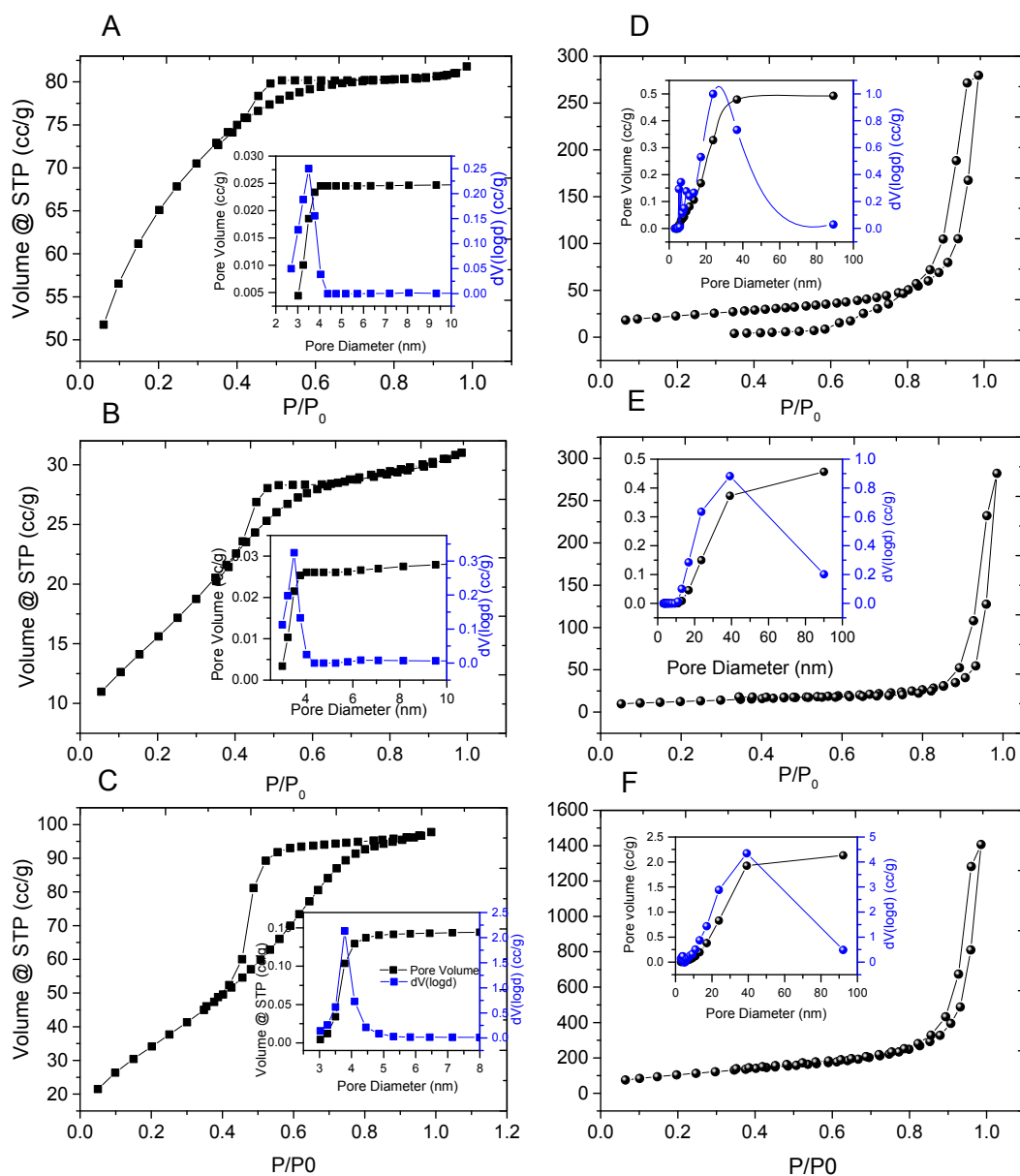


Figure 5-21: N₂ adsorption isotherms and their corresponding BJH pore size distribution (inset graphs) of sol-gel synthesised GO-PS-5 wt% (A, B and C) and GO-P25-5 wt% (D, E and F) as-synthesised, calcined at 450 °C and hydrothermally treated respectively from top to bottom

Table 5-8: BET Surface area and BJH pore size distribution data of as-synthesised GO-PS-5 wt% and GO-P25-5 wt% and after thermal and hydrothermal treatment

Sample	BET surface area (m ² /g)	Total pore volume (cc/g)	Average pore size (nm)
GO-PS-5 wt%	210.4	0.027	3.2
GO-PS-5-CA wt%	60.35	0.031	3.5
GO-PS-5-HT wt%	134.5	0.15	3.78
GO-P25-5 wt%	78.63	0.493	5.28
GO-P25-5-CA wt%	43.11	0.456	23.8
GO-P25-5-HT wt%	338	2.133	23.8

Secondly, P25 TiO₂ nanoparticles look quite uniform and there is no lump or agglomerated particle in the image. So the increase in surface area can be due to the de-bundling of TiO₂ particles due to the pressure of the supercritical water which increase the surface area of the composite. Another feature of this TEM image is elongation of TiO₂ particles which increases the aspect ratio which can be resulted the increase in surface area.

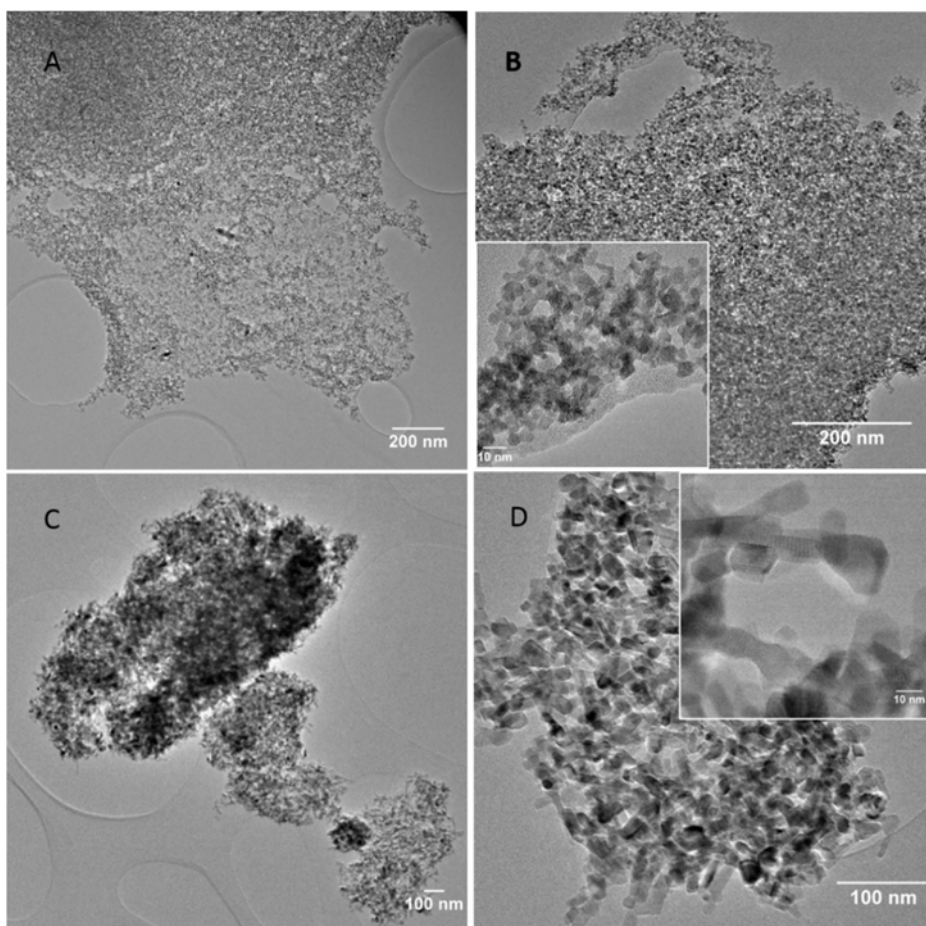


Figure 5-22: TEM images of GO-PS-5 wt% (A, B) and GO-P25-5 wt% (C, D) hydrothermally treated at 170 C for 20 hrs

SEM images of GO-PS-5 wt% and GO-P25-5 wt% after hydrothermal treatment (A, C) and annealing (B, D) respectively are shown in Figure 5-23. While hydrothermally treated GO-PS-5 wt% (A) is more uniform with uniform graphene distribution between layers, the annealed sample looks more dense and agglomerate. This results in easy re-dispersion of hydrothermally reduced samples in water for photocatalysis experiment and provides more surface area for adsorption and catalysis which is in good agreement with BET surface area analysis.

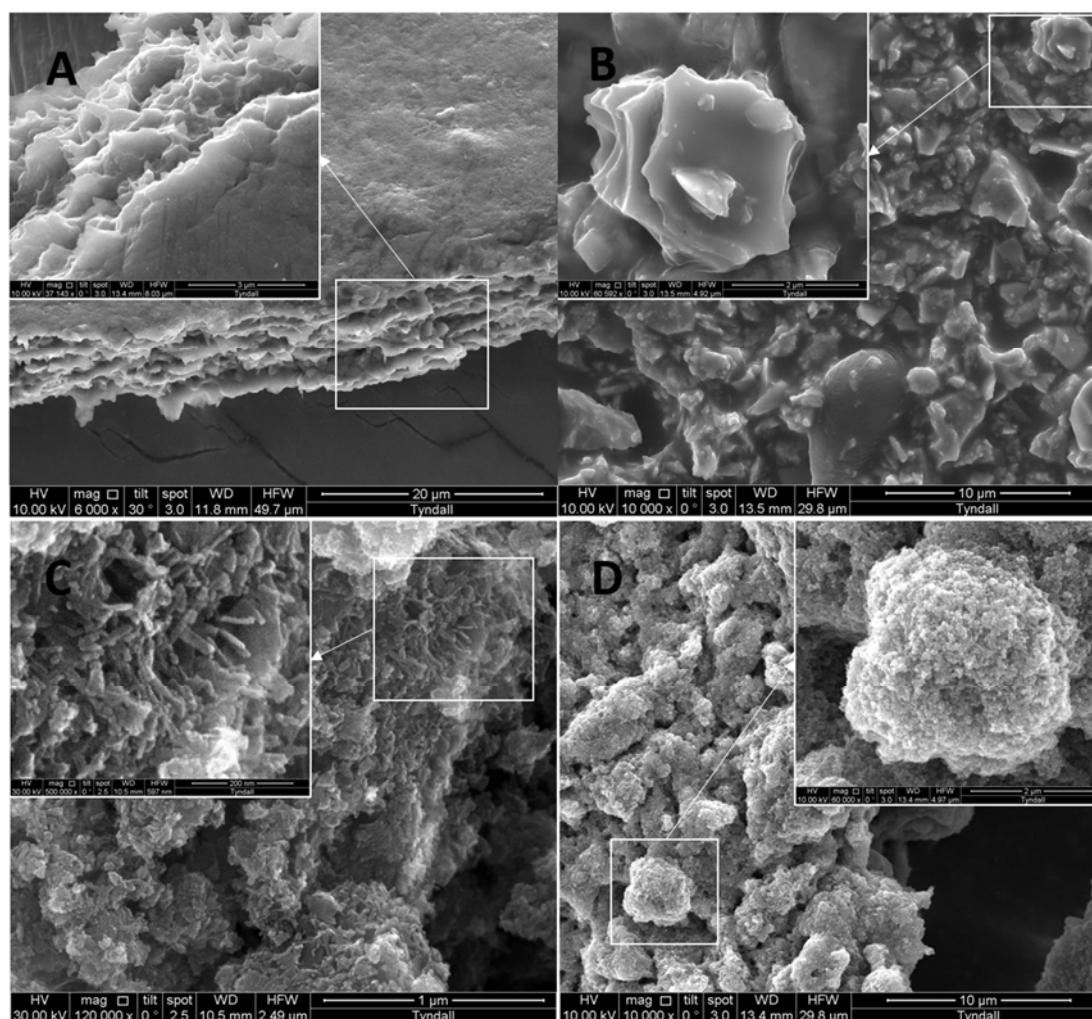


Figure 5-23: SEM images of GO-PS-5 wt%, hydrothermally reduced (A) and calcined (B) and GO-P25-5 wt%, hydrothermally reduced (C) and calcined (D).

SEM images of GO-P25-5 wt% after hydrothermal treatment shows elongation of TiO_2 into very short nano-rods exactly as confirmed by TEM images shown Figure 5-22. We suggested that this particular growth of nano-particles to nano-rods might be due to temperature and pressure inside the vessel which promotes TiO_2 growth along with their preferential direction. This special morphology might be the reason of high surface area and photocatalytic activity of GO-P25-5-HT sample. However for GO-P25-5 wt% sample which was annealed at 450 °C the particulate morphology of TiO_2 with large agglomerated particle can be distinguished. For both type of composites calcination resulted in more lumpy and agglomerated materials which have less surface area comparing their original powder without ant treatment. This is absolutely in agreement with the BET surface area data in Table 5-8. In order to see how annealing dramatically decreases the accessible surface area we performed N_2 adsorption on so-gel synthesised GO-PS composite containing 20 wt% graphene oxide before and after calcination which the surface area and pore information data is reported in Table 5-9.

As discussed previously increasing graphene oxide content increases the total surface area of the composite for example TiO₂/GO composite containing 5 wt% of GO (GO-PS-5 wt%) has surface area of 210 m²/g and pore volume of 0.027 cc/g while increasing the GO content up to 20 wt% increases the surface area to 554 m²/g and 0.797 cc/g respectively. However after annealing GO-PS-20 wt% sample the surface area and pore volume were dramatically decreased to 177 m²/g and 0.043 cc/g. This results in agreement with previous data on annealed samples confirm that annealing TiO₂/GO composite is not suitable method to crystallise TiO₂ and reduce graphene oxide due to the loss of porosity and encouraging agglomeration of the resulting powder which results in less accessible surface area for adsorption of pollutants and light.

Table 5-9: BET Surface area and BJH pore size distribution data for GO-PS-20 wt% before and after calcination

Sample	BET surface area (m ² /g)	Total pore volume (cc/g)	Average pore size (nm)
GO-PS-20 wt%	554.08	0.797	3.78
GO-PS-20-CA wt%	176.98	0.043	3.47

It should be noted that in addition to the surface area, morphology and porosity, the crystalline structure of TiO₂ plays an important role in photocatalysis activity. It has been found that anatase phase shows higher UV photocatalytic activity due to higher band gap (3.2 eV versus 3.0 eV for rutile) which reduces the rate of electron-hole recombination. Also the smaller the crystallite size the higher photocatalytic activity^{384,385}. In order to check TiO₂ phase and crystallinity XRD patterns of as-synthesised GO-PS-5 wt% and its hydrothermally treated and annealed form in comparison with GO-P25-5 wt% and its reduced forms are presented in Figure 5-24. Comparing the two type of composite shows that sol-gel synthesised composite has smaller crystallite size as discussed previously in section 5.2.2. The smaller crystallite size result in noisy patterns with smaller peak-to-peak ration. In both composite small amount of rutile exist which is almost equal in both type of composite. Calcination and hydrothermal treatment slightly changed the crystallite size of anatase which might be due to crystallisation of the amorphous phase in composite which hinders the growth step. However hydrothermal treatment increases the crystallinity of P25 TiO₂ particles while the phase composition stays stable. Therefore it can be concluded that the difference between photocatalytic activity of composites after calcination and hydrothermal treatment it is more related to the porosity and surface area rather than crystallite structure. Also another important characteristic which may be related to the improved photocatalysis of hydrothermally treated over calcined sample is the

electrical resistivity. We explained previously that in addition to crystallisation of TiO₂, the main purpose of the post-treatment is to reduce graphene oxide to graphene to increase the conductivity of the composite which will affect charge transfer and separation within particles. Accordingly four-point probe resistivity measurements showed that the resistivity of as-synthesised GO-PS-5 wt% ($1.5 \times 10^3 \pm 500 \text{ K}\Omega.\text{sq}^{-1}$) considerably decreased to $250 \pm 20 \text{ K}\Omega.\text{sq}^{-1}$ for calcined sample and to that $110 \pm 12 \text{ K}\Omega.\text{sq}^{-1}$. The lower resistivity in hydrothermally treated sample can be due to the homogeneous distribution of graphene sheets layered within the composite as shown in SEM images of Figure 5-23 and also higher degree of reduction under supercritical conditions. The lower resistivity (higher conductivity) enhances charge transfer which results in higher photocatalytic activity.

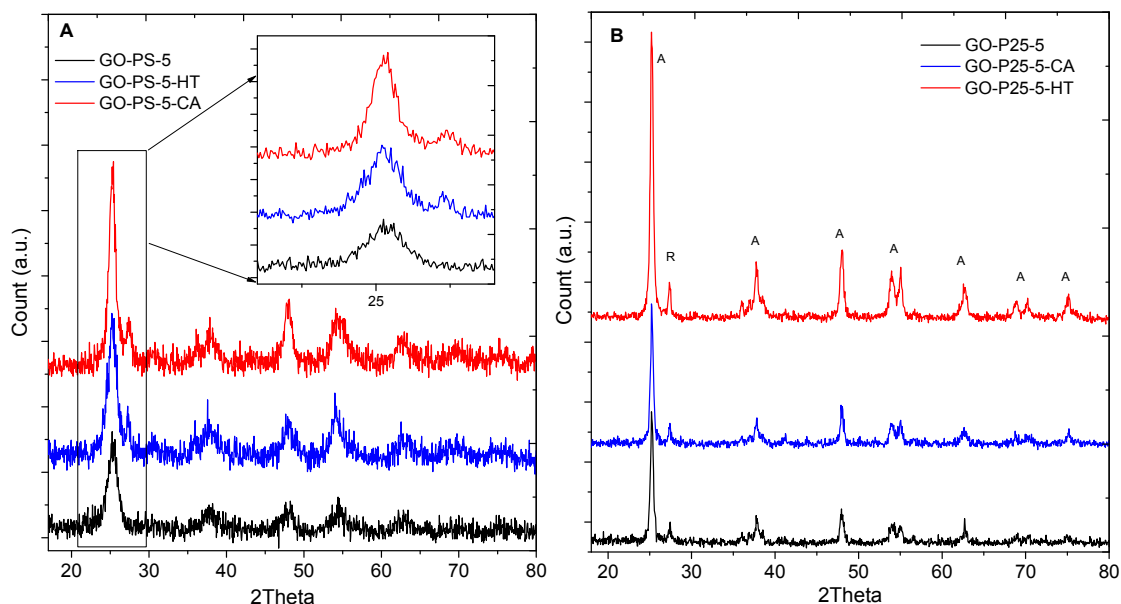


Figure 5-24: X-ray diffraction patterns of GO-PS-5 wt% (A) and GO-P25-5 wt% (B) composites before and after hydrothermal (HT) and calcination (CA)

CHAPTER 6: TiO₂ Nanotubes/graphene composite

Synthesis and Photocatalytic properties

6.1. Introduction

Few different approaches have been used so far to synthesize TiO₂ modified graphene nanocomposites with the highest photocatalytic efficiency especially within extended light wavelength to visible range. It has been reported that, TiO₂-carbon nanotube composites show enhanced photocatalytic activity because of facilitated electron transfer from TiO₂ to highly conductive carbon nanotubes (CNTs) which prohibits electron-hole recombination³⁸⁶. The expensive cost of CNTs, metal catalyst impurities and difficult de-bundling of CNTs limits the potential application of CNTs in large scale particularly for water treatment. In contrast, graphene is much cheaper, easy to make in large scale with lower price without any impurity. Therefore our approach in this chapter is to use graphene as the conductive platform and synthesis TiO₂ in the form of nanotube to provide maximum interfacial contact between graphene and TiO₂ instead of using expensive CNTs. In contrast to TiO₂ nanoparticles, TiO₂ nanotubes (TNTs) have larger surface area (inner and outer surface) and larger aspect ratio which increase the contact between TiO₂ and graphene. Larger interfacial contact between TNTs and graphene should favour charge separation, and the high aspect ratio of TNTs enhances the photocatalytic activity²²⁸. Although, there have been numerous attempts to prepare different photocatalysts with reduced graphene-TiO₂, there are currently no reports on growing TiO₂ nanotubes on reduced graphene sheets in one pot. Also there has been no report on comparing one dimensional TiO₂ nanotubes and nanofibers immobilised on the surface of graphene with graphene/TiO₂ nanoparticle composites.

Herein, we report a facile hydrothermal route to produce TiO₂ nanotubes and nanofibers then immobilising them on the surface of graphene oxide and reducing GO to rGO via the second hydrothermal treatment or thermal treatment. In another method we used one pot route to synthesise TiO₂ nanotubes in-situ on the surface of reduced graphene oxide via hydrothermal treatment in strong alkaline solution. While TNTs were grown on the GO surface, a

simultaneous reduction of GO to rGO was observed. We reported that rGO/TiO₂ nanotube (rGO-TNT) composites exhibit excellent photocatalytic activity towards decomposing famotidine drug under both UV and visible light while rGO/TiO₂ nanoparticles show very low visible light efficiency. This enhancement can be due to facilitated charge transfer via larger interface of TiO₂ as well as improving the charge separation via conductivity pathways on graphene.

6.2. Results and Discussion

6.2.1. TiO₂ nanotubes

As described previously in materials and methods chapter (section 3.6.2), TiO₂ nanotube synthesis were optimised by varying hydrothermal treatment temperature and time. The morphology of the resulting TNTs were identified by TEM and SEM imaging. It was observed that formation of TNTs happens in hydrothermal treatments above 110 °C which is in agreement with other reports.^{387,388}

In order to obtain optimum temperature to synthesise TNTs with the hollow structure with the highest aspect ratio TEM images of as-synthesised TNTs were collected. As shown in Figure 6-1A at 110 °C still some nanoparticles, as well as a kind of amorphous titanium oxide material can be observed on the nanotube and nanosheets surfaces which indicates that the temperature is not high enough to initiate large enough nanosheets necessary for nanotubes formation. Also small nanosheets can be found in sample which is not rolled into tubular form because of the small size of the sheets. By increasing the temperature up to 130 °C nanotubes have more pronounced feature with thin walls and loose structure. They more look like curled sheets which could not completely close up to nanotubes and they also have quite short length (smaller than 500 nm). At higher temperatures (180 °C) nanofibers form with large aspect ratio (length > 1 µm) as shown in Figure 6-1C. The resulting powder contains nanofibers that are mostly joined in bundles with average diameter of 100 nm and individual nanofibers diameter of 30-50 nm (as also shown in Figure 6-13) and length of 3-5 µm. They do not have inner channels which obviously will provide less available catalytic surface area.

Therefore to have high aspect ratio but hollow tubular structure we can guess that ideal temperature is between 110 < T < 180 °C. Figure 6-2 shows schematically how morphology of the resulting powder varies by adjusting hydrothermal treatment parameter or post processing condition ranging from nanosheets to nanotubes and nanofibers¹⁰¹. In low temperature formation of nanosheets are favourable however the aspect ratio increases with increasing

temperature and in temperatures higher than 150 °C they tend to crystalline into more bulky structures.

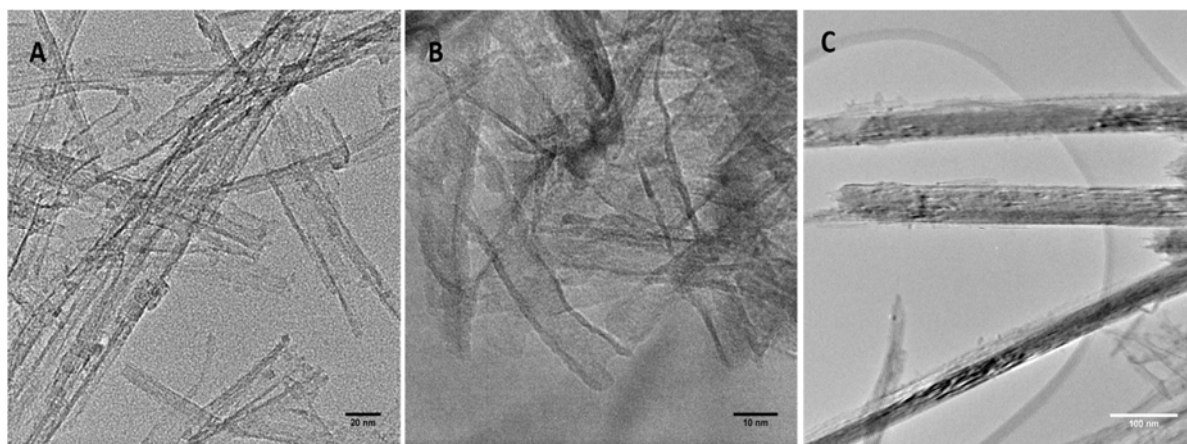


Figure 6-1: TEM images of TNTs formed by 24 hrs of hydrothermal treatment at 110, 130, 180 °C for A, B and C respectively.

Figure 6-3 shows a representative TEM images of the optimum TNTs sample synthesised by hydrothermal treatment at 150 °C for 24 hours. Nanotubes have a distinguished geometry, that is, long cylinders with a hollow cavity lying though the centre along their length. The aspect ratio (i.e., length divided by diameter) of nanotubes is usually greater than ten and can achieve several thousands. The walls of titanate nanotubes are always multi-layered and the number of layers varies from two to ten. The as-synthesised nanotubes are usually straight and tend to curl up after thermal or hydrothermal post-treatment. It should be noted that no sign of TiO₂ aggregates were observed after hydrothermal treatment, which might be due to complete dissolution of TiO₂ particles during the hydrothermal treatment and reforming into titanate nanosheets which were rolled into TNT during the acid treatment. However XRD results shows small amount of anatase in TNT structure. Therefore this can be as a result of efficient de-agglomeration of TiO₂ particles during alkaline treatment. TEM image (Figure 6-3 A and B) demonstrate that TNTs contain entangled multi-walled nanotubes with number of walls ranging from 4 to 8 layers. Nanotubes have lengths up to 1-3 μm , outer diameters between 15 and 20 nm and inner diameters of 10-12 nm. As also confirmed by SEM images in Figure 6-4, the resulting TNTs are quite uniform in diameter and straight.

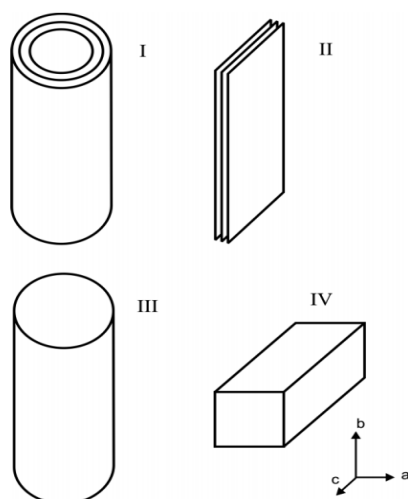


Figure 6-2: Four different morphologies observed during alkaline hydrothermal reaction of TiO_2 . Nanotubes (I), nanosheets (II), nanorods or nanowires (III), and nanofibers or nanobelts (IV). a, b and c are crystallographic axes³⁸⁹.

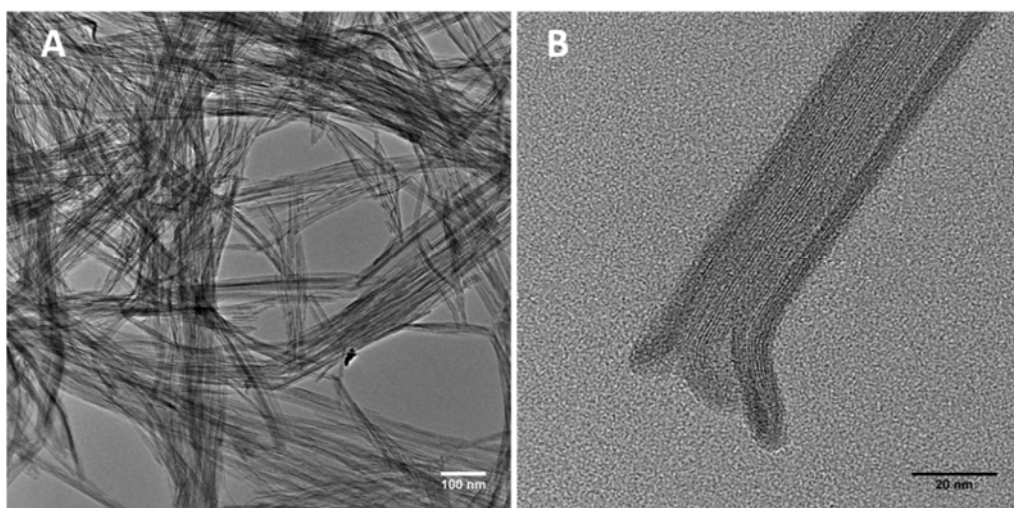


Figure 6-3: TEM images of TNTs hydrothermally synthesised TNTs at 150 °C for 24 hrs. HRTEM image of B shows that TNTs are 15-20 nm in outer diameter and 3 nm thick walls composed of multi layers of titanate sheets rolled into micron length TNT nanotubes

The crystalline structure of the samples was studied by XRD and Raman spectroscopy (Figure 6-5). Raman spectra of as- synthesised TNTs after washing and without any further treatment and sample which was hydrothermally treated at 150 °C for 24 hours (TNT-HT) are shown in Figure 6-5. The results were compared with the Raman spectra of commercial P25 powder as starting material for TNTs synthesis. As described previously (section 5.2.2), standard single crystalline anatase shows six Raman active vibrational modes, located at 144 (E_g), 197 (E_g), 399 (B_{1g}), 513+519 ($A_{1g}+B_{1g}$), and 639 (E_g) cm^{-1} . For commercial P25 TiO_2 , six Raman

active modes appear at 140 cm^{-1} (E_g), 193 cm^{-1} (E_g), 393 cm^{-1} (B_{1g}), 513 cm^{-1} ($A_{1g} + B_{1g}$), and 634 cm^{-1} (E_g).

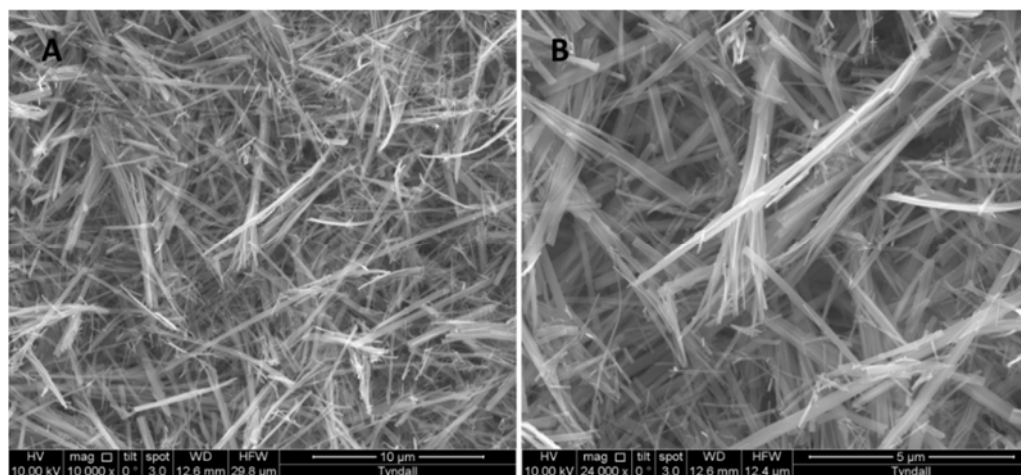


Figure 6-4: SEM images of hydrothermally synthesised TNTs at 150 °C for 24 hrs

As-synthesised TNTs sample shows features at 165 , 265 , 288 , 450 and 664 cm^{-1} which are typically detected in hydrothermally synthesized titanium oxide nanotubes. The origin of these bands is not completely clear, but is usually associated with Ti-O-Ti crystal phonons in titanate structures^{387,390,391}. Comparing the vibration bands of as-synthesised TNT with P25 shows the presence of three completely different peaks at 266 , 289 and 450 cm^{-1} which is attributed to the vibration modes of titanate sheets. However peaks at 165 and 664 cm^{-1} can be assigned to anatase E_g vibration bands with 25 and 30 cm^{-1} blue shift respectively. This blue shift might be related to the small crystallite size, doping effect or oxygen deficiency of nanotubes. These two set of vibration modes can be as a result of having a mixture of crystalline anatase and titanate nanosheets. The presence of the anatase bands in as-synthesised TNTs could be related to very small and undissolved particles of P25 precursor or intrinsic vibration of anatase TNTs structures. After second hydrothermal treatment titanate bands disappear completely and the resulting spectrum corresponds to anatase TiO_2 modes and matches with vibration bands of starting P25 powder. Although the intensity of anatase bands in hydrothermally treated titanium oxide nanotubes (TNT-HT in Figure 6-5B) is much lower than in crystalline anatase in P25 which is due to small crystallite size.

XRD patterns of as synthesised TNTs (TNT) and post-treated samples (TNT-CA: calcined at 450 °C for 2 hours and TNT-HT: post-hydrothermal treatment at 150 °C for 24 hours) with standard P25 TiO_2 samples are displayed in Figure 6-5. For TNT sample without any post treatment two main peaks can be identified, one in 2θ at 16° which corresponds to (110) planes of titanate, the second one at 22° corresponds to (211) plane of titanate and third

one is very small peak at 48° related to (020) planes of titanate nanotubes. These features are commonly assigned to titanate structures formulating as $H_2Ti_nO_{n+1}$ ($n = 2, 3, 4$)³⁹²⁻³⁹⁴. There is also a small peak at 25° on the shoulder of titanate (211) which corresponds to (101) plane of anatase TiO_2 . This is in agreement with Raman data which shows the as-synthesised TNT is a mixture of anatase and titanate nanotubes. However the peaks are broad and have low intensity, corresponding to polycrystalline materials composed of very small size crystallites.

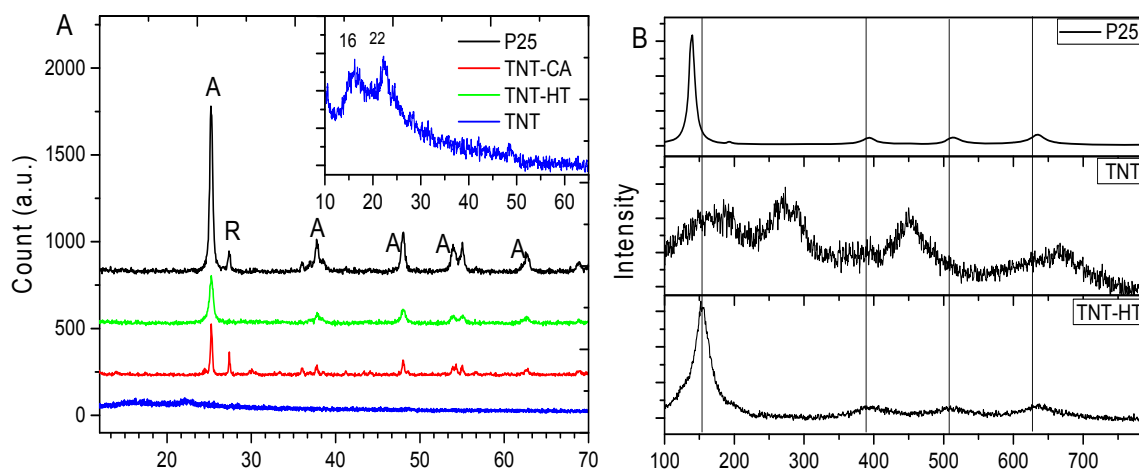


Figure 6-5: (A): XRD of as-synthesised TNTs compared with starting P25 powder, calcined TNTs at $450^\circ C$ for 2 hrs (TNT-CA) and hydrothermally treated TNTs at $150^\circ C$ for 20 hrs (TNT-HT). (B): Raman spectra of as-synthesised TNTs comparing P25 TiO_2 powder and hydrothermally treated TNTs (TNT-HT)

After second hydrothermal treatment titanate nanotubes transforms into pure anatase structure as shown in XRD pattern in accordance with Raman data. TiO_2 powder after calcination at $450^\circ C$ is crystalline mixture of anatase and rutile phases similar to P25 powder but with larger amount of rutile which can be identified from the intensity ratio of (110) peak of rutile $2\theta=27.5^\circ$ to the intensity of (101) peak of anatase at $2\theta=24^\circ$. Since anatase has the highest photocatalytic activity therefore we consider the second hydrothermal treatment the best method for transforming titanate into crystalline TiO_2 nanotube.

SEM images of TNTs (hydrothermal treatment at $150^\circ C$ for 24 hrs) after second hydrothermal treatment (A and B) and after calcination at $450^\circ C$ (C and D) are shown in Figure 6-6. They are both having similar morphology and nanotube size however the hydrothermally treated sample looks less compact and agglomerated which can be due to the presence of critical water during the process which prevent nanotubes from agglomeration.

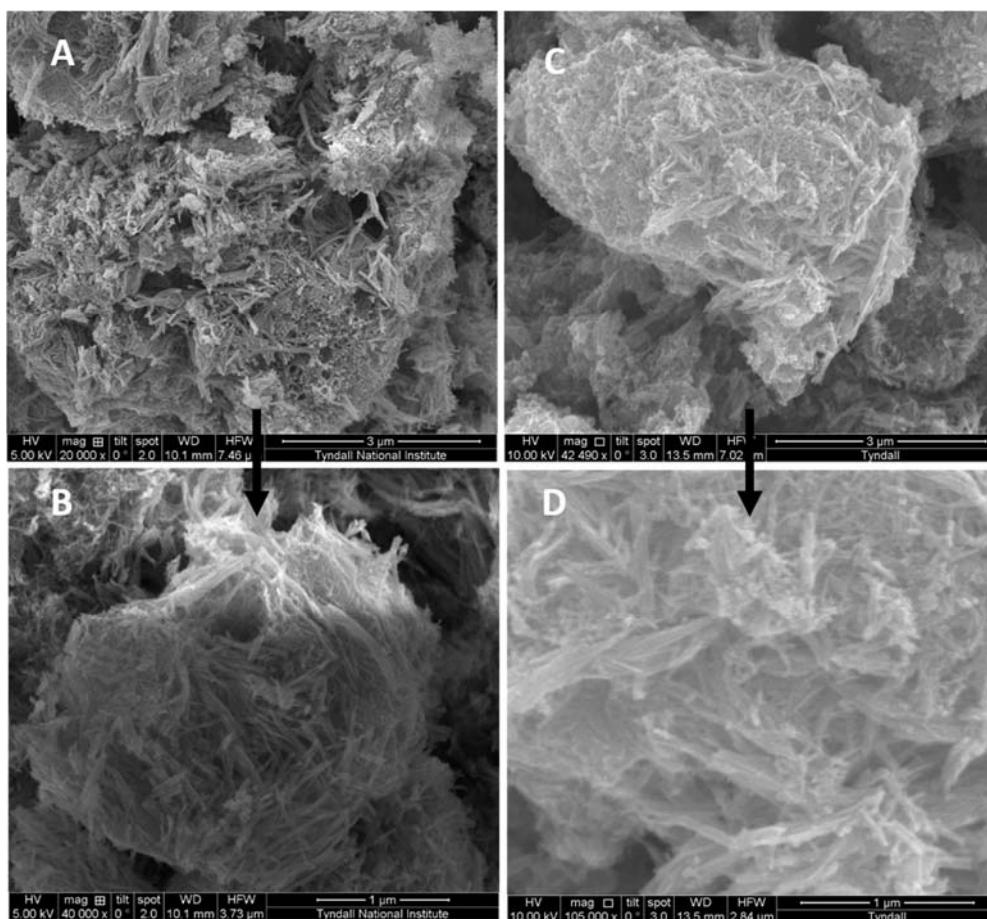


Figure 6-6: SEM images of TNTs synthesised at 150 °C for 24 hrs; (A,B) after second hydrothermal treatment at 150 °C for 24 hrs (TNT-HT). (C, D) after calcination at 450 °C for 2 hrs (TNT-CA)

After optimising synthesis procedure of TiO_2 nanotubes, 10 wt% of graphene oxide was chosen in order to make reduced graphene oxide rGO/TNT composite via three different routes. In first route TNTs which was made at 150 °C washed and then mixed with 10 wt% of GO (GO-TNT) and half of the bath was hydrothermally treated at 150 °C for another 24 hrs in order to crystallise TiO_2 and reduced GO to rGO at the same time (rGO-TNT-HT). The other half was calcined under N_2 atmosphere at 450 °C (rGO-TNT-CA). Through another one pot route, TiO_2 P25 powder was mixed with 120 ml of 10 M NaOH and 10 wt% of GO and loaded into autoclave after 30 min of sonication which then treated hydrothermally at 150 °C for 24 hrs. The resulting powder washed with HCl and water and labelled as rGO-TNP-HT.

In Figure 6-7 TEM images of rGO-TNT-HT (A,C) and rGO-TNP-HT (B, D) are shown. Both composite seem to have similar features, however nanotubes in rGO-TNP-HT sample shows thinner walls than nanotubes in rGO-TNT-HT composite. This can be due to the presence of GO sheets during hydrothermal treatment which prevents stacking of titanate sheets. It can be suggested that TiO_2 nanoparticles after dissolution form titanate nanosheets on the surface of large graphene oxide sheets which has low surface energy rather than stacking on other titanate

sheets which creates multiwall titanate nanotubes. Therefore it could be predicted that in-situ synthesise of titanate nanosheets on the surface of GO will result in more uniform morphology and TiO₂ nanotubes with thinner walls.

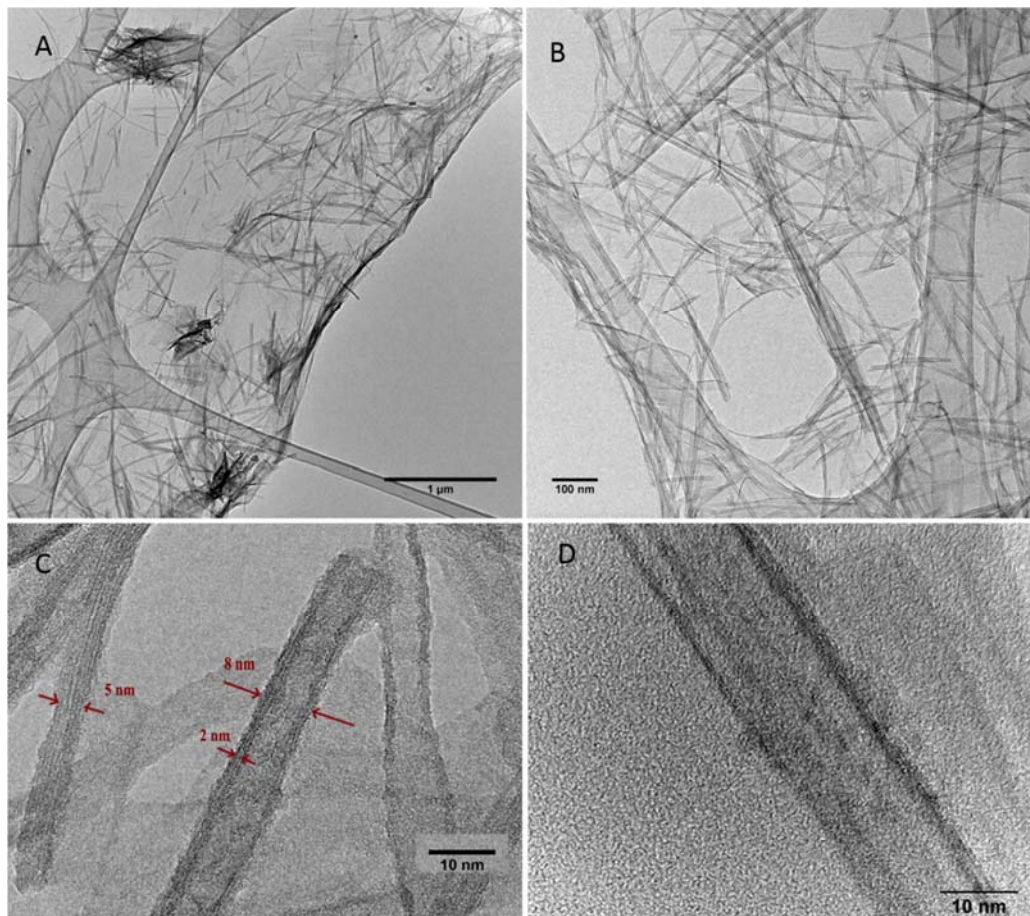


Figure 6-7: (A, C): TEM images of 10 wt% rGO-TNT-HT composite and HRTEM image of nanotubes. (B,D): TEM and HRTEM image of one-pot synthesized 10 wt% rGO-TNP

In Figure 6-8 the XRD patterns of rGO/TNT composites comparing with mixed GO-TNT composite without any post-treatment are plotted. In GO-TNT sample a broad peak around 10 degree is related to (001) plane of graphene oxide which is disappeared after thermal and hydrothermal treatment confirming efficient reduction of GO to rGO. It was also observed that diffraction peaks related to anatase phase are becoming more pronounce upon thermal and hydrothermal treatment however in contrast with the XRD pattern of treated pure TNT shown in Figure 6-5, the diffraction peak at $2\theta=16^\circ$ which corresponds to titanate (110) plane became weaker but is still present in pattern, while in rGO-TNP-HT sample this peak is not detected. This is not clear why (110) peak is present in composite materials after post-treatment while it completely disappeared in pure TNT samples after thermal and hydrothermal post-treatment. However its absence in rGO-TNP sample in agreement with TEM data can confirm that via

one-pot synthesis method single layer titanate nanosheets were produced which efficiently turned into thin mostly single wall TiO_2 nanotubes.

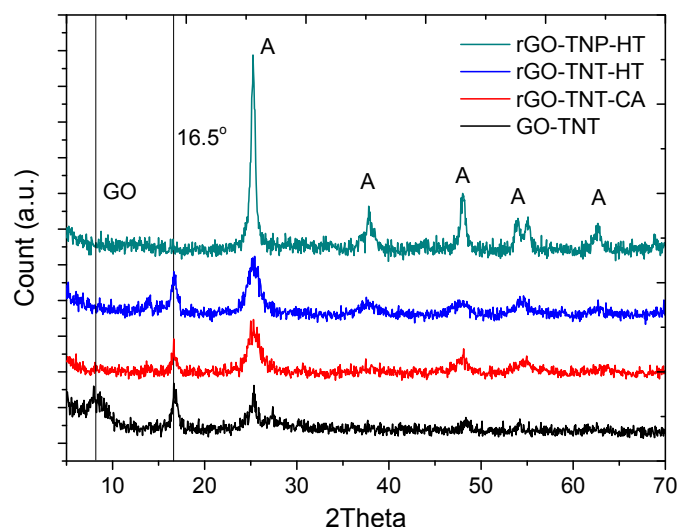


Figure 6-8: XRD of GO and rGO/TNT composite synthesise via different routes

SEM images of the three 10 wt% rGO/TNT composite after thermal and hydrothermal post-treatments in three magnifications (1, 2, 3) are shown in Figure 6-9. Among the three samples rGO-TNT-CA looks less uniform since free graphene oxide sheets can be identified in the image (a2). The samples which reduced hydrothermally (rGO-TNT-HT) is more uniform with less free GO sheet. All three samples have globular morphology which is due to crumbling of GO covered with TiO_2 nanotubes and agglomerated TNTs into spheres. In-situ synthesis of nanotubes on the surface of GO shows some difference in arrangement of nanotubes on the surface of GO. They seem to have more interaction with GO and have less TNT agglomeration which results in more efficient charge transfer from TNTs to the underlying reduced graphene oxide.

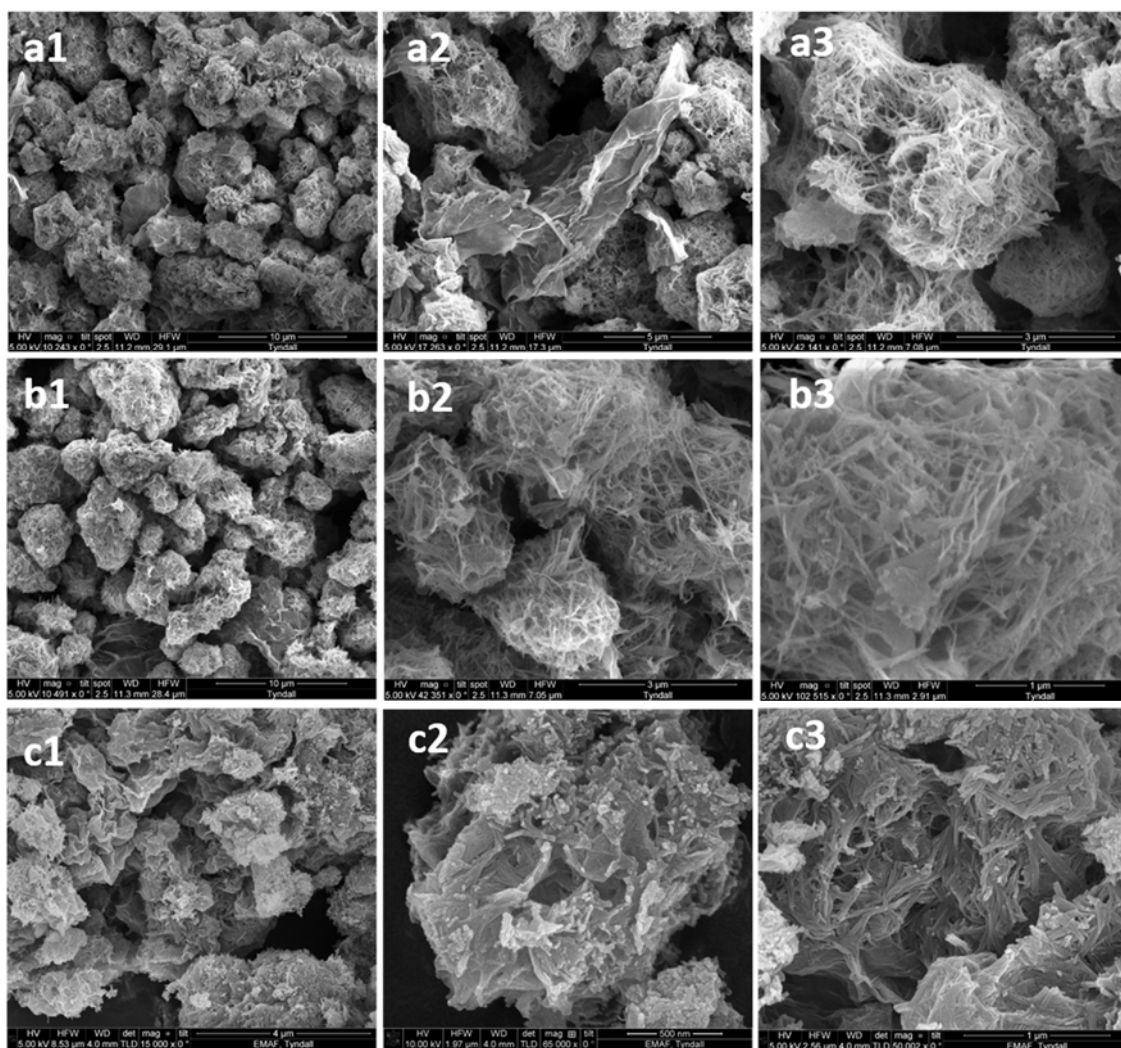


Figure 6-9: SEM images of 10 wt% rGO/TNT composites; rGO-TNT-CA (a1, 2, 3), rGO-TNT-HT (b1, 2, 3), rGO-TNP-HT (c1, 2, 3)

Raman spectroscopy shown in Figure 6-10 also confirms that rGO-TNP-HT contains anatase phase (without any band vibrations of titanate) in combination to rGO. All vibration bands assigned to anatase and the other two peaks in at 1350 and 1600 cm^{-1} are assigned to D (disordered sp^2 carbons) and G (stretching mode of graphite) band of graphene respectively. The higher intensity of G and to D band reveals efficient reduction of graphene oxide to graphene. In order to study the surface area which is very important parameter for catalytic activity, N_2 adsorption/desorption isotherm were collected after degassing samples overnight. Adsorption isotherms of pure TNTs after second hydrothermal treatment as well as three post-treated 10 wt% rGO-TNT composites with their corresponding Barrett–Joiner–Halenda (BJH) pore-size distribution are shown in Figure 6-11. The Brunauer–Emmett–Teller (BET) surface area and total pore volume were estimated to be $339\text{ m}^2\text{ g}^{-1}$ and $1.09\text{ cm}^3\text{ g}^{-1}$, respectively. The isotherm could be classified as a type-IV isotherm, indicating the presence of mesopores. The average

pore size was calculated to be 6.68 nm using BJH method which is in accordance with average inner diameter of TiO₂ nanotubes, as shown in the inset of Figure 6-11.

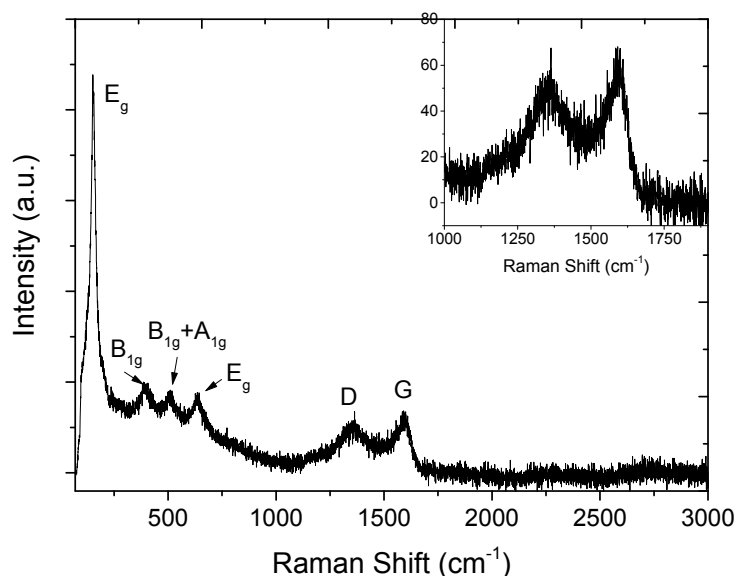


Figure 6-10: Raman spectra of 10 wt% rGO-TNP-HT composite

Specific surface areas, pore volume and average pore width of titanium oxide nanotubes and three rGO-TNT 10 wt% GO were calculated from nitrogen adsorption data and are summarized in Table 6-1. Specific surface areas for both rGO-TNP-HT and rGO-TNT-HT powders is 330 m² g⁻¹. It should be noted that the surface area of pure TNTs and all TNT composites are much larger than its starting P25 commercial powder (30 m² g⁻¹) due to the open mesoporous structure of titanium oxide nanotubes. Pore size distributions for all samples demonstrate the presence of mesopores of < 5 nm, in combination with large macropores corresponding to aggregate pores. Mesopores of <5 nm could be associated to the inner nanotube channels, while large pores could correspond to adsorption sites in the entangled nanotube network and big spaces between the nanotube aggregate or graphene oxide that was observed in SEM images as well (Figure 6-9). Surface areas of the thermally treated sample (rGO-TNT-CA) is around 310 m² g⁻¹, which is slightly lower than the hydrothermally treated samples. This is indicative of the collapse of the nanotube mesoporous structure or agglomeration during the heating.

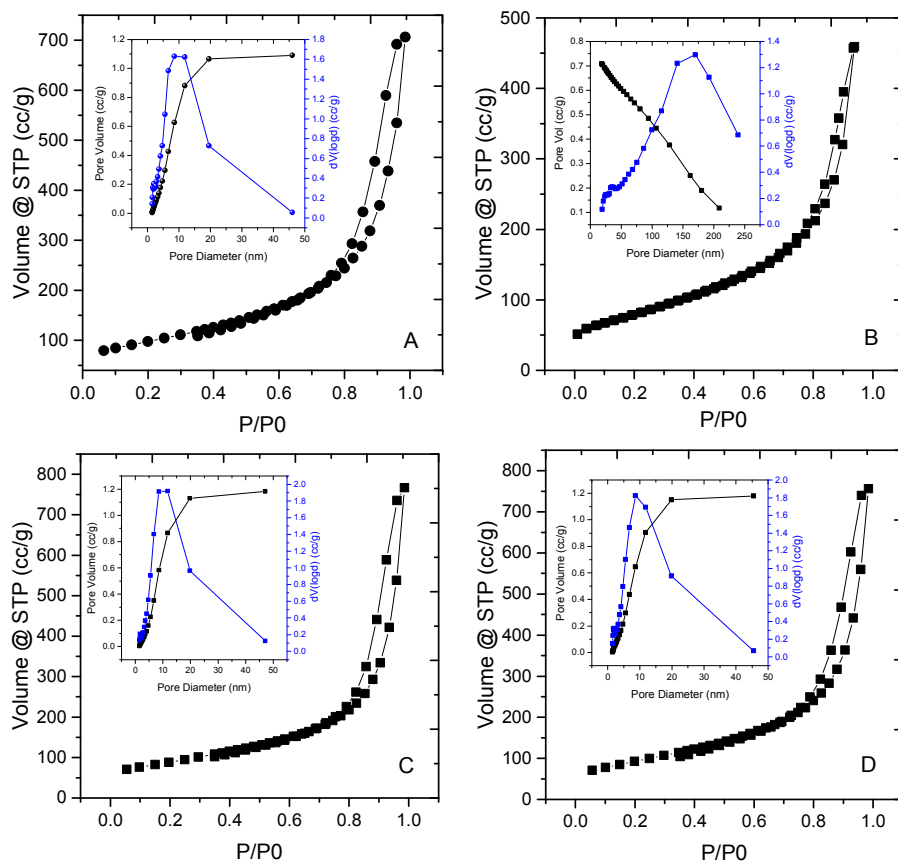


Figure 6-11: N₂ adsorption isotherms of TNTs and 10 wt% rGO-TNT composites prepared via different routes

Table 6-1: BET surface area and pore characterisation of TNT and rGO-TNT composites

Sample	BET surface area (m ² /g)	Total pore volume (cc/g)	Average pore size (nm)
TNT-HT	339	1.09	6.68
rGO-TNP-10 wt%	330	0.71	8.6
rGO-TNT-10-HT	330	1.83	8.5
rGO-TNT-10-CA	310	1.18	6.75

6.2.2. UV and Visible light Photocatalytic Properties

Famotidine was chosen as the model pharmaceutical compound to evaluate the photocatalytic activity of the prepared TiO₂ nanotubes/graphene composites under UV and visible light irradiation ($\lambda > 400$ nm) in comparison with TiO₂ nanoparticle/graphene composites. As we described in Chapter 5, normally photocatalytic degradation follows pseudo-first order kinetics:

$$\ln\left(\frac{C_0}{C}\right) = K_{app} \times t$$

The photocatalytic activities of rGO/TiO₂ nanotube composites (TNT-HT, rGO-TNP-10, rGO-TNT-10-HT, rGO-TNT-10-CA) in comparison with rGO/TiO₂ nanoparticle composites (rGO-PS-10-HT and rGO-P25-10-HT) towards degradation of 35 mg ml⁻¹ of famotidine are shown in Figure 6-12 and the extracted data is summarized in Table 6-2. The degradation rate constant of famotidine without addition of any catalyst (UV and visible photolysis) is 0.0022 and 0.0004 min⁻¹ for UV and visible photolysis respectively. Addition of 0.2 mg. L⁻¹ of TNT-HT catalyst increases the rate constant about 3 times however slightly decreases visible catalytic activity which is due to the decrease in initial concentration adsorbed by the catalyst. However adding same amount of rGO-TNP-HT containing 10 wt% of rGO increases the UV and visible rate constants 17 and 27 times respectively. This composite is the only one among others which removed 100% of the pollutant during the time of experiment with high rate constant (0.013 min⁻¹). The visible rate constant for other composites varies between 0.0003 and 0.003 min⁻¹. This massive enhancement in visible light activity of rGO-TNP composite can be due to dissolution of defected graphene in highly alkaline solution and doping TiO₂ nanotube under critical condition of hydrothermal treatment under heat and pressure. Comparing rate constant and removal efficiencies listed in Table 6-2 shows that nanotube composites degrade famotidine with higher rate than TiO₂ nanoparticle composites. As described in previous section this can be due to larger interface contact between TNTs and underlying graphene which facilitate charge transfer from TiO₂ to graphene and inhibit electron-hole recombination.

Since the size of the UV and visible immersion well reactors were different therefore the volume and catalyst doing were slightly different in both experiment. Also the difference in adsorption capacity of each composite during adsorption to reach equilibrium (as shown in light-off part of Figure 6-12 A and B) which results in different initial concentration for catalysis experiment may interfere with interpreting data correctly. Therefore the rate constants were multiplied by the amount of famotidine which was degraded only by photocatalysis experiment and was used as a scale to compare photocatalytic of each composite correctly without involving adsorption stage. This factor represents how effectively a catalyst can degrade in definite time and involves catalyst dosage and degradation rate together with unit of mg.g⁻¹.min⁻¹ which corresponds to the amount of famotidine (μg) which can be degraded by one gram of catalyst in one minute irradiation time. The result is listed as K_{app}.q × 10⁻³ in Table 6-2. Among all of the composites rGO-TNP shows the highest UV and visible K_{app}.q of 2.6 and 0.77 mg g⁻¹ min⁻¹ respectively. Considering this parameter as a scale, UV photocatalytic activity of all composites listed in Table 6-2 can be ranked as: rGO-TNP-10 >> rGO-TNT-10-HT > rGO-TNT-10-CA > rGO-PS-10-

HT> TNT-HT > rGO-P25-10-HT. The visible activity order of composites is: rGO-TNP-10 >> rGO-TNT-10-HT > rGO-TNT-10-CA and rGO-TiO₂ nanoparticle composites and pure TNT show almost no visible photocatalytic activity. The enhancement in photocatalytic properties of rGO-TNP composites over pure TNTs and other graphene/TiO₂ composites can be described by two different mechanisms. First, visible light can be absorbed by the carbon doped TNT, with electrons transferred from the valence band to the conduction band of TiO₂. The excited electrons can then be transferred to graphene with holes remaining on the surface of TiO₂ taking part in the photocatalysis reactions. This mechanism was first proposed by Hoffmann to describe the photocatalytic enhancement of TiO₂/carbon nanotube composites³⁹⁵. Another explanation is that graphene can absorb visible light and its excited electrons are then transferred to the conduction band of doped TiO₂. Then, the positively charged graphene makes a hole in TiO₂ valence band by removing an electron from it. Positively charged doped TiO₂ can then react with water, producing hydroxyl radicals which would then degrade the organic molecules³⁹⁶. Therefore graphene can act as both photo- sensitizer and also charge trapper resulting in enhancement in photocatalytic activity of synthesized catalysts.

Table 6-2: UV and Visible-light photocatalytic activities of various rGO/TNT composites in comparison with rGO/TiO₂ nanoparticle composites for degradation of famotidine

Sample	UV-Photocatalysis				Solar-Photocatalysis			
	Removal %	$K_{app} \times 10^{-3}$ (min ⁻¹)	R ²	$K_{app} \cdot q$ $\times 10^{-3}$	Removal %	$K_{app} \times 10^{-3}$ (min ⁻¹)	R ²	$K_{app} \cdot q$ $\times 10^{-3}$
Photolysis	32	2.2	0.91	NA	10.5	0.48	0.97	NA
TNT-HT	76.5	7.3	0.90	396.025	8.2	0.37	0.90	4.3845
rGO-TNP-10	100	37.5	0.99	2606.25	100	13.2	0.90	777.48
rGO-TNT-10-HT	100	39.6	0.96	2227.5	43	3.22	0.99	73.1584
rGO-TNT-10-CA	96.8	22.4	0.96	1835.68	37	2.26	0.96	122.492
rGO-PS-10-HT	91	13.7	0.97	905.433	6.6	0.40	0.95	1.98
rGO-P25-10-HT	57.3	4.6	0.96	136.804	7.7	0.48	0.94	2.76

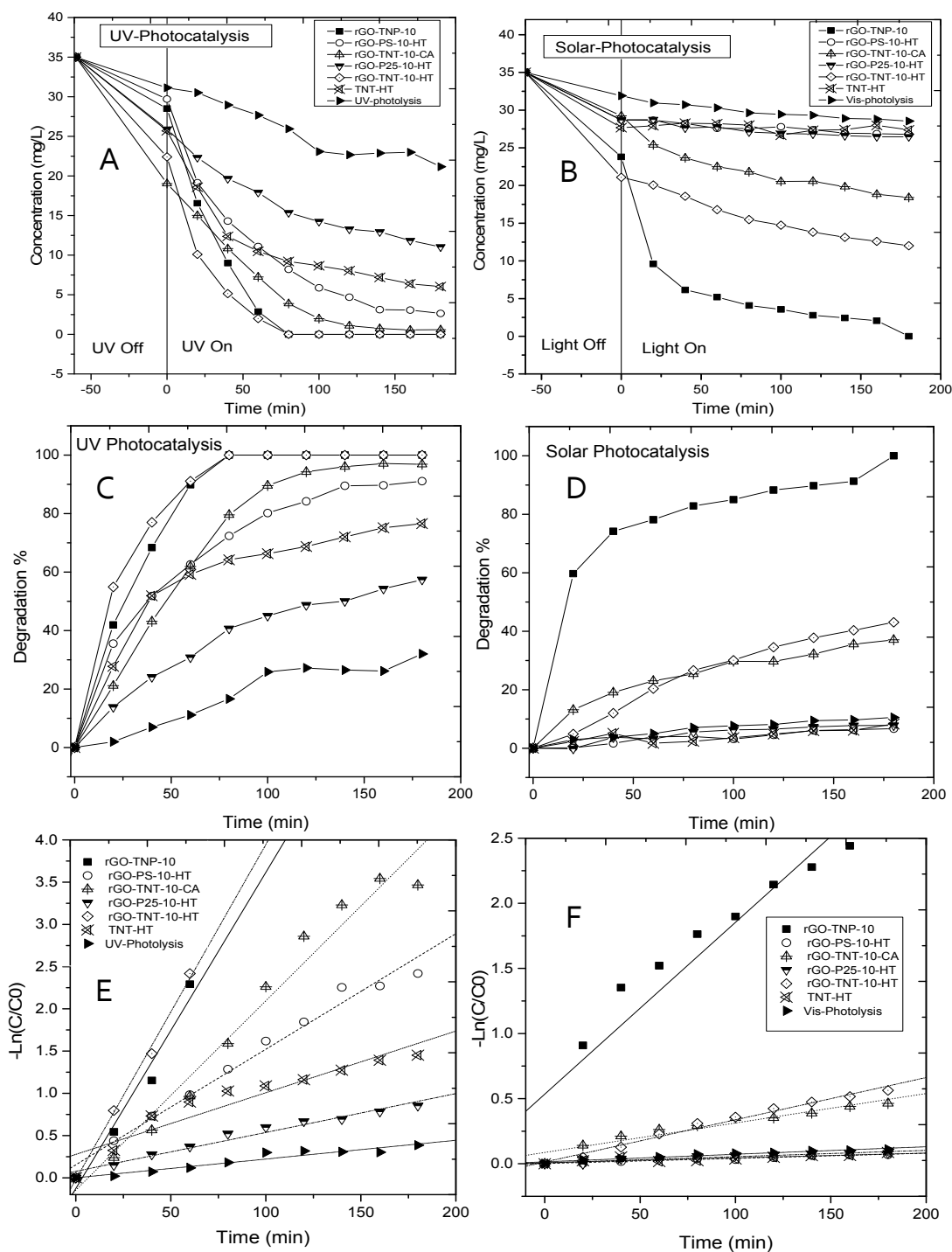


Figure 6-12: UV and visible light photocatalytic activity of Photolysis of TNT-HT, rGO-TNP-10, rGO-TNT-10-HT, rGO-TNT-10-CA in comparison with rGO/TiO₂ nanoparticle composites rGO-PS-10-HT and rGO-P25-10-HT towards degradation of 35 mg ml⁻¹ of famotidine. All HT composites were treated hydrothermally at 150 °C for 24 hrs, CA samples were annealed at N₂ atmosphere at 450 °C for 2 hrs. In each label 10 represent the wt% of graphene in composite.

6.2.3. TiO₂ nanofiber

By treating TiO₂ powder in 10 M sodium hydroxide in 200 °C we obtained TiO₂ solid nanofibers (without any channel or porosity) with large aspect ratio which could be interesting for photocatalysis. Figure 6-13 show SEM images of as-synthesised TiO₂ nanofibers after washing with 0.1 M HCl. In the image very long nanofibers (4-5 μm) with diameter ranging from 30 to 100 nm which are agglomerated into bundles can be seen. According to the phase diagram of TiO₂ morphology depending on the alkalinity of the dispersion and the temperature of the hydrothermal treatment it also can be confirmed that fibrous morphology is the most stable form of TiO₂ at 200 °C and 10 M NaOH solution.

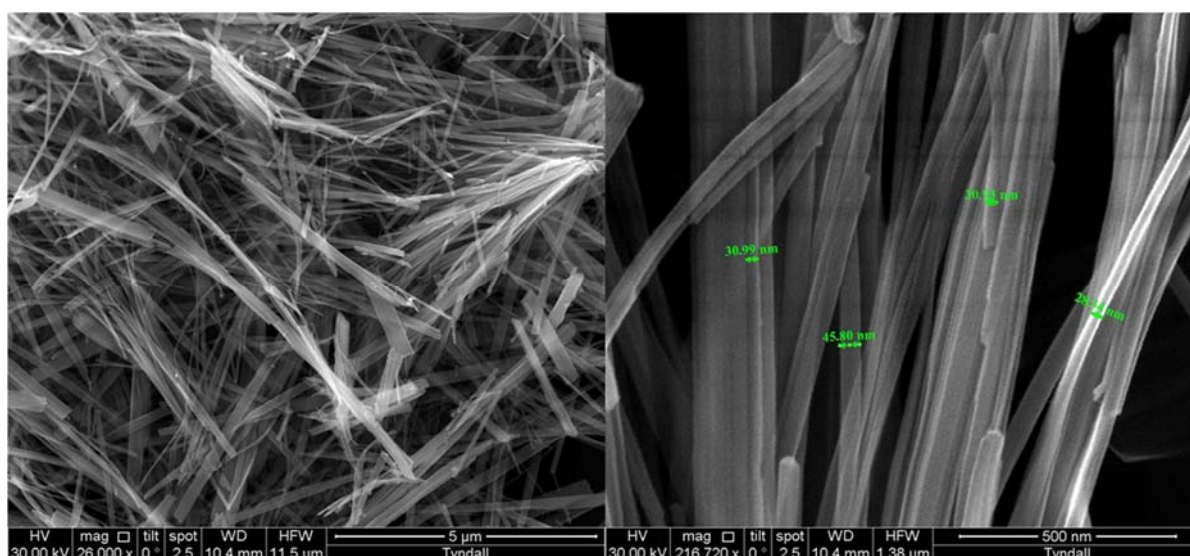


Figure 6-13: SEM images of TiO₂ nanofibers synthesised by hydrothermal treatment of P25 in 10 M NaOH at 200 °C for 24 hours

The closed structure of TiO₂ nanofibers results in small surface area (BET surface area of 64 m² g⁻¹) which is not in favour of photocatalysis due to decreased contact between organic pollutants and catalyst surface. This bulky morphology of TiO₂ nanofibers was clearly observed in TEM images shown in Figure 6-15. The as-synthesised nanofibers have a mixture of amorphous and crystalline structure which implies a post annealing treatment in order to increase crystallinity of the nanofibers.

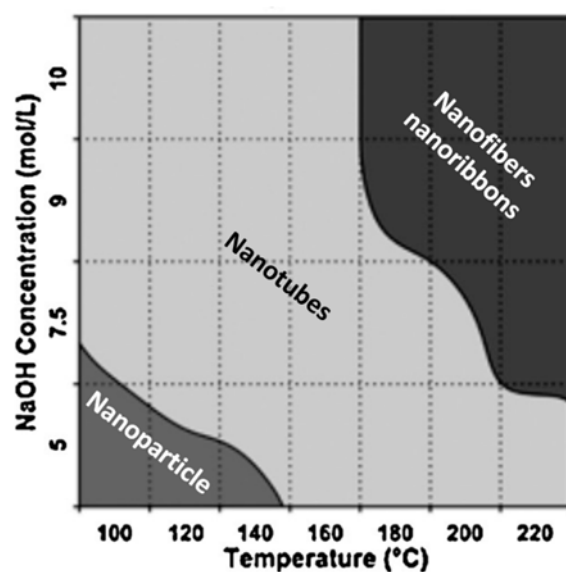


Figure 6-14: Dependence of morphological phase diagrams on hydrothermal conditions⁹⁹

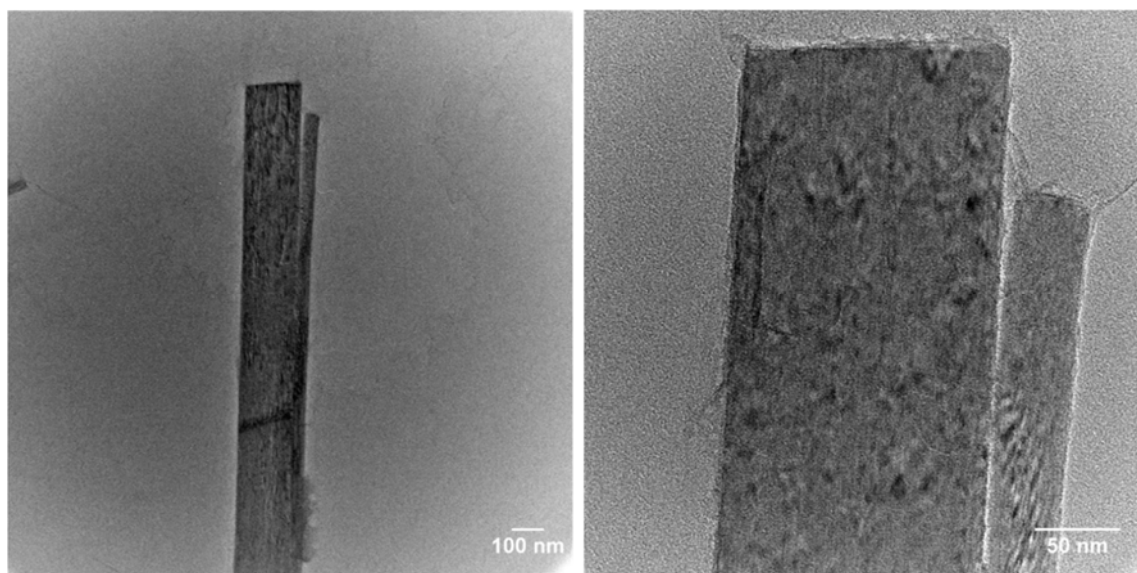


Figure 6-15: TEM images of as-synthesised TiO₂ nanofibers

In order to study photocatalytic activity of TiO₂ nanofibers, half of the as produced batch of nanofibers was calcined at 450 °C for 2 hrs as control sample and the other half was mixed with 10 wt% of graphene oxide and was annealed in N₂ atmosphere under similar conditions. This annealing temperature has been previously confirmed a suitable temperature to crystallise TiO₂ and reduce graphene oxide into graphene at the same time. Raman spectra of calcined nanofibers in comparison with the starting P25 powder are shown in

Figure 6-16. This is in agreement with Raman spectra of annealed TiO₂ nanotubes and nanoparticles and shows the resulting powder contains mainly anatase phase and little amount of rutile phase.

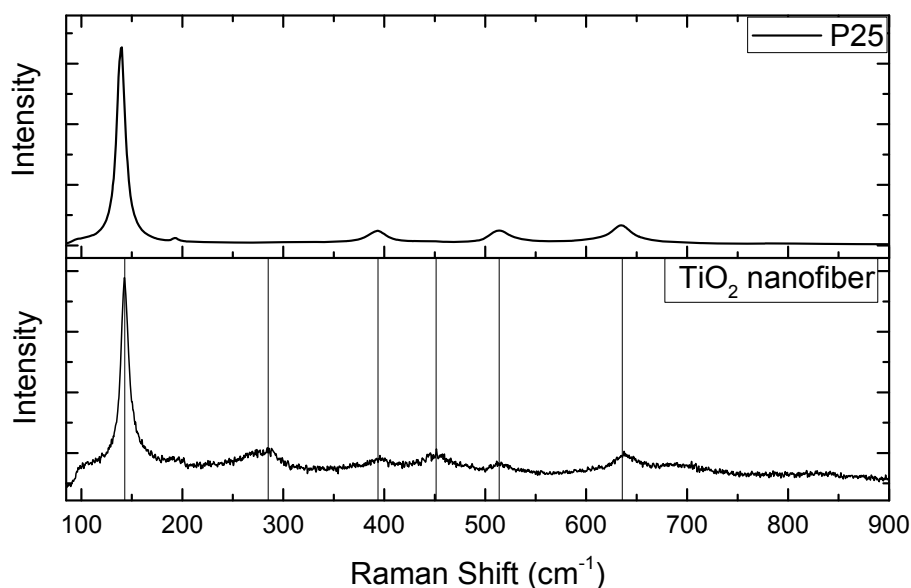


Figure 6-16: Raman spectra of annealed TiO₂ nanofibers comparing with P25 TiO₂ source

SEM images of the annealed TiO₂ nanofibers (A and B) and 10 wt% rGO/TiO₂ nanofibers are shown in Figure 6-17. Comparing Figure 6-13 with Figure 6-17 shows that after calcination the diameter of the nanofiber increase which might be due to agglomeration of nanofibers in each bundle. However the morphology stays similar. TiO₂ nanofiber/graphene composite which was made by mixing 10 wt% of graphene oxide with as-synthesised fibres and annealing at 450 °C for 2 hrs is shown in Figure 6-17. One interesting feature of TiO₂ nanofiber/graphene composite comparing nanotube composite is that after post thermal or hydrothermal treatment the morphology of fibres did not change. For nanotubes they deflected, tangled and curled into globular morphology however because of large diameter of nanofibers and probably larger young modulus they are not prone to deflection. Therefore we see layered structure of nanofibers and graphene sheets in between. As shown in cross-section SEM in Figure 6-17C, TiO₂ nanofibers create a sandwich like structure with graphene sheets and as it can be seen clearly in image D, nanofibers covered with a thin and transparent reduced graphene oxide sheet. This morphology could be ideal for photocatalysis application which efficient charge separation can take place because of uniform distribution of graphene between layers of TiO₂ nanofibers.

Photocatalysis degradation of 35 mg/L of famotidine with 0.3 g/L of catalyst under both UV and visible light were performed and samples were analysed within equal time intervals using HPLC after separation the catalyst with filtration. All the experiments were carried out after 1 hour of dark adsorption to reach equilibrium concentration on the surface of catalyst. In

Figure 6-18 concentration of the supernatant solution versus irradiation (and adsorption) time and their pseudo-first order kinetics plot as well as photocatalytic degradation efficiencies are plotted versus time. The rate constant parameter (K_{app}), extracted from slope of linear fitting of kinetic plots as well as fitting goodness (R^2), final removal efficiency and amount of famotidine degradation by 1 g of catalyst per minute ($K_{app} \times q$) are summarized in Table 6-3. By adding calcined nanofibers (NF-CA) to the solution rate constant was increased 4 times for UV photocatalysis while slightly decreased for visible light experiment. This reduction in rate constant is due to initial adsorption of some famotidine on nanofibers also scattering of light by nanofibers which reduced the interaction of solar light with famotidine. By adding graphene to nanofibers the rate constant increase 50 % and the UV removal efficiency increased from 77 % to 100%. Also the visible activity increase 10 times comparing pure TiO_2 nanofibers.

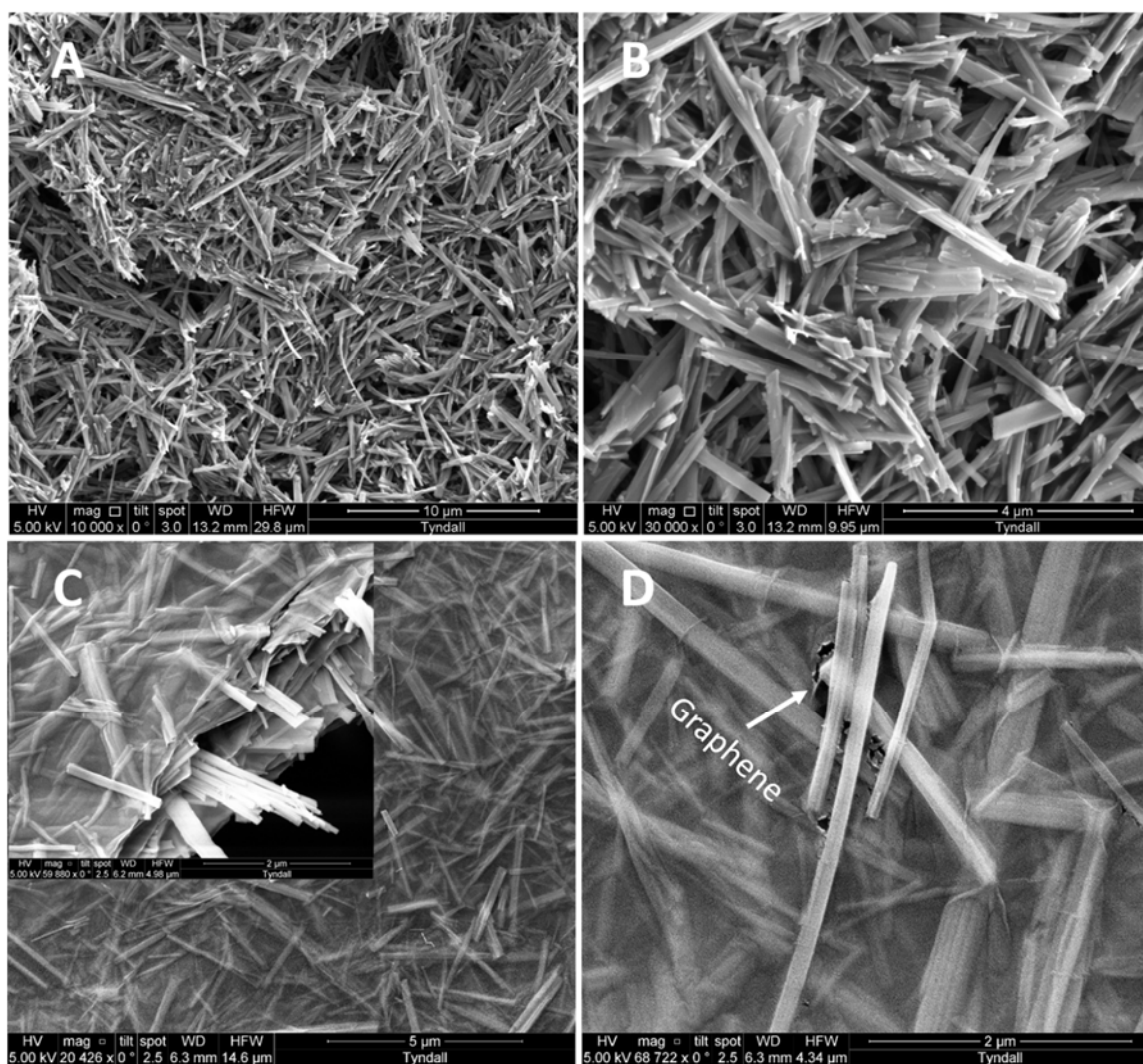


Figure 6-17: SEM images of TiO_2 nanofibers calcined at 450 °C for 2 hrs (A, B) and images of rGO- TiO_2 nanofiber containing 10 wt% of graphene after thermal reduction

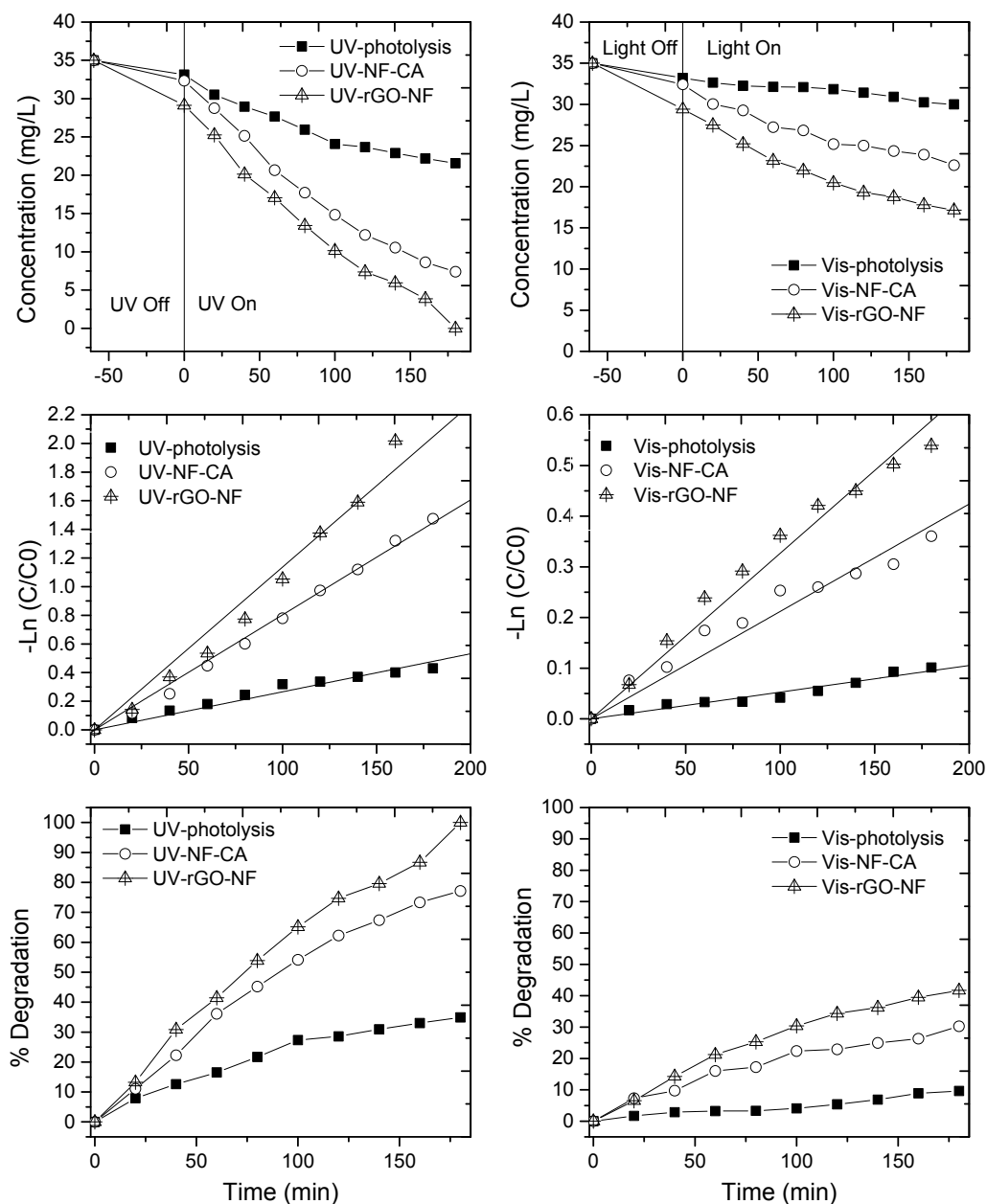


Figure 6-18: UV and photocatalytic activity of TiO_2 nanofibers and rGO/TiO_2 nanofibers

The enhancement in visible catalytic performance of the composite comparing pure TiO_2 nanofibers can be described by the photo-sensitization effect of graphene in composite which absorbs more light rather than scattering by nanofibers. This improves quantum efficiency of the composite. Electron-hole separation by graphene also is another mechanism which effectively enhances performance of the composite catalyst under both UV and visible light irradiation. Comparing $K_{\text{app}} \cdot q$ ($\text{mg} \cdot \text{g}^{-1} \cdot \text{min}^{-1}$) can give us better insight to the

photocatalytic activity of the catalyst. For pure TiO₂ nanofibers this value is around 10 for visible and 500 for UV light catalysis (50 times higher under UV than visible) while it is around 100 and 800 for visible and UV respectively (8 times higher for UV). So it can be seen that by adding graphene to the system, the catalyst can be engineered effectively for solar light degradation of pollutant which is more environmentally viable without the need for any external source of energy. Although TiO₂ nanofiber/graphene composites can be classified as an efficient photocatalyst (comparing TiO₂ nanoparticles and their composites with graphene) however by comparing $K_{app}\cdot q$ value for rGO/nanotubes which is around 2500 averagely, one can be concluded that even though rGO/TiO₂ nanofiber composites are more efficient than TiO₂ nanoparticles and their graphene composites however still rGO/TiO₂ nanotubes are far better than any other catalyst studied so far under both UV and visible light irradiation.

Table 6-3: UV and Visible-light photocatalytic activities of pure TiO₂ nanofiber and with 10 wt% rGO composite comparing photolysis for degradation of 35 mg/L famotidine with catalyst dosage of 0.3 g/L

Sample	UV-Photocatalysis				Solar-Photocatalysis			
	Removal %	$K_{app}\times 10^{-3}$ (min ⁻¹)	R ²	$K_{app}\cdot q$ $\times 10^{-3}$	Removal %	$K_{app}\times 10^{-3}$ (min ⁻¹)	R ²	$K_{app}\cdot q$
Photolysis	34	2.66	0.99	NA	10	0.52	0.99	NA
NF-CA	77	8.03	0.99	500.5	30	0.37	0.99	9.1
rGO-TNF-CA	100	11.37	0.99	830	42	3.3	0.99	101.2

6.3. Conclusion

In this chapter it has been shown that TiO₂ nanotube/graphene composite are an effective photocatalyst for degradation of organic pollutants from water. This can be due to high active surface area, porous structure of TiO₂ nanotubes, and large interface contact between nanotubes and underlying conductive graphene which acts as photo-sensitizer and charge trapper. The rate of photocatalytic degradation of famotidine by rGO/TNT composites under both UV and visible light irradiation are considerably higher than rGO/TiO₂ nanoparticle and nanofiber composites. One main advantages of rGO/TNT composite beside its highest UV and visible photocatalytic activity is the ease of post separation. One of the most challenging steps which prevents semiconductor photocatalysis from being commercially viable technology in large scale is very difficult post separation of catalyst from clean water after illumination due to the nanosize of the catalyst. TiO₂ accumulation in environment can be detrimental for aquatic living organism and humans therefore post separation of TiO₂ is necessary beside the need for recovery and reuse of the catalyst. This process typically can be done by high speed centrifugation which is not

feasible in large scale or using ultrafiltration and nanofiltration which increases the cost of process due to high energy consumption. In contrast TiO_2 nanotube/graphene composites can be quickly settle at the bottom of sedimentation tanks within a minute (as shown in Figure 6-19) without need to centrifuge or filtration without scarifying the photocatalytic activity which may result in by increasing the size of semi-conductor catalyst.

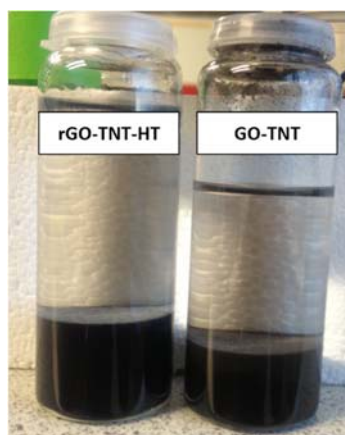


Figure 6-19: photo of rGO and GO/TiO_2 nanotubes one minute after shaking

CHAPTER 7: TiO₂ Beads/graphene composite Synthesis and Photocatalytic properties

7.1. Introduction

Mesoporous titania-based materials with a crystalline framework have received significant research attention especially for energy storage and conversion and solar cells. For these purposes synthesis of morphologies with high degree of crystallinity and porosity is very important. Various forms of mesoporous TiO₂ structures such as films, beads, monoliths and 3D networks, and tubes have been prepared via different synthesis routes so far^{96,261,397-402}. We particularly are interested in monodisperse TiO₂ beads with a micrometer-sized diameter for photocatalysis purification of water, because of easy post recovery of the particles after treatment without the need for centrifuge and filtration. Having mesoporous structure will prevent the reduction in photocatalysis due to low surface area or increase band gap because these beads still are composed of small crystal and particles of TiO₂ which are bind together into a large micro-bead while maintain a porous structure in their body. However one effect which may interfere with photocatalysis in large amount of light scattering by the particles especially under visible light. Therefore making graphene/TiO₂ bead composite might help to sensitize micro-beads and absorb more light. Herein we synthesised crystalline mesoporous TiO₂ beads composite with reduced graphene oxide with surface areas up to 310 m²/g and pore diameter from 10 to 150 nm through modified sol-gel and solvothermal method. As synthesised mesoporous beads have a narrow size distribution with average diameter of 500 nm and are composed of anatase TiO₂ nanocrystals.

7.2. Results and Discussion

The method to produce rGO/TiO₂ mesoporous beads is a 4 step process in this order 1) sol-gel, 2) solvothermal pore development, and 3) beads calcination in air, 4) hydrothermal reduction of Go to rGO in composite. Solvothermal treatment in ethanol is necessary in order to develop mesoporous structure through dissolution of organic compounds in TiO₂ beads body. After calcination of powder performed in air to burn large amount of HAD and TTIP residues within TiO₂ beads so that the final product is mainly microspheres with very narrow size

distribution as shown in SEM images a1 to a3 in Figure 7-1. The final material contained monodisperse beads with a diameter of 500 nm which in some parts are agglomerated together during calcination and formed larger microbeads. In higher magnification image (a3) the rough surface of a broken beads reveals small TiO_2 particles which are connected together into a 3D mesoporous structure as also confirmed by TEM images individual beads shown in Figure 7-2. The corresponding XRD pattern presented in Figure 7-3 indicates well-resolved diffraction peaks corresponding to the reflections of anatase TiO_2 . The crystal size estimated from the full width at half maximum of the (101) peak of anatase at $2\theta=25^\circ$ using the Scherrer equation (described in materials and method chapter) indicated that each TiO_2 beads contains nanocrystals with average crystallite size of 10 nm which is in a good agreement with that measured crystals from TEM images. SEM images of b1 to b3 shows the morphology of the rGO-TBs composite after hydrothermal reduction. Graphene is mainly covered surface of TiO_2 beads efficiently, however in the image free graphene sheets are also visible.

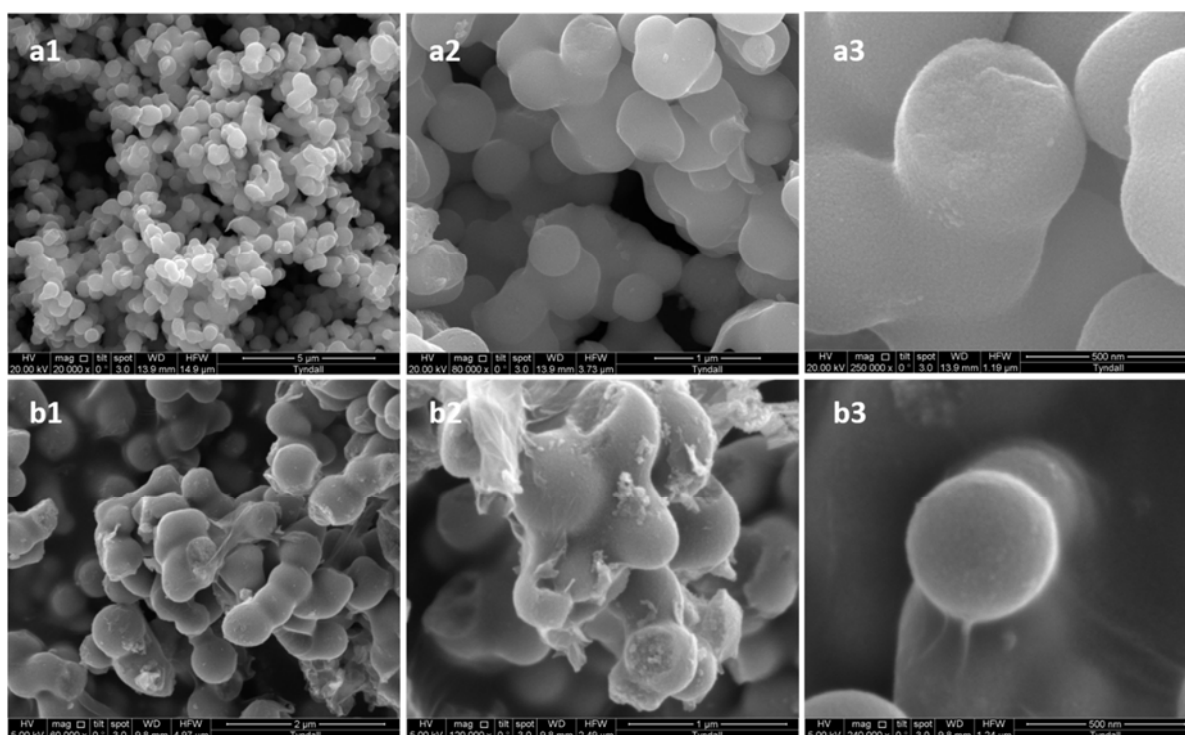


Figure 7-1: SEM images of hydrothermally treated and calcined TiO_2 beads TBs (a1,2,3) and TiO_2 beads with 10 wt% reduced graphene oxide rGO-TBs after hydrothermal treatment (b1, 2, 3)

In Figure 7-2 TEM image of rGO-TBs composite with 10 wt% of rGO after hydrothermal treatment at 170 C for 10 hrs indicate that each TiO_2 bead composed of smaller TiO_2 crystallites with average diameter of 10 ± 2 nm with small pores in between which shows

the mesoporous structure of the beads as also confirmed by N₂ adsorption isotherm shown in Figure 7-4.

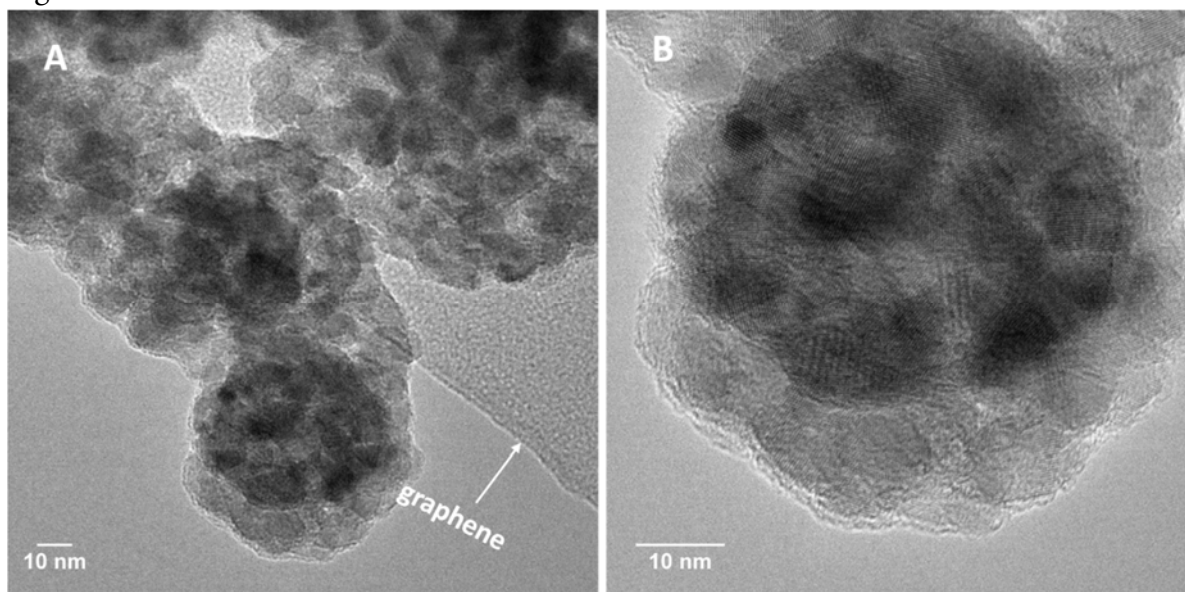


Figure 7-2: TEM images of rGO-TBs showing the poly-crystallinity and mesoporous structure of TiO₂ beads

XRD patterns of pure TiO₂ beads and rGO-TBs are shown in Figure 7-3 which indicates anatase structure of TiO₂ beads in pure and composite form.

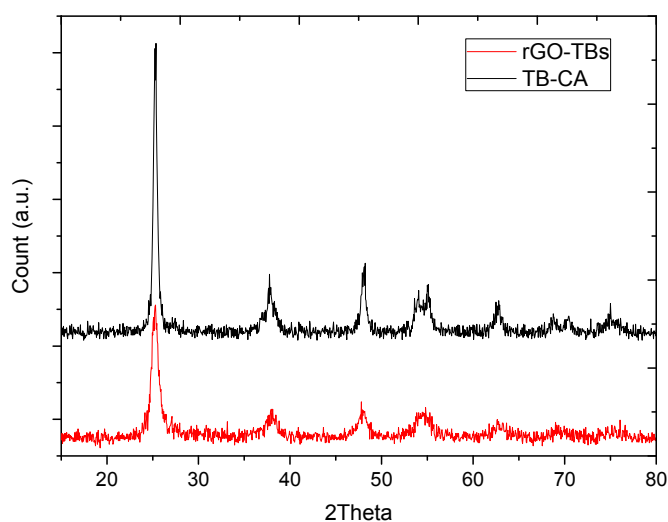


Figure 7-3: XRD patterns of TiO₂ beads and TiO₂ beads with 10 wt% graphene composite

In order to examine the surface area of the composite, N₂ adsorption isotherm experiment was carried out after degassing the sample for 5 hours in vacuum. The results indicate that TiO₂ beads have mesoporous morphology with BET surface area of 310 m²/g, pore volume of 0.71 and pore diameter of 9 nm which is in agreement with TEM images.

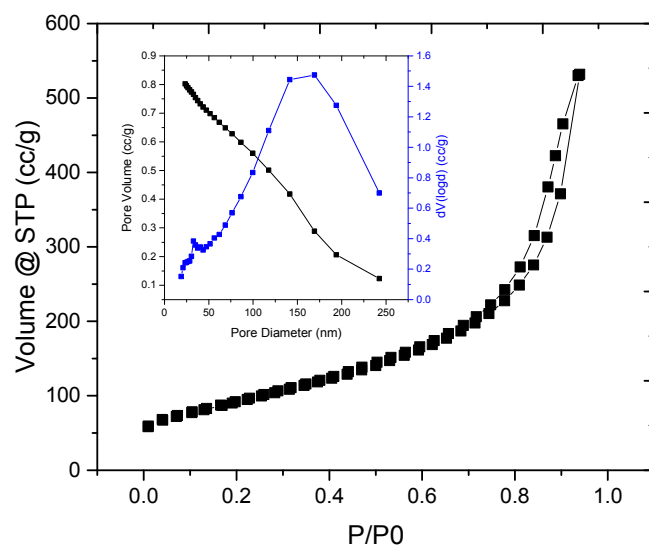


Figure 7-4: N₂ adsorption isotherms of 10 wt% rGO-TBs composite with BJH pore distribution (inset)

Therefore considering all the data from TEM, XRD and BET surface area we estimate that TiO₂ bead structure could be reasonably good catalyst for UV and visible light degradation of organic pollutants especially after combining with graphene which will enhance pollutant adsorption of the surface of composite along with photosensitization effect for visible light activity and charge carrier separation due to electrical conductivity of graphene. To confirm that we performed UV and solar light photocatalysis experiments for degradation of famotidine in next section.

7.3. UV and Visible light Photocatalytic activity

For photocatalysis experiments same dosage of both catalyst were used to degrade 35 mg/L of famotidine after 1 hour of dark adsorption. The results are shown in Figure 7-5 and the extracted data are listed in Table 7-1. The results shows that pure TiO₂ beads also have reasonably good UV photocatalysis performance but poor visible light activity therefore adding graphene improves visible light activity dramatically (7 fold increase in rate constant) while enhances UV activity by 70% (increasing the rate constant from 10 to 70). The high UV photocatalytic activity of TiO₂ beads can be related to its high surface area. However the poor visible light activity of TiO₂ beads can be described by taking into account that the size of TiO₂ beads are similar to the wavelength of visible light ($\lambda > 450$ nm) which will increase light scattering dramatically. Scattering of light prevent effective light adsorption by TiO₂ beads so that the material will not perfume well under visible light irradiation.

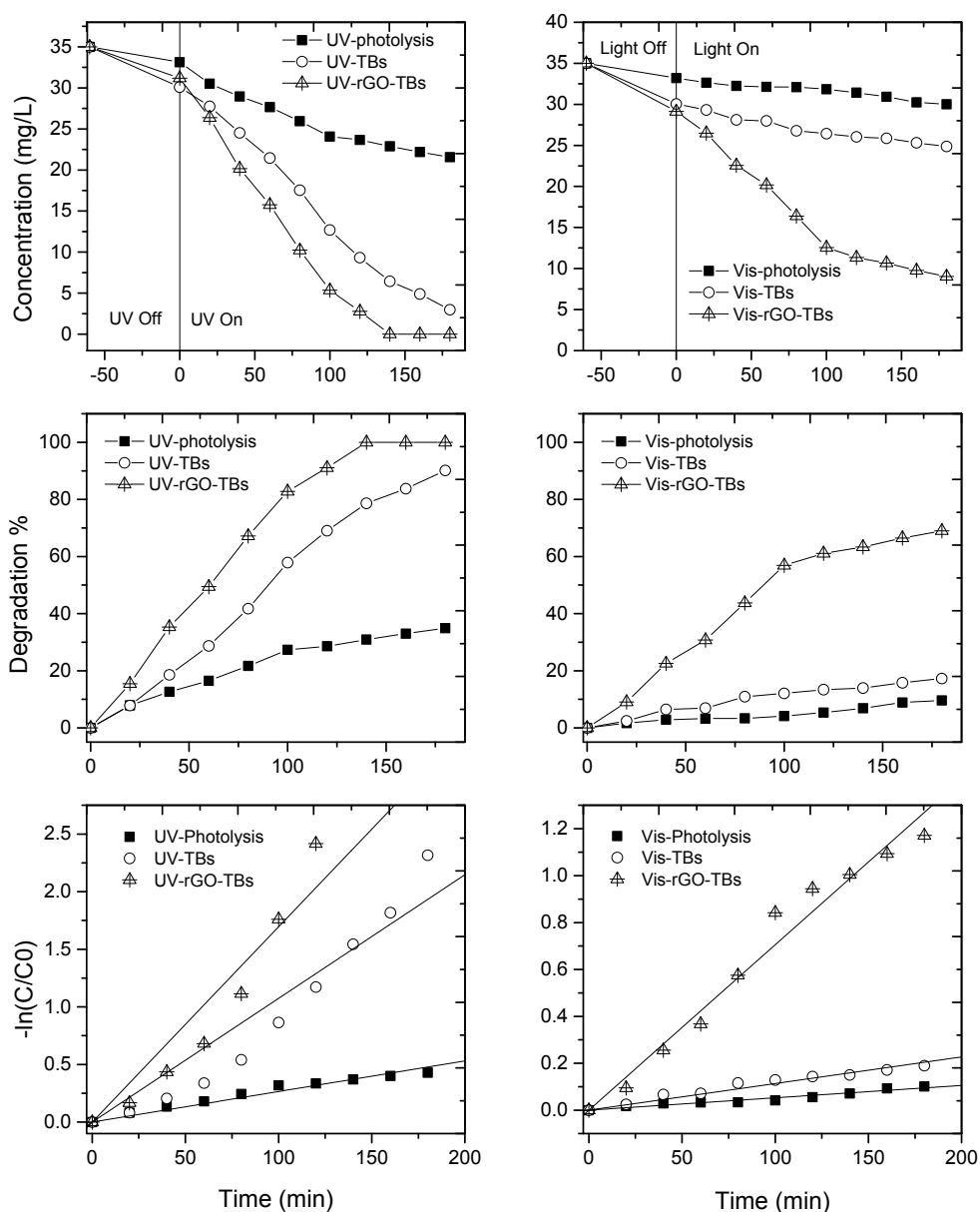


Figure 7-5: UV and Visible-light photocatalytic activities of pure TiO₂ beads (TBs) calcined at 450 °C and TiO₂ beads with 10 wt% rGO composite (rGO-TBs) hydrothermally reduced at 170 °C for 10 hrs comparing photolysis degradation towards degradation of 35 mg/L famotidine with catalyst dosage of 0.3 g/L

Adding graphene on the surface of TiO₂ beads will act as a sensitizer which will absorb more light and initiates TiO₂ excitation to producer electron-hole pairs.

Table 7-1: UV and visible light photocatalysis data for TBs and rGO/TBs

Sample	UV-Photocatalysis	Solar-Photocatalysis
--------	-------------------	----------------------

	Removal %	$K_{app} \times 10^{-3} \text{ (min}^{-1}\text{)}$	R^2	Removal %	$K_{app} \times 10^{-3} \text{ (min}^{-1}\text{)}$	R^2
Photolysis	34	2.66	0.99	10	0.52	0.99
TBs	90.13	10.7	0.98	17.27	1.1	0.99
rGO-TBs	100	17	0.98	42	7.1	0.99

7.4. Conclusion

In summary, we synthesized highly catalytically active graphene/TiO₂ beads composite through combining sol-gel/thermal/solvothermal/hydrothermal reaction path which pores were developed inside beads and graphene oxide was reduced to graphene effectively. Graphene-TiO₂ beads exhibited very good UV and visible light activity with a rate constant of 0.017 and 0.007 min⁻¹ respectively which is much higher than that of standard P25 powder. The excellent catalytic activity of graphene/TiO₂ beads is attributed to a thin two-dimensional of graphene covered on the surface of TiO₂, large surface area of beads, and large adsorption capacity of the composite. Graphene as electron sink absorbs photo-generated electrons from the conduction band of TiO₂ and prevents recombination. One advantages of this composite is very post-separation and recovery only by gravity force in short time which make it attractive for large scale solar light water treatment plant

CHAPTER 8: Conclusion

This research aims to study a new hybrid graphene based nano-material for water treatment process based on adsorption with graphene and graphene oxide and photocatalytic oxidation using TiO_2 . Both processes having several drawbacks in application scale and it appeared interesting to study the performance of the adsorption process and photocatalysis separately and combination of adsorption and photocatalytic oxidation in a complementary process. Therefore, the contribution of this work is included two principal parts: a preliminary one which was described in current report is to describe the adsorption properties of different type of organic pollutants on graphene oxide integrated adsorbents. Secondly, the investigation of the photocatalytic degradation of these pollutants using integrated TiO_2 with different morphologies and via different approaches.

The main conclusions derived from current investigation are summarized as follows:

- The first part of this study consisted of fully characterization of graphene oxide sponge and graphene produced via different method such as oxidation-reduction and exfoliation and comparing them with commercially provided graphene nano-sheets. The physical and chemical properties of the resulting graphene oxide and reduced graphene oxide such as morphology, surface chemical functionality, crystallinity, sheet size, specific surface area, pore volume and pore size were evaluated and compared with a commercial graphene reference. The results indicated that the produced graphene is mainly consisted of single layer graphene sheet with high crystallinity and large sheet size as the commercial ones was mainly composed of defected graphite and not graphene. The various type of functional groups as well as wrinkles and defects on the graphene basal plane proved to be promising for this project future applications.
- Conventional N_2 adsorption technique did not provide an accurate data on actual surface area of graphene based material since they were reduced during degassing process and their physical and chemical functionality was totally changed. MB adsorption technique was introduced in this report for the first time as an efficient method in order to examine

the actual surface area of graphene and graphene based material. The surface area of graphene oxide was obtained is about 2605 m²/g which is the closest reported number to is theoretical surface area around 2630 m²/g.

- Graphene oxide sponge indicated huge adsorption capacity towards MB and different pharmaceuticals. It was found that pH does not affect the adsorption capacity significantly. This can highlight graphene based adsorbent as an ideal adsorbent to remove different types of pollutant from industrial effluent with wide range of pH from highly acidic to basic.
- Graphene oxide sponge comparing to activated carbon offers higher adsorption capacity, quicker adsorption and more versatility towards adsorption of different types of pollutants. Therefore as a new and unique 2D carbon nanomaterial, graphene has been proved to construct different and promising adsorbents in the field of environmental remediation.
- The second part of current report focused on immobilization of graphene oxide on the surface of cheap substrates in order to create a multicomponent adsorbent as well as prevent graphene oxide from leaching into the water. Among all the substrates, dolomite/graphene oxide composite showed great ability for adsorption of MB, dolomite is an abundant mineral which has application as an adsorbent bed for industrial wastewater specially to remove dyes from effluent. Despite the rather low surface area dolomite/graphene oxide showed superior adsorption capacity towards MB comparing to bare dolomite that validates the use of this composite as a replacement for dolomitic adsorbent for industrial wastewater treatment material.
- Third part of the thesis focused on synthesis of graphene/TiO₂ nanoparticle with the highest photocatalytic activity. It was found that mixing pre-synthesized and commercially available TiO₂ did not improved photocatalytic activity of the composite comparing with the pure TiO₂ powder effectively. This can be due to first, weak interaction of TiO₂ with graphene which make it difficult to transfer photo-generated electron to the surface of GO especially that this composite should work in aqueous environment under vigorous agitation. Secondly since TiO₂ did not interact with graphene effectively, adding graphene to the system only makes the light penetration to water more challenging. However synthesizing TiO₂ via sol-gel in situ on the surface of graphene oxide and then reducing it via thermal or hydrothermal treatment provides more efficient catalyst for UV photocatalysis. One important observation in this section was UV photocatalysis reduction of graphene oxide into partially reduced graphene during the light irradiation which will improve the activity of the composite via cycling.

- In forth section of our study TiO_2 nanotubes and nanofibers were used in order to produce an effective catalyst for water treatment. We chose three different route in order to make the most efficient composites. The results showed that TiO_2 nanotubes synthesized in one pot in-situ on the surface of 10 wt% of graphene have extraordinary photocatalytic activity especially under visible light comparing other composites of this current research. This can be attributed to double doping effect which is doping of dissolved carbon into TiO_2 crystal structure under high temperature and pressure of the hydrothermal process and doping effect of photosensitization by graphene nanosheets. The very unique morphology of TiO_2 nanotubes including large surface area, large channels within tubes, large aspect ratio in combination with high adsorption capacity of graphene, light absorption, electron sink ability, transparency and electron conductivity of graphene makes the most efficient composite suitable for effective UV and solar light water treatment.
- In last part of study, mesoporous TiO_2 beads/graphene composites were made by sol-gel/solvothermal/ hydrothermal process in order to have high surface area of mesoporous TiO_2 along with light absorption and conductivity of graphene. The results showed that adding graphene improves the visible light activity of the composite dramatically which may be attributed to light absorption by graphene which reduced large scattering of solar light by TiO_2 particles
- Our final conclusion is that combining two dimensional graphene sheets with high electron mobility with one dimensional TiO_2 nanotubes is the best match to make graphene/ TiO_2 composite which can be due to large interface of nanotubes with graphene as a result of high aspect ratio of nanotubes. Considering the unique properties of graphene such as transparency, high surface area, high electrical conductivity and 2D structure, graphene can offer its unique properties and possibly induce new performance, such as high adsorption capacity, extended light adsorption range, and excellent charge separation-transportation capability it can improves photocatalytic activity of TiO_2 composite when added in optimum amount. This composite are very interesting for future water treatment plants in more environmentally friendly manner.

CHAPTER 9: Future Work

As mentioned before the main purpose of current research is to design an efficient integrated photocatalyst material which is able to adsorb high amount of pollutants on the surface in contact with TiO_2 photocatalyst in order to increase the low efficiency of photocatalysis especially for trace pollutants. However there are still huge amount of work needs to be conducted to combine this material with a designed reactor to be able to work with real type of wastewater and light illumination. Future works for the rest of current research can be proposed as follow:

- Studying the physics and chemistry of graphene interaction with TiO_2 using electrochemical impedance spectroscopy (EIS) method in electrochemical cell to investigate the effect of graphene in charge transfer kinetics of TiO_2
- Determining the band gap of all TiO_2 forms such as nanoparticles, nanotubes and nanofibers without graphene and with various amount of graphene oxide and reduced graphene by means of diffuse reflectance spectroscopy
- Study the photoconductivity and photoluminescence properties of graphene/ TiO_2 composite under irradiation of various wavelength of laser lights
- Investigating the performance of TiO_2 nanotube/graphene composite for photocatalytic water splitting and hydrogen reduction in order to produce hydrogen fuel
- Studying the simultaneous and alternative removal of multi-component and specific pollutants in complex system such as real wastewater.
- Investigating the interaction of different pollutant with different chemical structure with and without benzene ring while adsorbed on the surface of graphene oxide and graphene/ TiO_2 composite.
- Comparing graphene/ TiO_2 composite with activated carbon/ TiO_2 or carbon nanotube composite to find out whether the photocatalytic activity of graphene/ TiO_2 composites in degradation of pollutant is truly different from other TiO_2 /carbon composite materials.
- Studying the degradation mechanism of a selected pollutant in order to identify intermediates and degradation pathways using mass spectroscopy technique.

- Immobilizing the composite on the surface of a planar substrate such as glass or polymeric substrates in order to eliminate the post recovery process of the composite and increase the light absorption efficiency.
- Investigating the performance of the composite in continuous conditions using a fixed bed type photocatalytic reactor (Figure 9-1).

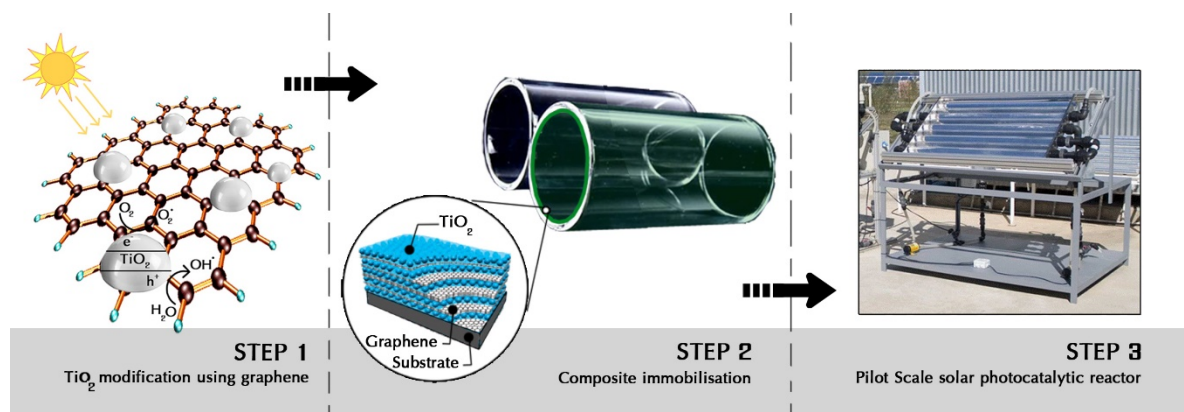


Figure 9-1: Proposed pilot scale reactor in order to study performance of graphene/ TiO_2 composite in a continuous flow of real wastewater under solar light irradiation

As we found, the amount of defects on graphene basal plane and conductivity of graphene which are related adversely, have very important effect on adsorption of pollutants and improvement of TiO_2 photocatalytic activity within the composite. If the debate is to be moved forward, a better understanding of defects on graphene properties needs to be developed and the maximum defects without sacrificing the electronic conductivity of graphene, must be determined. Since attaching TiO_2 on defect free graphene is very challenging, I suggest that a new method should be developed to anchor TiO_2 via an external driving force such as sonochemical method or chemical functionalisation of graphene. This study will provide valuable information which would help to establish a greater degree of accuracy on the effect of graphene properties on photocatalysis improvement of graphene/ TiO_2 composites.

Another fruitful area for further research is studying two dimensional materials other than graphene such as layered transitional metal dichalcogenides (MX_2 : $\text{M}=\text{Mo}$, W and $\text{X}=\text{S}$, Se , Te), transition metal oxides, or layered double hydroxides and combining spectacular electronic, optical and catalytic properties of these materials with photocatalytic properties of TiO_2 to obtain the most efficient solar light composite catalyst for water remediation and clean energy by solar water splitting.

References

1. WHO Pharmaceuticals in drinking-water. **2012**, WA 30.5.
2. Diop, S.; M'mayi, P.; Lisbjerg, D.; Johnstone, R. Vital Water Graphics: An Overview of the State of the World's Fresh and Marine Waters; Incumbent: 2002.
3. Graphics, U. V. W. An overview of the state of the world's fresh and marine waters **2008**.
4. Halling-Sørensen, B.; Nors Nielsen, S.; Lanzky, P. F.; Ingerslev, F.; Holten Lützhøft, H. C.; Jørgensen, S. E. Occurrence, fate and effects of pharmaceutical substances in the environment- A review. *Chemosphere* **1998**, 36, 357-393.
5. Naddeo, V.; Meriç, S.; Kassinos, D.; Belgiorno, V.; Guida, M. Fate of pharmaceuticals in contaminated urban wastewater effluent under ultrasonic irradiation. *Water Res.* **2009**, 43, 4019-4027.
6. Heberer, T. Occurrence, fate, and removal of pharmaceutical residues in the aquatic environment: A review of recent research data. *Toxicol. Lett.* **2002**, 131, 5-22.
7. Lim, S. J.; Fox, P. Estimating the persistence of organic contaminants in indirect potable reuse systems using quantitative structure activity relationship (QSAR). *Sci. Total Environ.* **2012**, 433, 1-7.
8. Nikolaou, A.; Meric, S.; Fatta, D. Occurrence patterns of pharmaceuticals in water and wastewater environments. *Analytical and bioanalytical chemistry* **2007**, 387, 1225-1259.
9. Santos, L. H. M. L. M.; Araújo, A. N.; Fachini, A.; Pena, A.; Delerue-Matos, C.; Montenegro, M. C. B. S. M. Ecotoxicological aspects related to the presence of pharmaceuticals in the aquatic environment. *J. Hazard. Mater.* **2010**, 175, 45-95.
10. Henschel, K.; Wenzel, A.; Diedrich, M.; Fliehdner, A. Environmental hazard assessment of pharmaceuticals. *Regulatory Toxicology and Pharmacology* **1997**, 25, 220-225.
11. Ternes, T. A.; Meisenheimer, M.; McDowell, D.; Sacher, F.; Brauch, H.; Haist-Gulde, B.; Preuss, G.; Wilme, U.; Zulei-Seibert, N. Removal of pharmaceuticals during drinking water treatment. *Environ. Sci. Technol.* **2002**, 36, 3855-3863.

12. Kolpin, D. W.; Furlong, E. T.; Meyer, M. T.; Thurman, E. M.; Zaugg, S. D.; Barber, L. B.; Buxton, H. T. Pharmaceuticals, hormones, and other organic wastewater contaminants in U.S. streams, 1999-2000: A national reconnaissance. *Environmental Science and Technology* **2002**, 36, 1202-1211.
13. Bound, J.; Voulvoulis, N. Household disposal of pharmaceuticals as a pathway for aquatic contamination in the United Kingdom. *Environ. Health Perspect.* **2005**, 113, 1705-1716.
14. Ashton, D.; Hilton, M.; Thomas, K. V. Investigating the environmental transport of human pharmaceuticals to streams in the United Kingdom. *Sci. Total Environ.* **2004**, 333, 167-184.
15. Thomas, K.; Hilton, M. The occurrence of selected human pharmaceutical compounds in UK estuaries. *Mar. Pollut. Bull.* **2004**, 49, 436-480.
16. Mompelat, S.; Thomas, O.; Le Bot, B. Contamination levels of human pharmaceutical compounds in french surface and drinking water. *J. Environ. Monit.* **2011**, 13, 2929-2939.
17. Roberts, P.; Thomas, K. The occurrence of selected pharmaceuticals in wastewater effluent and surface waters of the lower Tyne catchment. *Sci. Total Environ.* **2006**, 356, 143-196.
18. Sui, Q.; Huang, J.; Deng, S.; Yu, G.; Fan, Q. Occurrence and removal of pharmaceuticals, caffeine and DEET in wastewater treatment plants of beijing, china. *Water Res.* **2010**, 44, 417-426.
19. Seiler, R. L.; Zaugg, S. D.; Thomas, J. M.; Howcroft, D. L. Caffeine and pharmaceuticals as indicators of waste water contamination in wells. *Ground Water* **1999**, 37, 405-410.
20. Crathorne, B.; Fielding, M.; Steel, C. P.; Watts, C. D. Organic compounds in water: Analysis using coupled-column high-performance liquid chromatography and soft-ionization mass spectrometry. *Environ. Sci. Technol.* **1984**, 18, 797-802.
21. Stuer-Lauridsen, F.; Birkved, M.; Hansen, L.; LÃ¼tzhÃ¼ft, H.; Halling-SÃ¸rensen, B. Environmental risk assessment of human pharmaceuticals in denmark after normal therapeutic use. *Chemosphere* **2000**, 40, 783-876.
22. Carballa, M.; Omil, F.; Lema, J.; Llombart, M.; GarcÃ­a-Jares, C.; RodrÃ­guez, I.; GÃ³mez, M.; Ternes, T. Behavior of pharmaceuticals, cosmetics and hormones in a sewage treatment plant. *Water Res.* **2004**, 38, 2918-2944.

23. Steger-Hartmann, T.; Länge, R.; Schweinfurth, H.; Tschampel, M.; Rehmann, I. Investigations into the environmental fate and effects of iopromide (Ultravist), a widely used iodinated X-ray contrast medium. *Water Res.* **2002**, 36, 266-274.
24. Carballa, M.; Omil, F.; Lema, J.; Llompart, M.; Garc a-Jares, C.; Rodr guez, I.; G mez, M.; Ternes, T. Behavior of pharmaceuticals, cosmetics and hormones in a sewage treatment plant. *Water Res.* **2004**, 38, 2918-2944.
25. Behera, S. K.; Kim, H. W.; Oh, J.; Park, H. Occurrence and removal of antibiotics, hormones and several other pharmaceuticals in wastewater treatment plants of the largest industrial city of Korea. *Sci. Total Environ.* **2011**, 409, 4351-4360.
26. Ternes, T. A., Ed.; In *Human Pharmaceuticals, Hormones And Fragrances: The Challenge of Micropollutants in Urban Water Management*; IWA Publishing group: United Kingdom, 2006.
27. Mompelat, S.; Le Bot, B.; Thomas, O. Occurrence and fate of pharmaceutical products and by-products, from resource to drinking water. *Environ. Int.* **2009**, 35, 803-817.
28. Reddersen, K.; Heberer, T. Multi compound methods for the detection of pharmaceutical residues in various waters applying solid phase extraction (SPE) and gas chromatography with mass spectrometric (GC MS) detection. *Journal of separation science* **2003**, 26, 1443-2893.
29. Jones, O. A.; Lester, J. N.; Voulvoulis, N. Pharmaceuticals: A threat to drinking water? *Trends Biotechnol.* **2005**, 23, 163-167.
30. Daughton, C. Pharmaceutical ingredients in drinking water: Overview of occurrence and significance of human exposure. *Emerging contaminants: pharmaceuticals, personal care products and organohalogenes* **2010**.
31. Huerta-Fontela, M.; Galceran, M. T.; Ventura, F. Occurrence and removal of pharmaceuticals and hormones through drinking water treatment. *Water Res.* **2011**, 45, 1432-1442.
32. Jelic, A.; Gros, M.; Ginebreda, A.; Cespedes-S nchez, R.; Ventura, F.; Petrovic, M.; Barcelo, D. Occurrence, partition and removal of pharmaceuticals in sewage water and sludge during wastewater treatment. *Water Res.* **2011**, 45, 1165-1176.
33. Mompelat, S.; Thomas, O.; Le Bot, B. Contamination levels of human pharmaceutical compounds in French surface and drinking water. *J. Environ. Monit.* **2011**, 13, 2929-2939.

34. Heberer, T.; Reddersen, K.; Mechlinski, A. From municipal sewage to drinking water: Fate and removal of pharmaceutical residues in the aquatic environment in urban areas. *Water science and technology: Journal of the International Association, Water Pollution Research* **2002**, 46, 81-89.
35. Boyd, G. R.; Reemtsma, H.; Grimm, D. A.; Mitra, S. Pharmaceuticals and personal care products (PPCPs) in surface and treated waters of louisiana, USA and ontario, canada. *Sci. Total Environ.* **2003**, 311, 135-149.
36. Yang, S.; Carlson, K. Evolution of antibiotic occurrence in a river through pristine, urban and agricultural landscapes. *Water Res.* **2003**, 37, 4645-4701.
37. Behera, S. K.; Kim, H. W.; Oh, J.; Park, H. Occurrence and removal of antibiotics, hormones and several other pharmaceuticals in wastewater treatment plants of the largest industrial city of korea. *Sci. Total Environ.* **2011**, 409, 4351-4360.
38. Watkinson, A.; Murby, E.; Kolpin, D.; Costanzo, S. The occurrence of antibiotics in an urban watershed: From wastewater to drinking water. *Sci. Total Environ.* **2009**, 407, 2711-2734.
39. Tamtam, F.; Mercier, F.; Le Bot, B.; Eurin, J.; Tuc Dinh, Q.; Clément, M.; Chevreuil, M. Occurrence and fate of antibiotics in the seine river in various hydrological conditions. *Sci. Total Environ.* **2008**, 393, 84-179.
40. Dietrich, D.; Webb, S.; Petry, T. Hot spot pollutants: Pharmaceuticals in the environment. *Toxicol. Lett.* **2002**, 131, 1-4.
41. Ferrari, B.; Paxäus, N.; Lo Giudice, R.; Pollio, A.; Garric, J. Ecotoxicological impact of pharmaceuticals found in treated wastewaters: Study of carbamazepine, clofibrac acid, and diclofenac. *Ecotoxicol. Environ. Saf.* **2003**, 55, 359-429.
42. Koutsouba, V.; Heberer, T.; Fuhrmann, B.; Schmidt-Baumler, K.; Tsipi, D.; Hiskia, A. Determination of polar pharmaceuticals in sewage water of greece by gas chromatography-mass spectrometry. *Chemosphere* **2003**, 51, 69-144.
43. Buser, H.; Müller, M. D.; Theobald, N. Occurrence of the pharmaceutical drug clofibrac acid and the herbicide mecoprop in various swiss lakes and in the North Sea. *Environmental Science and Technology* **1998**, 32, 188-192.
44. WHO WHO model lists of essential medicines. March **2011**, 17th.

45. Khetan, S.; Collins, T. Human pharmaceuticals in the aquatic environment: A challenge to green chemistry. *Chem. Rev.* **2007**, 107, 2319-2383.
46. Cooper, E.; Siewicki, T.; Phillips, K. Preliminary risk assessment database and risk ranking of pharmaceuticals in the environment. *Sci. Total Environ.* **2008**, 398, 26-59.
47. Schwab, B. W.; Hayes, E. P.; Fiori, J. M.; Mastrocco, F. J.; Roden, N. M.; Cragin, D.; Meyerhoff, R. D.; D'Aco, V. J.; Anderson, P. D. Human pharmaceuticals in US surface waters: A human health risk assessment. *Regulatory Toxicology and Pharmacology* **2005**, 42, 296-312.
48. Carlsson, C.; Johansson, A.; Alvan, G.; Bergman, K.; K  hler, T. Are pharmaceuticals potent environmental pollutants? Part I: Environmental risk assessments of selected active pharmaceutical ingredients. *Sci. Total Environ.* **2006**, 364, 67-154.
49. Bound, J.; Voulvoulis, N. Pharmaceuticals in the aquatic environment--a comparison of risk assessment strategies. *Chemosphere* **2004**, 56, 1143-1198.
50. Wennmalm  ; Gunnarsson B Public health care management of water pollution with pharmaceuticals: Environmental classification and analysis of pharmaceutical residues in sewage water. *Drug Information Journal* **2005**, 39, 291-297.
51. Thorsten Reemtsma, M. J., Ed.; In *Organic Pollutants in the Water Cycle: Properties, Occurrence, Analysis & Environmental Relevance of Polar Compounds*; WILEY-VCH: 2006.
52. Ternes, T. A.; Joss, A.; Siegrist, H. Peer reviewed: Scrutinizing pharmaceuticals and personal care products in wastewater treatment. *Environ. Sci. Technol.* **2004**, 38, 392A-399A.
53. Diaz-Cruz, M.; L  pez, d. A.; Barcel  , D. Environmental behavior and analysis of veterinary and human drugs in soils, sediments and sludge. *TrAC Trends in Analytical Chemistry* **2003**, 22, 340-691.
54. Laffler, D.; Rambke, J.; Meller, M.; Ternes, T. A. Environmental fate of pharmaceuticals in Water/Sediment systems. *Environ. Sci. Technol.* **2005**, 39, 5209-5218.
55. G  bel, A.; Thomsen, A.; Mc Ardell, C. S.; Joss, A.; Giger, W. Occurrence and sorption behavior of sulfonamides, macrolides, and trimethoprim in activated sludge treatment. *Environ. Sci. Technol.* **2005**, 39, 3981-3989.

56. Stumpf, M.; Ternes, T. A.; Wilken, R.; Silvana Vianna Rodrigues; Baumann, W. Polar drug residues in sewage and natural waters in the state of rio de janeiro, brazil. *Sci. Total Environ.* **1999**, 225, 135-141.
57. Scheytt, T.; Mersmann, P.; Lindstadt, R.; Heberer, T. Determination of sorption coefficients of pharmaceutically active substances carbamazepine, diclofenac, and ibuprofen, in sandy sediments. *Chemosphere* **2005**, 60, 245-298.
58. Joss, A.; Keller, E.; Alder, A. C.; Göbel, A.; McArdell, C. S.; Ternes, T.; Siegrist, H. Removal of pharmaceuticals and fragrances in biological wastewater treatment. *Water Res.* **2005**, 39, 3139-3152.
59. Scheytt, T.; Mersmann, P.; Lindstadt, R.; Heberer, T. Determination of sorption coefficients of pharmaceutically active substances carbamazepine, diclofenac, and ibuprofen, in sandy sediments. *Chemosphere* **2005**, 60, 245-298.
60. Oller, I.; Malato, S.; Sánchez-Perez, J. Combination of advanced oxidation processes and biological treatments for wastewater decontamination--a review. *Sci. Total Environ.* **2011**, 409, 4141-4207.
61. De Witte, B.; Van Langenhove, H.; Demeestere, K.; Dewulf, J. Advanced oxidation of pharmaceuticals: Chemical analysis and biological assessment of degradation products. *Crit. Rev. Environ. Sci. Technol.* **2011**, 41, 215-242.
62. Sievers, M. In 4.13 - Advanced Oxidation Processes; Editor-in-Chief: Peter Wilderer, Ed.; Treatise on Water Science; Elsevier: Oxford, 2011; pp 377-408.
63. José, H. J.; Gebhardt, W.; Moreira, R. F. P. M.; Pinnekamp, J.; Schröder, H. F. Advanced oxidation processes for the elimination of drugs resisting biological membrane treatment. *Ozone: Science and Engineering* **2010**, 32, 305-312.
64. Matilainen, A.; Sillanpää, M. Removal of natural organic matter from drinking water by advanced oxidation processes. *Chemosphere* **2010**, 80, 351-365.
65. Andreozzi, R.; Caprio, V.; Insola, A.; Marotta, R. Advanced oxidation processes (AOP) for water purification and recovery. *Catalysis today* **1999**, 53, 51-59.
66. Huber, M.; Canonica, S.; Park, G.; von Gunten, U. Oxidation of pharmaceuticals during ozonation and advanced oxidation processes. *Environ. Sci. Technol.* **2003**, 37, 1016-1040.

67. Munter, R. Advanced oxidation processes—current status and prospects. *Proc.Estonian Acad.Sci.Chem* **2001**, 50, 59-80.
68. Andreozzi, R.; Campanella, L.; Frayse, B.; Garric, J.; Gonnella, A.; Lo Giudice, R.; Marotta, R.; Pinto, G.; Pollio, A. Effects of advanced oxidation processes (AOPs) on the toxicity of a mixture of pharmaceuticals. *Water Science and Technology* **2004**, 50, 23-28.
69. Pera-Titus, M.; García-Molina, V.; Banos, M. A.; Giménez, J.; Esplugas, S. Degradation of chlorophenols by means of advanced oxidation processes: A general review. *Applied Catalysis B: Environmental* **2004**, 47, 219-256.
70. Comninellis, C.; Kapalka, A.; Malato, S.; Parsons, S. A.; Poulios, I.; Mantzavinos, D. Advanced oxidation processes for water treatment: Advances and trends for R&D. *Journal of Chemical Technology and Biotechnology* **2008**, 83, 769-776.
71. Parsons, S. Advanced oxidation processes for water and wastewater treatment. Iwa Publishing: 2004.
72. Gültekin, I.; Ince, N. H. Synthetic endocrine disruptors in the environment and water remediation by advanced oxidation processes. *J. Environ. Manage.* **2007**, 85, 816-832.
73. D.S. Chaudahry, S. Vigneswaran, V. Jegatheesan, H.H. Ngo, W.G. Shim, S.H. Kim Granular activated carbon adsorption in tertiary wastewater treatment; experiments and models. *Wat. Sci. Technol* **2002**, 47, 113-120.
74. Snyder, S. A.; Adham, S.; Redding, A. M.; Cannon, F. S.; DeCarolis, J.; Oppenheimer, J.; Wert, E. C.; Yoon, Y. Role of membranes and activated carbon in the removal of endocrine disruptors and pharmaceuticals. *Desalination* **2007**, 202, 156-181.
75. Ternes, T. A.; Meisenheimer, M.; McDowell, D.; Sacher, F.; Brauch, H.; Haist-Gulde, B.; Preuss, G.; Wilme, U.; Zulei-Seibert, N. Removal of pharmaceuticals during drinking water treatment. *Environ. Sci. Technol.* **2002**, 36, 3855-3863.
76. Fujishima, A. Electrochemical photolysis of water at a semiconductor electrode. *Nature* **1972**, 238, 37-38.
77. Fujishima, A.; Honda, K. Photolysis-decomposition of water at the surface of an irradiated semiconductor. *Nature* **1972**, 238, 37-38.

78. Carey, J. H.; Lawrence, J.; Tosine, H. M. Photodechlorination of PCB's in the presence of titanium dioxide in aqueous suspensions. *Bull. Environ. Contam. Toxicol.* **1976**, 16, 697-701.
79. Shahrezaei, F.; Mansouri, Y.; Zinatizadeh, A. A. L.; Akhbari, A. Process modeling and kinetic evaluation of petroleum refinery wastewater treatment in a photocatalytic reactor using TiO₂ nanoparticles. *Powder Technol* **2012**, 221, 203-212.
80. Ahmed, S.; Rasul, M. G.; Brown, R.; Hashib, M. A. Influence of parameters on the heterogeneous photocatalytic degradation of pesticides and phenolic contaminants in wastewater: A short review. *J. Environ. Manage.* **2011**, 92, 311-330.
81. Oyama, T.; Otsu, T.; Hidano, Y.; Koike, T.; Serpone, N.; Hidaka, H. Enhanced remediation of simulated wastewaters contaminated with 2-chlorophenol and other aquatic pollutants by TiO₂-photoassisted ozonation in a sunlight-driven pilot-plant scale photoreactor. *Solar Energy* **2011**, 85, 938-944.
82. Mozia, S. Photocatalytic membrane reactors (PMRs) in water and wastewater treatment. A review. *Separation and Purification Technology* **2010**, 73, 71-91.
83. Ollis, D. F.; Pelizzetti, E.; Serpone, N. Photocatalyzed destruction of water contaminants. *Environmental Science and Technology; (United States)* **1991**, 25.
84. Serpone, N.; Pelizzetti, E. *Photocatalysis: Fundamentals and applications*; Wiley New York: 1989.
85. Liu, G.; Wang, J.; Zhu, Y.; Zhang, X. Destructive adsorption of carbon tetrachloride on nanometer titanium dioxide. *Phys.Chem.Chem.Phys.* **2004**, 6, 985-991.
86. Kabra, K.; Chaudhary, R.; Sawhney, R. L. Treatment of hazardous organic and inorganic compounds through aqueous-phase photocatalysis: A review. *Ind Eng Chem Res* **2004**, 43, 7683-7696.
87. Aspnes, D.; Moss, T. *Handbook on semiconductors. Vol.2*North-Holland, Amsterdam **1980**, 109.
88. Lee, S.; Park, S. TiO₂ photocatalyst for water treatment applications. *Journal of Industrial and Engineering Chemistry* **2013**, 19, 1761-1769.
89. Pelaez, M.; Nolan, N. T.; Pillai, S. C.; Seery, M. K.; Falaras, P.; Kontos, A. G.; Dunlop, P. S. M.; Hamilton, J. W. J.; Byrne, J. A.; O'shea, K.; Entezari, M. H.; Dionysiou, D. D. A review on the visible light active titanium dioxide photocatalysts for environmental applications. *Applied Catalysis B: Environmental*.

90. Chen, X.; Mao, S. S. Titanium dioxide nanomaterials: Synthesis, properties, modifications, and applications. *Chem. Rev.* **2007**, *107*, 2891-2959.
91. Chen, X. Synthesis and Investigation of Novel Nanomaterials for Improved Photocatalysis, Case Western Reserve University, 2005.
92. Gupta, S. M.; Tripathi, M. A review of TiO₂ nanoparticles. *Chinese Science Bulletin* **2011**, *56*, 1639-1657.
93. Sun, B. Understanding and Modifying TiO₂ for Aqueous Organic Photodegradation, University of Cincinnati, 2005.
94. Liu, M.; Piao, L.; Lu, W.; Ju, S.; Zhao, L.; Zhou, C.; Li, H.; Wang, W. Flower-like TiO₂ nanostructures with exposed {001} facets: Facile synthesis and enhanced photocatalysis. *Nanoscale* **2010**, *2*, 1115-1117.
95. Zheng, Z.; Huang, B.; Qin, X.; Zhang, X.; Dai, Y. Strategic synthesis of hierarchical TiO₂ microspheres with enhanced photocatalytic activity. *Chemistry-A European Journal* **2010**, *16*, 11266-11270.
96. Liu, B.; Nakata, K.; Sakai, M.; Saito, H.; Ochiai, T.; Murakami, T.; Takagi, K.; Fujishima, A. Mesoporous TiO₂ Core-Shell spheres composed of nanocrystals with exposed high-energy facets: Facile synthesis and formation mechanism. *Langmuir* **2011**, *27*, 8500-8508.
97. Kondo, Y.; Yoshikawa, H.; Awaga, K.; Murayama, M.; Mori, T.; Sunada, K.; Bandow, S.; Iijima, S. Preparation, photocatalytic activities, and dye-sensitized solar-cell performance of submicron-scale TiO₂ hollow spheres. *Langmuir* **2008**, *24*, 547-550.
98. Nakata, K.; Fujishima, A. TiO₂ photocatalysis: Design and applications. *Journal of Photochemistry and Photobiology C: Photochemistry Reviews* **2012**, *13*, 169-189.
99. Liu, N.; Chen, X.; Zhang, J.; Schwank, J. W. A review on TiO₂-based nanotubes synthesized via hydrothermal method: Formation mechanism, structure modification, and photocatalytic applications. *Catalysis Today* **2014**, *225*, 34-51.
100. Wong, C. L.; Tan, Y. N.; Mohamed, A. R. A review on the formation of titania nanotube photocatalysts by hydrothermal treatment. *J. Environ. Manage.* **2011**, *92*, 1669-1680.
101. Nakahira, A.; Kubo, T.; Numako, C. Formation mechanism of TiO₂ derived titanate nanotubes prepared by the hydrothermal process. *Inorg. Chem.* **2010**, *49*, 5845-5852.

102. Scherer, C. J. B. a. G. W. The physics and chemistry of sol-gel processing; Boston Academic press: 1990.
103. Wang, C.; Ying, J. Y. Sol-gel synthesis and hydrothermal processing of anatase and rutile titania nanocrystals. *Chemistry of Materials* **1999**, 11, 3113-3120.
104. Macwan, D.; Dave, P. N.; Chaturvedi, S. A review on nano-TiO₂ sol-gel type syntheses and its applications. *J. Mater. Sci.* **2011**, 46, 3669-3686.
105. Feng, X.; Shankar, K.; Varghese, O. K.; Paulose, M.; Latempa, T. J.; Grimes, C. A. Vertically aligned single crystal TiO₂ nanowire arrays grown directly on transparent conducting oxide coated glass: Synthesis details and applications. *Nano letters* **2008**, 8, 3781-3786.
106. Komiyama, H.; Kanai, T.; Inoue, H. Preparation of porous, amorphous, and ultrafine TiO₂ particles by chemical vapor deposition. *Chem. Lett.* **1984**, 1283-1286.
107. Serp, P.; Kalck, P.; Feurer, R. Chemical vapor deposition methods for the controlled preparation of supported catalytic materials. *Chem. Rev.* **2002**, 102, 3085-3128.
108. Bedford, N. M. *Electrospun Fibers for Energy, Electronic, and Environmental Applications*, University of Cincinnati, 2011.
109. Cheng, Y.; Huang, W.; Zhang, Y.; Zhu, L.; Liu, Y.; Fan, X.; Cao, X. Preparation of TiO₂ hollow nanofibers by electrospinning combined with sol-gel process. *CrystEngComm* **2010**, 12, 2256-2260.
110. Meng, X.; Luo, N.; Cao, S.; Zhang, S.; Yang, M.; Hu, X. In-situ growth of titania nanoparticles in electrospun polymer nanofibers at low temperature. *Materials Letters* **2009**, 63, 1401-1403.
111. Tekmen, C.; Suslu, A.; Cocen, U. Titania nanofibers prepared by electrospinning. *Materials Letters* **2008**, 62, 4470-4472.
112. Nuansing, W.; Ninmuang, S.; Jarernboon, W.; Maensiri, S.; Seraphin, S. Structural characterization and morphology of electrospun TiO₂ nanofibers. *Materials Science and Engineering: B* **2006**, 131, 147-155.
113. Kumar, A.; Jose, R.; Fujihara, K.; Wang, J.; Ramakrishna, S. Structural and optical properties of electrospun TiO₂ nanofibers. *Chem. Mater.* **2007**, 19, 6536-6542.

114. Tang, Y.; Tao, J.; Zhang, Y.; Wu, T.; Tao, H.; Zhu, Y. Preparation of TiO₂ nanotube on glass by anodization of ti films at room temperature. *Transactions of Nonferrous Metals Society of China* **2009**, 19, 192-198.
115. Macak, J. M.; Hildebrand, H.; Marten-Jahns, U.; Schmuki, P. Mechanistic aspects and growth of large diameter self-organized TiO₂ nanotubes. *Journal of Electroanalytical Chemistry* **2008**, 621, 254-266.
116. Chen, X.; Schriver, M.; Suen, T.; Mao, S. S. Fabrication of 10 nm diameter TiO₂ nanotube arrays by titanium anodization. *Thin Solid Films* **2007**, 515, 8511-8514.
117. Chowdhury, P.; Moreira, J.; Gomaa, H.; Ray, A. K. Visible-solar-light-driven photocatalytic degradation of phenol with dye-sensitized TiO₂: Parametric and kinetic study. *Ind Eng Chem Res* **2012**, 51, 4523-4532.
118. Jiang, D.; Xu, Y.; Wu, D.; Sun, Y. Visible-light responsive dye-modified TiO₂ photocatalyst. *Journal of Solid State Chemistry* **2008**, 181, 593-602.
119. Rehman, S.; Ullah, R.; Butt, A.; Gohar, N. Strategies of making TiO₂ and ZnO visible light active. *J. Hazard. Mater.* **2009**, 170, 560-569.
120. Hou, J.; Yang, C.; Wang, Z.; Jiao, S.; Zhu, H. Bi₂O₃ quantum dots decorated anatase TiO₂ nanocrystals with exposed {0 0 1} facets on graphene sheets for enhanced visible-light photocatalytic performance. *Applied Catalysis B: Environmental* **2013**, 129, 333-341.
121. Asahi, R.; Morikawa, T.; Ohwaki, T.; Aoki, K.; Taga, Y. Visible-light photocatalysis in nitrogen-doped titanium oxides. *Science* **2001**, 293, 269-271.
122. Yu, J. C.; Yu, J.; Ho, W.; Jiang, Z.; Zhang, L. Effects of F-doping on the photocatalytic activity and microstructures of nanocrystalline TiO₂ powders. *Chemistry of materials* **2002**, 14, 3808-3816.
123. Hong, X.; Wang, Z.; Cai, W.; Lu, F.; Zhang, J.; Yang, Y.; Ma, N.; Liu, Y. Visible-light-activated nanoparticle photocatalyst of iodine-doped titanium dioxide. *Chemistry of Materials* **2005**, 17, 1548-1552.
124. Luo, H.; Takata, T.; Lee, Y.; Zhao, J.; Domen, K.; Yan, Y. Photocatalytic activity enhancing for titanium dioxide by co-doping with bromine and chlorine. *Chemistry of Materials* **2004**, 16, 846-849.

125. Bouras, P.; Stathatos, E.; Lianos, P. Pure versus metal-ion-doped nanocrystalline titania for photocatalysis. *Applied Catalysis B: Environmental* **2007**, 73, 51-59.
126. Choi, J.; Park, H.; Hoffmann, M. R. Effects of single metal-ion doping on the visible-light photoreactivity of TiO₂. *The Journal of Physical Chemistry C* **2009**, 114, 783-792.
127. Hufschmidt, D.; Bahnemann, D.; Testa, J. J.; Emilio, C. A.; Litter, M. I. Enhancement of the photocatalytic activity of various TiO₂ materials by platinisation. *J. Photochem. Photobiol. A* **2002**, 148, 223-231.
128. Li Puma, G.; Bono, A.; Krishnaiah, D.; Collin, J. G. Preparation of titanium dioxide photocatalyst loaded onto activated carbon support using chemical vapor deposition: A review paper. *Journal of Hazardous Materials* **2008**, 157, 209-219.
129. Arana, J.; Dona-Rodriguez, J.; Tello Rendón, E.; Garriga i Cabo, C.; González-Díaz, O.; Herrera-Melián, J.; Pérez-Peña, J.; Colón, G.; Navío, J. TiO₂ activation by using activated carbon as a support: Part I. surface characterisation and decantability study. *Applied Catalysis B: Environmental* **2003**, 44, 161-172.
130. Arana, J.; Dona-Rodriguez, J.; Tello Rendón, E.; Garriga i Cabo, C.; González-Díaz, O.; Herrera-Melián, J.; Pérez-Peña, J.; Colón, G.; Navío, J. TiO₂ activation by using activated carbon as a support: Part II. photoreactivity and FTIR study. *Applied Catalysis B: Environmental* **2003**, 44, 153-160.
131. LIU, J.; YANG, R.; LI, S. Preparation and application of efficient TiO₂/ACFs photocatalyst. *Journal of Environmental Sciences* **2006**, 18, 979-982.
132. Liu, S. X.; Chen, X. Y.; Chen, X. A TiO₂/AC composite photocatalyst with high activity and easy separation prepared by a hydrothermal method. *J. Hazard. Mater.* **2007**, 143, 257-263.
133. Wang, X.; Liu, Y.; Hu, Z.; Chen, Y.; Liu, W.; Zhao, G. Degradation of methyl orange by composite photocatalysts nano-TiO₂ immobilized on activated carbons of different porosities. *Journal of Hazardous Materials* **2009**, 169, 1061-1067.
134. Basha, S.; Barr, C.; Keane, D.; Nolan, K.; Morrissey, A.; Oelgemöller, M.; Tobin, J. M. On the adsorption/photodegradation of amoxicillin in aqueous solutions by an integrated photocatalytic adsorbent (IPCA): Experimental studies and kinetics analysis. *Photochemical & Photobiological Sciences* **2011**, 10, 1014-1022.

135. Keane, D.; Basha, S.; Nolan, K.; Morrissey, A.; Oelgemöller, M.; Tobin, J. Photodegradation of famotidine by integrated photocatalytic adsorbent (IPCA) and kinetic study. *Catalysis Letters* **2011**, 141, 300-308.
136. Basha, S.; Keane, D.; Morrissey, A.; Nolan, K.; Oelgemöller, M.; Tobin, J. Studies on the adsorption and kinetics of photodegradation of pharmaceutical compound, indomethacin using novel photocatalytic adsorbents (IPCAs). *Ind Eng Chem Res* **2010**, 49, 11302-11309.
137. Torimoto, T.; Okawa, Y.; Takeda, N.; Yoneyama, H. Effect of activated carbon content in TiO₂-loaded activated carbon on photodegradation behaviors of dichloromethane. *J. Photochem. Photobiol. A* **1997**, 103, 153-157.
138. Torimoto, T.; Ito, S.; Kuwabata, S.; Yoneyama, H. Effects of adsorbents used as supports for titanium dioxide loading on photocatalytic degradation of propylamide. *Environ. Sci. Technol.* **1996**, 30, 1275-1281.
139. Matos, J.; García-López, E.; Palmisano, L.; García, A.; Marci, G. Influence of activated carbon in TiO₂ and ZnO mediated photo-assisted degradation of 2-propanol in gas-solid regime. *Applied Catalysis B: Environmental* **2010**, 99, 170-180.
140. Cao, X.; Shiraishi, F. A mechanism of photocatalytic and adsorptive treatment of 2,4-dinitrophenol on a porous thin film of TiO₂ covering granular activated carbon particles. *Chem. Eng. J.* **2010**, 160, 651-659.
141. Foo, K. Y.; Hameed, B. H. Decontamination of textile wastewater via TiO₂/activated carbon composite materials. *Adv. Colloid Interface Sci.* **2010**, 159, 130-143.
142. Yao, S.; Li, J.; Shi, Z. Immobilization of TiO₂ nanoparticles on activated carbon fiber and its photodegradation performance for organic pollutants. *Particuology* **2010**, 8, 272-278.
143. Wang, X.; Hu, Z.; Chen, Y.; Zhao, G.; Liu, Y.; Wen, Z. A novel approach towards high-performance composite photocatalyst of TiO₂ deposited on activated carbon. *Appl. Surf. Sci.* **2009**, 255, 3953-3958.
144. Ravichandran, L.; Selvam, K.; Swaminathan, M. Highly efficient activated carbon loaded TiO₂ for photo defluorination of pentafluorobenzoic acid. *Journal of Molecular Catalysis A: Chemical* **2010**, 317, 89-96.
145. Hirsch, A. The era of carbon allotropes. *Nature materials* **2010**, 9, 868-871.

146. Iijima, S. Helical microtubules of graphitic carbon. *Nature* **1991**, 354, 56-58.
147. Novoselov, K. S. Electric field effect in atomically thin carbon films. *Science* **2004**, 306, 666-669.
148. Novoselov, K. S. Two-dimensional atomic crystals. *Proc. Natl. Acad. Sci. USA* **2005**, 102, 10451-10453.
149. Geim, A. K.; Novoselov, K. S. The rise of graphene. *Nat Mater* **2007**, 6, 183-191.
150. Neto, A. C.; Guinea, F.; Peres, N.; Novoselov, K. S.; Geim, A. K. The electronic properties of graphene. *Reviews of modern physics* **2009**, 81, 109.
151. Schaffhaeutl, C. L. on the combinations of carbon with silicon and iron, and other metals, forming the different species of cast iron, steel, and malleable iron. *The London and Edinburgh Philosophical Magazine and Journal of Science* **1840**, 16, 297-304.
152. He, H.; Klinowski, J.; Forster, M.; Lerf, A. A new structural model for graphite oxide. *Chemical physics letters* **1998**, 287, 53-56.
153. Lerf, A.; He, H.; Forster, M.; Klinowski, J. Structure of graphite oxide revisited||. *The Journal of Physical Chemistry B* **1998**, 102, 4477-4482.
154. Lerf, A.; He, H.; Riedl, T.; Forster, M.; Klinowski, J. ¹³C and ¹H MAS NMR studies of graphite oxide and its chemically modified derivatives. *Solid State Ionics* **1997**, 101-103, Part 2, 857-862.
155. Hummers Jr, W. S.; Offeman, R. E. Preparation of graphitic oxide. *J. Am. Chem. Soc.* **1958**, 80, 1339-1339.
156. Geim, A. K. Graphene: Status and prospects. *Science* **2009**, 324, 1530-1534.
157. Rao, C. e. e.; Sood, A. e.; Subrahmanyam, K. e.; Govindaraj, A. Graphene: The new Two-Dimensional nanomaterial. *Angewandte Chemie International Edition* **2009**, 48, 7752-7777.
158. Novoselov, K. S.; Blake, P.; Katsnelson, M. I. In *Graphene: Electronic Properties*; Editors-in-Chief: K. H. Jürgen Buschow; *Encyclopedia of Materials: Science and Technology* (Second Edition); Elsevier: Oxford, 2008; pp 1-6.
159. Du, X.; Skachko, I.; Barker, A.; Andrei, E. Y. Approaching ballistic transport in suspended graphene. *Nature nanotechnology* **2008**, 3, 491-495.

160. May, P.; Khan, U.; O'Neill, A.; Coleman, J. N. Approaching the theoretical limit for reinforcing polymers with graphene. *Journal of Materials Chemistry* **2012**, *22*, 1278-1282.
161. Potts, J. R.; Dreyer, D. R.; Bielawski, C. W.; Ruoff, R. S. Graphene-based polymer nanocomposites. *Polymer* **2011**, *52*, 5-25.
162. Kim, H.; Abdala, A. A.; Macosko, C. W. Graphene/polymer nanocomposites. *Macromolecules* **2010**, *43*, 6515-6530.
163. Guo, S.; Dong, S. Graphene nanosheet: Synthesis, molecular engineering, thin film, hybrids, and energy and analytical applications. *Chem. Soc. Rev.* **2011**, *40*, 2644-2672.
164. Kamat, P. V. Graphene-based nanoarchitectures. Anchoring semiconductor and metal nanoparticles on a two-dimensional carbon support. *The Journal of Physical Chemistry Letters* **2010**, *1*, 520-527.
165. Novoselov, K. S.; Fal, V.; Colombo, L.; Gellert, P.; Schwab, M.; Kim, K. A roadmap for graphene. *Nature* **2012**, *490*, 192-200.
166. Pumera, M. Electrochemistry of graphene: New horizons for sensing and energy storage. *The Chemical Record* **2009**, *9*, 211-223.
167. Novoselov, K.; Neto, A. C. Two-dimensional crystals-based heterostructures: Materials with tailored properties. *Phys. Scripta* **2012**, *2012*, 014006.
168. Berger, C.; Song, Z.; Li, X.; Wu, X.; Brown, N.; Naud, C.; Mayou, D.; Li, T.; Hass, J.; Marchenkov, A. N.; Conrad, E. H.; First, P. N.; de Heer, W. A. Electronic confinement and coherence in patterned epitaxial graphene. *Science* **2006**, *312*, 1191-1196.
169. Reina, A.; Jia, X.; Ho, J.; Nezich, D.; Son, H.; Bulovic, V.; Dresselhaus, M. S.; Kong, J. Large area, few-layer graphene films on arbitrary substrates by chemical vapor deposition. *Nano letters* **2008**, *9*, 30-35.
170. Li, X.; Cai, W.; An, J.; Kim, S.; Nah, J.; Yang, D.; Piner, R.; Velamakanni, A.; Jung, I.; Tutuc, E.; Banerjee, S. K.; Colombo, L.; Ruoff, R. S. Large-area synthesis of high-quality and uniform graphene films on copper foils. *Science* **2009**, *324*, 1312-1314.
171. Suk, J. W.; Kitt, A.; Magnuson, C. W.; Hao, Y.; Ahmed, S.; An, J.; Swan, A. K.; Goldberg, B. B.; Ruoff, R. S. Transfer of CVD-grown monolayer graphene onto arbitrary substrates. *ACS nano* **2011**, *5*, 6916-6924.

172. MingáLi, C. Nanoelectronic biosensors based on CVD grown graphene. *Nanoscale* **2010**, 2, 1485-1488.
173. Kim, K. S.; Zhao, Y.; Jang, H.; Lee, S. Y.; Kim, J. M.; Kim, K. S.; Ahn, J.; Kim, P.; Choi, J.; Hong, B. H. Large-scale pattern growth of graphene films for stretchable transparent electrodes. *Nature* **2009**, 457, 706-710.
174. Shih, C.; Vijayaraghavan, A.; Krishnan, R.; Sharma, R.; Han, J.; Ham, M.; Jin, Z.; Lin, S.; Paulus, G. L.; Reuel, N. F. Bi-and trilayer graphene solutions. *Nature nanotechnology* **2011**, 6, 439-445.
175. Zhang Qiong; He YunQiu; Chen XiaoGang; Hu DongHu; Li LinJiang; Yin Ting; Ji LingLi Structure and photocatalytic properties of TiO₂-graphene oxide intercalated composite. *Chin. Sci. Bull.* **2011**, 56, 331-339.
176. Dresselhaus, M. S.; Dresselhaus, G. Intercalation compounds of graphite. *Adv. Phys.* **2002**, 51, 1-186.
177. Ren, H.; Kang, F.; Jiao, Q.; Cui, Q. Kinetics of the thermal decomposition of intercalation compounds during exfoliation. *New Carbon Materials* **2006**, 21, 315-319.
178. Ma, R.; Sasaki, T. Nanosheets of oxides and hydroxides: Ultimate 2D Charge-Bearing functional crystallites. *Adv Mater* **2010**, 22, 5082-5104.
179. Walker, G. F.; Garrett, W. G. Chemical exfoliation of vermiculite and the production of colloidal dispersions. *Science* **1967**, 156, 385-387.
180. Hernandez, Y.; Nicolosi, V.; Lotya, M.; Blighe, F. M.; Sun, Z.; De, S.; McGovern, I.; Holland, B.; Byrne, M.; Gun'Ko, Y. K. High-yield production of graphene by liquid-phase exfoliation of graphite. *Nature Nanotechnology* **2008**, 3, 563-568.
181. Coleman, J. N. Liquid exfoliation of defect-free graphene. *Acc. Chem. Res.* **2012**, 46, 14-22.
182. Coleman, J. N.; Lotya, M.; O'Neill, A.; Bergin, S. D.; King, P. J.; Khan, U.; Young, K.; Gaucher, A.; De, S.; Smith, R. J.; Shvets, I. V.; Arora, S. K.; Stanton, G.; Kim, H.; Lee, K.; Kim, G. T.; Duesberg, G. S.; Hallam, T.; Boland, J. J.; Wang, J. J.; Donegan, J. F.; Grunlan, J. C.; Moriarty, G.; Shmeliov, A.; Nicholls, R. J.; Perkins, J. M.; Grievson, E. M.; Theuwissen, K.; McComb, D. W.; Nellist, P. D.; Nicolosi, V. Two-dimensional nanosheets produced by liquid exfoliation of layered materials. *Science* **2011**, 331, 568-571.

183. Coleman, J. N. Liquid-Phase exfoliation of nanotubes and graphene. *Advanced Functional Materials* **2009**, 19, 3680-3695.
184. Khan, U.; O'Neill, A.; Lotya, M.; De, S.; Coleman, J. N. High-Concentration solvent exfoliation of graphene. *Small* **2010**, 6, 864-871.
185. Khan, U.; Porwal, H.; O'Neill, A.; Nawaz, K.; May, P.; Coleman, J. N. Solvent-exfoliated graphene at extremely high concentration. *Langmuir* **2011**, 27, 9077-9082.
186. O'Neill, A.; Khan, U.; Nirmalraj, P. N.; Boland, J.; Coleman, J. N. Graphene dispersion and exfoliation in low boiling point solvents. *The Journal of Physical Chemistry C* **2011**, 115, 5422-5428.
187. Cunningham, G.; Lotya, M.; Cucinotta, C. S.; Sanvito, S.; Bergin, S. D.; Menzel, R.; Shaffer, M. S.; Coleman, J. N. Solvent exfoliation of transition metal dichalcogenides: Dispersibility of exfoliated nanosheets varies only weakly between compounds. *Acs Nano* **2012**, 6, 3468-3480.
188. Lotya, M.; King, P. J.; Khan, U.; De, S.; Coleman, J. N. High-concentration, surfactant-stabilized graphene dispersions. *ACS nano* **2010**, 4, 3155-3162.
189. Nicolosi, V.; Chhowalla, M.; Kanatzidis, M. G.; Strano, M. S.; Coleman, J. N. Liquid exfoliation of layered materials. *Science* **2013**, 340.
190. Dreyer, D. R.; Park, S.; Bielawski, C. W.; Ruoff, R. S. The chemistry of graphene oxide. *Chem. Soc. Rev.* **2010**, 39, 228-240.
191. Park, S.; Ruoff, R. S. Chemical methods for the production of graphenes. *Nature nanotechnology* **2009**, 4, 217-224.
192. Brodie, B. C. On the atomic weight of graphite. *Philosophical Transactions of the Royal Society of London* **1859**, 249-259.
193. Bagri, A.; Mattevi, C.; Acik, M.; Chabal, Y. J.; Chhowalla, M.; Shenoy, V. B. Structural evolution during the reduction of chemically derived graphene oxide. *Nature chemistry* **2010**, 2, 581-587.
194. Zhao, J.; Ren, W.; Cheng, H. Graphene sponge for efficient and repeatable adsorption and desorption of water contaminations. *J.Mater.Chem.* **2012**, 22, 20197-20202.

195. Gao, Y.; Li, Y.; Zhang, L.; Huang, H.; Hu, J.; Shah, S. M.; Su, X. Adsorption and removal of tetracycline antibiotics from aqueous solution by graphene oxide. *J. Colloid Interface Sci.* **2012**, *368*, 540-546.
196. Liu, F.; Chung, S.; Oh, G.; Seo, T. S. Three-dimensional graphene oxide nanostructure for fast and efficient water-soluble dye removal. *ACS Applied Materials & Interfaces* **2012**, *4*, 922-927.
197. Sudeep, P. M.; Narayanan, T. N.; Ganesan, A.; Shaijumon, M. M.; Yang, H.; Ozden, S.; Patra, P. K.; Pasquali, M.; Vajtai, R.; Ganguli, S. Covalently interconnected three-dimensional graphene oxide solids. *ACS nano* **2013**, *7*, 7034-7040.
198. Stankovich, S.; Dikin, D. A.; Piner, R. D.; Kohlhaas, K. A.; Kleinhammes, A.; Jia, Y.; Wu, Y.; Nguyen, S. T.; Ruoff, R. S. Synthesis of graphene-based nanosheets via chemical reduction of exfoliated graphite oxide. *Carbon* **2007**, *45*, 1558-1565.
199. Park, S.; An, J.; Potts, J. R.; Velamakanni, A.; Murali, S.; Ruoff, R. S. Hydrazine-reduction of graphite-and graphene oxide. *Carbon* **2011**, *49*, 3019-3023.
200. Gao, X.; Jang, J.; Nagase, S. Hydrazine and thermal reduction of graphene oxide: Reaction mechanisms, product structures, and reaction design. *The Journal of Physical Chemistry C* **2009**, *114*, 832-842.
201. Gao, W.; Alemany, L. B.; Ci, L.; Ajayan, P. M. New insights into the structure and reduction of graphite oxide. *Nature chemistry* **2009**, *1*, 403-408.
202. Shin, H.; Kim, K. K.; Benayad, A.; Yoon, S.; Park, H. K.; Jung, I.; Jin, M. H.; Jeong, H.; Kim, J. M.; Choi, J. Efficient reduction of graphite oxide by sodium borohydride and its effect on electrical conductance. *Advanced Functional Materials* **2009**, *19*, 1987-1992.
203. Tung, V. C.; Allen, M. J.; Yang, Y.; Kaner, R. B. High-throughput solution processing of large-scale graphene. *Nature nanotechnology* **2008**, *4*, 25-29.
204. Stankovich, S.; Dikin, D. A.; Piner, R. D.; Kohlhaas, K. A.; Kleinhammes, A.; Jia, Y.; Wu, Y.; Nguyen, S. T.; Ruoff, R. S. Synthesis of graphene-based nanosheets via chemical reduction of exfoliated graphite oxide. *Carbon* **2007**, *45*, 1558-1565.
205. Huh, S. H. Thermal reduction of graphene oxide. *Physics and Applications of Graphene—Experiments*, edited by S.Mikhailov (InTech, New York, 2011) **2011**.

206. Wei, Z.; Wang, D.; Kim, S.; Kim, S. Y.; Hu, Y.; Yakes, M. K.; Laracuent, A. R.; Dai, Z.; Marder, S. R.; Berger, C.; King, W. P.; de Heer, W. A.; Sheehan, P. E.; Riedo, E. Nanoscale tunable reduction of graphene oxide for graphene electronics. *Science* **2010**, 328, 1373-1376.
207. Kim, S. R.; Parvez, M. K.; Chhowalla, M. UV-reduction of graphene oxide and its application as an interfacial layer to reduce the back-transport reactions in dye-sensitized solar cells. *Chemical Physics Letters* **2009**, 483, 124-127.
208. Williams, G.; Seger, B.; Kamat, P. V. TiO₂-graphene nanocomposites. UV-assisted photocatalytic reduction of graphene oxide. *ACS Nano* **2008**, 2, 1487-1491.
209. Allen, M. J.; Tung, V. C.; Kaner, R. B. Honeycomb carbon: A review of graphene. *Chem. Rev.* **2009**, 110, 132-145.
210. Thostenson, E. T.; Ren, Z.; Chou, T. Advances in the science and technology of carbon nanotubes and their composites: A review. *Composites Sci. Technol.* **2001**, 61, 1899-1912.
211. Baughman, R. H.; Zakhidov, A. A.; de Heer, W. A. Carbon nanotubes--the route toward applications. *Science* **2002**, 297, 787-792.
212. Ren, X.; Chen, C.; Nagatsu, M.; Wang, X. Carbon nanotubes as adsorbents in environmental pollution management: A review. *Chem. Eng. J.* **2011**, 170, 395-410.
213. Byon, H. R.; Lee, S. W.; Chen, S.; Hammond, P. T.; Shao-Horn, Y. Thin films of carbon nanotubes and chemically reduced graphenes for electrochemical micro-capacitors. *Carbon* **2011**, 49, 457-467.
214. Cusano, A.; Consales, M.; Crescitelli, A.; Penza, M.; Aversa, P.; Veneri, P. D.; Giordano, M. Charge transfer effects on the sensing properties of fiber optic chemical nano-sensors based on single-walled carbon nanotubes. *Carbon* **2009**, 47, 782-788.
215. Guadagno, L.; Vertuccio, L.; Sorrentino, A.; Raimondo, M.; Naddeo, C.; Vittoria, V.; Iannuzzo, G.; Calvi, E.; Russo, S. Mechanical and barrier properties of epoxy resin filled with multi-walled carbon nanotubes. *Carbon* **2009**, 47, 2419-2430.
216. Terrones, M. Science and technology of the twenty-first century: Synthesis, properties, and applications of carbon nanotubes. *Annual review of materials research* **2003**, 33, 419-501.

217. Terrones, M.; Jorio, A.; Endo, M.; Rao, A. M.; Kim, Y. A.; Hayashi, T.; Terrones, H.; Charlier, J. C.; Dresselhaus, G.; Dresselhaus, M. S. New direction in nanotube science. *Materials Today* **2004**, 7, 30-45.
218. Woan, K.; Pyrgiotakis, G.; Sigmund, W. Photocatalytic Carbon-Nanotube-TiO₂ composites. *Adv Mater* **2009**, 21, 2233-2239.
219. Chen, M.; Zhang, F.; Oh, W. Synthesis, characterization, and photocatalytic analysis of CNT/TiO₂ composites derived from MWCNTs and titanium sources. *New Carbon Materials* **2009**, 24, 159-166.
220. Yu, H.; Quan, X.; Chen, S.; Zhao, H. TiO₂-multiwalled carbon nanotube heterojunction arrays and their charge separation capability. *The Journal of Physical Chemistry C* **2007**, 111, 12987-12991.
221. Eder, D.; Windle, A. H. Carbon-Inorganic hybrid materials: The Carbon-Nanotube/TiO₂ interface. *Adv Mater* **2008**, 20, 1787-1793.
222. Krishna, V.; Pumprueg, S.; Lee, S. H.; Zhao, J.; Sigmund, W.; Koopman, B.; Moudgil, B. M. Photocatalytic disinfection with titanium dioxide coated multi-wall carbon nanotubes. *Process Safety and Environmental Protection* **2005**, 83, 393-397.
223. Yao, Y.; Li, G.; Ciston, S.; Lueptow, R. M.; Gray, K. A. Photoreactive TiO₂/Carbon nanotube composites: Synthesis and reactivity. *Environ. Sci. Technol.* **2008**, 42, 4952-4957.
224. Gao, B.; Chen, G. Z.; Li Puma, G. Carbon nanotubes/titanium dioxide (CNTs/TiO₂) nanocomposites prepared by conventional and novel surfactant wrapping sol-gel methods exhibiting enhanced photocatalytic activity. *Applied Catalysis B: Environmental* **2009**, 89, 503-509.
225. Orlanducci, S.; Sessa, V.; Terranova, M. L.; Battiston, G. A.; Battiston, S.; Gerbasi, R. Nanocrystalline TiO₂ on single walled carbon nanotube arrays: Towards the assembly of organized C/TiO₂ nanosystems. *Carbon* **2006**, 44, 2839-2843.
226. Chen, Y.; Crittenden, J. C.; Hackney, S.; Sutter, L.; Hand, D. W. Preparation of a novel TiO₂-based pn junction nanotube photocatalyst. *Environ. Sci. Technol.* **2005**, 39, 1201-1208.
227. Wang, W.; Serp, P.; Kalck, P.; Faria, J. L. Visible light photodegradation of phenol on MWNT-TiO₂ composite catalysts prepared by a modified sol-gel method. *Journal of Molecular Catalysis A: Chemical* **2005**, 235, 194-199.

228. Yao, Y.; Li, G.; Ciston, S.; Lueptow, R. M.; Gray, K. A. Photoreactive TiO₂/carbon nanotube composites: Synthesis and reactivity. *Environ. Sci. Technol.* **2008**, *42*, 4952-4957.
229. Zhang, H.; Lv, X.; Li, Y.; Wang, Y.; Li, J. P25-graphene composite as a high performance photocatalyst. *ACS Nano* **2010**, *4*, 380-386.
230. Bai, S.; Shen, X. Graphene-inorganic nanocomposites. *RSC Adv.* **2012**, *2*, 64-98.
231. Lightcap, I. V.; Kosel, T. H.; Kamat, P. V. Anchoring semiconductor and metal nanoparticles on a two-dimensional catalyst mat. Storing and shuttling electrons with reduced graphene oxide. *Nano Letters* **2010**, *10*, 577-583.
232. Dong, P.; Wang, Y.; Guo, L.; Liu, B.; Xin, S.; Zhang, J.; Shi, Y.; Zeng, W.; Yin, S. A facile one-step solvothermal synthesis of graphene/rod-shaped TiO₂ nanocomposite and its improved photocatalytic activity. *Nanoscale* **2012**, *4*, 4641-4649.
233. Zhang, Y.; Tang, Z.; Fu, X.; Xu, Y. TiO₂- graphene nanocomposites for gas-phase photocatalytic degradation of volatile aromatic pollutant: Is TiO₂- graphene truly different from other TiO₂- carbon composite materials? *ACS nano* **2010**, *4*, 7303-7314.
234. Xin, X.; Zhou, X.; Wu, J.; Yao, X.; Liu, Z. Scalable synthesis of TiO₂/graphene nanostructured composite with high-rate performance for lithium ion batteries. *ACS nano* **2012**, *6*, 11035-11043.
235. Min, Y.; Zhang, K.; Chen, L.; Chen, Y.; Zhang, Y. Sonochemical assisted synthesis of a novel TiO₂/graphene composite for solar energy conversion. *Synth. Met.* **2012**, *162*, 827-833.
236. Zhang, X.; Sun, Y.; Cui, X.; Jiang, Z. A green and facile synthesis of TiO₂/graphene nanocomposites and their photocatalytic activity for hydrogen evolution. *Int J Hydrogen Energy* **2012**, *37*, 811-815.
237. Qiu, J.; Zhang, P.; Ling, M.; Li, S.; Liu, P.; Zhao, H.; Zhang, S. Photocatalytic synthesis of TiO₂ and reduced graphene oxide nanocomposite for lithium ion battery. *ACS Appl. Mater. Interfaces* **2012**.
238. Min, Y.; He, G.; Li, R.; Zhao, W.; Chen, Y.; Zhang, Y. Doping nitrogen anion enhanced photocatalytic activity on TiO₂ hybridized with graphene composite under solar light. *Separation and Purification Technology* **2013**, *106*, 97-104.

239. Rong, X.; Qiu, F.; Zhang, C.; Fu, L.; Wang, Y.; Yang, D. Preparation, characterization and photocatalytic application of TiO₂ graphene photocatalyst under visible light irradiation. *Ceram. Int.* **2014**.
240. Li, B.; Zhang, X.; Li, X.; Wang, L.; Han, R.; Liu, B.; Zheng, W.; Li, X.; Liu, Y. Photo-assisted preparation and patterning of large-area reduced graphene oxide–TiO₂ conductive thin film. *Chem. Commun.* **2010**, 46, 3499–3501.
241. Lee, E.; Hong, J.; Kang, H.; Jang, J. Synthesis of TiO₂ nanorod-decorated graphene sheets and their highly efficient photocatalytic activities under visible-light irradiation. *J. Hazard. Mater.* **2012**, 219–220, 13–18.
242. Chen, C.; Cai, W.; Long, M.; Zhou, B.; Wu, Y.; Wu, D.; Feng, Y. Synthesis of visible-light responsive graphene Oxide/TiO₂ composites with p/n heterojunction. *ACS Nano* **2010**.
243. Lambert, T. N.; Chavez, C. A.; Hernandez-Sanchez, B.; Lu, P.; Bell, N. S.; Ambrosini, A.; Friedman, T.; Boyle, T. J.; Wheeler, D. R.; Huber, D. L. Synthesis and characterization of titania-graphene nanocomposites. *Journal of Physical Chemistry C* **2009**, 113, 19812–19823.
244. Yang, X.; Qin, J.; Li, Y.; Zhang, R.; Tang, H. Graphene-spindle shaped TiO₂ mesocrystal composites: Facile synthesis and enhanced visible light photocatalytic performance. *J. Hazard. Mater.* .
245. Zhang, X.; Li, H.; Cui, X.; Lin, Y. Graphene/TiO₂ nanocomposites: Synthesis, characterization and application in hydrogen evolution from water photocatalytic splitting. *Journal of Materials Chemistry* **2010**, 20, 2801–2806.
246. Kemp, K. C.; Seema, H.; Saleh, M.; Le, N. H.; Mahesh, K.; Chandra, V.; Kim, K. S. Environmental applications using graphene composites: Water remediation and gas adsorption. *Nanoscale* **2013**, 5, 3149–3171.
247. Wang, D.; Li, X.; Chen, J.; Tao, X. Enhanced photoelectrocatalytic activity of reduced graphene oxide/TiO₂ composite films for dye degradation. *Chem. Eng. J.*
248. Gao, Y.; Pu, X.; Zhang, D.; Ding, G.; Shao, X.; Ma, J. Combustion synthesis of graphene oxide–TiO₂ hybrid materials for photodegradation of methyl orange. *Carbon* **2012**, 50, 4093–4101.
249. Zhao, D.; Sheng, G.; Chen, C.; Wang, X. Enhanced photocatalytic degradation of methylene blue under visible irradiation on graphene/TiO₂ dyade structure. *Applied Catalysis B: Environmental* **2012**, 111–112, 303–308.

250. Zhu, L.; Ghosh, T.; Park, C.; Meng, Z.; Oh, W. Enhanced sonocatalytic degradation of rhodamine B by graphene-TiO₂ composites synthesized by an ultrasonic-assisted method. *Chinese Journal of Catalysis* **2012**, 33, 1276-1283.
251. Yoo, D.; Cuong, T. V.; Pham, V. H.; Chung, J. S.; Khoa, N. T.; Kim, E. J.; Hahn, S. H. Enhanced photocatalytic activity of graphene oxide decorated on TiO₂ films under UV and visible irradiation. *Current Applied Physics* **2011**, 11, 805-808.
252. Wang, D.; Li, X.; Chen, J.; Tao, X. Enhanced photoelectrocatalytic activity of reduced graphene oxide/TiO₂ composite films for dye degradation. *Chem. Eng. J.* **2012**, 198-199, 547-554.
253. Zhang, H.; Lv, X.; Li, Y.; Wang, Y.; Li, J. P25-graphene composite as a high performance photocatalyst. *ACS Nano* **2010**, 4, 380-386.
254. Liang, Y.; Wang, H.; Casalongue, H. S.; Chen, Z.; Dai, H. TiO₂ nanocrystals grown on graphene as advanced photocatalytic hybrid materials. *Nano Research* **2010**, 3, 701-705.
255. Glassford, K. M.; Chelikowsky, J. R. Structural and electronic properties of titanium dioxide. *Phys. Rev. B* **1992**, 46, 1284-1298.
256. Chen, X.; Mao, S. S. Titanium dioxide nanomaterials: Synthesis, properties, modifications, and applications. *ChemInform* **2007**, 38, no-no.
257. Bell, N. J.; Ng, Y. H.; Du, A.; Coster, H.; Smith, S. C.; Amal, R. Understanding the enhancement in photoelectrochemical properties of photocatalytically prepared TiO₂-reduced graphene oxide composite. *The Journal of Physical Chemistry C* **2011**, 115, 6004-6009.
258. Gan, Z.; Wu, X.; Meng, M.; Zhu, X.; Yang, L.; Chu, P. K. Photothermal contribution to enhanced photocatalytic performance of graphene-based nanocomposites. *ACS nano* **2014**, 8, 9304-9310.
259. Adán-Más, A.; Wei, D. Photoelectrochemical properties of graphene and its derivatives. *Nanomaterials* **2013**, 3, 325-356.
260. Deegan, A. Pharmaceuticals in industrial wastewater and their removal using photo-Fenton's oxidation **2011**.
261. Chen, D.; Huang, F.; Cheng, Y.; Caruso, R. A. Mesoporous anatase TiO₂ beads with high surface areas and controllable pore sizes: A superior candidate for High-Performance Dye-Sensitized solar cells. *Adv Mater* **2009**, 21, 2206-2210.

262. Atkins, P. W. Physical chemistry, 1990. EDN **1978**, 4, 144.
263. Primer, A. Fundamentals of UV-visible spectroscopy. Copyright Hewlett-Packard Company, Hewlett-Packard publication.
264. Cullity, B. D. Elements of X-ray diffraction; Addison-Wesley Reading: 1978.
265. Park, J. S.; Reina, A.; Saito, R.; Kong, J.; Dresselhaus, G.; Dresselhaus, M. S. G' band raman spectra of single, double and triple layer graphene. Carbon **2009**, 47, 1303-1310.
266. Ferrari, A. C. Raman spectrum of graphene and graphene layers. Phys. Rev. Lett. **2006**, 97, 187401.
267. Behabtu, N.; Lomeda, J. R.; Green, M. J.; Higginbotham, A. L.; Sinitskii, A.; Kosynkin, D. V.; Tsentalovich, D.; Parra-Vasquez, A. N. G.; Schmidt, J.; Kesselman, E. Spontaneous high-concentration dispersions and liquid crystals of graphene. Nature nanotechnology **2010**, 5, 406-411.
268. Daughton, C. Pharmaceuticals as environmental pollutants: The ramifications for human exposure. International Encyclopedia of Public Health **2008**, 5, 66-168.
269. Stackelberg, P. E.; Gibs, J.; Furlong, E. T.; Meyer, M. T.; Zaugg, S. D.; Lippincott, R. L. Efficiency of conventional drinking-water-treatment processes in removal of pharmaceuticals and other organic compounds. Sci. Total Environ. **2007**, 377, 255-272.
270. Carlsson, C.; Johansson, A.; Alvan, G.; Bergman, K.; Kühler, T. Are pharmaceuticals potent environmental pollutants?: Part I: Environmental risk assessments of selected active pharmaceutical ingredients. Sci. Total Environ. **2006**, 364, 67-87.
271. Baumgarten, S.; Schröder, H. F.; Charwath, C.; Lange, M.; Beier, S.; Pinnekamp, J. Evaluation of advanced treatment technologies for the elimination of pharmaceutical compounds. Water Science and Technology **2007**, 56, 1-8.
272. Radjenovic, J.; Petrovic, M.; Barceló, D. Analysis of pharmaceuticals in wastewater and removal using a membrane bioreactor. Analytical and Bioanalytical Chemistry **2007**, 387, 1365-1377.
273. Radjenović, J.; Petrović, M.; Ventura, F.; Barceló, D. Rejection of pharmaceuticals in nanofiltration and reverse osmosis membrane drinking water treatment. Water Res. **2008**, 42, 3601-3610.

274. Molinari, R.; Pirillo, F.; Loddo, V.; Palmisano, L. Heterogeneous photocatalytic degradation of pharmaceuticals in water by using polycrystalline TiO₂ and a nanofiltration membrane reactor. *Catalysis Today* **2006**, 118, 205-213.
275. Ali, I.; Gupta, V. Advances in water treatment by adsorption technology. *Nature Protocols* **2007**, 1, 2661-2667.
276. Chong, M. N.; Jin, B.; Chow, C. W. K.; Saint, C. Recent developments in photocatalytic water treatment technology: A review. *Water Res.* **2010**, 44, 2997-3027.
277. Selishchev, D. S.; Kolinko, P. A.; Kozlov, D. V. Adsorbent as an essential participant in photocatalytic processes of water and air purification: Computer simulation study. *Applied Catalysis A: General* **2010**, 377, 140-149.
278. Zhang, W.; Zou, L.; Wang, L. Photocatalytic TiO₂/adsorbent nanocomposites prepared via wet chemical impregnation for wastewater treatment: A review. *Applied Catalysis A: General* **2009**, 371, 1-9.
279. Leary, R.; Westwood, A. Carbonaceous nanomaterials for the enhancement of TiO₂ photocatalysis. *Carbon*, In Press, Corrected Proof.
280. Ansón-Casaos, A.; Tacchini, I.; Unzué, A.; Martínez, M. T. Combined modification of a TiO₂ photocatalyst with two different carbon forms. *Appl. Surf. Sci.* **2013**, 270, 675-684.
281. Shao, X.; Lu, W.; Zhang, R.; Pan, F. Enhanced photocatalytic activity of TiO₂-C hybrid aerogels for methylene blue degradation. *Scientific reports* **2013**, 3.
282. Wang, H.; Yuan, X.; Wu, Y.; Huang, H.; Peng, X.; Zeng, G.; Zhong, H.; Liang, J.; Ren, M. Graphene-based materials: Fabrication, characterization and application for the decontamination of wastewater and wastegas and hydrogen storage/generation. *Adv. Colloid Interface Sci.* **2013**, 195-196, 19-40.
283. Loh, K. P.; Bao, Q.; Ang, P. K.; Yang, J. The chemistry of graphene. *Journal of Materials Chemistry* **2010**, 20, 2277-2289.
284. Nethravathi, C.; Rajamathi, M. Chemically modified graphene sheets produced by the solvothermal reduction of colloidal dispersions of graphite oxide. *Carbon* **2008**, 46, 1994-1998.

285. Zhou, Y.; Bao, Q.; Tang, L. A. L.; Zhong, Y.; Loh, K. P. Hydrothermal dehydration for the “green” reduction of exfoliated graphene oxide to graphene and demonstration of tunable optical limiting properties. *Chemistry of Materials* **2009**, 21, 2950-2956.
286. Dubin, S.; Gilje, S.; Wang, K.; Tung, V. C.; Cha, K.; Hall, A. S.; Farrar, J.; Varshneya, R.; Yang, Y.; Kaner, R. B. A one-step, solvothermal reduction method for producing reduced graphene oxide dispersions in organic solvents. *ACS Nano* **2010**, 4, 3845-3852.
287. Park, S.; An, J.; Jung, I.; Piner, R. D.; An, S. J.; Li, X.; Velamakanni, A.; Ruoff, R. S. Colloidal suspensions of highly reduced graphene oxide in a wide variety of organic solvents. *Nano letters* **2009**, 9, 1593-1597.
288. Zhang, J.; Yang, H.; Shen, G.; Cheng, P.; Zhang, J.; Guo, S. Reduction of graphene oxide vial-ascorbic acid. *Chemical Communications* **2010**, 46, 1112-1114.
289. Liang, M.; Wang, J.; Luo, B.; Qiu, T.; Zhi, L. High-efficiency and room-temperature reduction of graphene oxide: A facile green approach towards flexible graphene films. *Small* **2012**, 8, 1180-1184.
290. Li, Y.; Du, Q.; Liu, T.; Peng, X.; Wang, J.; Sun, J.; Wang, Y.; Wu, S.; Wang, Z.; Xia, Y.; Xia, L. Comparative study of methylene blue dye adsorption onto activated carbon, graphene oxide, and carbon nanotubes. *Chem. Eng. Res. Design* **2013**, 91, 361-368.
291. Ramesha, G. K.; Vijaya Kumara, A.; Muralidhara, H. B.; Sampath, S. Graphene and graphene oxide as effective adsorbents toward anionic and cationic dyes. *J. Colloid Interface Sci.* **2011**, 361, 270-277.
292. Zhao, G.; Jiang, L.; He, Y.; Li, J.; Dong, H.; Wang, X.; Hu, W. Sulfonated graphene for persistent aromatic pollutant management. *Adv Mater* **2011**, 23, 3959-3963.
293. Xu, J.; Wang, L.; Zhu, Y. Decontamination of bisphenol A from aqueous solution by graphene adsorption. *Langmuir* **2012**, 28, 8418-8425.
294. He, Y.; Liu, Y.; Wu, T.; Ma, J.; Wang, X.; Gong, Q.; Kong, W.; Xing, F.; Liu, Y.; Gao, J. An environmentally friendly method for the fabrication of reduced graphene oxide foam with a super oil absorption capacity. *J. Hazard. Mater.* **2013**, 260, 796-805.
295. Yang, S.; Chen, S.; Chang, Y.; Cao, A.; Liu, Y.; Wang, H. Removal of methylene blue from aqueous solution by graphene oxide. *J. Colloid Interface Sci.* **2011**, 359, 24-29.

296. Zhang, W.; Zhou, C.; Zhou, W.; Lei, A.; Zhang, Q.; Wan, Q.; Zou, B. Fast and considerable adsorption of methylene blue dye onto graphene oxide. *Bull. Environ. Contam. Toxicol.* **2011**, 87, 86-90.
297. Sun, L.; Yu, H.; Fugetsu, B. Graphene oxide adsorption enhanced by in situ reduction with sodium hydrosulfite to remove acridine orange from aqueous solution. *J. Hazard. Mater.* **2012**, 203-204, 101-110.
298. Wu, T.; Cai, X.; Tan, S.; Li, H.; Liu, J.; Yang, W. Adsorption characteristics of acrylonitrile, p-toluenesulfonic acid, 1-naphthalenesulfonic acid and methyl blue on graphene in aqueous solutions. *Chem. Eng. J.* **2011**, 173, 144-149.
299. Wang, S.; Sun, H.; Ang, H. M.; Tadé, M. O. Adsorptive remediation of environmental pollutants using novel graphene-based nanomaterials. *Chem. Eng. J.* **2013**, 226, 336-347.
300. Duquesne, S.; Bras, M. L.; Bourbigot, S.; Delobel, R.; Vezin, H.; Camino, G.; Eling, B.; Lindsay, C.; Roels, T. Expandable graphite: A fire retardant additive for polyurethane coatings. *Fire Mater.* **2003**, 27, 103-117.
301. Niyogi, S.; Bekyarova, E.; Itkis, M. E.; McWilliams, J. L.; Hamon, M. A.; Haddon, R. C. Solution properties of graphite and graphene. *J. Am. Chem. Soc.* **2006**, 128, 7720-7721.
302. Buchsteiner, A.; Lerf, A.; Pieper, J. Water dynamics in graphite oxide investigated with neutron scattering. *The Journal of Physical Chemistry B* **2006**, 110, 22328-22338.
303. Mellor, J. D. *Fundamentals of freeze-drying*. Academic Press Inc.(London) Ltd.: 1978; .
304. Schniepp, H. C.; Li, J.; McAllister, M. J.; Sai, H.; Herrera-Alonso, M.; Adamson, D. H.; Prud'homme, R. K.; Car, R.; Saville, D. A.; Aksay, I. A. Functionalized single graphene sheets derived from splitting graphite oxide. *J Phys Chem B* **2006**, 110, 8535-8539.
305. Loh, K. P.; Bao, Q.; Ang, P. K.; Yang, J. The chemistry of graphene. *Journal of Materials Chemistry* **2010**, 20, 2277-2289.
306. Gómez-Navarro, C.; Meyer, J. C.; Sundaram, R. S.; Chuvilin, A.; Kurasch, S.; Burghard, M.; Kern, K.; Kaiser, U. Atomic structure of reduced graphene oxide. *Nano Lett.* **2010**, 10, 1144-1148.
307. Terrones, M.; Botello-Méndez, A. R.; Campos-Delgado, J.; López-Urías, F.; Vega-Cantú, Y. I.; Rodríguez-Macías, F. J.; Elías, A. L.; Muñoz-Sandoval, E.; Cano-Márquez, A. G.; Charlier, J.;

- Terrones, H. Graphene and graphite nanoribbons: Morphology, properties, synthesis, defects and applications. *Nano Today* **2010**, 5, 351-372.
308. Szabó, T.; Berkesi, O.; Forgó, P.; Josepovits, K.; Sanakis, Y.; Petridis, D.; Dékány, I. Evolution of surface functional groups in a series of progressively oxidized graphite oxides. *Chemistry of materials* **2006**, 18, 2740-2749.
309. Szabó, T.; Berkesi, O.; Forgó, P.; Josepovits, K.; Sanakis, Y.; Petridis, D.; Dékány, I. Evolution of surface functional groups in a series of progressively oxidized graphite oxides. *Chemistry of materials* **2006**, 18, 2740-2749.
310. Szabó, T.; Tombácz, E.; Illés, E.; Dékány, I. Enhanced acidity and pH-dependent surface charge characterization of successively oxidized graphite oxides. *Carbon* **2006**, 44, 537-545.
311. Becerril, H. A.; Mao, J.; Liu, Z.; Stoltenberg, R. M.; Bao, Z.; Chen, Y. Evaluation of solution-processed reduced graphene oxide films as transparent conductors. *ACS nano* **2008**, 2, 463-470.
312. Huh, S. H. Thermal reduction of graphene oxide. *Physics and Applications of Graphene—Experiments* **2011**, 5.
313. Gao, X.; Jang, J.; Nagase, S. Hydrazine and thermal reduction of graphene oxide: Reaction mechanisms, product structures, and reaction design. *The Journal of Physical Chemistry C* **2009**, 114, 832-842.
314. Medhekar, N. V.; Ramasubramaniam, A.; Ruoff, R. S.; Shenoy, V. B. Hydrogen bond networks in graphene oxide composite paper: Structure and mechanical properties. *ACS nano* **2010**, 4, 2300-2306.
315. Krishnamurthy, S.; Lightcap, I. V.; Kamat, P. V. Electron transfer between methyl viologen radicals and graphene oxide: Reduction, electron storage and discharge. *J. Photochem. Photobiol. A.* **2011**, 221, 214-219.
316. McAllister, M. J.; Li, J.; Adamson, D. H.; Schniepp, H. C.; Abdala, A. A.; Liu, J.; Herrera-Alonso, M.; Milius, D. L.; Car, R.; Prud'homme, R. K.; Aksay, I. A. Single sheet functionalized graphene by oxidation and thermal expansion of graphite. *Chem. Mater.* **2007**, 19, 4396-4404.
317. Ishigami, M.; Chen, J.; Cullen, W.; Fuhrer, M.; Williams, E. Atomic structure of graphene on SiO₂. *Nano Letters* **2007**, 7, 1643-1648.

318. Santamarina, J.; Klein, K.; Wang, Y.; Prencke, E. Specific surface: Determination and relevance. *Canadian Geotechnical Journal* **2002**, 39, 233-241.
319. Marcano, D. C.; Kosynkin, D. V.; Berlin, J. M.; Sinitskii, A.; Sun, Z.; Slesarev, A.; Alemany, L. B.; Lu, W.; Tour, J. M. Improved synthesis of graphene oxide. *ACS Nano* **2010**, 4, 4806-4814.
320. Li, D.; Müller, M. B.; Gilje, S.; Kaner, R. B.; Wallace, G. G. Processable aqueous dispersions of graphene nanosheets. *Nature nanotechnology* **2008**, 3, 101-105.
321. Malard, L. M.; Pimenta, M. A.; Dresselhaus, G.; Dresselhaus, M. S. Raman spectroscopy in graphene. *Physics Reports* **2009**, 473, 51-87.
322. Dan, B.; Behabtu, N.; Martinez, A.; Evans, J. S.; Kosynkin, D. V.; Tour, J. M.; Pasquali, M.; Smalyukh, I. I. Liquid crystals of aqueous, giant graphene oxide flakes. *Soft Matter* **2011**, 7, 11154-11159.
323. Ni, Z.; Wang, Y.; Yu, T.; Shen, Z. Raman spectroscopy and imaging of graphene. *Nano Research* **2008**, 1, 273-291.
324. Ferrari, A.; Robertson, J. Interpretation of Raman spectra of disordered and amorphous carbon. *Physical review B* **2000**, 61, 14095.
325. Yang, D.; Velamakanni, A.; Bozoklu, G.; Park, S.; Stoller, M.; Piner, R. D.; Stankovich, S.; Jung, I.; Field, D. A.; Ventrice Jr, C. A. Chemical analysis of graphene oxide films after heat and chemical treatments by X-ray photoelectron and micro-Raman spectroscopy. *Carbon* **2009**, 47, 145-152.
326. Karaca, S.; Gürses, A.; Ejder, M.; Açıkyıldız, M. Adsorptive removal of phosphate from aqueous solutions using raw and calcinated dolomite. *J. Hazard. Mater.* **2006**, 128, 273-279.
327. Walker, G. M.; Hansen, L.; Hanna, J. ; Allen, S. J. Kinetics of a reactive dye adsorption onto dolomitic sorbents. *Water Res.* **2003**, 37, 2081-2089.
328. Stefaniak, E.; Bilinski, B.; Dobrowolski, R.; Staszczuk, P.; Wójcik, J. The influence of preparation conditions on adsorption properties and porosity of dolomite-based sorbents. *Colloids Surf. Physicochem. Eng. Aspects* **2002**, 208, 337-345.
329. Karaca, S.; Gürses, A.; Ejder, M.; Açıkyıldız, M. Adsorptive removal of phosphate from aqueous solutions using raw and calcinated dolomite. *J. Hazard. Mater.* **2006**, 128, 273-279.

330. Namasivayam, C.; Kavitha, D. Removal of congo red from water by adsorption onto activated carbon prepared from coir pith, an agricultural solid waste. *Dyes and Pigments* **2002**, 54, 47-58.
331. Pereira, M. F. R.; Soares, S. F.; Órfão, J. J.; Figueiredo, J. L. Adsorption of dyes on activated carbons: Influence of surface chemical groups. *Carbon* **2003**, 41, 811-821.
332. Faria, P. C. C.; Órfão, J. J. M.; Pereira, M. F. R. Adsorption of anionic and cationic dyes on activated carbons with different surface chemistries. *Water Res.* **2004**, 38, 2043-2052.
333. Fini, A.; Cavallari, C.; Ospitali, F. Diclofenac salts. V. examples of polymorphism among diclofenac salts with alkyl-hydroxy amines studied by DSC and HSM. *Pharmaceutics* **2010**, 2, 136-158.
334. Fini, A.; Garuti, M.; Fazio, G.; Alvarez-Fuentes, J.; Holgado, M. Diclofenac salts. I. fractal and thermal analysis of sodium and potassium diclofenac salts. *J. Pharm. Sci.* **2001**, 90, 2049-2057.
335. Fini, A.; Fazio, G.; Fernandez-Hervas, M.; Holgado, M.; Rabasco, A. Influence of crystallization solvent and dissolution behaviour for a diclofenac salt. *Int. J. Pharm.* **1995**, 121, 19-26.
336. Pei, Z.; Li, L.; Sun, L.; Zhang, S.; Shan, X.; Yang, S.; Wen, B. Adsorption characteristics of 1,2,4-trichlorobenzene, 2,4,6-trichlorophenol, 2-naphthol and naphthalene on graphene and graphene oxide. *Carbon*.
337. Liu, T.; Li, Y.; Du, Q.; Sun, J.; Jiao, Y.; Yang, G.; Wang, Z.; Xia, Y.; Zhang, W.; Wang, K.; Zhu, H.; Wu, D. Adsorption of methylene blue from aqueous solution by graphene. *Colloids and Surfaces B: Biointerfaces* **2012**, 90, 197-203.
338. Li, Y.; Du, Q.; Liu, T.; Sun, J.; Jiao, Y.; Xia, Y.; Xia, L.; Wang, Z.; Zhang, W.; Wang, K.; Zhu, H.; Wu, D. Equilibrium, kinetic and thermodynamic studies on the adsorption of phenol onto graphene. *Mater. Res. Bull.* **2012**, 47, 1898-1904.
339. Song, H. S.; Ko, C. H.; Ahn, W.; Kim, B.; Croiset, E.; Chen, Z.; Nam, S. Selective dibenzothiophene adsorption on graphene prepared using different methods. *Ind Eng Chem Res* **2012**.
340. Ji, L.; Chen, W.; Duan, L.; Zhu, D. Mechanisms for strong adsorption of tetracycline to carbon nanotubes: A comparative study using activated carbon and graphite as adsorbents. *Environ. Sci. Technol.* **2009**, 43, 2322-2327.

341. He, Y. Q.; Zhang, N. N.; Wang, X. D. Adsorption of graphene oxide/chitosan porous materials for metal ions. *Chinese Chemical Letters* **2011**, 22, 859-862.
342. Ghaly, M. Y.; Jamil, T. S.; El-Seesy, I. E.; Souaya, E. R.; Nasr, R. A. Treatment of highly polluted paper mill wastewater by solar photocatalytic oxidation with synthesized nano TiO₂. *Chem. Eng. J.* **2011**, 168, 446-454.
343. Friedmann, D.; Mendive, C.; Bahnemann, D. TiO₂ for water treatment: Parameters affecting the kinetics and mechanisms of photocatalysis. *Applied Catalysis B: Environmental* **2010**, 99, 398-406.
344. McCullagh, C.; Robertson, P. K. J.; Adams, M.; Pollard, P. M.; Mohammed, A. Development of a slurry continuous flow reactor for photocatalytic treatment of industrial waste water. *J. Photochem. Photobiol. A* **2010**, 211, 42-46.
345. Hofstadler, K.; Bauer, R.; Novalic, S.; Heisler, G. New reactor design for photocatalytic wastewater treatment with TiO₂ immobilized on fused-silica glass fibers: Photomineralization of 4-chlorophenol. *Environ. Sci. Technol.* **1994**, 28, 670-674.
346. Wang, Y.; Hong, C. TiO₂-mediated photomineralization of 2-chlorobiphenyl: The role of O₂. *Water Res.* **2000**, 34, 2791-2797.
347. Zhang, H.; Lv, X.; Li, Y.; Wang, Y.; Li, J. P25-graphene composite as a high performance photocatalyst. *ACS Nano* **2009**, 4, 380-386.
348. Qin, H.; Xu, Y.; Kim, J.; Hwang, T.; Kim, T. The effect of structure on the photoactivity of a graphene/TiO₂ composite. *Materials Science and Engineering: B*.
349. Ismail, A. A.; Geioushy, R. A.; Bouzid, H.; Al-Sayari, S. A.; Al-Hajry, A.; Bahnemann, D. W. TiO₂ decoration of graphene layers for highly efficient photocatalyst: Impact of calcination at different gas atmosphere on photocatalytic efficiency. *Applied Catalysis B: Environmental* **2013**, 129, 62-70.
350. Khalid, N. R.; Ahmed, E.; Hong, Z.; Sana, L.; Ahmed, M. Enhanced photocatalytic activity of graphene-TiO₂ composite under visible light irradiation. *Current Applied Physics* **2013**, 13, 659-663.
351. Shen, J.; Long, Y.; Li, T.; Shi, M.; Li, N.; Ye, M. One-pot polyelectrolyte assisted hydrothermal synthesis of TiO₂-reduced graphene oxide nanocomposite. *Mater. Chem. Phys.* **2012**, 133, 480-486.

352. Shi, M.; Shen, J.; Ma, H.; Li, Z.; Lu, X.; Li, N.; Ye, M. Preparation of graphene-TiO₂ composite by hydrothermal method from peroxotitanium acid and its photocatalytic properties. *Colloids Surf. Physicochem. Eng. Aspects* **2012**, 405, 30-37.
353. Qi, X. Upconversion-P25-graphene composite as an advanced sun light driven photocatalytic hybrid materials. *J. Mater. Chem.* **2012**.
354. Manga, K. K.; Zhou, Y.; Yan, Y.; Loh, K. P. Multilayer hybrid films consisting of alternating graphene and titania nanosheets with ultrafast electron transfer and photoconversion properties. *Advanced Functional Materials* **2009**, 19, 3638-3643.
355. Lambert, T. N.; Chavez, C. A.; Hernandez-Sanchez, B.; Lu, P.; Bell, N. S.; Ambrosini, A.; Friedman, T.; Boyle, T. J.; Wheeler, D. R.; Huber, D. L. Synthesis and characterization of TitaniaâGraphene nanocomposites. *The Journal of Physical Chemistry C* **2009**, 113, 19812-19823.
356. Wang, F.; Zhang, K. Reduced graphene oxide-TiO₂ nanocomposite with high photocatalytic activity for the degradation of rhodamine B. *Journal of Molecular Catalysis A: Chemical* **2011**, 345, 101-107.
357. Perera, S. D.; Mariano, R. G.; Nijem, N.; Chabal, Y.; Ferraris, J. P.; Balkus Jr., K. J. Alkaline deoxygenated graphene oxide for supercapacitor applications: An effective green alternative for chemically reduced graphene. *J. Power Sources* **2012**, 215, 1-10.
358. Li, Y.; Chu, J.; Qi, J.; Li, X. An easy and novel approach for the decoration of graphene oxide by Fe₃O₄ nanoparticles. *Appl. Surf. Sci.* **2011**, 257, 6059-6062.
359. Humaira Seema and K Christian Kemp and Vimlesh Chandra and Kwang,S.Kim Graphene-SnO₂ composites for highly efficient photocatalytic degradation of methylene blue under sunlight. *Nanotechnology* **2012**, 23, 355705.
360. Sreeprasad, T. S.; Maliyekkal, S. M.; Lisha, K. P.; Pradeep, T. Reduced graphene oxide-metal/metal oxide composites: Facile synthesis and application in water purification. *J. Hazard. Mater.* **2011**, 186, 921-931.
361. Wang, H.; Robinson, J. T.; Diankov, G.; Dai, H. Nanocrystal growth on graphene with various degrees of oxidation. *J. Am. Chem. Soc.* **2010**, 132, 3270-3271.
362. Wang, H.; Robinson, J. T.; Li, X.; Dai, H. Solvothermal reduction of chemically exfoliated graphene sheets. *J. Am. Chem. Soc.* **2009**, 131, 9910-9911.

363. Li, X.; Zhang, G.; Bai, X.; Sun, X.; Wang, X.; Wang, E.; Dai, H. Highly conducting graphene sheets and Langmuir–Blodgett films. *Nature nanotechnology* **2008**, 3, 538–542.
364. Lotya, M.; King, P. J.; Khan, U.; De, S.; Coleman, J. N. High-concentration, surfactant-stabilized graphene dispersions. *ACS Nano* **2010**, 4, 3155–3162.
365. Ng, Y. H.; Lightcap, I. V.; Goodwin, K.; Matsumura, M.; Kamat, P. V. To what extent do graphene scaffolds improve the photovoltaic and photocatalytic response of TiO₂ nanostructured films? *The Journal of Physical Chemistry Letters* **2010**, 1, 2222–2227.
366. Zhang, Y.; Tang, Z. -.; Fu, X.; Xu, Y. -. Engineering the unique 2D mat of graphene to achieve graphene-TiO₂ nanocomposite for photocatalytic selective transformation: What advantage does graphene have over its forebear carbon nanotube? *ACS Nano* **2011**, 5, 7426–7435.
367. Wang, J.; Zhou, Y.; Xiong, B.; Zhao, Y.; Huang, X.; Shao, Z. Fast lithium-ion insertion of TiO₂ nanotube and graphene composites. *Electrochim. Acta* **2013**, 88, 847–857.
368. Yang, Z.; Du, G.; Meng, Q.; Guo, Z.; Yu, X.; Chen, Z.; Guo, T.; Zeng, R. Synthesis of uniform TiO₂@ carbon composite nanofibers as anode for lithium ion batteries with enhanced electrochemical performance. *Journal of Materials Chemistry* **2012**, 22, 5848–5854.
369. Lin, Y.; Weng, C.; Lin, Y.; Shiesh, C.; Chen, F. Effect of C content and calcination temperature on the photocatalytic activity of C-doped TiO₂ catalyst. *Separation and Purification Technology* **2013**, 116, 114–123.
370. Zhang, H.; Du, G.; Lu, W.; Cheng, L.; Zhu, X.; Jiao, Z. Porous TiO₂ hollow nanospheres: Synthesis, characterization and enhanced photocatalytic properties. *CrystEngComm* **2012**, 14, 3793–3801.
371. Zhang, Y.; Wan, J.; Ke, Y. A novel approach of preparing TiO₂ films at low temperature and its application in photocatalytic degradation of methyl orange. *J. Hazard. Mater.* **2010**, 177, 750–754.
372. Ao, Y.; Xu, J.; Fu, D.; Shen, X.; Yuan, C. Low temperature preparation of anatase TiO₂-coated activated carbon. *Colloids Surf. Physicochem. Eng. Aspects* **2008**, 312, 125–130.
373. Liu, G.; Yang, H. G.; Sun, C.; Cheng, L.; Wang, L.; Lu, G. Q. M.; Cheng, H. Titania polymorphs derived from crystalline titanium diboride. *CrystEngComm* **2009**, 11, 2677–2682.

374. Swamy, V.; Kuznetsov, A.; Dubrovinsky, L. S.; Caruso, R. A.; Shchukin, D. G.; Muddle, B. C. Finite-size and pressure effects on the raman spectrum of nanocrystalline anatase TiO₂. *Physical Review B* **2005**, 71, 184302.
375. Zhu, K.; Zhang, M.; Chen, Q.; Yin, Z. Size and phonon-confinement effects on low-frequency Raman mode of anatase TiO₂ nanocrystal. *Physics Letters A*, **2005**, 340, 220-227.
376. Balaji, S.; Djaoued, Y.; Robichaud, J. Phonon confinement studies in nanocrystalline anatase-TiO₂ thin films by micro Raman spectroscopy. *J. Raman Spectrosc.* **2006**, 37, 1416-1422.
377. Xue, X.; Ji, W.; Mao, Z.; Mao, H.; Wang, Y.; Wang, X.; Ruan, W.; Zhao, B.; Lombardi, J. R. Raman investigation of nanosized TiO₂: Effect of crystallite size and quantum confinement. *The Journal of Physical Chemistry C* **2012**, 116, 8792-8797.
378. Malik, P. K. Dye removal from wastewater using activated carbon developed from sawdust: Adsorption equilibrium and kinetics. *J. Hazard. Mater.* **2004**, 113, 81-88.
379. Mall, I. D.; Srivastava, V. C.; Agarwal, N. K.; Mishra, I. M. Removal of congo red from aqueous solution by bagasse fly ash and activated carbon: Kinetic study and equilibrium isotherm analyses. *Chemosphere* **2005**, 61, 492-501.
380. Stauffer, D.; Aharony, A. *Introduction to percolation theory*; CRC press: 1994.
381. Coleman, J. N.; Curran, S.; Dalton, A.; Davey, A.; McCarthy, B.; Blau, W.; Barklie, R. Percolation-dominated conductivity in a conjugated-polymer-carbon-nanotube composite. *Physical Review B* **1998**, 58, R7492.
382. Vietmeyer, F.; Seger, B.; Kamat, P. V. Anchoring ZnO particles on functionalized single wall carbon nanotubes: excited state interactions and charge collection. *Adv Mater* **2007**, 19, 2935-2940.
383. Williams, G.; Kamat, P. V. Graphene– semiconductor nanocomposites: Excited-state interactions between ZnO nanoparticles and graphene oxide. *Langmuir* **2009**, 25, 13869-13873.
384. Fujishima, A.; Zhang, X.; Tryk, D. A. TiO₂ photocatalysis and related surface phenomena. *Surface Science Reports* **2008**, 63, 515-582.
385. Linsebigler, A. L.; Lu, G.; Yates Jr, J. T. Photocatalysis on TiO₂ surfaces: Principles, mechanisms, and selected results. *Chem. Rev.* **1995**, 95, 735-758.

386. Aryal, S.; Kim, C. K.; Kim, K.; Khil, M. S.; Kim, H. Y. Multi-walled carbon nanotubes/TiO₂ composite nanofiber by electrospinning. *Materials Science and Engineering: C* **2008**, 28, 75-79.
387. Ou, H.; Lo, S. Review of Titania nanotubes synthesized via the hydrothermal treatment: Fabrication, modification, and application. *Separation and Purification Technology* **2007**, 58, 179-191.
388. Bavykin, D. V.; Parmon, V. N.; Lapkin, A. A.; Walsh, F. C. The effect of hydrothermal conditions on the mesoporous structure of TiO₂ nanotubes. *J. Mater. Chem.* **2004**, 14, 3370-3377.
389. Bavykin, D. V.; Friedrich, J. M.; Walsh, F. C. Protonated titanates and TiO₂ nanostructured materials: Synthesis, properties, and applications. *Adv Mater* **2006**, 18, 2807-2824.
390. Qamar, M.; Yoon, C. R.; Oh, H. J.; Lee, N. H.; Park, K.; Kim, D. H.; Lee, K. S.; Lee, W. J.; Kim, S. J. Preparation and photocatalytic activity of nanotubes obtained from titanium dioxide. *Catalysis Today* **2008**, 131, 3-14.
391. Gao, T.; Fjellvåg, H.; Norby, P. Crystal structures of titanate nanotubes: A Raman scattering study. *Inorg. Chem.* **2009**, 48, 1423-1432.
392. Ma, R.; Fukuda, K.; Sasaki, T.; Osada, M.; Bando, Y. Structural features of titanate nanotubes/nanobelts revealed by Raman, X-ray absorption fine structure and electron diffraction characterizations. *The Journal of Physical Chemistry B* **2005**, 109, 6210-6214.
393. Tsai, C.; Teng, H. Structural features of nanotubes synthesized from NaOH treatment on TiO₂ with different post-treatments. *Chemistry of Materials* **2006**, 18, 367-373.
394. Chen, Q.; Du, G. H.; Zhang, S.; Peng, L. The structure of trititanate nanotubes. *Acta Crystallographica Section B* **2002**, 58, 587-593.
395. Hoffmann, M. R.; Martin, S. T.; Choi, W.; Bahnemann, D. W. Environmental applications of semiconductor photocatalysis. *Chem. Rev.* **1995**, 95, 69-96.
396. Wang, W.; Serp, P.; Kalck, P.; Faria, J. L. Visible light photodegradation of phenol on MWNT-TiO₂ composite catalysts prepared by a modified sol-gel method. *Journal of Molecular Catalysis A: Chemical* **2005**, 235, 194-199.
397. Yang, Y.; Wang, H.; Li, X.; Wang, C. Electrospun mesoporous W⁶⁺-doped TiO₂ thin films for efficient visible-light photocatalysis. *Materials Letters* **2009**, 63, 331-333.

398. Kumaresan, L.; Prabhu, A.; Palanichamy, M.; Murugesan, V. Synthesis of mesoporous TiO₂ in aqueous alcoholic medium and evaluation of its photocatalytic activity. *Mater. Chem. Phys.* **2011**, *126*, 445-452.
399. Ismail, A. A.; Bahnemann, D. W. Mesoporous Titania photocatalysts: Preparation, characterization and reaction mechanisms. *J. Mater. Chem.* **2011**, *21*, 11686-11707.
400. Muniz, E. C.; Góes, M. S.; Silva, J. J.; Varela, J. A.; Joanni, E.; Parra, R.; Bueno, P. R. Synthesis and characterization of mesoporous TiO₂ nanostructured films prepared by a modified sol-gel method for application in dye solar cells. *Ceramics International*, *37*(3), 1017-1024.
401. Yu, J.; Yu, H.; Cheng, B.; Zhao, X.; Zhang, Q. Preparation and photocatalytic activity of mesoporous anatase TiO₂ nanofibers by a hydrothermal method. *Journal of Photochemistry and Photobiology A: Chemistry* **2006**, *182*, 121-127.
402. Li, N.; Liu, G.; Zhen, C.; Li, F.; Zhang, L.; Cheng, H. Battery performance and photocatalytic activity of mesoporous anatase TiO₂ Nanospheres/Graphene composites by template-free self-assembly. *Advanced Functional Materials* **2011**, *21*(9), 1717-1722